The controls of radioelement distribution in the Etive and Cairngorm granites: Implications for heat production

Thesis

THE CONTROLS OF RADIOELEMENT DISTRIBUTION IN THE ETIVE AND CAIRNGORM GRANITES : IMPLICATIONS FOR HEAT PRODUCTION.

S.D. Barritt

September 1983

Department of Earth Sciences
THE OPEN UNIVERSITY

PAGE
NUMBERS
CUT OFF
IN THE
ORIGINAL

THE CONTROLS OF RADIOELEMENT DISTRIBUTION IN THE ETIVE AND CAIRNGORM GRANITES: IMPLICATIONS FOR HEAT PRODUCTION

A thesis presented for the degree of

Doctor of Philosophy

by

Sally D. Barritt

(B.Sc. Hons. Liverpool)

Department of Earth Sciences

The Open University

Milton Keynes

Buckinghamshire

England

September 1983

ABSTRACT

Radiometric, whole rock trace element and petrological studies are reported for two late Caledonian granite complexes from the Grampian Highlands, Scotland. These studies throw light on the magmatic history of the intrusions and, more particularly, on their radioelement geochemistry and heat production which is interpreted in a geothermal context.

The Etive Complex is a multiphase intrusion, ranging from diorite to granite in composition, emplaced by a cauldron subsidence mechanism. Its complex magmatic history involved crystal fractionation, both in-situ and at depth, coupled with episodic magma mixing in a deep magma chamber. Radioelement contents (means for the whole complex; 12.7 ppm Th, 2.9 ppm U, 4.1% K_2O) increase with magmatic differentiation and are concentrically zoned in the N Cruachan and Starav units. Mass balance calculations, incorporating radiometric, whole rock trace element, fission track and accessory phase microprobe data, show that uranium and thorium contents were, initially, controlled by the crystallisation of apatite + zircon + sphene ± allanite and chevkinite. Later, thorite and monazite became important thorium-hosts. Locally, enhanced uranium levels in the Starav Granites followed expulsion and limited outward migration of uranium-rich residual fluids. The distribution of radioelements in surface samples suggests that heat production decreases with depth in some units.

Similar studies have identified four units in the Cairngorm Granite; NE Granite - Porphyritic Granite - Microgranite - Main Granite. Radioelement contents increase with magmatic evolution from the NE Granite to the Main Granite; 26.5 → 32.3 ppm Th, 4.3 → 10.1 ppm U,

4.6 → 4.7% K_2O (mean values). Uranium and thorium contents were controlled, predominantly, by the crystallisation of apatite + zircon + sphene ± allanite in the NE Granite and of apatite + zircon + monazite + xenotime + Nb-Ta-oxides ± thorite ± uraninite in the Main Granite. Minor amounts of uranium reside in secondary sites in hydrothermally altered samples.

Modelled surface heat flow anomalies are 5.8 mW m^{-2} and 23.0 mW m^{-2} for the Etive Complex and Cairngorm Granite respectively. Comparison of calculated and preliminary heat flow measurements in the Cairngorm granite indicates that at least 35% of the observed heat flow arises from radioactive sources in the granite and that background heat flow is low.

CONTENTS

LIST OF CONTENTS

LIST OF FIGURES

LIST OF TABLES

LIST OF PLATES

LIST OF APPENDICES

ACKNOWLEDGEMENTS

This research was funded by a studentship from the Open University and fission track irradiations were financed by the Institute of Geological Sciences, both of whom are gratefully acknowledged. In particular I would like to thank Peter Simpson and Heather Auld of the I.G.S. Geochemical Division for organising fission track work.

Field work was carried out with the kind permission of the Nature Conservancy Council (particularly David Holland, Aviemore), the Forestry Commission, Mr. John MacDonald (Glen Avon Estates) and Dougie (Craig cottage, a legend unto himself). All are thanked for their assistance and cooperation.

Notwithstanding the traditions fo Ph.D. acknowledgements, my sincere thanks go to Geoff Brown, who patiently supervised and encouraged my efforts throughout this study.

Phil Potts was more than instrumental in setting up analytical systems for uranium and thorium analysis; his assistance and expertise are gratefully acknowledged. Thanks also go to Olwen Thorpe, John Watson and Pete Webb for their advice and assistance with analytical procedures. Special thanks are due to Andy Tindle for useful discussion and invaluable guidance with microprobe analyses.

The technical staff of the Open University Earth Sciences laboratories, particularly Ian Chaplin, Jill Hewitt and Moira Staerck, are thanked for their speedy and excellent production of thin sections.

Steve Perkins, Kingston Polytechnic, is thanked for his hospitality and useful discussion.

Many thanks go to Richard Tyson, Don Munn, John Exton, Jill Hewitt and Dave Rothery for suffering the delights of Scottish summers and taking the weight off my back!

The production of diagrams and maps in this thesis owes much to the cartographic expertise of John Taylor and Helen Boxall (and Simon); their assistance is gratefully acknowledged.

Dave Wright, Tony Shelton, Brian Biart and the staff of the Open University Computing Services are praised for divulging the intricacies of Fortran IV and the Phoenix system.

Marilyn Leggett, who diligently typed the manuscript is gratefully acknowledged for her skill and time.

Final production of this thesis would not have been possible without the practical assistance of Simon - many thanks!

I would like to give special thanks to my family, especially Mum and Dad, for their patience, understanding and support throughout this period of study.

Last, but not least, I dedicate this thesis in memory of Sam, whose friendship and devotion will always be remembered.

CHAPTER 1 INTRODUCTION

The primary aim of the present work is to determine the factors which controlled the content and distribution of radioelements in the Etive Complex and the Cairngorm Granite. These are two post-tectonic Caledonian intrusions situated in the Grampian Highlands of Scotland. The geological and economic significance of Uranium (U), Thorium (Th) and potassium (K) and the specific aims of this study are outlined in this introductory chapter.

1.1 RADIOGENIC HEAT PRODUCTION

Most of the heat being lost by the Earth at the present time is derived from the decay of the long-lived radionuclides ^{238}U (+^{235}U), ^{232}Th and ^{40}K (see Table 1.1). The importance of terrestrial heat flow,

Element	Naturally occurring long-lived radioisotopes	Percentage of natural element	Half-life (years)	Heat productivity of natural element ($\mu W\ kg^{-1}$)
K	^{40}K	0.012	1.3×10^{9}	34.74×10^{-4}
Th	^{232}Th	100	1.39×10^{10}	25.59
U	^{238}U	99.28	4.5×10^{9}	95.21
	^{235}U	0.71	7.1×10^{8}	
	^{234}U(daughter)	0.006	2.5×10^{5}	
	^{230}Th(daughter)	-	80,000	

Table 1.1 Major, naturally occurring, long-lived radioisotopes. Both ^{234}U and ^{230}Th are daughter products in the ^{238}U decay series. Heat production constants are from Rybach (1976).

which depends upon radioactive heat production, in constructing geochemical models of the crust and upper mantle and its implications for the

mechanisms of mantle convection in plate tectonics has been well demonstrated (see for example Sclater and Francheteau, 1970; Richardson, 1975).

The heat productivity of a given rock can be calculated from its U, Th and K content using the constants in Table 1.1. By comparison with their abundance in the mantle, K, U and Th are variably, but strongly concentrated in the different igneous, metamorphic and sedimentary rocks of the Earth's crust (Table 1.2). In particular, these elements may be significantly enriched in silicic and alkaline igneous rocks. It is evident from Tables 1.1 and 1.2 that although K is the most abundant radioelement in crustal rocks, U and Th are the major heat producing elements. For example, for a granite with radioelement abundances shown in Table 1.2. U, Th and K provide 41.0%, 45.2% and 13.8% of the total whole rock heat production respectively.

An empirical linear relationship between surface heat flow, q_o, and surface heat production, Ao, has been demonstrated in several, tectonically stable, granitic and metamorphic terrains (e.g. Birch et al., 1968; Pollack and Chapman, 1977; Richardson and Oxburgh, 1979):

$$q_o = q^* + A_oD$$

Different heat flow provinces are characterised by different values of q^*, the heat production from the mantle and lower crust, and D, a function of the thickness of the upper crustal radioactive layer (see Chapter 7). There also exists a negative correlation between the 'age' of continental crust (the time since it was last involved in a crust-forming and/or orogenic event) and its surface heat flow (Sclater and Francheteau, 1970; Pollack and Chapman, 1977). Clearly, heat productivity data is important in determining these crustal parameters. In Britain, determination of q_o and A_o in granitic, low grade metasedimentary and

	U ppm	Th ppm	K %	Th/U	Density g/cm^{-3}	Heat production μWm^{-3}
Granite/Rhyolite	3.9	16.0	3.6	4.1	2.67	2.44
Granodiorite/Dacite	2.3	9.0	2.6	3.9	2.72	1.48
Diorite, Quartzdiorite/Andesite	1.7	7.1	1.1	4.1	2.82	1.08
Gabbro/Basalt	0.5	1.6	0.4	3.2	2.98	0.31
Ultramafic: Peridotite	0.02	0.06	0.006	3.0	3.23	0.01
Ultramafic: Dunite	0.03	0.01	0.0009	3.3	3.28	0.002
Carbonates					2.6	
Limestones	2.0	1.5	0.3	0.75		0.62
Dolomites	1.0	0.8	0.7	0.80		0.36
Sandstones					2.4	
Quartzites	0.6	1.8	0.9	3.0		0.33
Arkoses	1.5	5.0	2.3	3.3		0.85
Greywackes	2.0	7.0	1.4	3.5		1.06
Shales	3.7	12.0	2.7	3.2	2.4	1.82
Deep sea sediments	3.5	7.0	2.5	2.0	1.3	1.79

Table 1.2 U, Th and K abundances and radioactive heat production in rocks; from Rybach, 1976.

metavolcanic basement rocks, in locations from Cornwall to southern Scotland, define a linear trend with $q^* = 27$ mW m^{-2} and $D = 16.6$ km (Richardson and Oxburgh, 1979). This value of D is large compared to that observed in other parts of the world (4.5 - 11.1 km) and may reflect relatively unfractionated crustal heat production. This may be due to the relatively low grade of metamorphism and relative lack of igneous activity in England and Wales during late Precambrian and Palaeozoic times (Richardson and Oxburgh, 1978). Data is sparse for the high grade metamorphic and igneous terrains of Scotland which may represent a separate heat flow province.

If the parameters q^* and D remain fairly constant for any heat flow province, then upper crustal rocks with high heat production (high A_0) will correspond to areas of enhanced surface heat flow (high q_0) and, therefore, temperature gradient.

1.2 HOT DRY ROCK GEOTHERMAL ENERGY

In the last six to seven years, igneous terrains with high heat production have been the focus of interest for their potential as economic hot dry rock (HDR) geothermal energy resources (e.g. Garnish, 1976; Costain et al., 1980; Brown et al., 1982). A mean geothermal gradient of at least 35 $^{o}C\ km^{-1}$, maintained to a depth of 3-4 km is estimated to be the economic minimum requirement (Rollin, 1982). The optimum sites for HDR exploration have been identified as granites with (i) high heat production and (ii) large volumes, preferably (iii) in a region with high background heat flow and (iv) with a low conductivity sedimentary cover (Brown et al., 1979).

In general terms, the relatively dense basic and intermediate

igneous intrusive rocks are comparatively depleted in heat producing radioelements while the less dense granites tend to be relatively enriched (Table 1.2; see also Chapter 2). Large negative Bouguer anomalies, indicative of voluminous low density bodies, associated with granitic intrusions may identify areas which are potentially of geothermal interest. Such gravity data are, however, not diagnostic of high heat production and independent information on the distribution of U, Th and K in an intrusive body is required for a preliminary assessment of its geothermal potential. It is important to know whether radioelement contents in surface samples are enriched, depleted or original in order to assess their probable distribution with depth in a pluton.

Recently, HDR developments have taken place in the Cornubian batholith of S.W. England. Whieldon et al., (1980) calculated the surface heat flow along a NW-SE section across the Carnmenellis granite, based on gravity models of the pluton and conductivity and heat production values from shallow boreholes. The modelled surface heat flow is in good agreement with measured values and supports the conclusion that the observed high heat flow values associated with the granites are due to their high heat production and contrast in thermal conductivity with the country rocks. Predicted sub-surface temperatures approach 180 ^{o}C at 5 km. The success of HDR well tests in the Carnmenellis pluton (Batchelor et al., 1980) and the recognition of other potential HDR sources in Britain (Brown et al., 1979; Rollin, 1982) emphasise the importance of detailed studies of the distribution of heat production in Caledonian granites associated with large negative Bouguer anomalies. As a precursor to expensive drilling programs for direct heat flow measurements, the determination of surface heat production and the factors controlling

metavolcanic basement rocks, in locations from Cornwall to southern Scotland, define a linear trend with $q^* = 27$ mW m^{-2} and $D = 16.6$ km (Richardson and Oxburgh, 1979). This value of D is large compared to that observed in other parts of the world (4.5 - 11.1 km) and may reflect relatively unfractionated crustal heat production. This may be due to the relatively low grade of metamorphism and relative lack of igneous activity in England and Wales during late Precambrian and Palaeozoic times (Richardson and Oxburgh, 1978). Data is sparse for the high grade metamorphic and igneous terrains of Scotland which may represent a separate heat flow province.

If the parameters q^* and D remain fairly constant for any heat flow province, then upper crustal rocks with high heat production (high A_0) will correspond to areas of enhanced surface heat flow (high q_0) and, therefore, temperature gradient.

1.2 HOT DRY ROCK GEOTHERMAL ENERGY

In the last six to seven years, igneous terrains with high heat production have been the focus of interest for their potential as economic hot dry rock (HDR) geothermal energy resources (e.g. Garnish, 1976; Costain et al., 1980; Brown et al., 1982). A mean geothermal gradient of at least 35 $^{o}C\ km^{-1}$, maintained to a depth of 3-4 km is estimated to be the economic minimum requirement (Rollin, 1982). The optimum sites for HDR exploration have been identified as granites with (i) high heat production and (ii) large volumes, preferably (iii) in a region with high background heat flow and (iv) with a low conductivity sedimentary cover (Brown et al., 1979).

In general terms, the relatively dense basic and intermediate

igneous intrusive rocks are comparatively depleted in heat producing radioelements while the less dense granites tend to be relatively enriched (Table 1.2; see also Chapter 2). Large negative Bouguer anomalies, indicative of voluminous low density bodies, associated with granitic intrusions may identify areas which are potentially of geothermal interest. Such gravity data are, however, not diagnostic of high heat production and independent information on the distribution of U, Th and K in an intrusive body is required for a preliminary assessment of its geothermal potential. It is important to know whether radioelement contents in surface samples are enriched, depleted or original in order to assess their probable distribution with depth in a pluton.

Recently, HDR developments have taken place in the Cornubian batholith of S.W. England. Whieldon et al., (1980) calculated the surface heat flow along a NW-SE section across the Carnmenellis granite, based on gravity models of the pluton and conductivity and heat production values from shallow boreholes. The modelled surface heat flow is in good agreement with measured values and supports the conclusion that the observed high heat flow values associated with the granites are due to their high heat production and contrast in thermal conductivity with the country rocks. Predicted sub-surface temperatures approach 180 ^{o}C at 5 km. The success of HDR well tests in the Carnmenellis pluton (Batchelor et al., 1980) and the recognition of other potential HDR sources in Britain (Brown et al., 1979; Rollin, 1982) emphasise the importance of detailed studies of the distribution of heat production in Caledonian granites associated with large negative Bouguer anomalies. As a precursor to expensive drilling programs for direct heat flow measurements, the determination of surface heat production and the factors controlling

radioelement distributions allow predictions to be made of the probable variation of heat production with depth in an intrusion. This information, combined with 3-dimensional gravity models, may be used to estimate the enhancement of surface heat flow due to the presence of the radiogenic body and hence, more clearly define areas suitable for further exploration. This is an explicit objective of this thesis in relation to the Etive Complex and the Cairngorm Granite.

1.3 RADIOELEMENTS IN GRANITES

The distribution and enrichment of radioelements in granites depends on factors such as the derivation and physico-chemical evolution of their magmas, and the effect of late-stage fluid phase diffusion and/or post-magmatic hydrothermal processes. The content and distribution of U and Th, the major heat producing elements, is particularly sensitive to the crystallisation and fractionation of various accessory minerals. Late-stage or post-magmatic hydrothermal processes may redistribute, enrich or deplete U (and rarely Th) in granites. Additionally, U may be depleted through weathering processes in near surface rocks. Both the large, plutonic-scale variations in U, Th and Th/U and the petrological location, particularly of U, are important indicators of the factors which controlled the distribution of these radioelements in an intrusion. It is not possible to divorce U and Th considerations from other trace element and minor phase studies and, therefore, an integrated geochemical/mineralogical approach is adopted in this thesis.

In addition to their importance with respect to HDR geothermal exploration, granitic intrusions may host, or provide source rocks for economic U (and Th) deposits. Such deposits range from syngentic disseminations in primary U-bearing accessory minerals and late-stage

pegmatitic deposits, to epigenetic hydrothermal veins in spatial association with granitic intrusions (e.g. Rogers et al., 1978; Cuney, 1978; Sørensen, 1970; Stewart et al., 1955). In the latter case, the high radioelement content of some granites may provide both a source of U and the heat required to initiate and support hydrothermal convective systems (Simpson et al., 1979; Fehn et al., 1978). Continental weathering of granites containing easily leached uraninite has also been proposed for the formation of vein-type U deposits in France (Barbier, 1974). Erosion of granites may also provide the source of both clastic material and U for sandstone-type deposits in adjacent sedimentary basins (e.g. Grutt, 1971).

1.4 AIMS OF THIS STUDY

The primary aim of this study is to determine both the radioelement content and the controls of radioelement distribution in the Etive Complex and the Cairngorm Granite, with a view to making a preliminary assessment of their HDR geothermal potential. More specifically, the aims are

i) to interpret the major and, particularly, the trace element geochemistry of each intrusion in terms of its petro-chemical evolution with an emphasis on the crystallisation and fractionation of radioelement-bearing accessory minerals.

ii) to conduct systematic radiometric surveys and hence determine the areal distribution of radioelements and heat production for each intrusion.

iii) to locate and identify U- and Th-bearing phases throughout the intrusion using fission track and electron microprobe techniques.

iv) to interpret data from (i) and (iii) in terms of the mass-balance of U and Th between the various host phases, the magmatic and

post-magmatic trends of these elements and the probable distribution of heat production with depth in each intrusion.

v) to apply this information to heat flow anomaly calculation procedures and estimate the probable temperature gradients and hence geothermal potential of these granites.

CHAPTER 2 THE DISTRIBUTION OF URANIUM AND THORIUM IN PLUTONIC ROCKS

The decay of ^{40}K provides an important, although often minor, contribution to the total heat production of plutonic rocks. However, the likely variation in this contribution over rocks of a broad compositional range is relatively small: from ∿0.1 μW m^{-3} in a gabbro of density 2.98 g cm^{-3} with 1% K, to ∿0.6 μW m^{-3} in an alkali granite of density 2.67 g cm^{-3} with 6% K. Contributions to heat production from the decay of ^{238}U (+^{235}U) and ^{232}Th are generally higher and show greater variation. Most of the discussion in this chapter is, therefore, restricted to the distribution of U and Th in plutonic rocks.

High U and Th levels have been observed in some volcanic and minor intrusive rocks (e.g. alkali dykes in Virginia, Tilling and Gottfried, 1969; rhyolites of Nellie Creek, Colorado, Zielinski, 1978), but, volumetrically, these are of little geothermal interest.

2.1 GEOCHEMICAL CHARACTERISTICS OF URANIUM AND THORIUM

The geochemistry of U and Th has been reviewed comprehensively by several authors (e.g. Adams et al., 1959; Gableman, 1977; Rogers and Adams, 1978). A summary of the most important aspects, which govern the behaviour of these elements during magmatic processes, is given below.

i) The large ionic radii of U (∿1.05 A) and Th (∿1.10 A) (Rogers and Adams, 1978), are incompatible with the molecular lattices of major rock-forming minerals. Thus, U and Th tend to accumulate in residual liquids during igneous differentiation, along with other large ions including REE's, Y, Ti, Nb and Zr. This incompatibility may be enhanced by the ability of both U^{4+} and Th^{4+} to form complexes with fluorine, chlorine and carbonate ions at moderate to high temperatures

(Bohse et al., 1976; Gableman, 1977).

ii) Similarities in the ionic radii, outer electron configuration, bond character and co-ordination number (8) with respect to oxygen of U^{4+}, Th^{4+}, Ce^{4+}, Zr^{4+} and Hf^{4+} result in similar crystal chemistries of these elements. The ionic radii of U^{4+} and Th^{4+} are also similar to those of the trivalent Ce and Y group elements and bivalent Ca. Isomorphous substitution of U^{4+} and Th^{4+} for $Ce^{4+(3+)}$, Zr^{4+}, Hf^{4+}, Y^{3+} and Ca^{2+} is common in accessory minerals such as apatite, sphene, zircon, monazite, allanite and xenotime (see Table 2.3). The electrostatic imbalance resulting from substitution of trivalent REE's is often compensated by the operation of a coupled substitution, e.g. $Ce^{3+}P^{4+} \rightleftarrows Th^{4+}Si^{4+}$ in monazite (Frondel, 1958). Similarly, the charge imbalance arising from the occupation of Ca^{2+} sites by U^{4+} or Th^{4+} in minerals such as apatite and allanite is compensated by an increase in OH^- or F^-. Precipitation of accessory phases may, therefore, incorporate some U and Th during the course of magmatic evolution.

iii) Since the ionic radii of U^{4+} and Th^{4+} are not identical, there is some relative fractionation of these elements in magmas (Rogers and Ragland, 1961); i.e. selective crystallisation of one element or the other in various accessory minerals.

iv) Unlike Th, U is capable of oxydation to the hexavalent state, forming the stable uranyl ion, UO_2^{2+}. Nearly all uranyl compounds (except phosphates, vanadates and arsenates) are readily soluble at low temperatures (Gableman, 1977). Because of this, an increase in the oxygen fugacity during the final stages of magmatic crystallisation, particularly in high level plutons, causes preferential separation of U relative to Th into residual fluids. The ability of U^{6+} to form fluorine and carbonate complexes may enhance this

accumulation. Relative fractionation of U and Th is, therefore, most apparent during the late stages of magmatic evolution. Post-magmatic hydrothermal fluids approaching the surface through fractures may also oxidise and redistribute U ions. U^{6+} is easily formed under surficial weathering conditions and U residing in sites accessible to groundwaters may be leached from the rock.

2.2 THE ABUNDANCE OF RADIOELEMENTS IN RELATION TO BULK GEOCHEMISTRY

The general tendency for U and Th abundances to increase toward the more petrologically differentiated igneous rock types has been well documented (e.g. Clark et al., 1966; Whitfield et al., 1959; Rogers and Ragland, 1961; Tilling and Gottfried, 1969; Rogers and Adams, 1978).

Compilations of abundance data reported in the literature for essentially calc-alkaline rock types are presented graphically in Figures 2.1 and 2.2. The scatter of values within any one rock group is high, particularly for granites (s.s.) but the general trend of increasing U and Th content with petrological evolution is clear. The slightly more alkalic rock types, monzonites and quartz-monzonites, show a wider range, and higher U and Th contents than calc-alkaline rocks with the same silica content, viz. diorites and quartz diorites (Figures 2.1 and 2.2). Enhanced U ($\geq$ 8-10 ppm) and Th ($\geq$ 25-30 ppm) contents are, with a few exceptions, limited to granites (s.s.) and some monzonites. Previously quoted mean U and Th contents for basic rocks (Table 2.1) agree with the compilations from this study (Figures 2.1 and 2.2), but those for more silicic rock types (Table 2.1) appear to be a little conservative compared with the range of data now available.

Uranium and Th contents of alkaline rocks (Figure 2.3) are extremely variable with a tendency to be higher than in their calc-alkaline equivalents (Rogers and Adams, 1978; Sørensen, 1970). Although

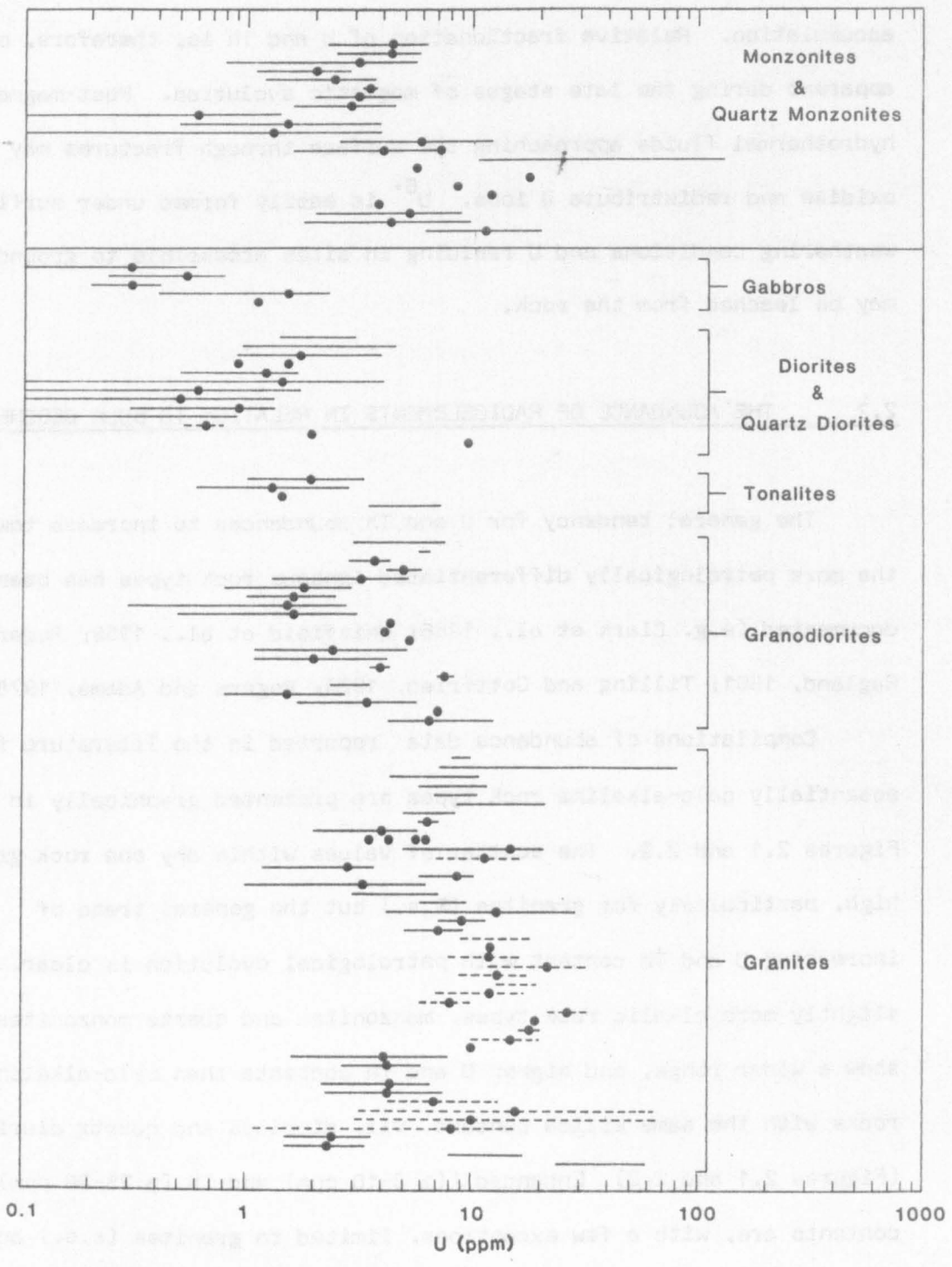

Figure 2.1 Uranium abundances in calc-alkaline rock types

Key: •, mean U content for pluton or unit
——, range of U contents for pluton or unit
---, ± 1σ on mean U content for pluton or unit.

Intrusions exhibiting obvious post-magmatic alteration and mineralisation have not been included.

References: Basham et al., 1979; Bowden et al., 1981; Cassidy, 1980; Costain et al., 1978; Cuney, 1978; Killeen and Heier, 1975; Lopez and Oyarzun, 1974; Larsen et al., 1955; Larsen and Gottfried, 1960; Leonova and Renn, 1964; Miller and Bunker, 1976; Moreau, 1976; O'Connor, 1981; Pagel, 1979; Pagel, 1982; Richardson, 1963; Rogers and Adams, 1978; Simpson et al., 1977; Staatz and Miller, 1976; Sørensen, 1970(1); Stuckless et al., 1977; Swanberg and Blackwell, 1973; Tammemagi and Smith, 1975; Tieh and Ledger, 1981; Tilling and Gottfried, 1969; Wilson and Åkerblom, 1980; Wollenberg and Smith, 1964.

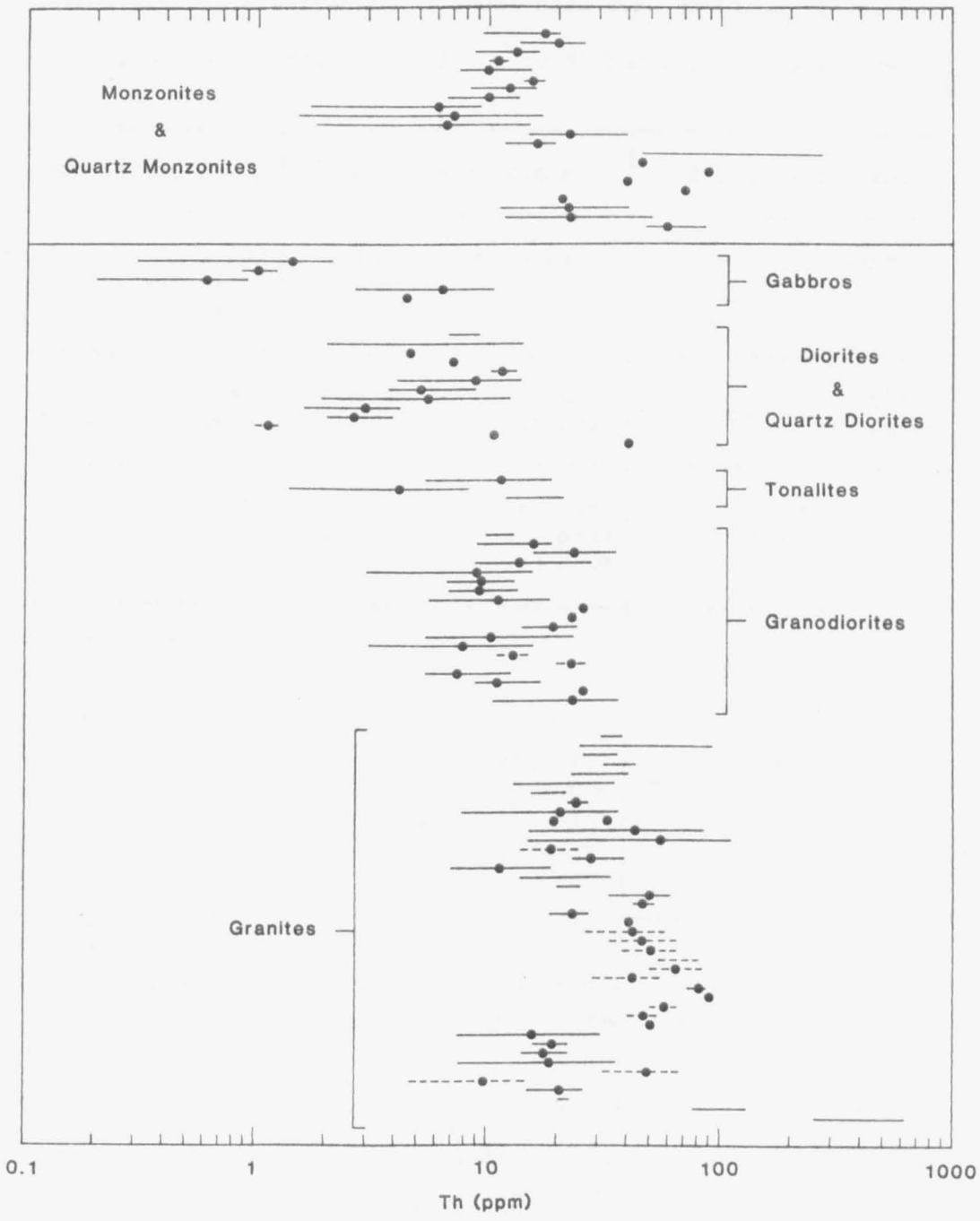

Figure 2.2 Thorium abundances in calc-alkaline rock types

Key: •, mean Th content for pluton or unit
——, range of Th contents for pluton or unit
--- , ± 1σ on mean Th content for pluton or unit.

References: Basham et al., 1979; Bowden et al., 1981; Cassidy, 1980; Costain et al., 1978; Cuney, 1978; Killeen and Heirer, 1975; Larsen and Gottfried, 1960; Leonova and Renn, 1964; Miller and Bunker, 1976; Moreau, 1976; O'Connor, 1981; Pagel, 1979; Pagel, 1982; Richardson, 1963; Rogers and Adams, 1978; Staatz and Miller, 1976; Sørensen, 1970; Stuckless et al., 1977; Swanberg and Blackwell, 1973; Tammemagi and Smith, 1975; Tilling and Gottfried, 1969; Wilson and Åkerblom, 1980; Wollenberg and Smith, 1964.

the lowest contents have been found in nepheline syenites, a trend towards increasing U and Th with silica content is not obvious.

Clark et al., 1960			Adams et al., 1959			Rogers & Adams, 1978		
Volcanic + intrusive rocks	mean (ppm)		Intrusive rocks	Range (ppm)		Volcanic + intrusive rocks	Range (ppm)	
	U	Th		U	Th		U	Th
Mafic rocks	0.9	2.7	Gabbro + diorite	0.3--2	0.5--5	Gabbro + basalt	0.3--0.9	0.5--2
Diorites + qtz. diorites	2.0	7.0	Granite + tonalite + monzonite	1-6	1-25	Diorite + grano-diorite	1.0--7.5	2-10
Grano-diorites	2.6	9.3						
Silicic rocks	4.7	20	Alkaline: any felds-pathoid rock	0.1--30		Granite + qtz. monzonite	2.0--10.0	10-20

Table 2.1 Average U and Th contents for igneous rock groups; from previous compilations.

In general, the U and Th content of plutonic rocks increases with both silica content and alkalinity (Figures 2.1 to 2.3; Tilling and Gottfried, 1969; Geramovsky, 1974; Sørensen, 1970). The latter association arises from the increased solubility of water and, particularly, other volatile components (e.g. F, Cl) with increasing alkalinity of silicate melts. Complexing of U and Th with fluorine, chlorine and carbonate ions may lead to the build up of considerable concentrations of U and Th during the differentiation and consolidation of alkaline melts. (Kogarko, 1974; Bohse et al., 1976). The trend

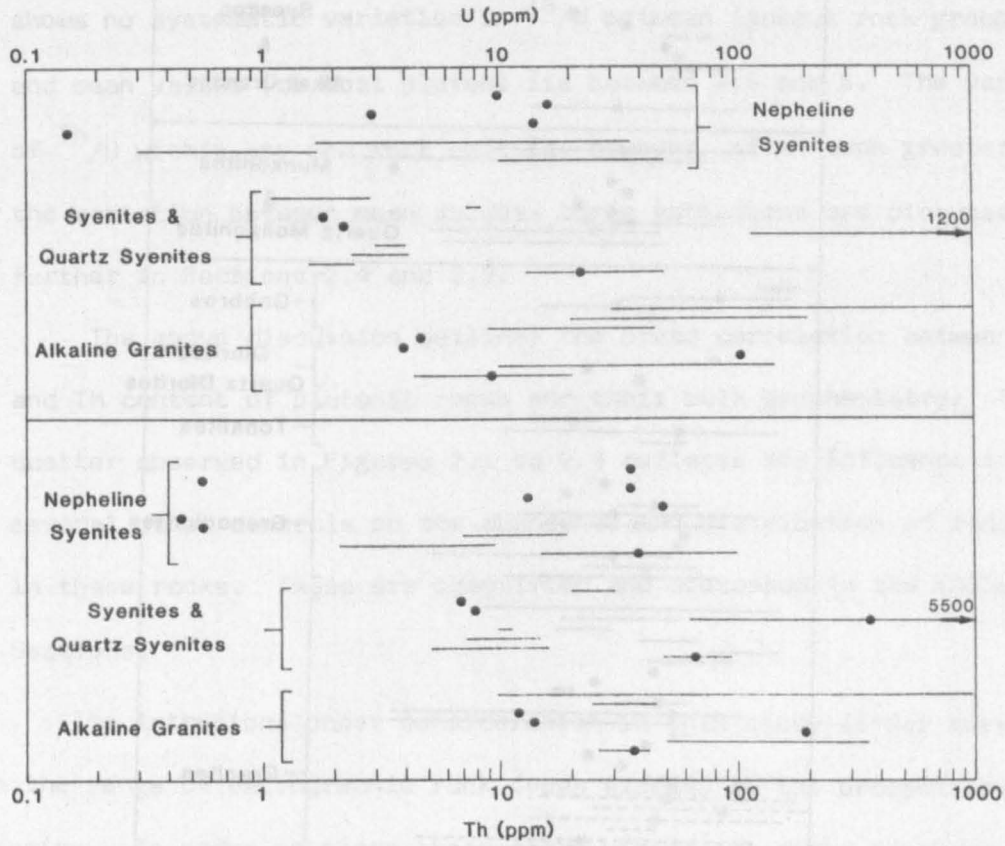

Figure 2.3 Uranium and thorium abundances in alkaline rock types
Key: •, mean Th or U content for pluton or unit
——, range of Th or U contents for pluton or unit
References: Bowden et al., 1981; Fowler, 1981; Labhart and Rybach, 1970; Rogers et al., 1978; Sørensen, 1970(1); Sørensen, 1970(2); Tilling and Gottfried, 1969.

towards increasing U and Th content with increasing alkalinity is apparent in rocks from modern arc environments. Calcic rocks, typical of primitive arc environments are generally poorer in radioelements than the calc-alkaline to alkali-calcic suites characteristic of mature continental arcs (Brown, 1982).

The variation of $^{Th}/U$ with bulk geochemistry has been considered by several workers. Larsen and Gottfried (1960), for example, found $^{Th}/U$ to be lower in gabbro than in more acidic rock types. In a study of 37 plutons in the U.S.A. and Canada, Whitfield et al., (1959) found that $^{Th}/U$ increased with the K-feldspar/plagioclase ratio but not with silica content. Conversely, $^{Th}/U$ appears to decrease with differentiation index in Thailand granites (Ishihara and Mochizuki, 1980). Figure 2.4

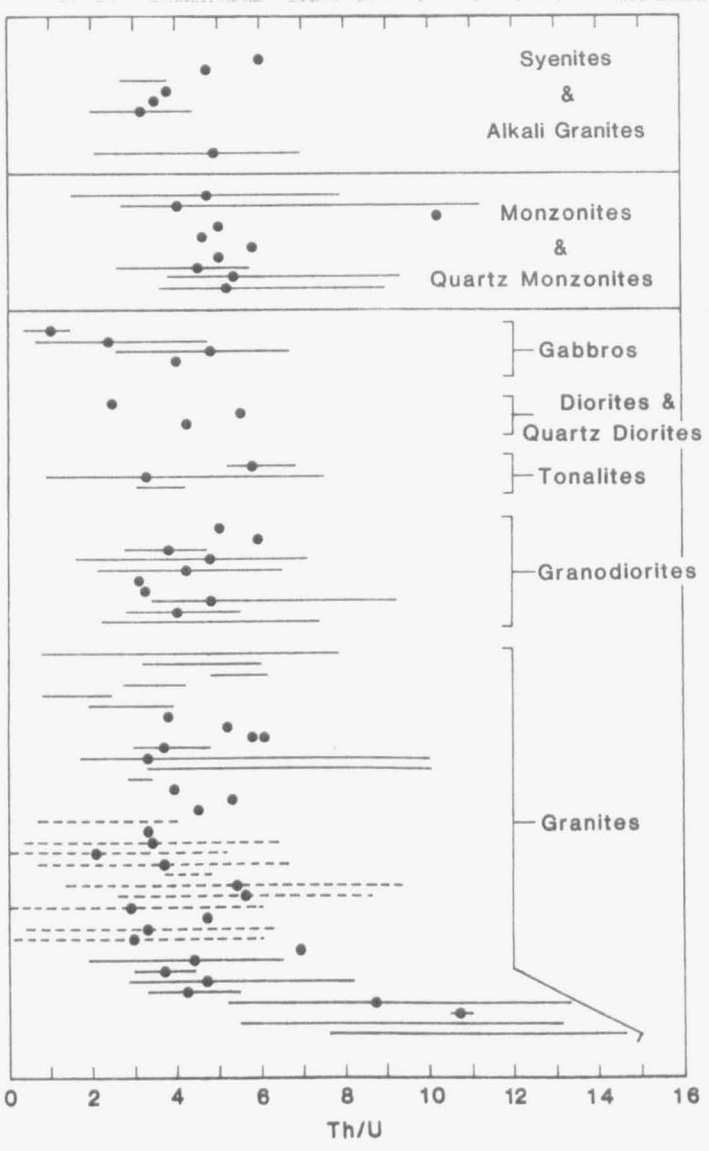

Figure 2.4 $^{Th}/U$ data for calc-alkaline and alkaline rock types

Key: •, mean $^{Th}/U$ value for pluton or unit
——, range of $^{Th}/U$ values for pluton or unit
---, ± 1σ on mean $^{Th}/U$ value.

References: Basham et al., 1979; Bowden et al., 1981; Cassidy, 1980; Costain et al., 1978; Cuney, 1978; Killeen and Heier, 1975; Labhast and Rybach, 1970; Leonova and Renn, 1964; Miller and Bunker, 1976; Moreau, 1976; Pagel, 1979; Pagel, 1982; Rogers et al., 1978; Rogers and Adams, 1978; Swanberg and Blackwell, 1973; Tilling and Gottfried, 1969; Wilson and Åkerblom, 1980; Wollenberg and Smith, 1964.

shows no systematic variation in $^{Th}/U$ between igneous rock groups, and mean values for most plutons lie between 2.5 and 6. The variation of $^{Th}/U$ within any one rock unit is, however, often much greater than the variation between mean values; these variations are discussed further in Sections 2.4 and 2.5.

The above discussion outlines the broad correlation between the U and Th content of plutonic rocks and their bulk geochemistry. The scatter observed in Figures 2.1 to 2.4 reflects the influence of several other controls on the abundance and distribution of radioelements in these rocks. These are identified and discussed in the following Sections.

The intrusions under consideration in this study differ markedly in the range of petrographic rock types exposed at the present level of erosion. In order to place these rocks within the above framework they have been classified using the chemical equivalent of the Streckeisen Modal QAP (F) diagram (Streckeisen and Le Maitre, 1979). Results are presented in Figure 2.4:1.

The Etive Complex encompasses a continuous spectrum of petrographic rock types, ranging from diorite-quartz diorite-quartz monzonite-granite-alkali-feldspar granite. The N. Cruachan unit, which plots in the 3a granite field on the normative diagram (figure 2.4:1 A) would probably plot in the 3b field on a modal diagram. This discrepancy is due to the dependance of the normative classification scheme on both the ratio of alkali feldspar to plagioclase, and the An content of the plagioclase. Hence, granites with approximately equal contents of alkali feldspar and plagioclase but with a low An content in the plagioclase, tend to plot as syeno-granites rather than adamellites. The N. Cruachan unit has approximately equal contents of alkali feldspar and plagioclase (see Figure 5.6), the latter being predominantly oligoclase with minor albite.

There are considerable uncertainties involved in placing empirical limits between field 9 and 10 (i.e. monzodiorites-diorites), due to discrepancies in the nomenclature of available data (Streckeisen and Le Maitre, 1979). Ambiguities, therefore, arise in classifying some of the Quarry Intrusion and S. Cruachan samples. However, comparison of the normative data presented in Figure 2.4:1 with result of modal analyses presented in Table 5.2 for the S. Cruachan units suggests that the normative classifications, as defined in Figure 2.4:1, are correct. The position of the Meall Odhar granite on the normative plot (Figure 2.4:1) is anomalous and is discussed further in Chapter 5.

The Cairngorm massif comprises a considerably more restricted range of petrographic rock types, lying predominantly in the alkali-feldspar field (Figure 2.4:1 B). Although the Cairngorm Main Granite samples are of similar ANOR composition to the Central Starav Granite of the Etive Complex, they are richer in normative quartz.

Based on these classifications and the general trends of U and Th shown in Figures 2.1-2.4 the alkali-calcic nature of both the central unit of the Etive Complex and the bulk of the Cairngorm massif highlight the potential of finding enhanced U and Th levels in these intrusions.

2.3 URANIUM AND THORIUM PROVINCES

Provincial differences in the U and Th content of igneous rocks, related fundamentally to magmatic source regions have been recognised by several workers. The Colorado Front Range, for example was recognised as a Th-rich province, with enhanced Th levels occurring in igneous rocks of all ages from Precambrian to Laramide (Cretaceous/Tertiary), in contrast with similar rock types outside the region (Phair and Gottfried, 1964; Howarth et al., 1981). The Th and U enrichment observed in the alkaline complexes of W Alaska was found to

persist in calc-alkaline plutons (Miller and Bunker, 1976). Uranium-rich granites in Sweden range in age from 1900 to 900 m.y., were intruded into rocks of continental, marine and volcanic arc environments, and show no apparent relationship to the distribution of Archaean basement (Wilson and Akerblom, 1982). These authors suggested that the

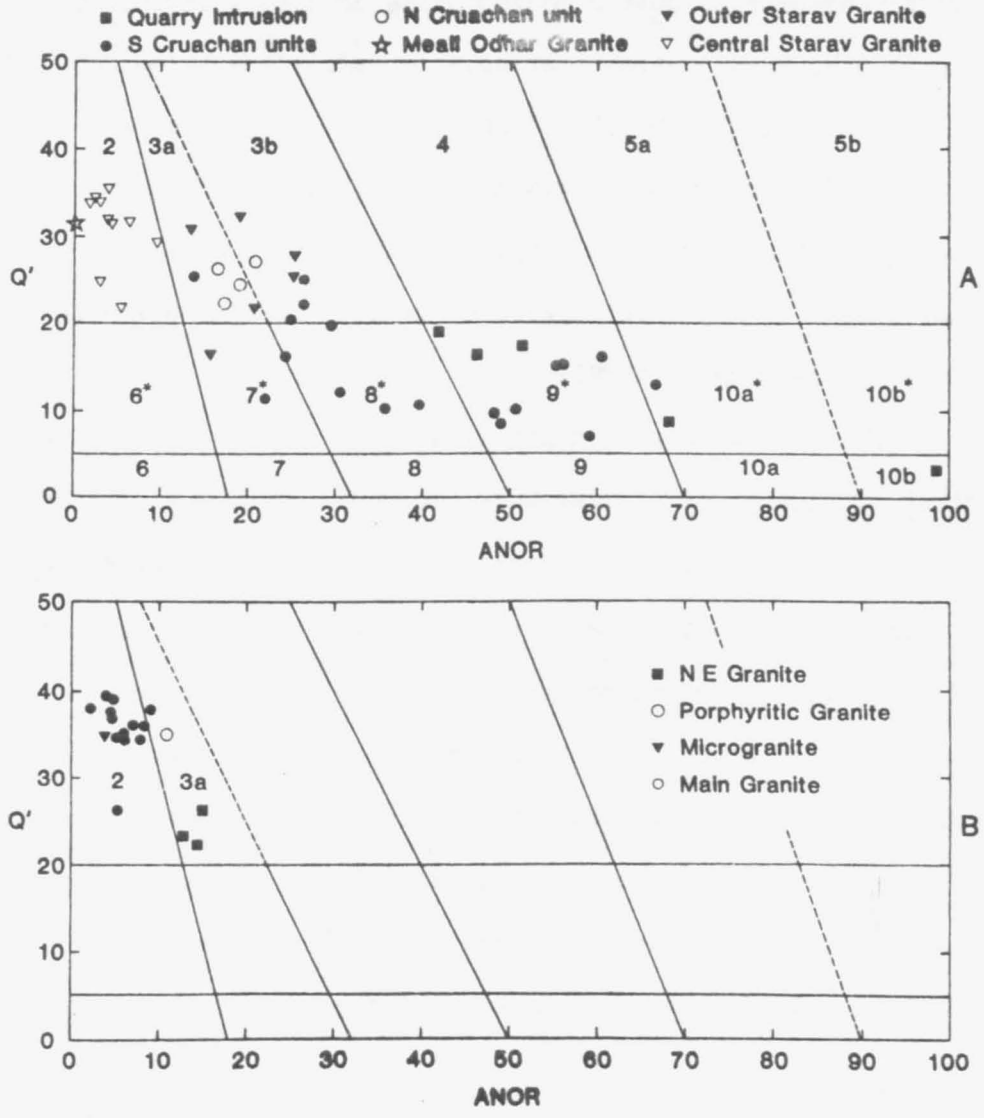

Figure 2.4:1 Plots of analyses for the Etive Complex (A) and the Cairngorm Granite (B) in the Streckeisen and Le Maitre (1979) normative fields. CIPW norms were calculated using whole rock major element data and Q' and ANOR determined:-

$$ANOR = 100.An/(Or + An)$$

$$Q' = 100.Q/(Q + Or + Ab + An)$$

The fields shown correspond approximately to those of the modal QAP diagram:
2, alkali feldspar granite; 3, granite (3a, syeno-granite; 3b, adamellite/monzogranite; 4, granodiorite; 5, tonalite; 6*, quartz alkali-feldspar syenite; 7*, quartz syenite; 8*, quartz monzonite; 9*, quartz monzodiorite; 10*, quartz diorite; 6, alkali-feldspar syenite; 7, syenite; 8, monzonite; 9, foid-bearing monzodiorite; 10, diorite.
Individual units of the Etive Complex (A) and the Cairngorm Granite (B) are discussed in detail in Chapters 5 and 6 respectively.

N Vasterbotten - S Norrbotten U province may be related to a major mantle heterogeneity with high U and F.

Differences in the U and Th contents of similar plutonic rocks within the same province have also been observed. For example, two diorite-monzodiorite-quartz monzodiorite complexes in the Massif des Ballons, S Vosges, contrast markedly in radioelement content:

N complex 1.9 to 8.5 ppm U, 10.5 to 39.4 ppm Th

S complex 9.4 to 17.7 ppm U, 39.7 to 88.7 ppm Th

These differences have been attributed to primary magma source variations, in particular to a greater degree of crustal contamination in the S complex magmas (Pagel, 1979).

Correlations between depth of emplacement and the radioelement content of plutons of similar bulk geochemistry have been noted. The heat production of quartz monzonites in the Idaho Batholith decreases with depth of intrusion (Swanberg, 1972) and a similar correlation applies to a suite of monzonites in Norway (Ormaasen and Raade, 1978). Several authors have noted the predominance of enhanced U and Th contents in high level, post orogenic intrusions emplaced in tensional environments (e.g. Simpson et al., 1979; Plant et al., 1980; Wilson and Akerblom, 1982; Steenfelt, 1982). Whether these correlations arise from the level of magma generation, the degree of partial melting, volatile scavaging as the magmas rise or the differentiation/crystallisation paths followed by magmas emplaced at various depths is uncertain.

2.4 EVOLUTIONARY TRENDS OF URANIUM AND THORIUM IN CO-MAGMATIC SUITES

Uranium and Th are generally enriched towards the youngest, most felsic, most silicic and potassic members of co-magmatic suites of plutonic rocks (e.g. Rogers and Adams, 1978; Tilling et al., 1970).

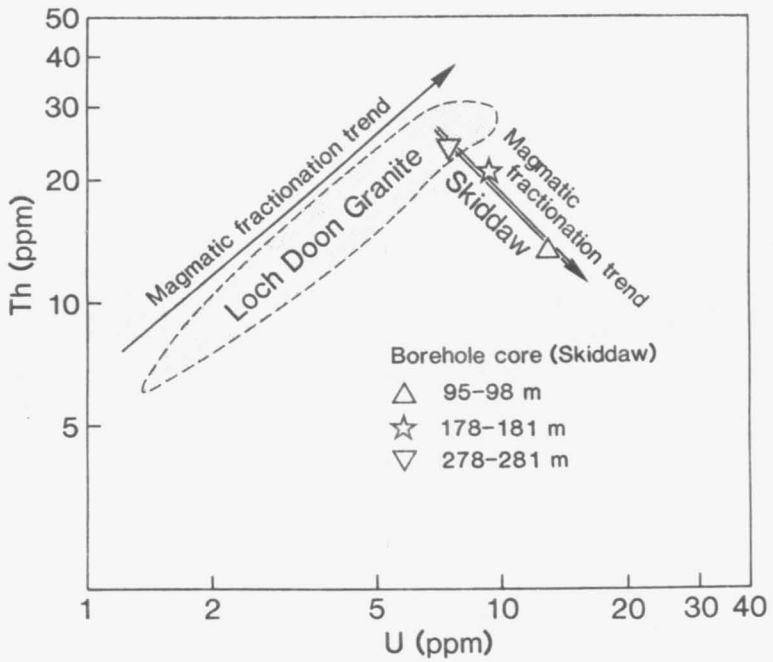

Figure 2.5 Primary magmatic trends of U and Th in the Loch Doon and Skiddaw 'granites'. Data for surface samples (Loch Doon) from Cassidy (1980). Borehole data (Skiddaw) from G. Brown and P. Webb (pers. comm).

In some cases, these elements have proved to be sensitive indicators of petrochemical evolution trends; for example Loch Doon, S Uplands (Cassidy, 1980; see Figure 2.5). Several indices of differentiation have been used to plot the variation of U and Th with magmatic evolution (e.g. $\%SiO_2$, %K, Larsen index) and all show increased scatter at high Th, and particularly, high U levels (e.g. Figure 2.6).

Enrichment of U and Th with differentiation does not always occur: the Enchanted Rock Batholith, Texas, exhibits a complex zonation from granodiorite and quartz monzonite to leucogranite, probably representing successive tappings of a magma chamber differentiating at depth (Ragland et al., 1966). Thorium levels do not follow the concentric zonation and, with the exception of anomalously high values (see below), remain essentially constant with differentiation. Uranium

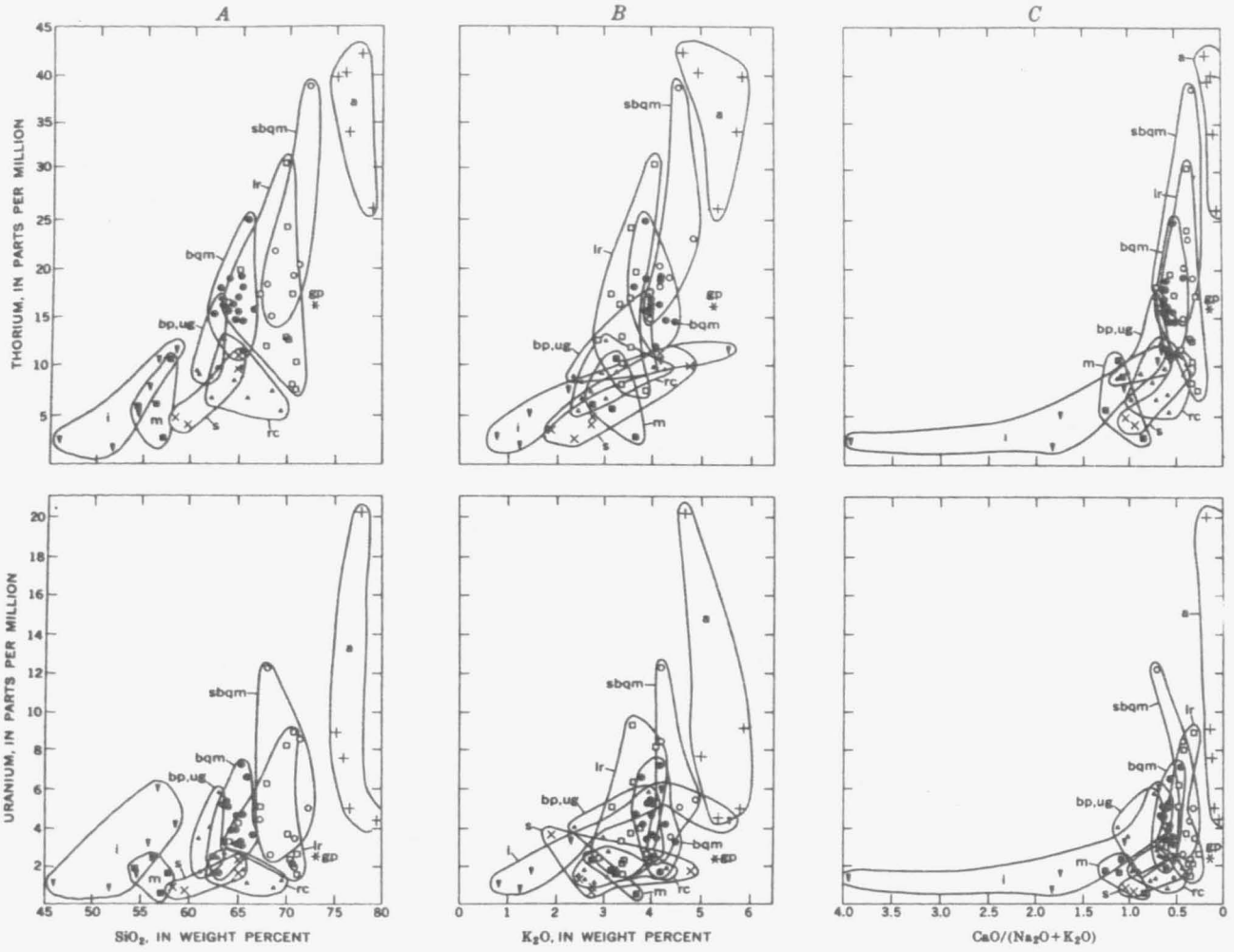

Figure 2.6 -Thorium and uranium contents in rocks of the Boulder batholith plotted against SiO_2, K_2O and $CaO/(Na_2O + K_2O)$. ▽= mafic inclusions in batholith rocks (i); ■ = mafic rocks (m); △= mafic granodiorites (bp, ug - Burton Park pluton and Unionville Granodiorite); ▲ = felsic granodiorite (rc, Rader Creek pluton); = Butte Quartz Monzonite (bqm); ○ = silicic facies of Butte Quartz Monzonite (sbqm); + = alaskite (a); □ = leucocratic rocks (b); × = satellitic plutons (s); * = granite porphyry (gp). (Data of tables 8 and 9). From Tilling and Gottfried, 1969.

content appears to decrease with magmatic evolution; this trend has been attributed to increasingly effective oxidative processes during crystallisation, resulting in partition of U into volatiles, some of which are lost from the magma (Ragland et al., 1966). Post-magmatic leaching of U through hydrothermal or surficial weathering processes may have accentuated this trend. Enhanced U and Th levels, occurring predominantly in the northern part of the Enchanted Rock Batholith, result from late stage hydrothermal activity and correlate with the presence of secondary allanite and sphene.

Depletion of both U and Th in minor, late stage differentiates has been observed in some intrusions; for example, in silica-rich, biotite- and hornblende-poor samples of the Sherman Granite, Wyoming (Zeilinski et al., 1981), and fine grained, leucocratic granites in the Lands End and Carnmenellis plutons, Cornwall (Tamemmagi and Smith, 1975). In the latter case, this may represent either magmatic depletion of U and Th or contamination with U-Th-poor roof rocks. Wholesale reduction of both U and Th in late stage differentiates is rare, however, in large intrusions. A more commonly observed magmatic trend is the depletion of Th with concomitant increase of U in late state differentiates of plutonic suites, for example: Granite Mountains, Wyoming (Stuckless et al., 1977), Boir Noirs Granite (Cuney, 1978), Thailand granites (Ishihara and Mochizuki, 1980), Skiddaw Granite (G. Brown, pers. comm; see Figure 2.5). In an extreme example, U is enriched by a factor of 4 in pegmatites of the Elberton Batholith, S Appalachians, and Th is depleted by a factor of 3 relative to the host granite (Wenner and Spaulding, 1982). This decoupling in the behaviour of U and Th is seen to a lesser extent, in the major granite phases. High oxygen fugacity in the magma, indicated by Fe-Ti-oxides, suggests that U was transported with volatiles into the pegmatites while Th crystallised

in the dry melt (Wenner and Spaulding, 1982). Alternatively, this trend may reflect the initial crystallisation of Th-bearing accessory minerals at an earlier stage than major U-bearing phases.

Where both U and Th contents increase with magmatic evolution, this trend is often accompanied by a decrease in the $^{Th}/U$ ratio; for example in the Illimaussaq intrusion, Greenland, where these variations are controlled by the crystallisation of primary U and/or Th bearing accessory minerals (Bohse et al., 1976).

In general, both U and Th contents tend initially to increase with magmatic evolution in suites of plutonic rocks. As differentiation continues, a decoupling in the behaviour of U and Th is frequently observed and may involve a decrease in Th content while U continues to be enriched, or a decrease in the $^{Th}/U$ ratio due to changes in the relative rates of U and Th enrichment. These primary magmatic trends are however, often overprinted by the effects of late stage fluid phase diffusion and/or hydrothermal activity, and surficial weathering, which remobilise, redistribute, and, particularly in the latter process, deplete U. Such interactions may result in systematic radioelement trends, as observed in the Aare and Mt. Blanc granites, Switzerland, where U-enriched hydrothermal fluids migrated outwards (the granites consolidated from their margins inwards), resulting in a concentric zonation of increasing U and decreasing $^{Th}/U$ ratio from centre to rim (Rybach and Buntebarth, 1981; Buntebarth, 1976). Non-systematic variations in U content and $^{Th}/U$ ratio may arise from post-magmatic hydrothermal activity and/or surficial weathering processes; for example in the Fleet intrusion (Cassidy, 1980).

In order to determine the relative importance of various processes on the content and distribution of radioelements in plutonic rocks and, specifically, to separate primary magmatic trends from post-

magmatic modifications, an integrated geological-geochemical-mineralogical study is required. Recognition of U depletion through surficial weathering is particularly pertinent to the evaluation of granitic geothermal resources when assessing the probable radioelement content, and hence heat production in rocks below the zone of groundwater circulation.

2.5 MINERAL SITES OF URANIUM AND THORIUM

Detailed investigations on the location of U and Th in plutonic rocks have been accomplished using autoradiographic, fission track and microprobe techniques. These methods are discussed further in Sections 4.3 and 4.4.

Uranium occupies a variety of sites in plutonic rocks, which may be grouped into four broad categories.

i) Medium-high concentrations in primary accessory minerals.

ii) 'Background' concentrations in rock-forming minerals.

iii) Variable concentrations adsorbed by secondary alteration products of primary minerals.

iv) Generally low level adsorption or accumulations along grain boundaries and microfractures.

Thorium also occurs in modes (i) and (ii), but its presence or absence in secondary alteration products or along grain boundaries and micro-fractures is less well documented. However, since modes (iii) and (iv) are due usually to post-magmatic hydrothermal processes and Th^{4+} has relatively poor mobility compared to U^{6+}, Th is less likely to be found in these locations.

Ranges of U and Th contents recorded for several major and accessory minerals are presented in Tables 2.2 and 2.3 respectively.

Because of the low levels of U and Th in major minerals, their contribution to whole rock radioelement contents is generally low; for example, quartz and feldspar in the Katemcy Granite, Texas, account for only 1.59 ppm U (Tieh and Ledger, 1981), and major minerals account for less than 2-3 ppm U in the highly radioactive Sao Pedro do Sul Granite, Portugal (Basham et al., 1979).

Mineral	Range U (ppm)	Range Th (ppm)	Range $^{Th}/_{U}$
Pyroxene	0.01-40	2 - 25	2 - 5
Olivine	0.01-0.05	∿0.02	low
Plagioclase	0.2 -5.0	0.5 - 3.0	1 - 5
K-feldspar	0.7 -7.4	3 - 7	2 - 6
Quartz	0.1 -10	0.5 - 10	1 - 5
Hornblende	0.2 -60	5 - 50	2 - 4
Biotite	1 -70	0.5 - 50	0.5 - 3
Muscovite	2 -11	-	-

Table 2.2 Concentration of U and Th in major minerals
Note that U and Th contents in some major minerals may be overestimated due to the presence of minute inclusion of U- and Th-rich accessory minerals.

Date from: Adams et al., 1959; Clark et al., 1966; Cuney, 1978; Rogers and Adams, 1978.

The behaviour of U and Th during magmatic consolidation is controlled predominantly by the availability of suitable sites in accessory host minerals (Table 2.3) and the crystallisation and fractionation histories of these phases; these are discussed below. Where rocks are affected by late-stage diffusion of magmatic fluids or post-magmatic hydrothermal processes, redistribution, loss or addition of U (and sometimes Th) may occur, giving rise to secondary radioelement sites i.e. (iii) and (iv). Such secondary locations commonly comprise amorphous Fe-oxides in altered biotites, martitised magnetite or pyrite, TiO_2 (leucoxene, anatase) alterations of ilmenite and sphene, secondary epidote or allanite and clays and hydrated Fe-oxides along microfractures.

MINERAL	RANGE U (%)	RANGE Th (%)	RANGE $^{Th}/_{U}$
Apatite $Ca_5(PO_4)_3$ (OH, F, Cl)	0.001 - 0.01	0.005 - 0.025	~1
Zircon $Zr(SiO_4)$	0.01 - 3.1 usually < 0.6	0.01 - 2	0.2 - 2
Sphene Ca $Ti(SiO_4)$ (O, OH, F)	0.001 - 0.07	0.01 - 0.89	1 - 3
Allanite $(Ca, Ce)_2(Fe^{2+}, Fe^{3+})Al_2O.OH(Si_2O_7)$ (Si_2O_4)	0.003 - 0.1	0.1 - .2	high
Monazite $(Ce, La, Th)PO_4$	0.05 - 1.6	0.03 - 20	high
Xenotime YPO_4	0.03 - 4	0.39 - 0.88	0.1 - low
Epidote $CaFe^{3+}Al_2O.OH(Si_2O_7)$ (Si_2O_4)	0.002 - 0.02	0.005 - 0.05	2 - 10
Magnetite + other opaques	0.0001- 0.003	0.00003- 0.002	-
Thorite $Th(SiO_4)$	3.1 -12.7	40 - 64	high
Uraninite UO_2 - U_2O_6	71 - 75	3 - 15	low
Multiple Nb-Ta-Ti-Y-REE-oxides	variable, generally < 10, up to 30	variable, but generally lower than U	usually $\leq$ 1
*Britholite $(Na, Ce, Ca)_5$ F $(SiO_4,PO_4)_3$	-	0.69	-
*Eudialyte $(Na, Ca, Fe)_6$ $Zr(OH, Cl)$ $(Si_3O_9)_2$	0.005 - 0.0869	0.003 - 0.034	< 1
*Pyrochlore $(Ca, Na)_2(Nb, Ta)_2O_6(O, OH, F)$	0.2	0.7	-
*Rinkite $(Ca, Na, Ce)_{12}(Ti, Zr)_2Si_7O_{31}H_6F_6$	0.3 - 1.2	0.3 - 0.43	$\leq$ 1
*Steenstrupine $Na_2Ce(Mn, Nb, Fe)H_2((Si, P)O_4)_3$	0.2 - 1.5	0.2 - 7.4	> 1

*Found predominantly in peralkaline rocks

Table 2.3 Concentration of Uranium and Thorium in accessory minerals

Data from: Barbier et al., 1967; Basham et al., 1979; Basham et al., 1982; Bohse et al., 1976; Cuney, 1978; Frondel, 1958; Pagel, 1982; Ragers and Adams, 1978; Staatz and Miller, 1976; Tindle, 1983; Vlasov, 1966; Yeliseyeva et al., 1974; Yeliseyeva, 1977.

Uranium residing in secondary sites and primary minerals that have already been 'softened' by hydrothermal processes is susceptible to leaching through surficial weathering (e.g. Cornish granites, Basham et al., 1982).

The relative distribution of U and Th between different sites, although dependent on the crystallisation and post-magmatic histories of individual plutons and even rock types, varies in a general way with whole rock contents and is particularly sensitive to the type of accessory minerals present. Where whole-rock U and Th levels are low to average, the most abundant host accessory minerals are usually zircon, sphene and apatite. Examples are generally less differentiated rock types such as diorites (e.g. Shetland, 1-3 ppm U; Simpson et al., 1977), granodiorites (e.g. Sierra Nevada, 3.9 ppm U, 14.0 ppm Th; Wollenberg, 1971) and tonalites (e.g. Loch Doon, 3-6 ppm U, 12-21 ppm Th, Cassidy, 1980). These minerals are also the major hosts of most of the U and much of the Th in some poorly radioactive granites (e.g. Enchanted Rock Batholith, 1.95 ppm U, Tieh et al., 1980). Less abundant accessories such as allanite and monazite in these rock types are often important Th hosts (e.g. Bendeleben quartz monzonite, Miller and Bunker, 1976; Sierra Nevada granodiorite, Wollenberg, 1971). Some of the increase in whole rock U and Th contents coincident with differentiation in co-magmatic suites may be reflected by an increase in the U and Th content of minerals such as zircon, apatite, sphene, allanite and monazite (Berzina et al., 1974), or variation in the modal percentages of these accessories (detailed discussion of the relative importance of each of these phases at various stages of magmatic evolution is presented in Chapters 5 and 6 with respect to the Etive and Cairngorm intrusions). Commonly, these trends are associated with the appearance of 'new' accessory phases such as xenotime, thorite, uraninite and multiple Nb-Ta-Ti-Y-REE-oxides (Table 2.3).

The presence of primary accessory phases accommodating high concentrations ($\gtrsim$ 5%) of U and Th has become increasingly recognised in radioelement-rich plutonic rocks. In the Conway granite, for example, 65% of whole rock Th (w.r. = 58 ± 6 ppm) resides in thorite and huttonite (monoclinic $ThSiO_4$); these phases also account for 42% of whole rock U (Richardson, 1963). The significance of accessory uraninite in U-rich Hercynian granites has been well documented in France (Barbier et al., 1967; Cuney, 1978), Portugal (Basham et al., 1979) and SW England (Ball and Basham, 1979; Basham et al., 1982). Uraninite may be an obvious primary phase, such as in the St. Sylvestre and Montagne-en-Vendée two-mica granites (Barbier et al., 1967) and in SW England granites (Ball and Basham, 1979), where it occurs as inclusions in rock-forming minerals. In other granites, for example, Sao-Pedro do Sul, Portugal (Basham et al., 1979), the Ballons, Crêtes and Boirs Noirs granites, France (Pagel, 1982; Cuney, 1978), the petrogenesis of uraninite is less clear. In these granites, uraninite is located in intergranular sites, or associated with late muscovite and is probably of late-magmatic origin, crystallising from U-rich residual liquids. It is possible, however, that some uraninite was formed during the diffusion of a late-stage fluid phase with enhanced U levels derived from the leaching of primary accessory phases (cf. Cuney 1978, see Figure 2.8). Other high U and Th accessory phases include uranothorite, Nb-Ta-Ti-Y minerals such as columbite and samarskite and, in enriched alkaline rocks, U and Th have been found to reside in a spectrum of Ca, Na and REE accessory minerals (Table 2.3; Bohse et al., 1976; Kozlova and Gurvich, 1980; Bowden et al., 1981).

The significance of sporadic, high U phases with respect to their contribution to whole rock contents is illustrated in Figure 2.7. It is clear from this diagram, that extensive and detailed studies of

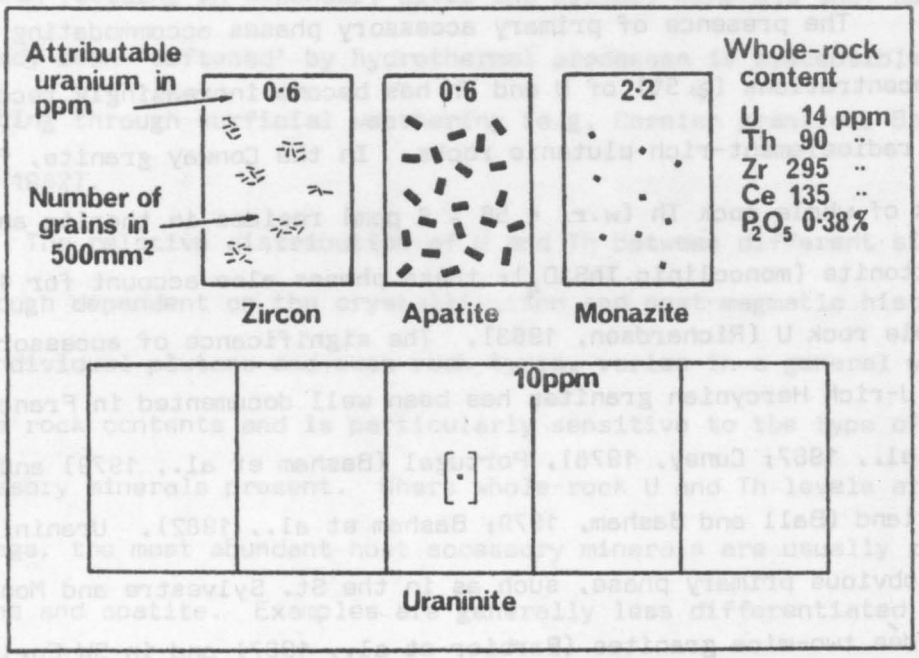

Figure 2.7 Diagrammatic representation of the uranium distribution in a sample of granite from Sao Pedro do Sul, Portugal, based on quantitative chemical and mineralogical data. From Basham et al., 1982.

several thin sections may be required in order to locate and identify major radioelement host minerals. Cuney (1978) also noted that the abundance of uraninite is proportional to whole rock U content, and although uraninite is scarce in the Ballons and Crêtes granites, where it is present, whole rock U contents are greater than 14 ppm.

Enhanced U levels may also be accommodated in secondary locations following late stage fluid diffusion, or post-magmatic hydrothermal activity. Uranium transported in such fluids may be of dual origin, comprising a primary magmatic component, partitioned into volatiles during the course of differentiation, and a secondary component leached from altered primary host minerals. In the Katemcy and Streeter granites, Texas, $\frac{1}{2}$ - $\frac{1}{3}$ of whole rock U (whole rock U = 6.8 and 15.5 ppm respectively) was found to reside in zircon, allanite and sphene, the remainder occurring as secondary distributions along the rims of biotite, apatite and fluorite, and as adsorptions in clays and hematite along

microfractures (Tieh and Ledger, 1981). Secondary distributions account for high U contents in the Helmsdale granite, Scotland, and are related to hydrothermal activity along major faults (Tweedie, 1979; Plant et al., 1980). Secondary epidote accommodates large percentages of enhanced U and Th levels in the Enchanted Rock batholith (Rogers et al., 1966) and the Granite Mountains, Wyoming (Stuckless et al., 1981).

The distribution of U and Th in plutonic rocks can be highly complex, with primary magmatic trends controlled predominantly by the crystallisation sequence of minor accessory phases and late or post-magmatic modification causing redistribution, addition or loss of U (and rarely Th). For example, early crystallisation of thorite and monazite in the Boir Noirs granite (Figure 2.8) led to Th depletion in residual magmas and late, fine grained facies have lower Th contents and no thorite. According to Cuney (1978), although both zircon and monazite were partially altered by deuteric fluids, releasing both U and Th, much of the U remained locally, associated with pyrite, and most of the Th remained fixed in a secondary phosphatic phase. Uraninite crystallised from enriched magmatic fluids, mainly along microfractures representing fluid escape channels, except in fine grained granite where its textural relationship is of a primary phase. Later hydrothermal and supergene alteration led to further leaching and redistribution of U (Figure 2.8).

Similarly, the depletion of Th relative to U with differentiation in the Crêtes granite was attributed to early crystallisation of thorite (Pagel, 1982). Early crystallisation of chevkinite (a REE-Ti-silicate) in syenites of the Shira Complex, Nigeria, led to depletion of both U and Th in the later, peralkaline granites (Bowden et al., 1981).

In summary, the common accessory minerals apatite, zircon, sphene, allanite, monazite and xenotime seldom account for more than 5-6 ppm U

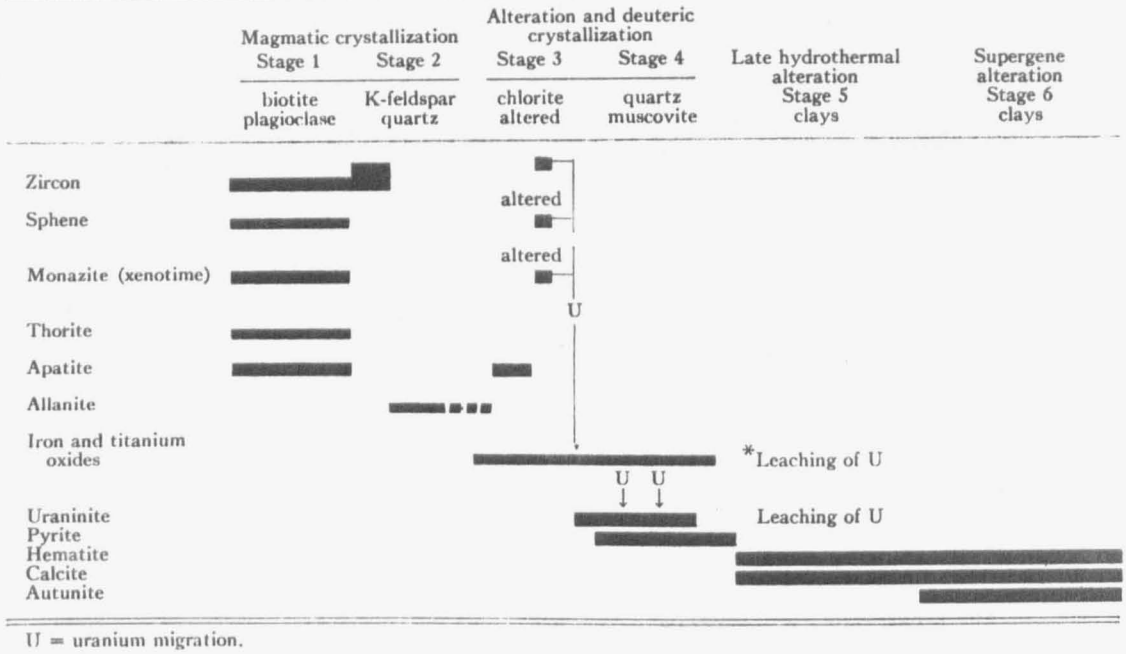

Figure 2.8 Paragenesis of the accessory minerals of the Boirs Noirs Granite from Cuney (1978).

*Most of the U was probably derived directly from late magmatic fluids.

in plutonic rocks. Allanite and particularly monazite, however, may accommodate large percentages of whole rock Th contents (up to ∿20 ppm) and along with early crystallising thorite may lead to depletion of Th relative to U in late differentiates. Considerable concentrations of U and Th may reside in sporadically distributed, and hence often undetected, high U and Th accessory phases. Late, and post-magmatic processes lead to leaching and redistribution, particularly of U, which may be relocated in alteration products of primary minerals, or adsorbed along crystal boundaries and microfractures.

2.6 THE EFFECTS OF WEATHERING

The solubility of U under oxidising conditions renders it highly susceptible to remobilisation in surficial weathering environments. Uranium residing in secondary locations is often readily accessible to circulating meteoric waters, but U may also be leached from primary phases, depending on the textural relationships and degree of metamictisation of host accessory minerals, the degree of alteration of the whole rock, and the rate of uplift and erosion.

Where most of the U is held in resistate early formed phases such as apatite, zircon and monazite, no difference is observed in the radioelement content of weathered surface samples and fresh core samples; for example in the Sierra Nevada granodiorite (Wollenberg and Smith, 1968) and the Boulder Batholith (Tilling and Gottfried, 1969). However, in the Granite Mountains, Wyoming, where 65% of whole rock U (w.r. U≈ 19.7 ppm) in fresh drill-core samples is located in biotite and hydrothermal epidote, the same minerals only account for 35% of whole rock U in surface samples (w.r. U≈ 10.9 ppm). The remaining (∿7 ppm) U in both fresh and weathered samples is located predominantly in primary accessory minerals, and U losses due to surficial weathering are attributed almost entirely to leaching of biotite and epidote during Tertiary uplift and erosion (Stuckless and Nkomo, 1980; Stuckless et al., 1981). Discordant U-Pb ages, compared to concordance in Rb-Sr, Th-Pb and Pb-Pb systems, also indicate 50-75% U loss from surface samples of these granites (Stuckless and Ferreira, 1976).

Oxydation, hydration and disappearance of uraninite from surface samples, reducing whole-rock U contents by 5-10 ppm, has been reported by several workers (e.g. Ball and Basham, 1979; Ranchin, 1968). The solubility of uraninite decreases with Th content, and preservation of this phase in surface samples of the Crêtes granite has been attributed

to the presence of 10% ThO_2. (Pagel, 1982). However, low Th uraninite persists in the weathering zone in the Sao Pedro do Sul granite, Portugal, due to its inclusion in resistant phases such as muscovite (Basham et al., 1979). Similarly, uraninite survives in quartz in surface samples of French granites (e.g. Barbier et al., 1967).

Determination of the radioelement content of plutonic rocks from surface samples, therefore, may not always be representative of abundances below the weathering zone, particularly where uraninite or hydrothermal minerals are important U hosts. A detailed knowledge of the location of U is a useful guide in assessing the probability of U depletion in surface samples and more definitive estimates are possible from studies of U-Th-Pb systematics and equilibrium in the ^{238}U decay series (Zielinski et al., 1981).

2.7 SIGNIFICANCE TO ESTIMATES OF HEAT PRODUCTION

From a geothermal standpoint, the most interesting exploration targets are laterally and vertically extensive intrusions with uniformly high radioelement contents. These are most likely to be highly differentiated plutons, particularly alkaline granites. In the absence of borehole control on the variation of radioelements with depth in an intrusion, a knowledge of the mineral location and variation of U and Th at outcrop level gives some indication of the processes which controlled their origin and distribution and hence probable trends of heat production in the third dimension can be estimated. If radioelement distributions are homogeneous at outcrop level and U and Th are concentrated predominantly in primary phases, then it is probable that these characteristics are preserved at depth. Where U and $^{Th}/U$ values are highly scattered at outcrop and significant percentages of U

reside in secondary locations, then remobilisation via hydrothermal fluids is indicated. In this case, extrapolation of radioelement contents in the third dimension are difficult without further information, such as the depth of intrusion, the level of erosion and the extent of the hydrothermal system. Evidence of U loss from partially weathered primary accessory phases such as uraninite or from secondary locations may imply that U levels increase below the zone of surficial weathering.

A detailed investigation of the origin of U and Th distributions at outcrop level is important in preliminary assessments of the geothermal potential of granitic intrusions and is applied in this thesis to the Etive and Cairngorm granites.

CHAPTER 3 CALEDONIAN PLUTONISM IN BRITAIN

3.1 GEOLOGICAL AND TECTONIC SETTING

The British Caledonides form part of an orogenic fold belt which, viewed on a pre-Atlantic rifting reconstruction (Figure 3.1), is continuous from Greenland and Scandinavia, through Britain, to the Appalachians. The evolution of this fold belt is attributed to convergence of the pre-450 m.y. 'American' and 'European' plates during closure of the former Iapetus ocean. Abundant evidence indicates that final closure across the British sector took place during Silurian times, the suture following the Solway-Nevan-Shannon zone (Figure 3.2; Phillips et al., 1976; Mitchell and McKerrow, 1975; Kennedy, 1979).

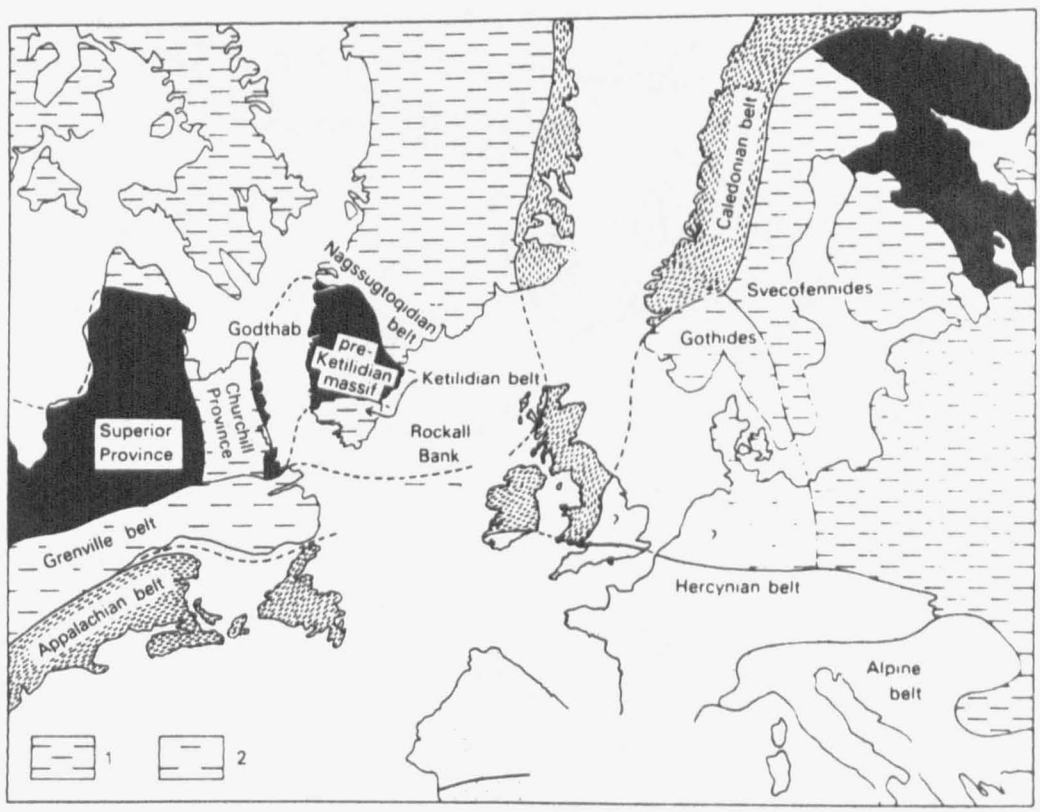

Figure 3.1 Pre-Atlantic rifting reconstruction showing the extent of the Caledonian-Appalachian orogenic belt. From Anderton et al., 1979. 1, 2500-1700 Ma cratons and orogenic belts; 2, 1300-900 Ma cratons and orogenic belts.

Referring to Figure 3.2, the northern province is characterised by 2900 m.y. Lewisian basement (Hamilton et al., 1979) which crops out as amphibolites and refractory granulites north of the Moine Thrust. To the south, this basement is thought to underlie the late Precambrian-lower Palaeozoic rocks of the Orthotectonic Caledonides which comprise granulite facies Moines and Dalradian metasediments. In the Midland

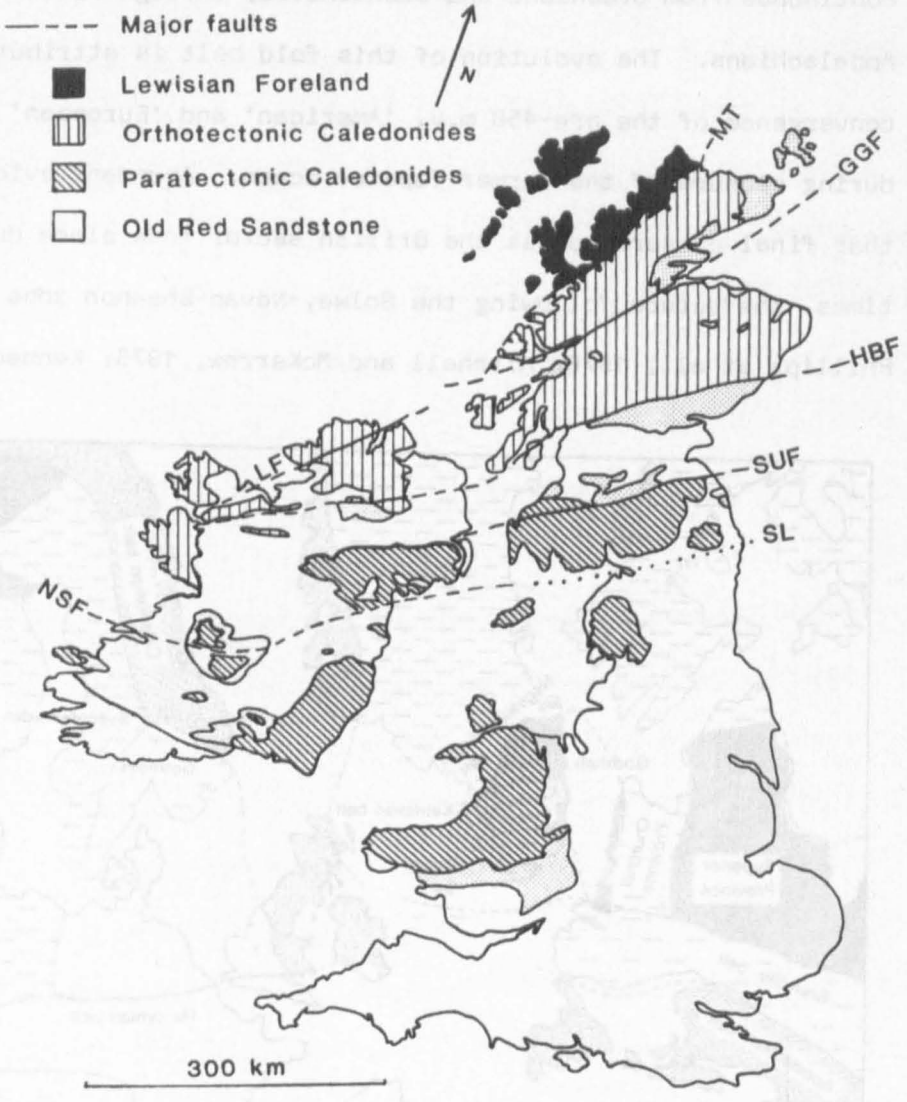

Figure 3.2 Generalised map showing the major structural and tectonic subdivisions of the British Caledonides. MT, Moine Thurst; GGF, Great Glen Fault; HBF, Highland Boundary Fault; SUF, Southern Uplands Fault; LF, Leannan Fault; NSF, Nevan-Shannon Fault; SL, Solway Line.

Valley, on the downthrow side of the Highland Boundary Fault, lower

Palaeozoic sediments are overlain by a cover of post-Caledonian, Devonian and Carboniferous rocks. Evidence of granulite facies, gneissic clasts in Carboniferous volcanic vents of the Midland Valley suggest that Proterozoic basement continues at depth in this region (Upton et al., 1979). Seismic data (Bamford et al., 1978) support this conclusion and further, indicate a major discontinuity in basement characteristics north and south of the Southern Uplands Fault (Figure 3.3), placing the Caledonian suture, in terms of ancient foundation, along this zone.

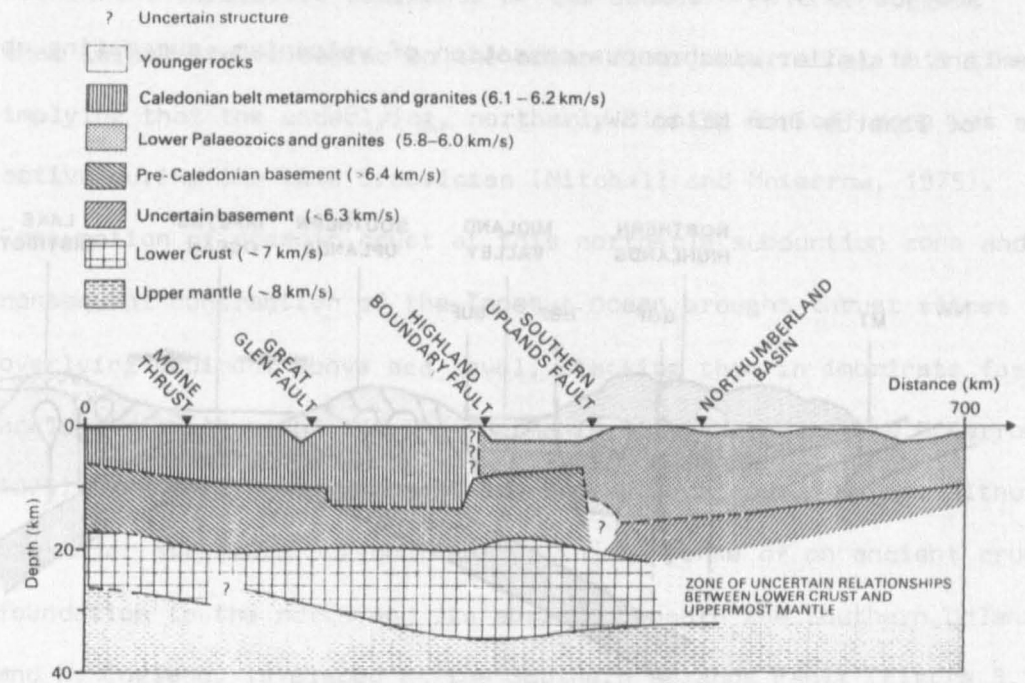

Figure 3.3 Cross-section through the crust and upper mantle of Northern Britain; after Bamford et al., (1978).

There is no evidence of Pre-Caledonian basement beneath the southern, paratectonic Caledonides (Brown et al., 1981). The greywacke-shale sequences, interbedded with minor calc-alkaline volcanics, of the Southern Uplands, N. England and Wales have been interpreted as accretionary prisms of marginal and back arc basin sediments, analagous to those found at modern destructive plate margins. They are thought to overlie, directly, Iapetus ocean crust (McKerrow et al., 1977; Thorpe,

1981). These lower-Palaeozoic rocks are characterised by steep cleavages, upright folds and regional metamorphism rarely exceeding greenschist grade.

Caledonian plate tectonic models have been discussed by several authors (e.g. Dewey, 1969; Fitton and Hughes, 1970; Phillips et al., 1976; McKerrow, 1976). Figure 3.4 summarises the available data in a mid-Silurian (c. 440 m.y.) reconstruction showing almost complete closure of the Iapetus ocean. Further, Phillips et al., (1976) noted a decrease in age of post-tectonic granites (see Section 3.2) from Scotland (∿400 m.y.), south-west through Ireland (∿360 m.y.) to Canada (∿360 m.y.) and a similar diachronous cessation of volcanism, suggesting oblique closure of Iapetus from NE to SW.

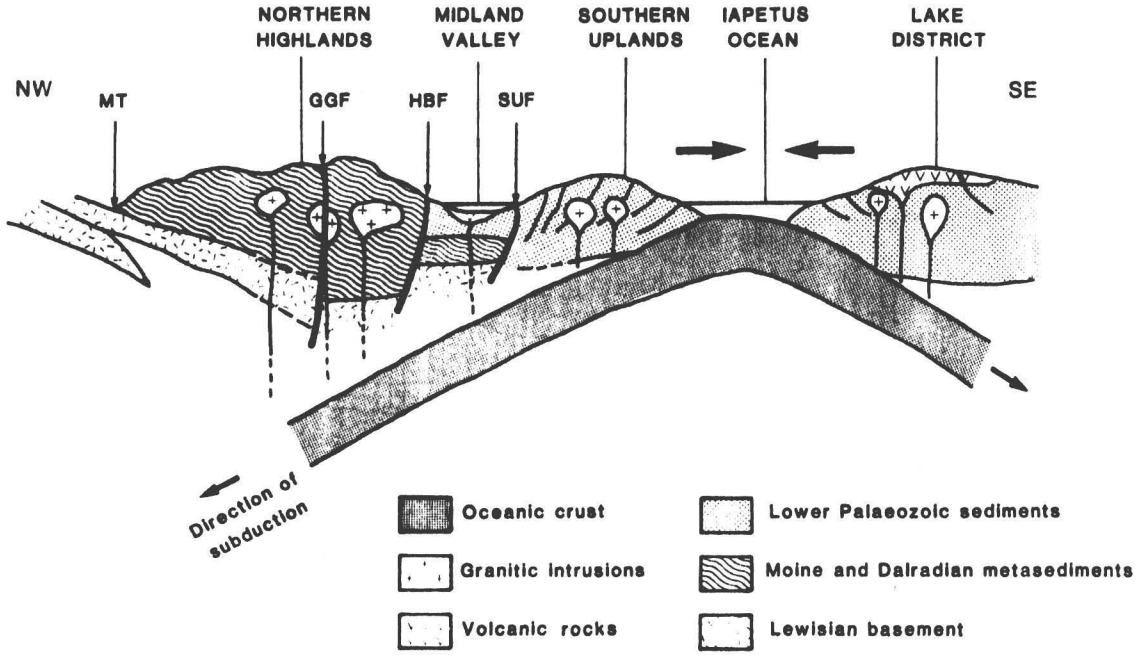

Figure 3.4 Plate tectonic model of the Caledonides in Northern Britain, showing almost complete closure of the Iapetus ocean in mid-Silurian times. Modified from Phillips et al., (1976); after Cassidy (1980).

The prolonged history (mid-Cambrian to late Silurian) of Caledonian deformation, metamorphism and uplift in the northern province is linked to the convergence of Lewisian continental foreland, under

thrust to the south-east, and Iapetus oceanic crust, subducted to the north-west (Phillips et al., 1976; see Figure 3.4). The metamorphic climax in the northern Caledonides (c. 500 m.y.; Dewey and Pankhurst, 1970; Brown and Hughes, 1973) pre-dates, or is contemporaneous with suturing, which, on the basis of sedimentological and structural evidence occurred between 470-410 m.y. (Phillips et al., 1976). The termination of volcanism in the Lake District at approximately 473 m.y. was interpreted by Phillips et al., (1976) as marking the end of southerly subduction. Rhyolitic lavas of late Caradoc age (458-448 m.y.) within the turbiditic sediments of the Southern Uplands suggest that island arc volcanism on the ocean floor occurred at this time, implying that the underlying, northerly-dipping Benioff zone was still active during the late Ordovician (Mitchell and McKerrow, 1975). Consumption of oceanic crust at this northerly subduction zone and consequent contraction of the Iapetus Ocean brought thrust slices of overlying sediment above sea level, stacking them in imbricate fashion, analogous to those of the Indo-Burman Ranges (Mitchell and McKerrow, 1975), and forming the present day Southern Uplands. Hence, although the major structural discontinuity, in the sense of an ancient crustal foundation to the north and its absence beneath the Southern Uplands and N. England, is placed at the Southern Uplands Fault (Figure 3.3), final suturing occurred along the Solway line (Figure 3.4).

3.2 THE EVOLUTION OF CALEDONIAN PLUTONISM

An important component of crustal evolution during the Caledonian orogeny is recorded by a wide-ranging suite of pre-, syn- and post-tectonic, calc-alkaline intrusions. These intrusions were emplaced during the time interval 650-380 m.y., increasing in frequency and volume as closure of the Iapetus Ocean progressed, the larger,

batholithic complexes being predominantly post-tectonic.

The first detailed classification of Caledonian plutonism was attempted by Read (1961), who identified three broad, age and petrologically related groups, based on their deformational age and contrasting styles of emplacement. These groups are:

i) 'Older granites', comprising relatively small, pretectonic intrusions and associated migmatite complexes, occurring predominantly in northern Scotland and pre-dating the metamorphic climax (see Section 3.1). These intrusions are generally biotite-hornblende gneisses, ranging in composition from diorite to adamellite with occasional alkaline complexes.

ii) Early, 'forceful' post-metamorphic intrusions characterised by deformational margins, sometimes with the development of contact migmatites.

iii) Later, 'permitted' intrusions with discordant margins and low pressure thermal aureoles.

Most of the 'newer granites' (groups (ii) and (iii) above) vary internally from diorite to adamellite or granite, with a trend from mainly dioritic to more granitic compositions from 'forceful' to 'permitted' suites. Read (1961) placed the principal evolutionary division between 'Older' granites and migmatites, emplaced before or during the major metamorphic episode, and the 'newer' granites which post-date regional metamorphism.

Read's classification has formed the basis of all subsequent attempts to summarise the evolutionary sequence of Caledonian plutonism; for example, Leake (1978), Pankhurst and Sutherland (1982) and Brown et al., (1981). Table 3.1 summarises the age, petrological, geophysical, geochemical and isotopic data used by Brown et al., (1981) to divide Caledonian intrusions into two broad groups (radioelement data will be discussed in Section 3.3). These authors group Read's

Characteristic References	GROUP 1: PRE-MID-SILURIAN (>410 m.y.) 28 intrusions in the northern province 5 intrusions in the southern province	GROUP 2: SILURO-DEVONIAN (390-410 m.y.) 30 intrusions in the northern province 4 intrusions in the Southern Uplands 9 intrusions in the southern province
Intrusive style and broad petrological characteristics (8, 11)	Two groups are identified: a) Pre-tectonic (>460 m.y.), small plutons and migmatite complexes. Diorite-adamellite in composition + occasional alkaline complexes. Mainly biot-hnbld gneisses with K'spar > plag. b) Post-tectonic (410-460 m.y.), mainly 'forceful', often heavily zoned granodioritic intrusions. Highly differentiated adamellite or granite units tend to be of minor extent. Essential hornblende present.	Mainly discordant granites and granodiorites, often of large areal extent. Some are associated with volcanic centres, e.g. Etive, Ben Nevis, or probable sub-surface cauldrons, e.g. Lochnager, and dyke swarms, indicating the prevailing tensional regime in which they were emplaced. Some are zoned from tonalite-granite, but several vary only from adamellite to granite, e.g. Shap, Cairngorm.
Residual gravity expression (1, 2, 3, 6)	58% - no residual anomalies; 16% - positive anomalies (<+130 g.u.); 26% - negative anomalies (>-90 g.u.). Positive anomalies indicate basic rocks beneath a thin granitic layer, e.g. Foyers. Where no anomaly or a small negative anomaly exists, and density contrasts with country rocks are significantly negative, e.g. Rogart, a small body is indicated.	25% - no residual anomaly; 0% - positive anomalies; 75% significant negative anomalies, often larger than -100 g.u. Indicate voluminous, low density bodies continuing to some depth (e.g. c. 12 km, Cairngorm). Some regional gravity lows over these intrusions have been modelled as sub-surface batholiths, e.g. Southern Uplands, NE Grampians, Lake District.
Aeromagnetic expression (2, 6)	58% have aeromagnetic expression characterised by multi-wavelength anomalies but few are expressed on the filtered aeromagnetic map; i.e. there are no >13 km wavelengths. Short wavelength anomalies may be due to the presence of Fe-Mg-rich rocks at depth, e.g. Foyers, or contact metamorphic effects.	N province: 85% have aeromagnetic expression (up to 650 nT, Etive), and many appear on the filtered anomaly map. Long wavelength anomalies are probably associated with magnetisation of basement rocks through which the magma's rose; an increase in magnetic components with depth in the plutons is inconsistent with gravity data. S province: 58% have aeromagnetic expression but only Cheviot appears on the filtered anomaly map. S Uplands: as S province. Differences between N and S provinces emphasise differences in the deep crustal characteristics of these regions and the lack of Proterozoic basement beneath the S Uplands.
Trace element contents. (7, 10, 12, 13)	Rarely produce anomalies with respect to their host metasediments. Contain low levels of LIL elements (e.g. U, Th, Rb) and relatively high levels of Zr, Sr and Ba. REEs have been shown to behave compatibly in the Foyers and Strontian complexes and chondrite normalised plots lack negative Eu anomalies.	Contrast with surrounding country rocks. Are often enriched in LIL and other incompatible elements, e.g. Li, Be, Mo. REEs in the Cairngorm Granite have been shown to behave incompatibly. The Loch Doon intrusion (S Uplands) has geochemical characteristics intermediate between group 1 and group 2.
Isotopic data (4, 5, 8, 9)	$(^{87}Sr/^{86}Sr)_I$ / $(^{143}Nd/^{144}Nd)_I$ / Inherited zircons N: 0.704-0.729 / 0.514 - 0.5121 / present S: 0.704-0.708 / No data / minor Some high initial Sr values and low initial Nd values, and the presence of inherited zircons in these intrusions suggest an important crustal component for magmas in the N province.	$(^{87}Sr/^{86}Sr)_I$ / $(^{143}Nd/^{144}Nd)_I$ / Inherited zircons N: 0.704-0.708 / 0.5116 - 0.5118 / trace or absent S: 0.704-0.708 / 0.5120 (one value) / trace or absent Initial Sr ratios suggest a strong contempory mantle component. However, low initial Nd ratios and the presence of minor inherited zircons indicate a partly crustal derivation, which, in the S province, had a short crustal residence time.
Provenance	Isotopic data suggest a multicomponent origin involving various crustal and juvenile sources. Enhanced geothermal gradients due to increased heat flow from the mantle (associated with fluid flow and/or rising magmas above a subduction zone), frictional heating (due to tectonic activity) and increased insulation (due to over-thrusting of metasedimentary layers) are probably the cause of local crustal metling.	It is unlikely that large volumes of differentiated, high LIL element magmas could have been derived from partial melting of underlying crust. In-situ fractionation of intermediate parental magmas is inconsistent with gravity data (such processes could have been operative in lower crustal magma chambers). A two-stage origin has been proposed (Simpson et al., 1979) involving underplating of basaltic-andesite magmas generated during subduction which are partially remelted during adiabatic decompression consequent on post-collision relaxion.

Table 3.1 Broad characteristics of Caledonian intrusions; mainly after Brown et al., (1981).
References: 1, Bott (1974); 2, Brown and Locke (1980); 3, El-Batroukh (1975); 4, Hamilton et al., (1980); 5, Harmon and Halliday (1980); 6, Locke (1980); 7, Pankhurst (1979); 8, Pankhurst and Sutherland (1982); 9, Pidgeon and Aftalion (1978); 10, Plant et al., (1980); 11, Read (1961); 12, Watson and Plant (1979); 13, I.G.S. Geochemical atlas of Great Britain.

'Older granites' with all pre-410 m.y. intrusions of mid-Ordovician and Silurian age, placing the major boundary between these and later, post-410 m.y. Siluro-Devonian intrusions. Figure 3.5 shows the distribution of these intrusive groups in the northern and southern provinces of the British Caledonides.

It can be seen from Table 3.1 that this revised classification is probably associated with an important change in magma volume, as follows:

From 1) Earlier, pre-mid-Silurian ('older' and 'forceful') intrusions of varied composition and calc-alkaline affinity. These intrusions are of limited volume, have low levels of incompatible elements comparable with those of regional crustal rocks, were derived from various sources which involved an important crustal component, and were emplaced in a prevailing compressional regime.

To 2) Siluro-Devonian ('permitted') calc-alkaline to alkali-calcic intrusions of granodiorite to granite composition. Although these intrusions more closely resemble the Cordilleran batholiths of modern ocean-continent convergence zones than do group 1 intrusions, they have neither the range of composition nor the uniformely low initial $^{87}Sr/^{86}Sr$ ratios observed in Andean granitoids (Pitcher, 1983). These voluminous, discordant, Siluro-Devonian intrusions have high levels of incompatible elements and were derived predominantly from juvenile sources, although a small, crustal component may have been introduced into most magmas.

Within the above framework of temporal progression from early 'forcefully' emplaced intrusions to late 'permitted' intrusions, there are exceptions; for example, the Rosses granite, an early member of the Donegal Complex (Figure 3.5) was passively emplaced but the intrusion of

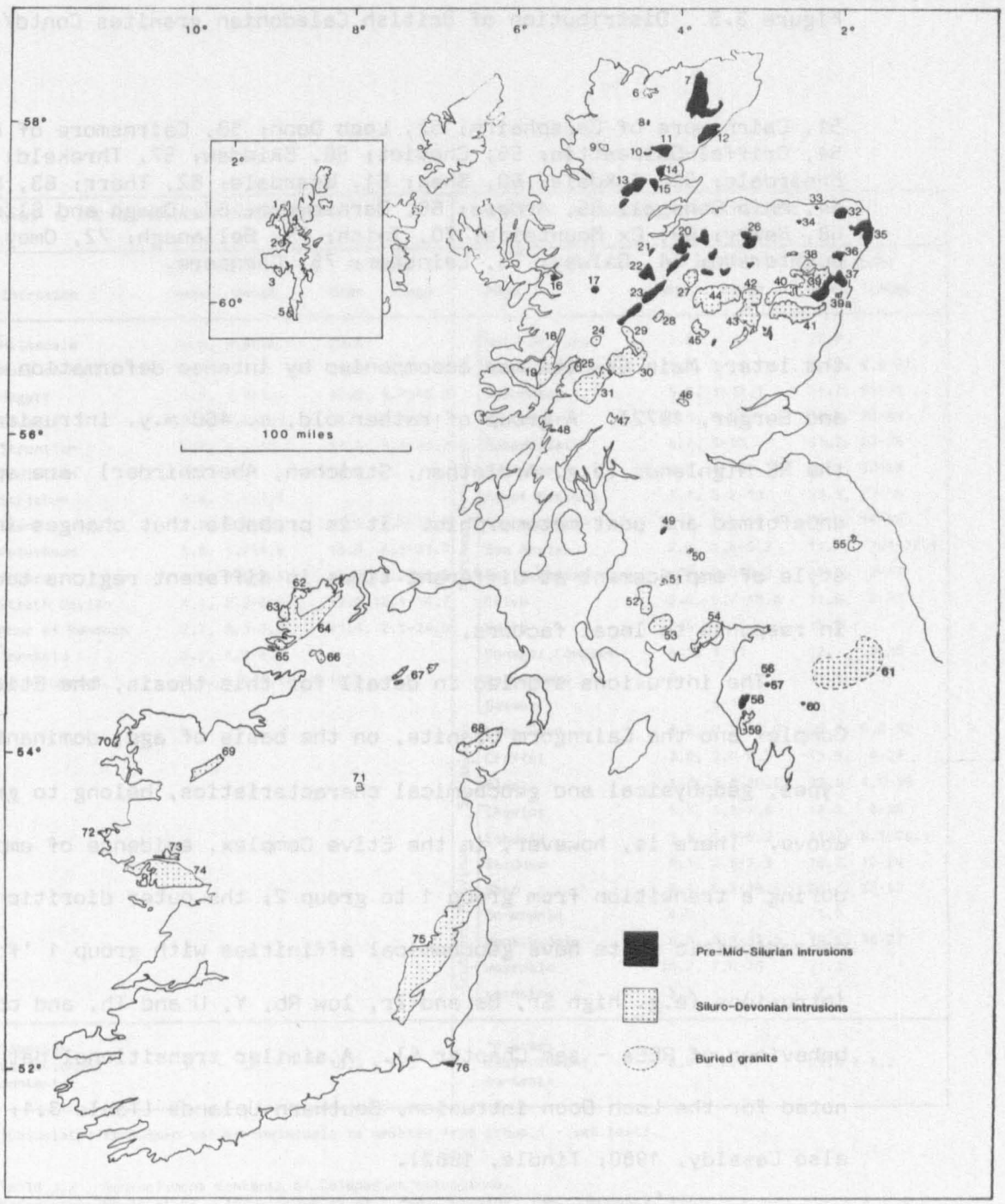

Figure 3.5 Distribution of British Caledonian granites.

1, North Maven; 2, Muckle Roe; 3, Standsting; 4, Graven; 5, Sppiggie; 6, Ben Loyal; 7, Strath Halladale; 8, Vagastie Bridge; 9, Borrolan; 10, Grudie; 11, Lairg Rogart; 12, Helmsdale; 13, Carn Chuinneag; 14, Migdale; 15, Fearn; 16, Ratagain; 17, Cluanie; 18, Ardgour; 19, Strontian; 20, Moy; 21, Abriachan; 22, Foyers, 23, Strathspey; 24, Ben Nevis; 25, Ballachulish; 26, Ben Rinnes; 27, Monadhliath; 28, Laggan; 29, Strath Ossian; 30, Moor of Rannoch; 31, Etive; 32, Strichen; 33, Longmanhill; 34, Aberchirder; 35, Peterhead, 36, Ardlethen; 37; Aberdeen; 38, Bennachie; 39, Hill of Fare; 39a, Skene complex; 40, Ballater; 41, Mount Battock; 42, Glen Gairn; 43, Lochnagar; 44, Cairngorm; 45, Ben Vuirich; 46, Comrie; 47, Garabal Hill; 48, Kilmelford; 49, Distinkhorn; 50, Spango Water;

Figure 3.5 Distribution of British Caledonian granites Contd/...

51, Cairnsmore of Carsphairn; 52, Loch Doon; 53, Cairnsmore of Fleet; 54, Criffel-Dalbeattie; 55, Cheviot; 56, Skiddaw; 57, Threkeld; 58, Ennerdale; 59, Eskdale; 60, Shap; 61, Weardale; 62, Thorr; 63, Rosses; 64, Main Donegal; 65, Ardara; 66, Barnsemore; 67, Omagh and Slieve Gullion; 68, Newry; 69, Ox Mountains; 70, Inish; 71, Bellanagh; 72, Omey; 73, Oughterard; 74, Galway; 75, Leinster; 75, Carnsore.

the later, Main Granite was accompanied by intense deformation (Pitcher and Berger, 1972). A group of rather old, c. 460 m.y. intrusions, in the NE Highlands (e.g. Ardlethen, Strichen, Aberchirder) are apparently undeformed and post-metamorphic. It is probable that changes in the style of emplacement at different times in different regions took place in response to local factors.

The intrusions studied in detail for this thesis, the Etive Complex and the Cairngorm Granite, on the basis of age, dominant rock types, geophysical and geochemical characteristics, belong to group 2 above. There is, however, in the Etive Complex, evidence of emplacement during a transition from group 1 to group 2; the outer dioritic and monzodioritic units have geochemical affinities with group 1 'forceful' intrusions (e.g. high Sr, Ba and Zr, low Rb, Y, U and Th, and compatible behaviour of REEs - see Chapter 5). A similar transitional nature was noted for the Loch Doon intrusion, Southern Uplands (Table 3.1; see also Cassidy, 1980; Tindle, 1982).

3.3 URANIUM AND THORIUM IN CALEDONIAN INTRUSIONS

The concept of broad age-related plutonic groups is reinforced by differences in the radioelement contents of pre-mid-Silurian and Siluro-Devonian intrusions (Table 3.2). Group 2 intrusions have, on average,

GROUP 1: PRE-MID-SILURIAN INTRUSIONS					GROUP 2: SILURO-DEVONIAN INTRUSIONS				
		U (ppm)		Th (ppm)			U (ppm)		Th (ppm)
	Intrusion	mean	range	mean range		Name	mean	range	mean range
Northern Province	Helmsdale	8.6,	3.6-18.1	23.0	Northern Province	Hill of Fare	5.0		27.0
	Ross of Mull	2.7		6.3		Glen Gairn	5.6,	1-18	12.9, 4.3-27
	Rogart	1.7,	1.1-3.1	10.6, 9.2-16.5		Lochnagar	5.0,	1-12.1	21.7, 11-31
	Cluanie	2.2,	1.2-3.5	3.9, 2.7-5.1		Bennachie	10.5,	6-22	34.7, 26-44
	Strontian	3.6,	1.1-10.2	11.5, 3.1-26.7		Monadhliath	8.7,	6-13	31.2, 22-35
	Ardlethen	7.1		4.7		Ballater	8.8,	4-16	35.2, 27-68
	Strichen	3.4,	2.6-4.5			Mount Battock	7.1,	3.2-13	33.3, 22-55
	Skene	2.9,	1.6-5.1	11.5, 7.9-18.6		Cairngorm	10.3,	2.3-18.4	29.3, 14-55
	Peterhead	3.8,	1.7-4.6	15.0, 6.3-21.7		Ben Nevis	2.8,	1.6-5.2	11.7, 7.4-17.4
	Foyers	1.5,	0.5-3.5	5.2, 2.2-10.8		Ballachulish	4.8,	2.0-9.2	24.0, 2-47
	Strath Ossian	4.1,	2.9-6.9	13.0,12.1-14.7		Etive	3.0,	0.7-16.8	11.6, 2-30
	Moor of Rannoch	2.7,	0.9-6.9	11.4, 2.1-24.0		Newry	4.5		13.2
Southern Province	Threkeld	3.2,	1.9-4.6			Donegal Complex	4.1,	1-11	12, 5-20
	Mount Sorrel	3.8,	1.0-4.1	19.2		Barnsemore	8.1		25.1
						Galway		5-15	
					S. Uplands	Loch Doon	4.6,	0.2-12.0	15.7, 0.2-32
						Criffel	3.9,	2.0-6.2	15.6, 4-24
						Fleet	4.7,	1.8-10.6	23.1, 4.5-35
					Southern Province	Cheviot	5.7,	4.5-7.6	18.2, 4-29
						Eskdale	3.3,	1.1-6.2	11.2, 6.1-25.1
						Skiddaw	4.1,	2.5-7.3	18.3, 12-24
						Shap	8.5,	6.3-14.8	28.7, 23-53
						Ennerdale	4.6		21.0
						Wensleydale	6.7,	3.1-13.5	19.6, 18-27
						Weardale	10.7,	7.0-20	21.3
						Leinster	3.1		7.7
	*Average radioelement contents	3.5 ± 1.9		10.3 ± 4.5		*Average radioelement contents	6.0 ± 2.5		21.3 ± 8.2

*Calculated from mean values (Helmsdale is omitted from group 1 - see text).

Table 3.2 Radioelement contents of Caledonian intrusions.
References: Bowie et al., 1973; Brown et al., 1982; Cassidy, 1980; Hennessy, 1979; Hennessy, 1981; O'Connor, 1981; Plant et al., 1980; Simpson et al., 1979; Tweedie, 1979.

twice the U and Th content of Group 1 intrusions, although again there are several with transitional characteristics; for example, Ben Nevis, Etive, Loch Doon (Table 3.2). As outlined in Chapter 2, variations in the radioelement content of plutonic rocks may reflect magma provenance, magmatic evolution or later hydrothermal/mineralisation processes. This section summarises the available data concerning the distribution of U and Th in British Caledonian intrusions.

Little is known of the content and distribution of radioelements in the 'older' pre-metamorphic granites, but regional geochemical maps indicate that no U levels above regional background are associated with them (Watson and Plant, 1979).

Few of the 'forceful' intrusions included in group 1 of Brown et al., (1981) have been studied in detail with respect to their radioelement distribution. Fission track studies (Bowie et al., 1973) of the Peterhead (2 samples) and Strichen (5 samples) biotite granites, show U to be located predominantly in the primary accessory minerals zircon, apatite, sphene, and minor allanite and monazite. Minor quantities of U are associated with chloritised biotites, and where whole rock U values exceed 4.0 ppm, some U is located in secondary hematite (Bowie et al., 1973). Uranium and Th show a normal differentiation trend (see Chapter 2) in many 'forceful' intrusions; for example, in the Foyers Complex mean U and Th contents increase from 1.5 ppm and 5.1 ppm in tonalite and granodiorite to 3.5 ppm and 10.1 ppm in adamellite respectively (Plant et al., 1980).

The Helmsdale intrusion is exceptional in having uncharacteristically high Th and particularly U contents for a group 1 granite (see Table 3.2). The higher Th content is probably related to thorite, identified in heavy mineral concentrates from streams draining this intrusion (Gallagher, 1971). The high U contents have been attributed to post-emplacement

enrichment during faulting and uplift; the U content increases with degree of alteration, obscuring any primary distributions that may have been present (Gallagher, 1971; Bowie et al., 1973; Watson and Plant, 1979). Fission track studies (Bowie et al., 1973) show that the main concentrations of U within the granite are associated with chloritised biotite, both as a secondary distribution and primary concentrations in included zircon and apatite. Enriched U levels occur in uraniferous veinlets associated with fluorite, and adsorbed in limonite in fault zones. Watson and Plant (1979) suggested that this mineralisation is the result of the interaction of circulating meteoric waters in deep fault zones, with rising magmatic fluids containing U and F derived from an underlying magma chamber; the existence of a more extensive granite mass at depth below Helmsdale is inferred from aeromagnetic evidence.

In view of their higher U and Th contents (Table 3.2) and voluminous, low density masses (Section 3.2), the Siluro-Devonian granites are of greater potential geothermal interest than group 1 intrusions. Detailed radiometric mapping, coupled with fission track studies, has been carried out on several of these intrusions in the Southern Uplands and the Lake District (Cassidy, 1980). Radioelement concentrations in the Loch Doon intrusion exhibit a concentric zonation which parallels in-situ magmatic differentiation trends from diorite to granite (Figure 3.6). Additionally, Tindle (1982) found that although high U contents are present in microgranite (6.2 ppm) and aplite dykes (10.9 ppm), Th is relatively depleted in these highly evolved rocks; 16.6 ppm and 4.6 ppm respectively. Uranium contents in the Loch Doon were initially controlled by the crystallisation of the primary accessory minerals apatite, zircon, sphene and minor allanite (in order of

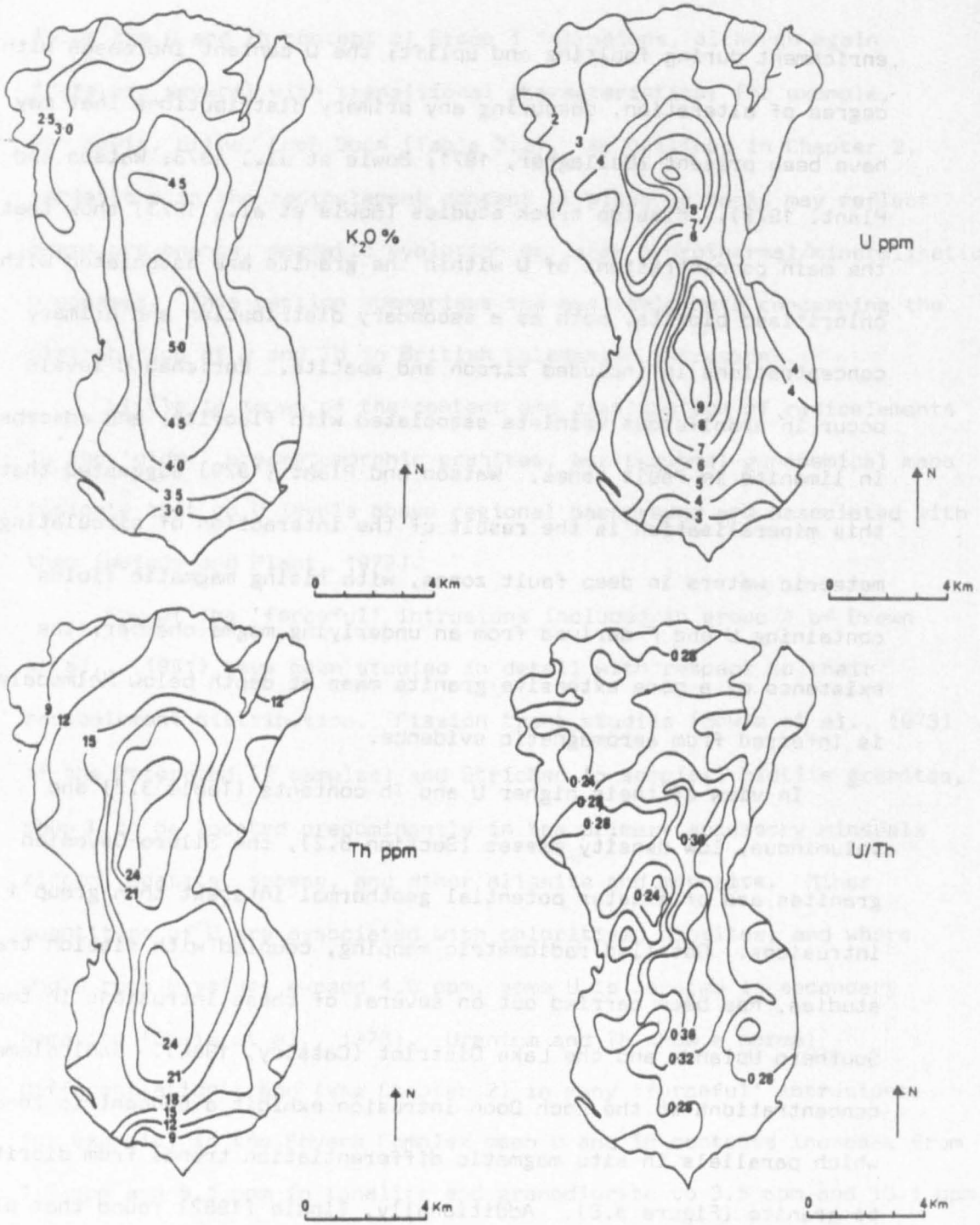

Figure 3.6 Radioelement distribution in the Loch Doon intrusion, from Cassidy (1980).

appearance in the crystallisation sequence from diorite to granite; Cassidy, 1980). Sporadic monazite and xenotime are the main primary hosts for U in the microgranite and aplite dykes (Tindle, 1982). In the granite, microgranite and aplites, secondary U occurs in chloritised biotite, grain boundaries and microfractures, probably representing late-stage remobilisation and deposition of U, possibly associated with rapid expulsion of volatiles from these residual melts (Tindle, 1982). The major control on the distribution of U and Th in the Loch Doon intrusion appears to have been primary magmatic differentiation and is reflected in the linear correlation between these elements (Figure 3.7). Depletion of Th and the consequent decrease in $^{Th}/U$ ratio in the most evolved rocks was probably due to fractionation of Th-bearing phases (e.g. allanite, sphene, monazite) in the magma, as observed in several highly differentiated intrusions (Section 2.3). Late-stage remobilisation/addition of U was of minor extent.

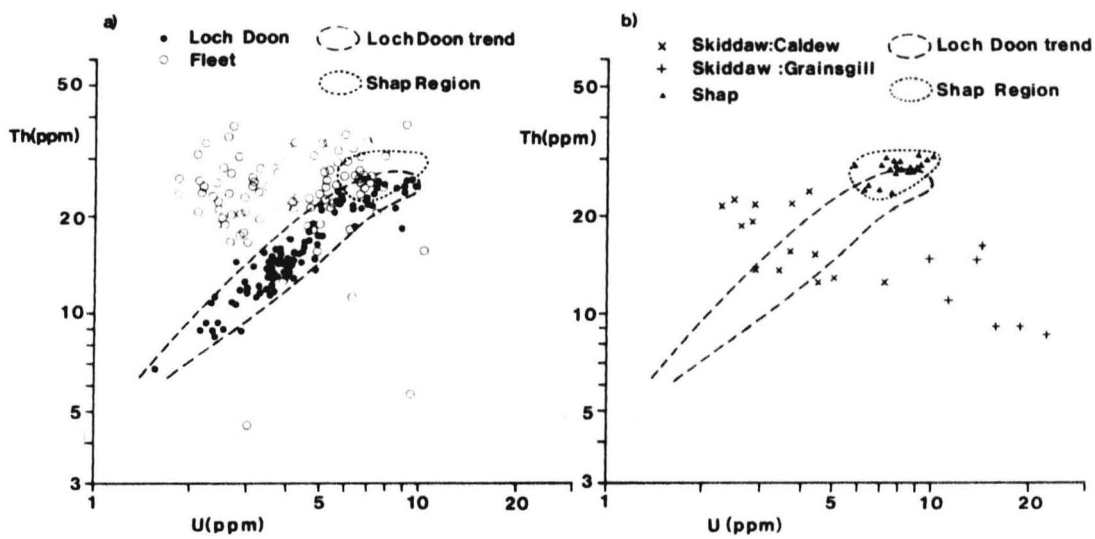

Figure 3.7 U-Th relationships for the Southern Uplands and Northern England, Caledonian intrusions; from Brown et al., (1982). The Grainsgill and Caldew outcrops of the Skiddaw intrusion, (b), represent mineralised and unmineralised granites respectively. The Loch Doon and Shap distributions (from (a)), are indicated in outline in (b).

The Fleet intrusion, Southern Uplands, which varies from an outer, coarse-grained biotite granite to an inner, fine-grained biotite-muscovite granite, exhibits a progressive decrease in Th content with fractionation towards the centre of the intrusion, but U shows no systematic variation (Figure 3.8). Fission track studies (Cassidy, 1980) reveal that although some U is held in primary accessory minerals, considerable percentages occur as low level dissemination in altered biotite and feldspar, and along grain boundaries. Secondary remobilisation of U in this intrusion, by post-magmatic hydrothermal fluids, is probably associated with mineralisation and U enrichment in the adjacent country rocks (Cassidy, 1980). The resulting U depletion and variable $^{Th}/U$ ratios (Figure 3.8) over the granite is reflected in the position of Fleet samples relative to the Loch Doon magmatic trend in Figure 3.7.

High U contents in the Shap Granite, Lake District, are held predominantly in primary accessory minerals, apatite, zircon, sphene, allanite, thorite and uraninite (P. Webb, pers. comm.); this intrusion lies at the most evolved end of the Loch Doon trend in Figure 3.7. Samples from Skiddaw (Lake District), however, are discordant to the Loch Doon trend (Figure 3.7), indicating remobilisation of U, probably associated with the extensive sericitisation, greisenisation and mineralisation evident in this granite (Cassidy, 1980; Brown et al., 1982) and which, in the mineralised Grainsgill outcrop, appears to be related to U enrichment. Although minor U depletion is evident in some unmineralised Caldew samples, the overall primary trend in fresh Skiddaw granite is a depletion in Th as U content increases (Figure 3.7).

The buried Weardale Granite, N. England, which is spatially associated with post-intrusive metalliferous mineralisation, is enriched

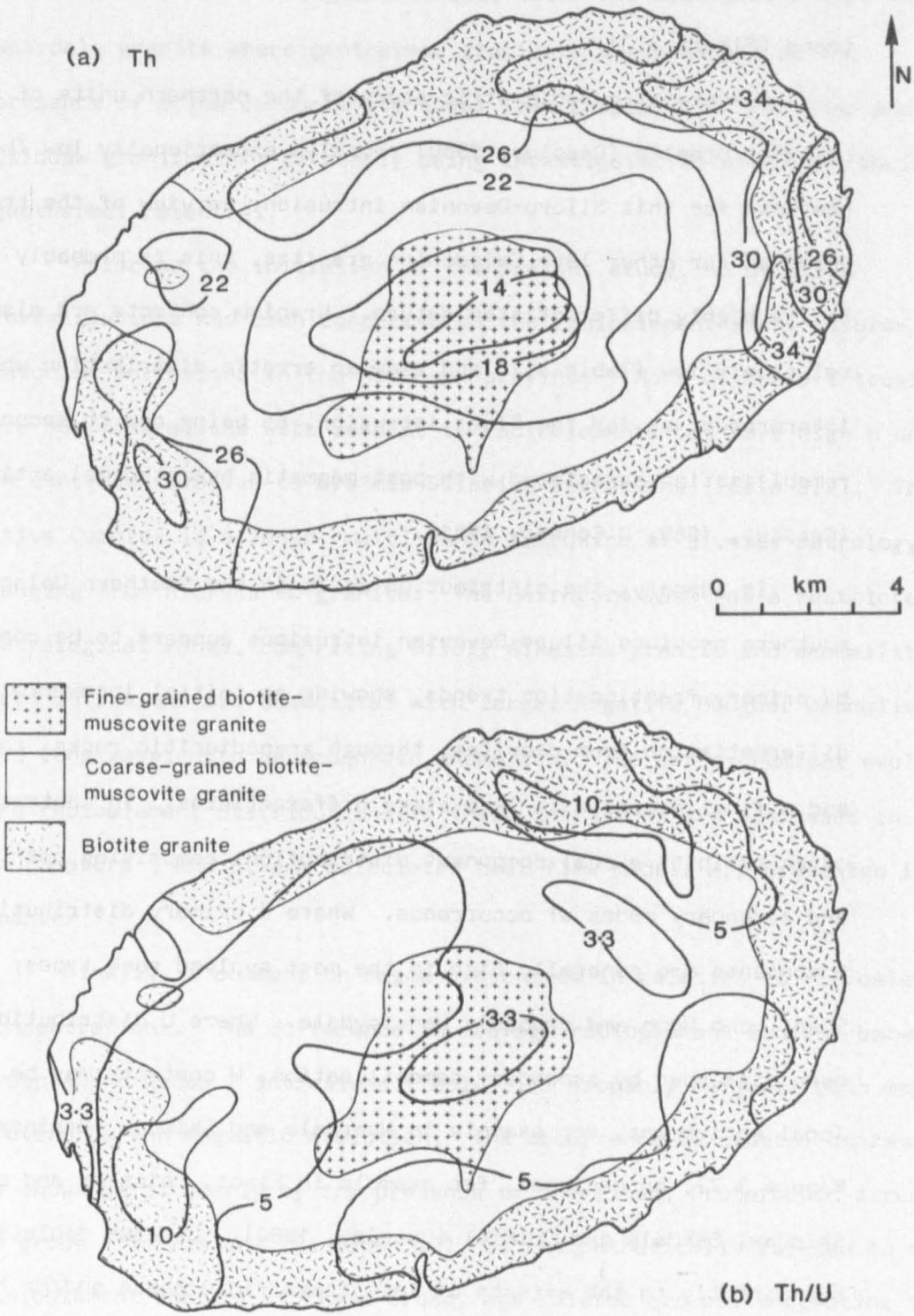

Figure 3.8 Distribution of Th (a) and Th/U (b) in the Fleet intrusion; from Cassidy (1980). Contour levels in (a) are in ppm Th.

in U, whereas the Wensleydale granite plots close to the Loch Doon trend (Figure 3.7).

A systematic radiometric study of the northern units of the Leinster Granite (Cassidy, 1980) revealed exceptionally low Th contents for this Siluro-Devonian intrusion; in view of the trends observed for other late Caledonian granites, this is probably related to its highly differentiated nature. Uranium contents are also relatively low (Table 3.2) and show an erratic distribution which is interpreted, as for the Fleet intrusion, as being due to secondary remobilisation associated with post-magmatic hydrothermal activity (Cassidy, 1980; O'Connor, 1981).

In summary, the distribution of Th in the Southern Uplands and southern province Siluro-Devonian intrusions appears to be controlled by primary fractionation trends, showing an initial increase with differentiation from diorites, through granodioritic rocks, to granites, and a final decrease in late-stage differentiates. In contrast, U often exhibits a dual component distribution, comprising both primary and secondary modes of occurrence. Where a primary distribution prevails, U contents are generally high in the most evolved rock types; for example Shap, Loch Doon amd probably Wensleydale. Where U distributions have been disturbed by secondary remobilisation, U contents may be high due to local enrichment, for example in Weardale and Skiddaw (Grainsgill outcrop; Figure 3.7), or depleted, for example in Fleet, Leinster and parts of Skiddaw, Eskdale and Criffel (Cassidy, 1980). Uranium depletion may be due directly to the effects of late-stage fluid-phase and/or hydrothermal processes, or to subsequent removal of labile U from secondary sites by surficial weathering processes.

Plutons with uniformly high U and Th contents and large, low density volumes are of particular geothermal interest. Indeed, high

heat flow (92 mW m^{-2}; England et al., 1980) has been proved over the Weardale granite where geothermal gradients are enhanced by the presence of a low conductivity cover (see Chapter 1). The Shap and Skiddaw granites are currently being investigated to establish their geothermal potential.

Prior to the initiation of the present study, no detailed investigations had been conducted on the radioelement-rich, Siluro-Devonian intrusions in the northern province. Most of these intrusions are not mineralised with respect to radioelements but have high U and Th contents relative to Pre-mid-Silurian intrusions (Table 3.2). The Etive Complex is a zoned, multi-phase intrusion of diverse petrology ranging from diorite to granite. The Cairngorm mass has a restricted petrological range, comprising mildly alkaline granite and adamellite. Both intrusions are associated with large, negative Bouguer anomalies and long wavelength aeromagnetic anomalies. The petro-chemical evolution and radioelement distributions in these intrusions are discussed in detail in Chapters 5 and 6, and calculated heat flow models are presented in Chapter 7.

Finally, a comment on magma provenance in relation to radioelement concentrations. The difference in average radioelement content between group 1 and group 2 intrusions (Table 3.2) probably reflects both magma provenance and magmatic evolution. The occurrence of crustal contamination, as shown particularly by the presence of inherited, Proterozoic zircons in group 1 intrusions (Section 3.2), is antipathetically related to mean radioelement content of these broad, age-related groups, suggesting that magmas with high levels of U and Th are not primarily of crustal origin; in contrast to the proposal of Halliday (1981). Possible sources for the high U, Th and other LIL element contents of siluro-Devonian intrusions

are:

i) Remelting of juvenile underplate which had undergone intense volatile fluxing and LIL element enrichment (Simpson et al., 1979; Brown et al., 1981). Differing degrees of partial melting in such a source region may account for both the different petrological ranges and trace element contents between pre-mid-Silurian and Siluro-Devonian, post-tectonic intrusions.

ii) Melting at different levels in a vertically stratified mantle wedge, with a lower zone enriched in incompatible elements; a model proposed by Thirlwall (1982) to account for the systematic variation in major and trace element geochemistry and Nd-Sr isotopes of Caledonian, calc-alkaline volcanics.

iii) In-situ or lower level magmatic fractionation. Large scale in-situ fractionation is inconsistent with the gravity data for Siluro-Devonian intrusions. However, it may be possible to obtain vertical zonation of trace element concentrations with little variation in major element concentrations in silicic magma chambers (Hildreth, 1979). Alternatively, extensive fractionation of basaltic-andesite magma at lower crustal levels may have been important.

A combination of (i), (ii) and (iii) may apply and, additionally, some U may have been derived from partial melting or scavenging of crustal rocks, particularly in the southern province where lower crustal rocks are less depleted (Blaxland et al., 1979).

CHAPTER 4 ANALYTICAL TECHNIQUES

Six major analytical techniques were employed in this study:

i) Gamma-ray spectrometry: for in-situ analysis of whole rock U, Th and K_2O contents.

ii) Epithermal neutron activation analysis (E.N.A.A.): used for determination of U and Th contents of powdered rock samples, essentially for calibration of the gamma-ray spectrometer.

iii) X-ray Fluorescence (XRF): to determine K_2O contents of powdered rock samples for calibration of the gamma-ray spectrometer, and selected trace element analyses.

iv) Instrumental neutron activation analysis (INAA): for supplementary REE analyses.

v) Fission track analysis: for location of U-bearing mineral phases in polished thin sections.

vi) Electron microprobe analysis: for identification and quantitative analysis of mineral phases located by method (v).

Routine operation of XRF and INAA systems has been established by the technical staff of the Open University (Appendix A). Techniques (i), (ii), (v) and (vi) are discussed in detail below.

4.1 GAMMA-RAY SPECTROMETRY

The areal extent, topographic relief and inaccessibility to vehicles of the intrusions under consideration negated the feasibility of conventional sample collection as an effective survey technique. A method for rapid, in-situ determination of radioelement content was required.

The portable gamma-ray spectrometer has proved to be a versatile tool for the in-situ determination of radioelement concentrations on both small and large scale surveys (e.g. Wollerberg and Smith, 1968; Killeen and Carmichael, 1970; Løvborg et al., 1971; Cassidy 1980). This method of radioelement mapping offers two major advantages over conventional sample collection techniques:

a) A larger volume is analysed: An 'effect sample' of 30-50 kg is analysed (Løvborg et al., 1971; see Section 4.1:2); an order of magnitude larger than normal, homogenized hand samples analysed by laboratory methods. The speed and simplicity of operation also permits representative coverage at individual localities.

b) 'Immediate' results: Simple equations convert raw field counts to element abundances allowing in-situ appraisal of survey results and assessment of further requirements.

One possible disadvantage lies in the need to assume secular equilibrium between parent and daughter isotopes, particularly in the ^{238}U series (see Section 4.1:2). The spectrometer calibration technique used in this study, however, indicates little deviation from secular equilibrium. Another limitation, although not significant in this study, is the low precision of K analyses in the presence of high U or Th concentrations. Analyses become meaningless when U and/or Th contents exceed ∿100 ppm (Løvborg et al., 1971).

4.1:1 Operational theory of the gamma-ray spectrometer

Cassidy (1980) presented a comprehensive study of natural gamma-ray sources and the operational parameters of a gamma-ray spectrometer. Here, only information essential to the understanding of the use and limitations of this instrument is summarised; the reader should refer to Cassidy (1980) for experimental and theoretical details.

Figure 4.1 presents schematically the gamma-ray spectra associated with K, U and Th, and certain of their daughter products. The background continua result from gamma-ray interactions with surrounding material and the detector crystal (compton scattering). Summation of such spectra, superimposed on an additional small background contribution derived from extraneous sources (see Section 4.1:2), produces a complex total rock spectrum (Figure 4.2). Although prominent emissions below 1 MeV occur in both the U and Th decay series (Grasty and Darnley, 1971), these peaks are swamped by 'compton' and extraneous background. Photons of energies 1.46, 1.76 and 2.62 MeV are generally accepted as being the most suitable for the measurement of K, U and Th respectively and result from the decay of ^{40}K, ^{214}Bi in the ^{238}U series, and ^{208}Tl in the ^{232}Th series.

The instrument employed in this work was a portable 4-channel gamma-ray spectrometer, Model GR 410 coupled with a NaI(Tl) scintillation detector, Model GPX-21, both manufactured by Geometrics Services (Canada) Ltd. Coupling was via a five conductor, coiled interface cable and 12 x 1.5 volt alkaline D-cell batteries were used as the power source. Total weight, including the carrying frame is approximately 9 kg. Figure 4.3 is a simplified flow diagram of the functions performed by the various components of the system. A fundamental improvement in this system over the DISA 400 model employed by Cassidy is the continual monitoring of the reference source providing instant warning of gain drift in the photomultiplier tube. The PMT stability is affected by 4 variables:

a) Temperature changes: Gain coefficient = $-0.5\%\ °C^{-1}$

b) Fluctuation of the H.V. power supply: a 1 volt change in supply causes a 1% gain shift.

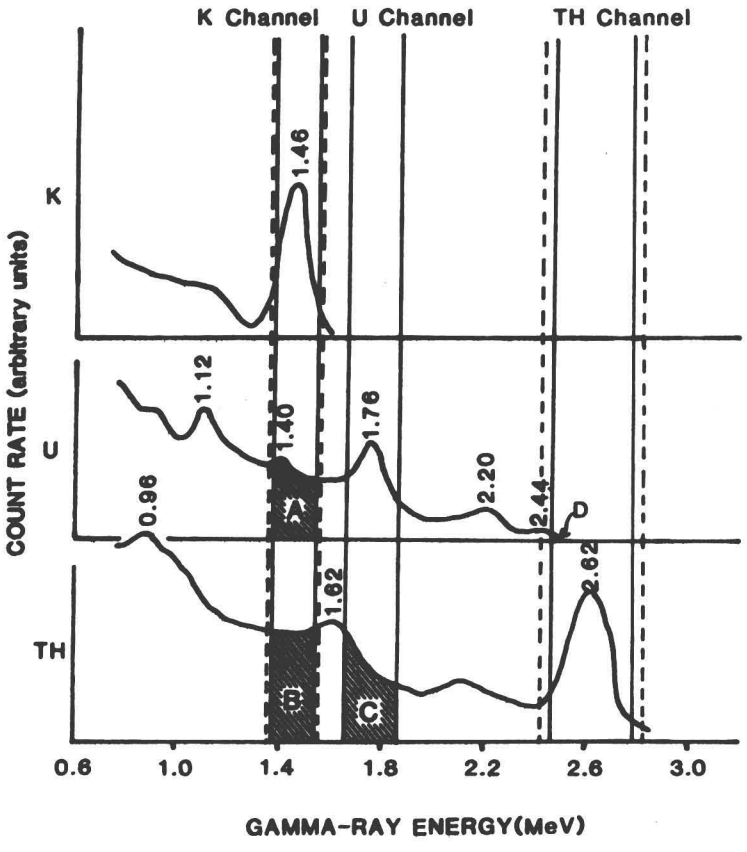

Figure 4.1 Schematic spectrograms for individual K, U and Th sources. From Cassidy (1980).
Shaded areas = stripping corrections to channel counts (see text).
Dashed lines = window widths used by Cassidy (1980).
Solid channel limits = window widths used in this study.

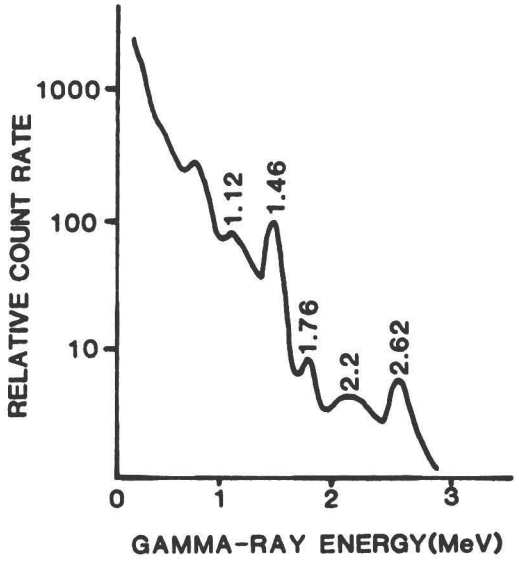

Figure 4.2 Example of total rock γ-ray spectrum, from an outcrop of granite-gneiss with 5.4 ppm Th, 1.7 ppm U and 3.4% K. From Doig (1968).

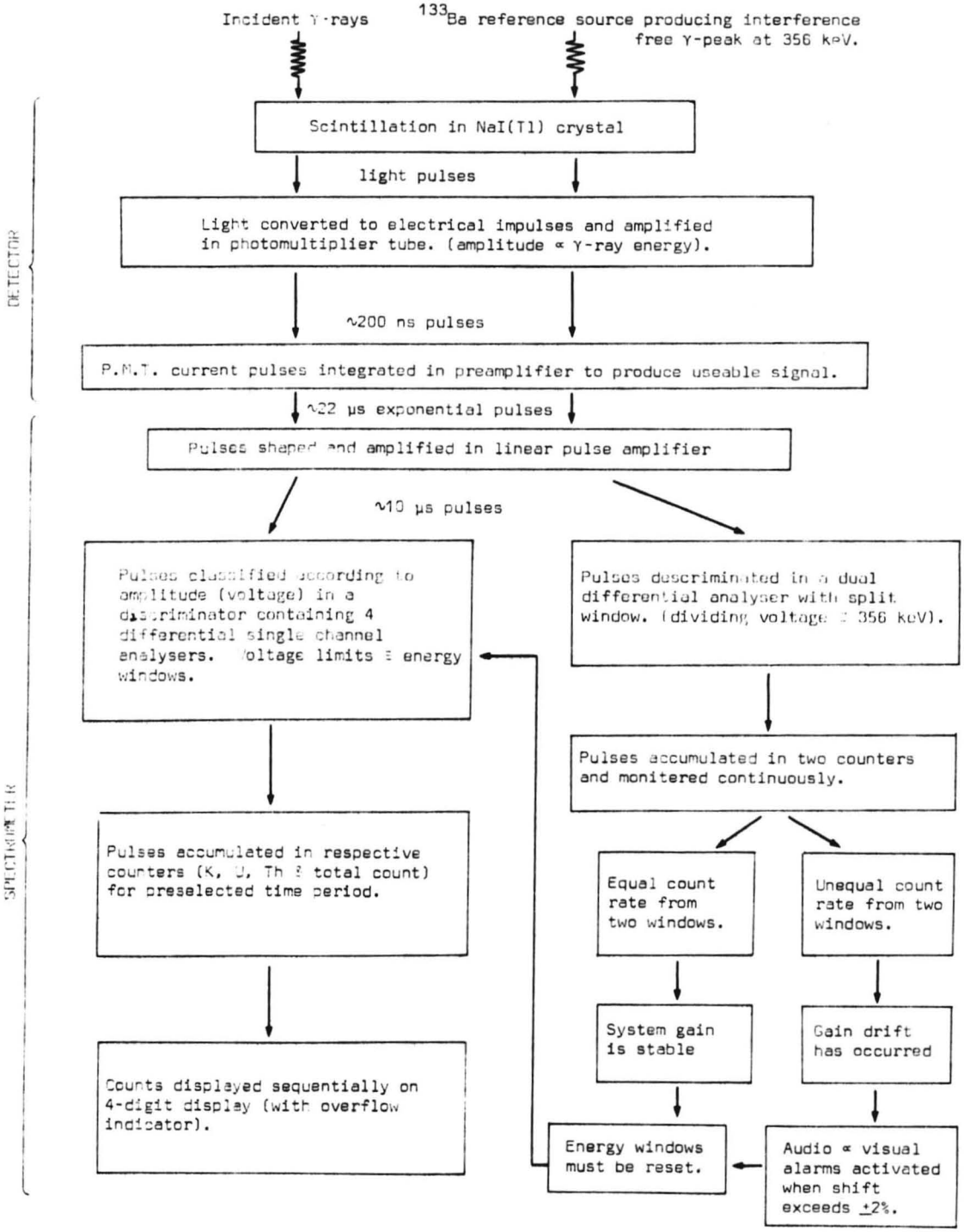

Figure 4.3 Simplified flow diagram of the operational theory of gamma-ray spectrometer system, GPX-21 + GR410.

c) High count rates: Sensitivity may be subject to 'dead-time' effects, i.e. the inability of the circuitry to process more than one event at a time. Dead time for the GR 410 is specified as 10 μs and the count rate correction formula is:

$$C_o = \frac{C_i}{1 \times (Ci \times 10^{-6})}$$

where C_o = output count rate, C_i = input count rate (in counts s^{-1}). For maximum count rates observed in this study, $C_o \simeq 1000$ counts s^{-1}, $C_i = 1001$ counts s^{-1}, i.e. a counting loss of 0.1%.

d) Ageing: Long term gain drift due to crystal deterioration. The control range for gain correction is ±12%, any larger drift necessitates internal adjustment. Audio and visual alarms are activated for drifts > ±2%. A preliminary experiment was conducted to monitor the effect of gain drift within these permitted limits on the channel count rates (Figure 4.4). Count rates are within statistical error in all channels for gain drifts between -2% and +1%. A gain offset of +2% produced consistently low channel counts. During field use the gain was checked both before and after individual readings and stations recounted if drifts greater than ±1% occurred.

Window settings are adjusted by three potentiometers in the instrument housing. To determine optimum settings individual peaks were scanned using a 1 kg jar of KCl, a 10 g jar a specpure ThO_2 and a 10 g jar of specpure U_3O_8 as sources. A 5 cm thick block of granite was placed between detector and source in each case to simulate the peak distortion under field conditions. Results are presented in Figure 4.5 For the well defined K and Th (^{208}Tl) peaks the energy equivalent window widths used were narrower than those employed by

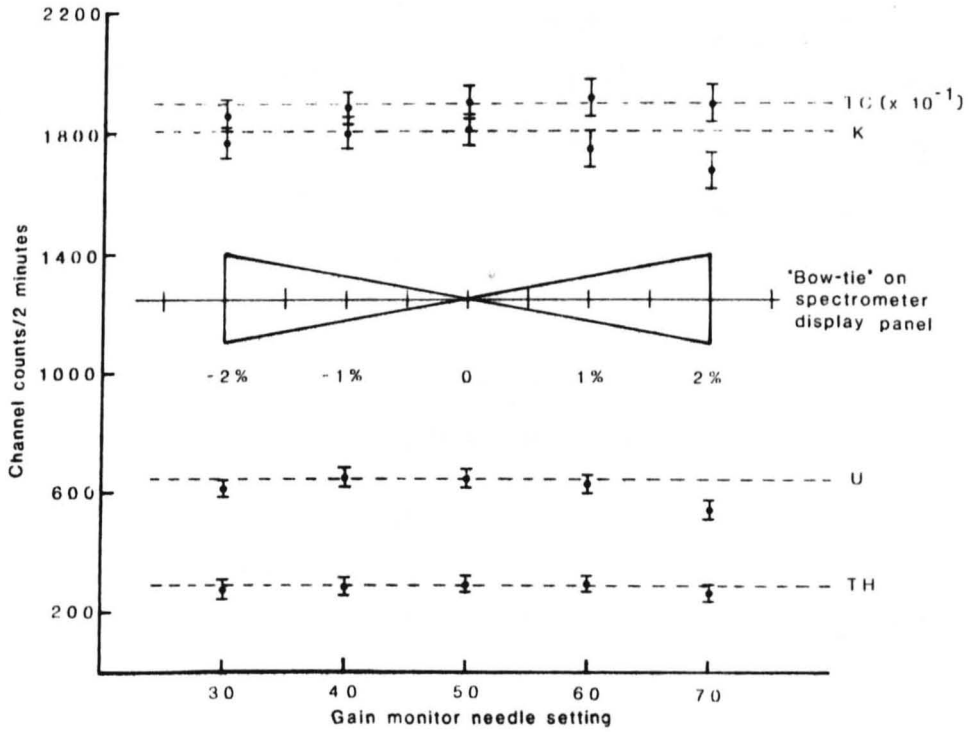

Figure 4.4 Channel count rates for gain variations between $\pm$ 2%. Readings were taken with the detector on an approx. 1 m^2 x 16 cm thick, slab of Cornish granite.
Error bars are derived from counting statistics, i.e. $\pm N^{\frac{1}{2}}$.

Cassidy (1980) (see Figure 4.1). A relatively wide window was maintained for the poorly defined U(^{214}Bi) peak. Table 4.1 summarises the energy window settings employed in this study.

Table 4.1 Energy equivalent window settings for gamma-ray spectrometer

ELEMENT	ENERGY PEAK	WINDOW WIDTH	POTENTIOMETER SETTING	CHANNEL No.
TOTAL COUNT	all energies	between 0.5 - 3.0 MeV.		1
K (^{40}K)	1.46 MeV	176 KeV	4.86	2
U (^{214}Bi)	1.76 MeV	210 KeV	5.79	3
Th(^{208}Tl)	2.62 MeV	320 KeV	8.66	4

From Figure 4.1, it is clear that raw count data in channels 2, 3

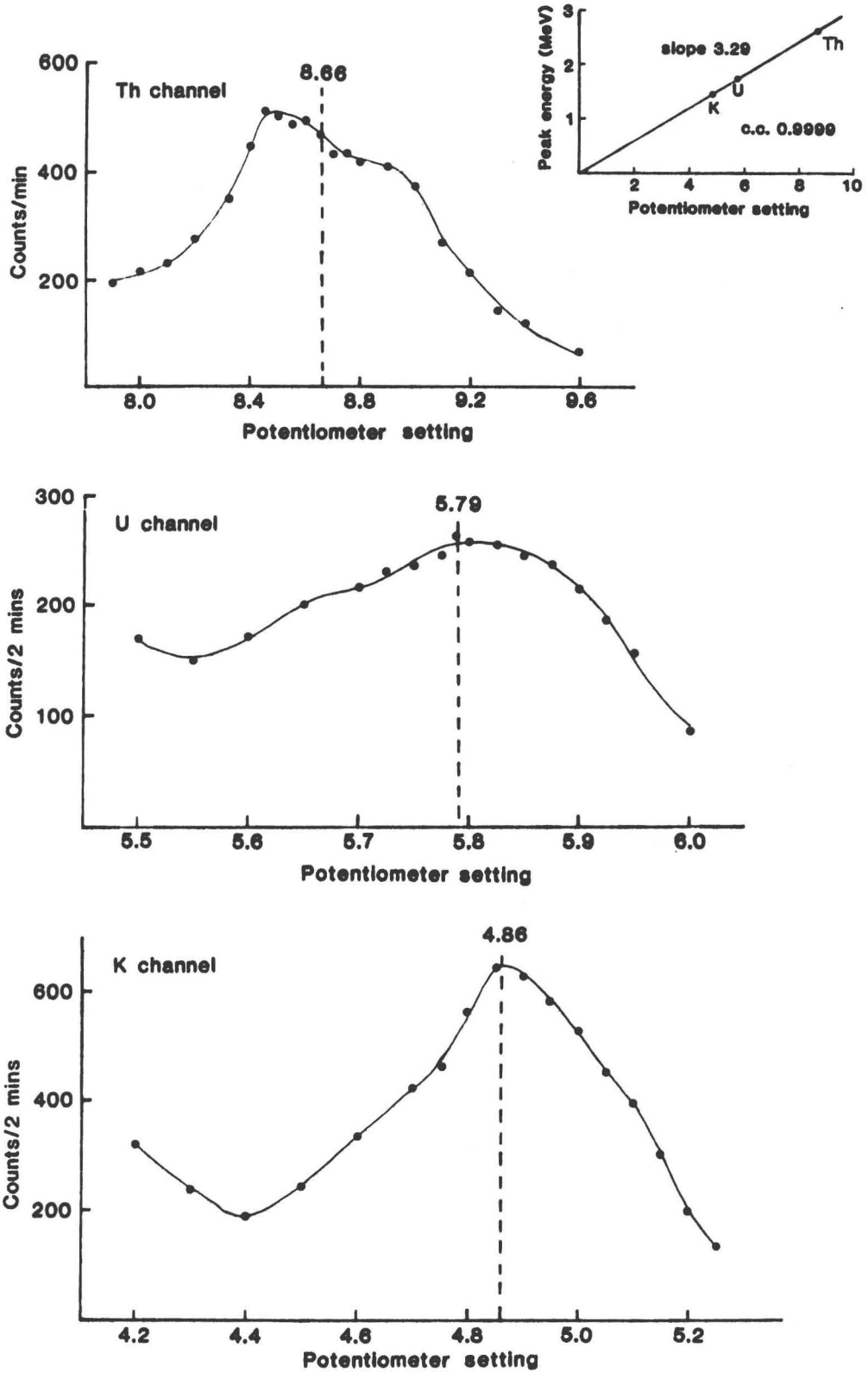

Figure 4.5 Determination of central peak positions in Th, U and K channels.
Dashed lines show potentiometer settings employed for field readings, inset shows the linearity between optimum potentiometer settings and peak energies.

and 4 (Table 4.1) are not directly proportional to the K, U and Th contents of the source. Corrections must be applied to remove:

i) Background radiation from extraneous sources

ii) Counts in the U channel due either directly to emissions from Th duaghter products, or to compton scattering of higher energy γ-rays, i.e. area C in Figure 4.1.

iii) Counts in the K channel due to decays in the U and Th series, either directly, or as a result of compton scattering, i.e. areas A and B in Figure 4.1.

iv) A small contribution to the Th channel counts coming from the high energy tail of the 2.44 MeV peak in the U series, i.e. area D in Figure 4.1. The narrow Th window width employed minimised this contribution to a negligible level.

After stripping, the count rates become proportional to the relevant radioisotope concentrations. Neglecting the contribution to the Th channel from area D, the three equations relating raw counts to U, Th and K contents may be expressed as:-

$$\text{PPM Th} = \frac{C_{Th} - B_{Th}}{S_1} \qquad \text{(i)}$$

$$\text{PPM U} = \frac{C_U - B_U - R_1 C'_{Th}}{S_2} \qquad \text{(ii)}$$

$$\%K_2O = \frac{C_K - B_K - R_3 C'_U}{S_3} \qquad \text{(iii)}$$

where C_{Th}, C_U, C_K = raw count rates in Th, U, and K channels respectively.

B_{Th}, B_U, B_K = background counts in Th, U and K channels respectively.

C'_{Th}, C'_U = stripped count rates in Th and U channels respectively

R_1, R_2, R_3 = stripping ratios representing contributions to the U and K count rates due to Th and U, expressed as ratios of count rates in the relevant channels.

S_1, S_2, S_3 = sensitivity constants relating 'stripped' count rates

to radioelement contents.

4.1:2 Parameters relating to the validity of calibration and field use

Certain parameters relating to the characteristics of the source must be fully considered before calibration and field application of the spectrometer:

a) Source-detector geometry

The need to maintain a constant source-detector geometry has been observed by many workers (Doig, 1968; Grasty and Darnley, 1971; Løvborg et al., 1971; Cassidy, 1980), the accepted configuration being a solid angle of detection of 2π. Effectively, this implies a source with a planar surface, and dimensions exceeding the volume of rock contributing to the detected γ-rays (Figure 4.6). The 'effective volume' will vary with rock density, but the mass remains constant since variations in the volume concentration of 'active' material are exactly compensated by γ-ray attenuation lengths (Wormold and Clayton, 1976); linear attenuation (μ) = density x mass absorption coefficient. Hence, the response of the spectrometer remains independent of density provided that the dimensions of the outcrop are sufficient (Figure 4.6). A variation in mean atomic number of the source material does affect attenuation but this is generally insignificant for geological samples (Løvborg, 1972).

The linear attenuation of γ-rays in air is approximately 20% per 100 ft, or 0.07% per 10 cm (Darnley, 1972), i.e. negligible for small detector elevations. The practical application of this relationship provides a method for maintaining an effective 2π source by raising the detector above any small scale surface irregularities. Limitations on detector elevation then arise from the horizontal extent of the outcrop and the increasing bias towards shallow sampling and possible weathering effects (Figure 4.6).

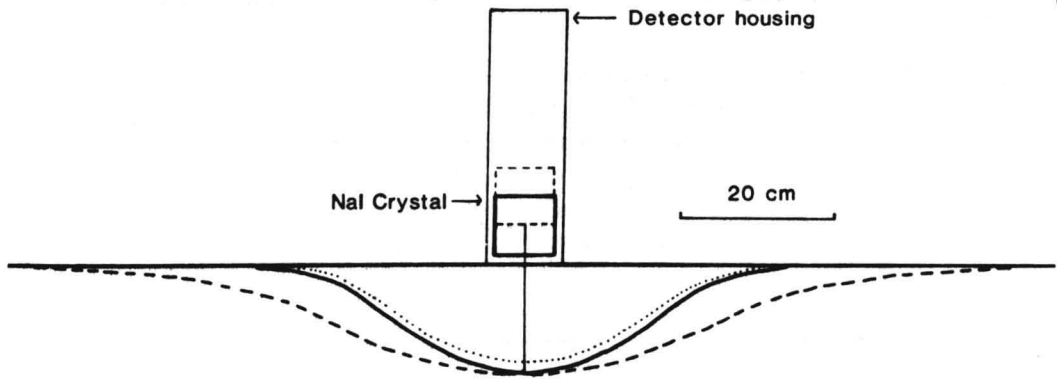

Figure 4.6 Dimensions of source volume; adapted from Løvborg et al. (1971). Vertical cross-section showing the dimensions of the 'effective sample' for a detector placed directly on a 2 surface (solid curve), and at an elevation of 5 cm (dashed curve), for 2.62 MeV γ-rays. Rock density ≅2.8 g cm^{-3}; mass enclosed by solid curve ≅49 Kg. Dashed curve = equivalent sample for 1.76 MeV γ-rays (detector on surface).

b) Secular equilibrium

The quantitative determination of radioelements by gamma-ray spectrometry assumes:-

i) The ratio of abundance of the measured radioactive isotope to other isotopes of the given element is constant in nature.

ii) Secular equilibrium exists between parent isotopes, ^{238}U and ^{232}Th, and their respective measured decay products, ^{214}Bi and ^{208}Tl.

The decay series of ^{232}Th is characterised by daughter products with short half-lives of ≤6.7 years; in particular, the relatively mobile isotope, $^{220}_{86}Rn$, has $T_{\frac{1}{2}}$ = 55 sec. and is unlikely to 'escape' before decaying. Hence, although Th may be leached during the initial stages of weathering (Pliler and Adams, 1962), disequilibrium is unlikely to persist.

Uranium tends to form soluble, highly mobile compounds on oxidation to U^{6+}; this, combined with the geologically significant half-lives and diverse geochemistry of some of its daughters, renders this series far more susceptible to disequilibrium (see Table 4.2). The most probable cause of disequilibrium in granitic rocks is the leaching of U due to

ISOTOPE	HALF-LIFE	POSSIBLE CAUSE OF DISEQUILIBRIUM	EFFECT
$^{238}_{92}U$	2.51×10^9 y	Loss of ^{238}U by oxidation and solution in weathering zone.	RaeU > U
$^{234}_{90}TH$	24.1 d		
$^{234}_{91}Pa$	1.18 m		
$^{234}_{92}U$	2.48×10^5 y	Fractionation of ^{234}U from ^{238}U by 'recoil' at the solid-liquid interface, preferential oxidation and removal in solution in weathering zone.	RaeU < U
$^{230}_{90}TH$	8.0×10^4 y	Low solubility, remains in place when U is leached.	RaeU > U
$^{226}_{88}Ra$	1622 y	May be fractionated from ^{238}U by differential adsorption or crystallisation - only relevant to post-leaching deposition.	Not effective at outcrop
$^{222}_{86}Rn$	3.825 d	Gaseous phase; may migrate if favourable porosity, due to microfractures.	RaeU < U
$^{218}_{84}Po$	3.05 m		
$^{214}_{83}Pb$	26.8 m		
$^{214}_{83}Bi$	19.7 m		
$^{214}_{84}Po$			
	} three daughters omitted		
$^{206}_{86}Pb$			

Table 4.2 ^{238}U decay series: adapted from Livinson and Coetzee (1978).
RaeU = Radon equivalent uranium
y = years; d = days; m = minutes
The time interval required to achieve secular equilibrium is ~10 x half-life of the longest lived daughter = 2.5×10^6 y.

recent (<2.5 x 10^6 y) weathering (Levinson and Coetzee, 1978). Such processes may involve the selective leaching of ^{234}U relative to ^{238}U because of decay-related recoil at the solid-liquid interface (e.g. Zelinski et al., 1981; Nkomo et al., 1970), or depletion of both U isotopes relative to ^{230}Th (see Table 4.2). Migration of radon may also cause disequilibrium although, because of its short half-life, this is rarely substantial (Tanner, 1963).

c) Homogeneity

Cassidy (1980) concluded that inhomogeneous distribution of radioelements within the sample volume is the major source of error in the determination of U, Th and K by gamma-ray spectrometry. Considerable percentages of whole rock U and Th may be held in sporadically dispersed high U / Th accessory phases (Section 2.5). It follows that the effects of inhomogeneity are unlikely to be eliminated, but may be assessed by taking several readings, wherever possible, at closely spaced intervals on each outcrop.

d) Background radiation

The two major sources of background counts are cosmic-ray interactions with either rock or detector, and atmospheric radon originating from nearby rocks and soils. Station to station monitoring of background radiation is impractical since it would require a cumbersome lead shield and a calculated or measured average is generally used. In the present study, values calculated by extrapolation of calibration curves were used (Section 4.1:3). Spatial and temporal variations in background may arise from variations in cosmic activity, concentration of atmospheric dust and radon beneath trees and bushes (Killeen and Carmichael, 1970), or heavy rainfalls causing near-surface concentration of dust and radon (Graston and Darnley, 1971). Variations in background counts are, however, unlikely to exceed the error on

calculated values.

4.1:3 Calibration of gamma-ray spectrometers

Cassidy (1980) argued that the advantages of a calibration method based on field standards, measured under the same conditions as the unknowns, outweigh the greater theoretical accuracy afforded by using artificial sources. If the prerequisites for geometry, homogeneity and secular equilibrium are satisfied at each calibration station then the particular characteristics of the survey environment are automatically accounted for (e.g. spectrum shape, background radiation).

The method adopted here is essentially that used by Cassidy (1980) with the implementation of the following improvements: critical selection of calibration stations based on homogeneity, collection of core samples from directly below the detector and improved precision on the laboratory analysis of U, Th and K. Collection of calibration samples was carried out in conjunction with the field survey; selection was based on both the range of channel counts and ratios between channel counts. Calibration curves could then be constructed from the maximum range of radioelement abundances encountered. Unfortunately, progress was interrupted by two major malfunctions, and the eventual loss of the original spectrometer (through no fault of the present author). The change in characteristics due to replacement parts and the new spectrometer necessitated three separate calibrations. These will be referred to subsequently as: spec I (before first malfunction), spec II (before loss), spec III (new).

a) Spec III

Stripping ratios: These were calculated directly from field

data, but, as will be shown in section 4.1:3C, results for R_2 and R_3 (equations (i) and (ii), Section 4.1:1) were unsatisfactory. Supplementary measurements were made on a set of doped concrete blocks constructed at the Archaeology Department, Oxford University, (Figure 4.7).

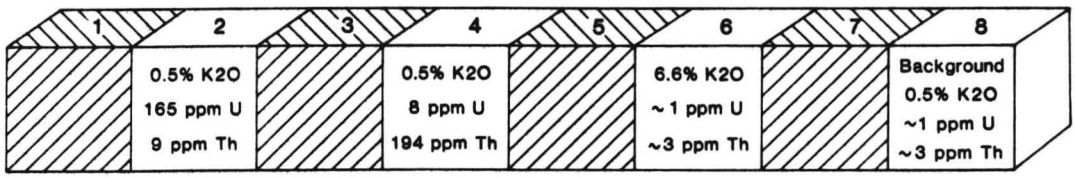

Figure 4.7 Configuration of doped concrete blocks used for calculation of stripping ratios. Radioelement contents of blocks 1, 3, 5 and 7 are as in block 8. Density of blocks = 1.90 g cm^{-3}.

After subtracting background radiation, i.e. that measured on block 8, the channel count rates for blocks 2 and 4 may be expressed as follows (Cassidy, 1980):

$$U_C = a_1 \times \text{ppm U} + a_2 \times \text{ppm Th} \quad \text{(iv)}$$

$$Th_C = a_3 \times \text{ppm U} + a_4 \times \text{ppm Th} \quad \text{(v)}$$

$$K_C = a_5 \times \text{ppm U} + a_6 \times \text{ppm Th} \quad \text{(vi)}$$

where the a_i's are constants dependent on both stripping ratios and channel sensitivities.

It follows that the stripping ratios, as defined in Section 4.1:1 are:

$$R_1 = \frac{\text{Counts in U channel due to Th}}{\text{Counts in Th channel due to Th}} = \frac{a_2}{a_4}$$

similarly, $R_2 = \frac{a_6}{a_4}$, $R_3 = \frac{a_5}{a_1}$ (R_4 = U contribution to Th channel)

Count rates recorded on the doped blocks are summarised in Table 4.3. Count times were adjusted for optimum statistics without overflow.

Table 4.3 Count rates recorded on doped blocks using spec (III)

BLOCK No.	COUNTING PERIOD	COUNTS/2 MINS TH CHANNEL	U CHANNEL	K CHANNEL
8 (BG)	14 mins	158 ± 5	275 ± 6	850 ± 11
7	10 mins	141 ± 5	265 ± 7	874 ± 13
6 (K)	14 mins	143 ± 4	269 ± 6	2027 ± 17
5	10 mins	246 ± 7	314 ± 8	831 ± 13
4	6 mins	1802 ± 24	1342 ± 21	1745 ± 24
3	10 mins	269 ± 7	542 ± 10	943 ± 14
2 (U)	2 mins	187 ± 14	7030 ± 83	3313 ± 57
1	10 mins	121 ± 5	440 ± 9	751 ± 12

Substituting the values for blocks 2 and 4 in equations (iv), (v) and (vi) results in three sets of simultaneous equations which may be solved for the six a_i's, giving:

$R_1 = 0.47 \pm 0.04$, $R_2 = 0.48 \pm 0.06$, $R_3 = 0.36 \pm 0.08$, and

$R_4 = -0.002 \pm 0.0004$.

Final errors in stripping ratios are a combination of counting statistics and the uncertainties on radioelements contents. Within the accuracy of the instrument $R_4 \equiv 0$, which is to be expected considering the narrow Th window employed.

The following points apply to the validity of the above method for calculating stripping ratios.

i) For a density of 1.90 g cm^{-3} (Figure 4.7) the 'effective volume' for 2.62 MeV γ-rays is bounded by a radius of 42 cm and a depth of 16 cm (Løvborg et al., 1971). The dimensions of the blocks are insufficient to match field conditions. However, since the spectrometer

does not 'see' more than one doped block at a time and ratios are considered, the stripping ratios remain valid. Clearly, sensitivity constants based on these measurements would be incorrect, since, for example, the observed count rates in blocks 1, 3 and 5 exceeded background (Table 4.3). Any small errors in stripping ratios are compensated when calculating sensitivity constants from field data.

ii) The isotope ^{228}Ac, which occurs early in the ^{232}Th decay series, emits a low intensity of γ-rays detectable in the U and K channels. If the Th ore used to dope the blocks is in disequilibrium then R_1 and R_2 may be slightly overestimated. R_3 and R_4 are unaffected by disequilibrium.

iii) Killeen and Carmichael (1970) found it necessary to calculate two sets of calibration equations for low and high count rates; above and below 20, 40 and 60 c.p.m in the Th, U and K channels respectively. Few measurements in this study fell into the low count rate bracket and instrumental dead time limits were not exceeded.

iv) Differences in matrix effects between the concrete blocks and granite are compensated by calculating sensitivity constants from field data.

Sensitivity constants and background

Where possible, cores (1 inch diameter, ∿9 inches long) were drilled for use as calibration samples. This method was preferred since 'fresh' samples could be collected from directly below the detector, thus minimising inhomogeneity effects. Ten minute counts were recorded at selected field stations. Drilling sites were limited for logistical reasons and, where further stations were required to extend the radioelement range of calibration, several closely spaced

readings were recorded to ensure homogeneity and a sample removed with a sledge hammer.

With obvious weathering removed, all samples were crushed, powdered and dried before analysis according to the methods described in Section 4.2 and Appendix A. Preliminary regression lines were constructed of stripped count rates vs. element concentration (see Cassidy, 1980; Doig 1968). After rejection of certain data points (see below) final calibration lines were computed, Figures 4.8, 4.9, and 4.10. A semi-quantitative approach to data rejection was adopted, with the following results:

i) E106 was rejected from all data sets due to its deviation from each linear trend. Significantly, this station exhibited the largest standard deviation on field counts and the sample was collected by the less favoured technique, using a sledge hammer.

ii) C118, again not a core sample was rejected from the U and K calibrations. Field counts in the Th channel were constant for all readings but considerable variation was observed in the U and K channels. Sparsely dispersed orthoclase phenocrysts (∿2-2.5 cm long) may account for the erratic K variation, but the cause of the high U value (Figure 4.9) is unknown.

iii) C101 was rejected from U and Th lines. The friable nature of this coarsely porphyritic sample suggests that leaching of both U and Th by recent weathering processes may have caused disequilibrium in both decay series (significantly this sample lies above both calibration lines).

The small amount of scatter about the calibration lines exhibited by the remaining points is probably, largely due to inhomogeneity effects, incurred by the sampling process. The good correlation

coefficients (Figures 4.8 and 4.9) indicate that conditions of secular equilibrium are satisfied and, since analyses were made on relatively fresh samples, the calibration lines apply to radioelement concentrations below extreme surficial weathering effects.

Final conversion equations for spec III are:

$$\text{ppm Th} = \frac{C_{Th} - 27.6}{17.5}$$

all counts per 2 mins.

$$\text{ppm U} = \frac{C_U - 71.1 - 0.47\, C_{Th}'}{45.6}$$

$$\%K_2O = \frac{C_K + 80.0 - 0.48\, C_{Th}' - 0.36\, C_U'}{418.8}$$

The negative background calculated for K probably arises from the narrow concentration range over which the equation is defined, and although a different calibration may apply at lower K levels, the above equation remains valid for this survey.

Empirical errors may be derived by calculating the standard error of estimate, s (Killeen and Carmichael, 1970).

$$s = \frac{\Sigma_i\, (X - X_i(\text{calc}))}{N}$$

where X_i = laboratory analysis and $X_i(\text{calc})$ = analysis from field data.

This gives a precision of ±2.2 ppm Th, ±0.9 ppm U and ±0.2% K_2O. These figures incorporate a 'geological' factor, that is they include indeterminable errors due to possible inhomogeneous distribution of radioelements in the source volume and probably represent a lower limit to analytical precision. They do, however, give a realistic estimate of the total precision on the survey technique.

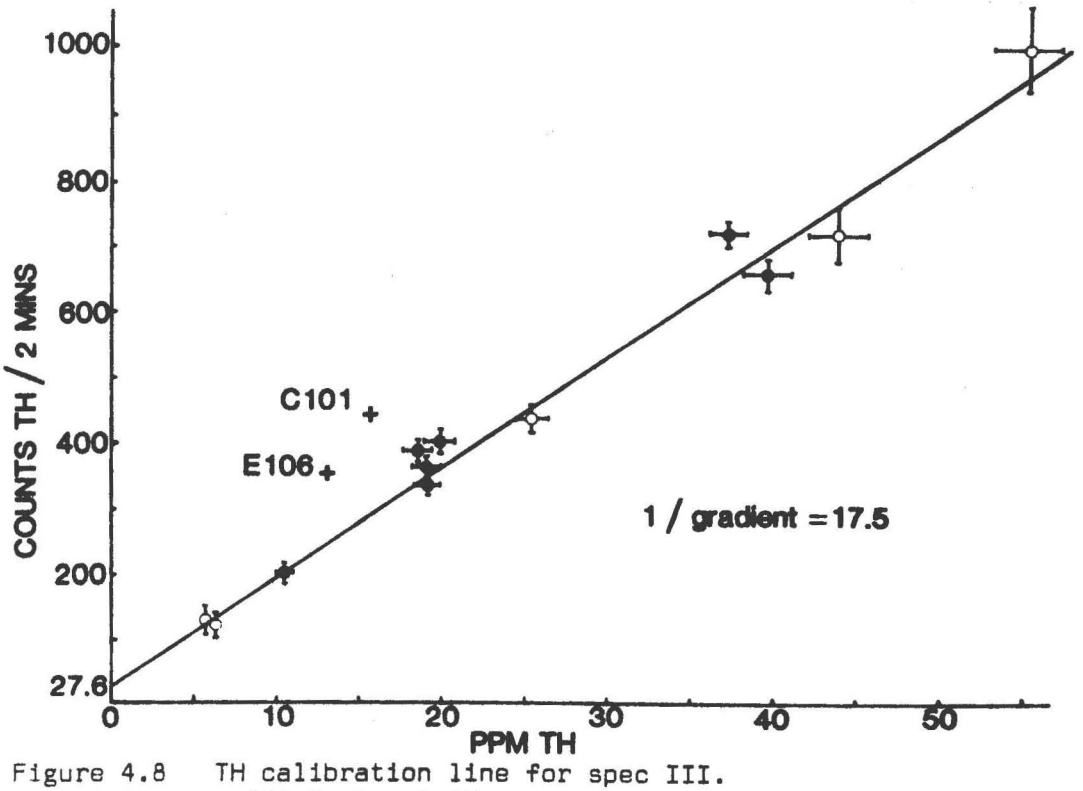

Figure 4.8 TH calibration line for spec III.
Correlation coefficient = 0.97.
Lablled crosses = rejected data (error bars not included).
Closed circles = core samples.
Open circles = sledge hammer samples.
Error bars based on counting statistics and analytical errors.

b) Spectrometers I and II

These spectrometers were unavailable for independent measurement of stripping ratios and so a mathematical approach was adopted, based only on field standardisation sites. Again, the calibration samples comprised both cores and 'sledge hammer samples'. Conversion parameters were determined using multiple regression of 2, 3 and 4 variables for Th, U and K calibrations respectively. Equations (i), (ii) and (iii) may be written:

$$\text{ppm Th} = \frac{-B_{Th}}{S_{Th}} + \frac{1}{S_{Th}} \cdot C_{Th} \qquad \text{(vii)}$$

$$\text{ppm U} = \frac{-B_{U}}{S_{U}} + \frac{1}{S_{U}} \cdot C_{U} - \frac{R_1 . C_{Th}'}{S_{U}} \qquad \text{(viii)}$$

$$\%K_2O = \frac{-B_{K}}{S_{K}} + \frac{1}{S_{K}} \cdot C_{K} - \frac{R_2 . C_{Th}'}{S_{K}} - \frac{R_3 . C_{U}'}{S_{K}} \qquad \text{(ix)}$$

The Open University 'Geostats' multiple regression program was used

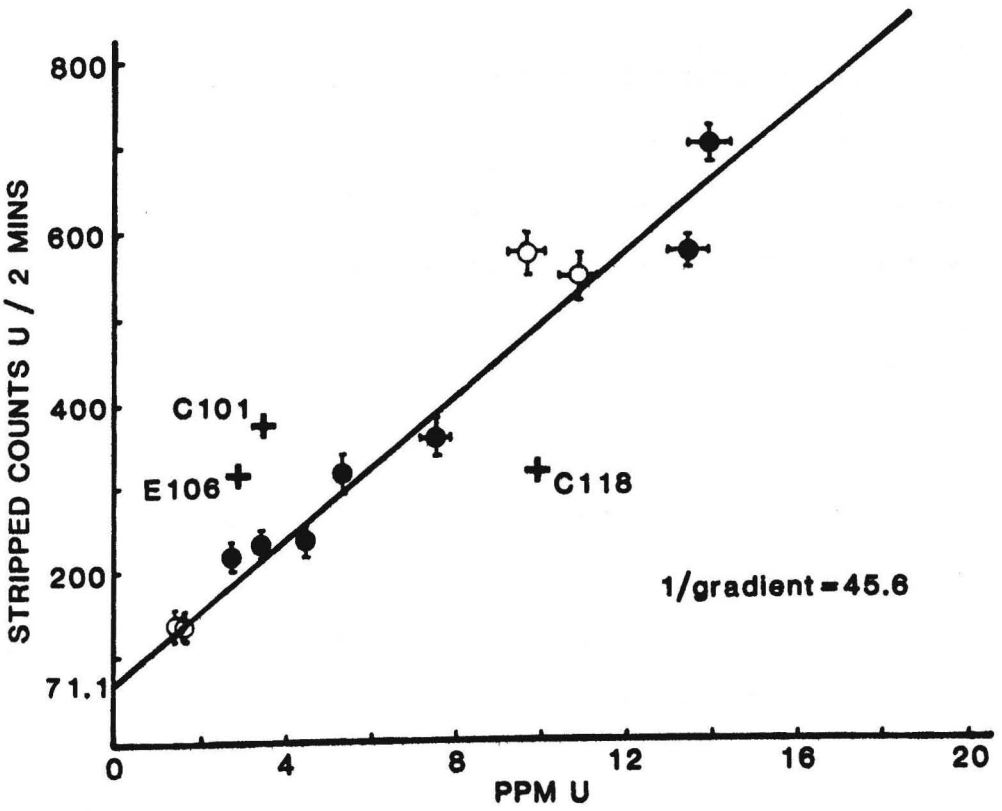

Figure 4.9 U calibration line for spec III. Correlation coefficient = 0.96, symbols as Figure 4.8.

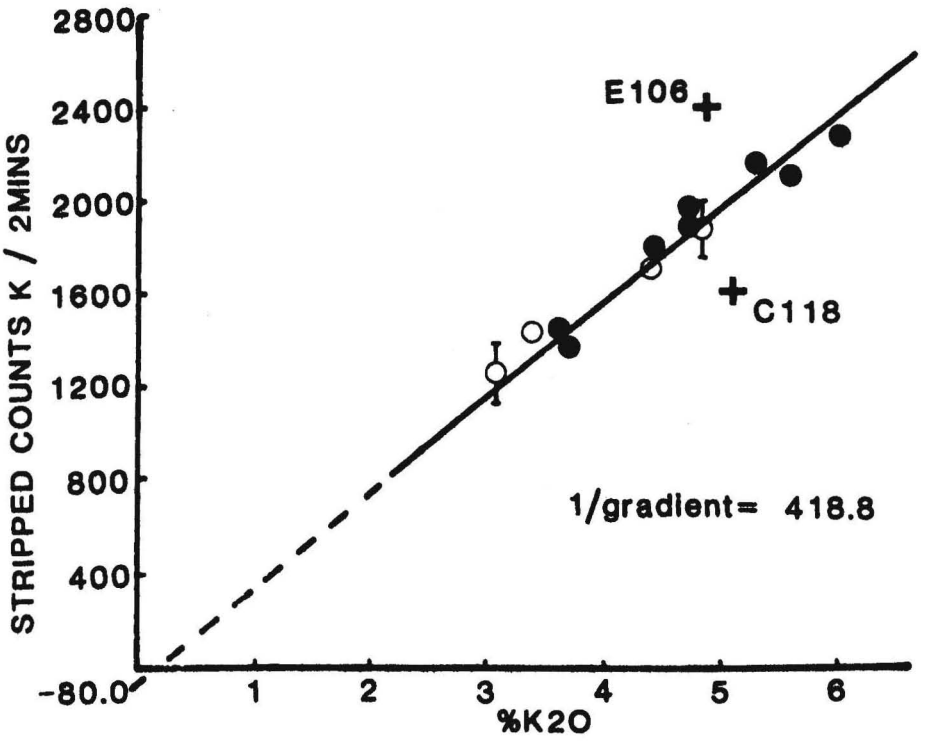

Figure 4.10 K calibration line for spec III. Correlation coefficient = 0.93, symbols as Figure 4.8.

to evaluate partial regression coefficients from observed channel counts (per 2 mins) and analysed radioelement contents of calibration samples for all standardisation sites.

To check the validity of this method the data for spec III were processed in this manner and results compared with the previous calibration.

Since stripping ratios are not involved in equations (i) and (vii) the same linear regression line applies in both cases and S_{Th} and B_{Th} are as before (see Figure 4.8).

R_1 is unknown, and hence U channel counts may not be stripped of contributions from Th series disintegrations. Multiple regression of ppm U with C_U and C_{Th}' gives:

$$B_U = 80.1,\ R_1 = 0.44,\ S_U = 47.5,\ \text{corr. coeff.} = 0.96$$

Similarly, multiple regression of 4 variables; $\%K_2O$, C_K, C_U' and C_{Th}' gives:

$$B_K = -330.8,\ R_2 = -0.28,\ R_3 = 0.42,\ S_K = 533.9,\ \text{corr. coeff.} = 0.94$$

The values obtained for B_U, R_1 and S_U using this mathematical approach are very similar to those calculated using the doped blocks in addition to field standardisation stations. The values for B_K, R_2, R_3 and S_K, however, show a large discrepancy which probably arises from: a) the narrow range of the dependent variable ($\%K_2O$) and b) from the fact that $C_K \gg C_U' > C_{Th}'$. Point b means that relatively large variations in R_3, and particularly R_2, are easily accommodated in minimising the root mean square deviations. Although the values for B_K, R_2, R_3 and S_K obtained by this regression are mathematically correct, their substitution in equation (iii) does not produce an entirely meaningful relationship, since R_2 cannot be negative (refer to area B in Figure 4.1).

Substituting the previously calculated value of R_2 (0.48) and regressing $\%K_2O$ with $(C_K - 0.48C_{Th}')$ and C_U' gives:-

B_K = -199, R_3 = -.39, S_K = 440.3 corr. coeff. = 0.93

i.e. within the errors of the previous calibration.

As a realistic assessment of the validity of this method, the U and K_2O contents of two stations with differing $^{Th}/_{U}$ ratios were calculated from the above constants, and from those of the previous calibration:- results are presented in Table 4.4. All values agree within 2.2% except for one K_2O value (6.1% high). In the latter case, errors in R_2 and R_3 are emphasized by high U and Th contents.

In applying this technique to specs I and II, R_4 was taken as zero: results are presented in Table 4.5. These constants were used to reduce the relevant raw count data, the K_2O results being viewed with caution where errors in R_2 and R_3 became significant (i.e. at high U and Th contents).

Stn. No.	Channel	Counts /2 mins	PPM U		% K_2O		
			1st Calib.	2nd Calib.	1st Calib.	2nd Calib.	R_2 as a variable
C64	K	2251					
	U	415	3.6	3.55	5.0	5.0	4.9
	Th	405					
C72	K	2529					
	U	1051	14.2	14.0	4.9	4.85	5.2
	Th	720					

Table 4.4 U and K_2O contents of two field stations calculated from three sets of calibration constants for spec III.

1st calib. - using independent measurement of stripping ratios
2nd calib. - using multiple regression.

c) Comparison of spectrometer calibrations

During the course of field studies, four base stations were established to monitor both long and short term intra- and inter-system variations. Two subsidiary stations were also used for daily records when working from more remote areas.

No systematic or random variations beyond one sigma counting errors were observed for any spectrometer, with the exception of those

	SPEC I	SPEC II
TOTAL No. OF CALIBRATION STATIONS	8 cores + 3 hammer samples	3 cores + 9 hammer samples
TH No. Stns.	10	11
TH Range	0.2 - 18.5 ppm	0.6 - 23.4 ppm
TH S_{TH}	16.2	17.7
TH B_{TH}	15.2	2.1
TH Corr. Coeff.	0.96	0.95
U No. Stns.	10	8
U Range	0.6 - 4.9 ppm	0.4 - 4.7 ppm
U Su	91.3	85.2
U Bu	-2.9	-3.6
U R_1	0.62	0.30
U Corr. Coeff.	0.95	0.94
K_2O No. Stns.	9	* 11
K_2O Range	0.3 - 5.2%	0.4 - 5.4%
K_2O S_K	212.4	306.5
K_2O B_K	2.6	0.23
K_2O R_2	0.77	0.3
K_2O R_3	0.45	0.3
K_2O Corr. Coeff.	0.93	0.97

Table 4.5 Calibration constants for SPECS I and II obtained by multiple regression.

*Regression of $\%K_2O$ v. C_K, Cu and C_{TH} for Spec II resulted in:- $R_2 = -3.5$, $R_3 = 2.5$.
By constraining either R_2 or R_3 to be + ve always resulted in R_3 or R_2 being - ve.
∴ Both R_2 and R_3 were constrained and a linear regression performed. (Values of R_2 and R_3 were chosen to give the best correlation coefficient).

associated with major malfunctions.

Three of the base stations were common to specs I and II, and two to all three spectrometers. Table 4.6 presents concentration data calculated from the relevant calibration equations at these stations. Results are well within the precision limits calculated in Section 4.1:3 a. Unfortunately, all three common stations lie at the lower end of the concentration range but, where possible, overlapping surveys were carried out with the three spectrometers which showed no discrepancies in radioelement trends and abundances at higher levels.

Stn. No.	Channel	SPEC I		SPEC II		SPEC III	
		Counts /2 mins	Radio-element content	Counts /2 mins	Radio-element content	Counts /2 mins	Radio-element content
E3	% K_2O	111	0.38	132	0.38		
	ppm U	38	0.37	31	0.35		
	ppm Th	27	0.73	19	0.95		
E27	% K_2O	1004	3.85	1310	3.97	1623	3.86
	ppm U	229	1.85	195	1.93	199	1.72
	ppm Th	117	6.28	117	6.49	133	6.02
B1	% K_2O	590	2.23	717	2.16	888	2.20
	ppm U	104	0.59	83	0.66	139	0.53
	ppm Th	101	5.30	103	5.70	121	5.34

Table 4.6 Comparison of base station radioelement contents using relevant calibration equations for specs I, II and III.

4.2 ANALYSIS OF CALIBRATION SAMPLES - EPITHERMAL NEUTRON ACTIVATION ANALYSIS

Two analytical techniques were used for the laboratory determination of radioelements in calibration samples and analysis of samples where field gamma ray data were unobtainable.

An established ED-XRF system at the Open University was used for determination of K_2O (see Appendix A). This system has a detection limit of 0.05% K_2O and a 2σ error on accuracy of less than 0.1% at 4.0% K_2O.

An analytical technique for the determination of low concentrations of U and Th had not previously been established at the Open University. Factors influencing the present authors decision on which method to adopt are outlined in Table 4.7. Two techniques appear capable of the required accuracy, precision and detection limits for both U and Th;

METHOD	ACCURACY, PRECISION & DETECTION LIMITS	AVAILABILITY OF FACILITIES	REFERENCES
LABORATORY γ-RAY SPECTROMETRY	Precision and detection limits dependent upon counting statistics c.f. field spectrometer. Accuracy, esp. for U dependant on secular equilibrium. ∴ RaeU measured. Minimal sample preparation + large sample measured.	No laboratory spectrometer at the Open University.	Stuckless et al., 1977 (1) Stuckless et al., 1977 (2)
ISOTOPE DILUTION + MASS SPECTROMETRY	Good precision on both U & Th (∿2%) with a detection limit ∿0.5 ppm. Some problems with dissolution of minor phases (e.g. zircons), would effect accuracy. Complex sample preparation.	Mass spectrometer and 'clean lab' available, but machine time is limited.	Rosholt, Zartman & Nkomo - 1973. Stuckless et al., 1977
FISSION TRACK COUNTING	Small sample analysed introduces inhomogeneity errors of ∿ ±10%. Mutual interference means results depend on $^{TH}/_{U}$ ratio.	Reactor facilities available at A.W.R.E. Aldermaston. Two irradiations necessary - costly.	Stuckless et al., 1977 Wollenberg - 1977
DELAYED NEUTRON COUNTING	U is major interference on Th analysis - limits accuracy when $^{TH}/_{U}$ is low. Sensitivity for Th only 1% that for U. High $^{TH}/_{U}$ ratios (>8) can introduce errors on U analysis but generally excellent results for U. Minimal sample preparation. Careful control on neutron flux & travel time to detector required.	Reactor and analytical facilities available at A.W.R.E. Aldermaston. Two irradiations required for U & Th analysis - costly and subject to demand.	Amiel - 1962 Cumming - 1974 Stuckless et al., 1977
FLUORIMETRY	Complicated sample preparation, dissolution problems and matrix effects, limit accuracy, ∿ ±10%, at 10 ppm U. Error increases at lower concentrations. No information found on application to Th analysis.	No fluorimeter at Open University.	Stuckless et al., 1977 Grimbert, 1971
NEUTRON ACTIVATION ANALYSIS i) THERMAL	Precision of 5% on Th & detection limit 0.1 ppm. Cannot use for U. Minimal sample preparation.	Technique used routinely at O.U. for determination of R.E.E. Reactor facilities at Ascot.	Potts, Thorpe, Watson - 1981 Baedecker, Rowe, Steinnes - 1976.
ii) EPITHERMAL	Increased precision on Th due to reduction of "background" activity (∿2%). U activity enhanced-statistics superior to Th. No mutual interference. Minimal sample preparation.	Use same equipment as thermal activation + Cadmium tube - available at Ascot. Possibly can co-ordinate with INAA irradiations.	Brunfelt & Steinnes - 1969. Hennessy - 1978

Table 4.7 Commonly applied techniques for geochemical analysis of U and Th.

viz isotope dilution coupled with mass spectrometry, and epithermal neutron activation analysis (ENAA). The problems involved in the complex sample preparation for the former are surmountable (Rosholt et al., 1973) but the technique was rejected on the basis of limited spectrometer time. No logistical problems were apparent for ENAA and so this technique was duly adopted and developed during this study to optimise the use of available equipment.

4.2:1 Principles of epithermal neutron activation analysis

The application of ENAA relies on the preferential activation of specific nuclides when irradiated with high energy (~0.4 - 1 MeV), epithermal neutrons. The principles and potential of ENAA are discussed in detail by Steinnes (1971), and Baedecker et al., (1977).

Thermal (~0 - 0.4 MeV) neutrons can be excluded from the irradiating flux by wrapping samples in cadmium foil which exhibits a high absorption cross-section in this energy region. The usefulness of ENAA for any element requires that its cadmium ratio (R_{Cd}) is low in relation to that of all interfering nuclides.

$$R_{Cd} = \frac{\text{activation rate in total neutron spectrum}}{\text{activation rate in epithermal neutron spectrum}}$$

A significant advantage with respect to silicate rocks is an improvement in the peak: background ratio for elements with low R_{Cd}, due to a reduction in the activity of, in particular, ^{46}Sc, ^{59}Fe, ^{60}Co and ^{51}Cr under epithermal irradiation (Baedecker et al., 1977). The reduction in background activity for the experimental conditions employed in this study is approximately 40% at 96 KeV.

Energy specta are accumulated on solid state germanium detectors. Pioneer applications of neutron activation analysis to silicate rocks employed only coaxial Ge(Li) detector systems, with a resolution of approximately 2-4 KeV (Gorden et al., 1968; Brunfelt and Steinnes, 1969). The potential of high resolution (500 eV), low energy photon spectrometers (L.E.P.S.) for accumulation of the 0-200 KeV spectrum was successfully investigated by Hetogen and Gibels (1971), who found both a reduction in spectral interference, and an improvement in peak: background ratios.

4.2:2 Application to the analysis of Uranium and Thorium

The relevant (n, γ) reactions induced in the reactor, and the resulting decay series are:

$$^{238}_{92}U + ^{1}_{0}n \rightarrow ^{239}_{92}U + \gamma \xrightarrow[23.5m]{\beta^-} ^{239}_{93}Np \xrightarrow[2.35d]{\beta^-} ^{239}_{94}Pu \xrightarrow{\alpha} ^{235}_{92}U$$

$$^{232}_{90}Th + ^{1}_{0}n \rightarrow ^{233}_{90}Th + \gamma \xrightarrow[22m]{\beta^-} ^{233}_{91}Pa \xrightarrow[27.4d]{\beta^-} ^{233}_{92}U \xrightarrow{\alpha} ^{229}_{90}Th$$

m = minutes, d = days

Photon emissions accompany each stage of decay but those most convenient to measure (with half lives in the order of days) result from the decay of ^{239}Np and ^{233}Pa; relevant characteristics of the most prominent photo-emissions are given in Table 4.8. As can be seen from these data, the main advantage of ENAA in this application lies in the high advantage factor, F_a, for U over nuclides following the $\frac{1}{v}$ law.

RADIOISOTOPES	PROMINENT PEAK ENERGIES (KeV)	RADIATION TYPE	RELATIVE INTENSITY	POSSIBLE INTERFERENCE PEAKS (KeV) [1]		R_{Cd} [2] INTERFERENCE		F_a [3]	HALF-LIFE OF INTERFERENCE	FEASIBILITY OF PEAK FOR U/TH DETERMINATION
^{233}Pa	13.61	$U_{L\alpha 1+2}$	97							Matrix absorption effects
	16.43	$U_{L\beta 2}$	47							at low energies
	17.22	$U_{L\beta 1}$	100	17.25	^{239}Np	1.3		0.34	2.35 d	Cannot resolve
Half-life = 27.4d	94.65	$U_{K\alpha 2}$	61	93.9	^{160}Tb	2.9		0.76	72 d	Good - Resolved from all interferences
R_{Cd} = 3.8				93.6	^{168}Yb	7.8		2.05	32 d	with L.E.P.S.
^4Fa w.r.t. a $\frac{1}{v}$ nuclide = 13	98.43	$U_{K\alpha 1}$	100	97.5	^{153}Sm	3.6		0.95	46.8 h	
				97.5	^{153}Gd	118		31.0	242 d	Good - Resolved from all interferences
				99.5	^{239}Np	1.3		0.34	2.35 d	with L.E.P.S.
	103.8	γ	?	103.2	^{153}Sm	3.6		0.95	46.8 h	
				103.2	^{153}Gd	118		31.0	242 d	Cannot resolve from Np peak
				103.7	^{239}Np	1.3		0.34	2.35 d	
	111.0	γ	13	110.0	^{169}Yb	7.8		2.05	32 d	Low intensity peaks, poor
	111.3	$U_{K\beta 1}$	18	110.0	^{169}Yb	7.8		2.05	32 d	counting statistics.
	299.9	γ	15	298.6	^{160}Tb	2.9		0.76	72 d	Low intensity peak, not easily resolved.
	311.9	γ	100	309.6	^{160}Tb	2.9		0.76	72 d	Good - Marginal overlap, usually insignificant
	340.3	γ	4	343.4	Hf	13.3		3.5	42.5 d	V. Low intensity - poor statistics
^{239}Np	14.28	$Pu_{K\alpha 1+2}$	68	14.11	^{81}Br	3.4		2.6	35.4 h	Matrix absorption effects
	17.25	$Pu_{L\beta 2}$	27	17.22	^{233}Pa	3.8		2.9	27.4 d	at low energies
Half-life = 2.35d	18.28	$Pu_{L\beta 1}$	83							
	99.46	$Pu_{K\alpha 2}$	48	98.4	^{233}Pa	3.8		2.9	27.4 d	Good, marginal overlap
R_{Cd} = 1.3				100.1	^{182}Ta	1.9		1.5	115 d	
^4Fa w.r.t. a $\frac{1}{v}$ nuclide = 55	103.65	$Pu_{K\alpha 1}$	75	103.2	^{153}Sm	3.6		2.8	46.8 h	
				103.2	^{153}Gd	118		31.0	242 d	Cannot resolve from Pa peak
				103.8	^{233}Pa	3.8		2.9	27.4 d	
	106.1	γ	100	none						Very good
	228.2	γ	60	229	^{182}Ta	1.9		1.5	115 d	Cannot resolve
	277.5	γ	65	none						Good
	315.7	γ	7							low intensity peaks, poor
	334.1	γ	10							statistics

Table 4.8 Characteristics of photo-emissions from the decay of ^{233}Pa(Th) and ^{239}Np(U).

1 - Only peaks within 3 x detector resolutions are considered.

2 - R_{Cd}'s from Steinnes (1971) - will vary slightly with irradiation conditions.

3 - The advantage factor $F_a = \frac{(R_{Cd})_d}{(R_{Cd})_D}$ where d and D denote the interfering nuclide and the nuclide in question, respectively (Brune and Jirlow, 1964)

4 - These are taken from Steinnes (1971) and represent the F_a of U/Th with respect to a nuclide following the $\frac{1}{v}$ law, i.e. w.r.t. those nuclides responsible for most of the background continuum.

h = hours, d = days, L.E.P.S. = Low Energy Photon Spectrometer.

The experimental procedure was a compromise between facilities available, logistics and theoretical considerations and is outlined in points (a) to (e) below.

a) Sample preparation: 0.3 g aliquots of dried, homogenised rock powder were sealed in polythene capsules and placed in polythene vials with standards and flux monitors, as shown in Figure 4.11. Space for up to four batches per irradiation was available. Calibration of the primary standard, AC(OURS) is discussed in Section 4.2:3 and use of the secondary standard in Section 4.2:4.

b) Irradiation: Vials were placed in a cadmium clad core tube at the University of London Reactor Centre, Ascot, and subject to an epithermal neutron flux of approximately 10^{10} n cm^{-2} s^{-1} for 24-30 hours (one week of reactor operation).

c) Cooling time: 4-5 days is necessary to allow for the decay of particularly ^{24}Na ($T_{\frac{1}{2}}$ = 15 hours) to comply with safety regulations. Extension of this period would prove disadvantageous in view of the short half life of ^{239}Np.

d) Energy spectrum recorded: From Table 4.8 it is clear that maximum precision would be obtained by averaging analyses from the 94.9, 98.4 and 311.9 KeV peaks for Th, and the 99.5, 106.1 and 277.5 KeV peaks for U. However, for optimum utilisation of detector ranges and resolution, this requires two counting periods per sample, recording 90-108 KeV emissions on a L.E.P.S. and 260-320 KeV emissions on a coaxial Ge(Li) detector. Considering the short $T_{\frac{1}{2}}$ of ^{239}Np, such a procedure would be statistically impractical without sacrificing throughput. Only the lower energy region, including all peaks up to the ^{239}Np 106.1 KeV peak, was recorded using an Ortec hyperpure

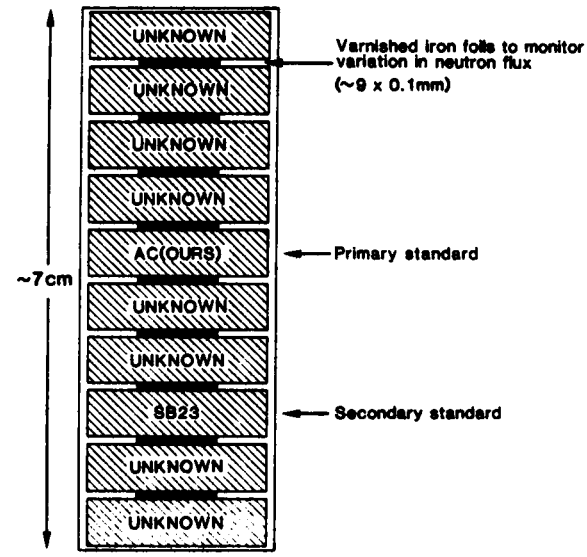

Figure 4.11 Packing of samples for irradiation

germanium L.E.P.S., with an active area of 16 mm^2, active depth of 7 mm and resolution of 535 eV at 122 KeV.

e) Count time: Maximum counts per sample were required within the restriction that 40 samples should be counted within one half life of ^{239}Np. 3000 s counts per sample, with 10 mins for data output and sample changing meets the above criteria. The iron foils were counted first to determine the variation in neutron flux across the container (see Figure 4.11). Data were processed using spectroscopy amplifiers (Ortec 472A) and accumulated on a Northern Scientific Econ II 4K multichannel analyser.

A typical spectrum is illustrated in Figure 4.12. A peak fitting program, Sampo (Routti and Prussin, 1969; modified by D. Wright, Open University, 1979) was used to calculate peak areas. Peaks were fitted to a Gaussian function with exponential tails, the shape parameters across the spectrum being set from the well defined 94.7 and 106.1 KeV peaks on each run. Corrections were applied to account for neutron flux variation and differences in cooling times. Corrected peak areas

were then compared with those of the primary standard spectrum for the same run yielding element abundances for each peak. Final results are the averages of relevant peaks (Figure 4.12), weighted according to Sampo fit errors.

4.2:3 Calibration of the primary standard

The 'in-house' standard used was a fine-grained, peralkaline microgranite from Ailsa Craig, N.W. Scotland, AC(OURS). Calibration of this standard for REE's and several other traces, including Th, was achieved by INAA (Potts et al., 1981). These authors used a standard additions method involving dry mixing of specpure trace element oxide powders with AC(OURS). Trace elements were divided into two groups to reduce photopeak interferences and three incrementally spiked samples of AC(OURS) were prepared for each group. Increments were approximately equal to elemental concentrations in unspiked AC(OURS). Four duplicate samples were analysed along with the unspiked powder and the whole procedure repeated as an independent check on weighing and homogeneity errors. Plots of corrected peak areas v. ppm trace element added were constructed and trace element contents of AC(OURS) calculated by extrapolation. This method produced a precision of better than 6.3% (1σ) for Th. Calibrations were refined by comparing Open University analyses of four U.S.G.S. standards, AGV-1, BCR-1, G-2 and GSP-1 with published analyses obtained by a critical survey of over 70 references. Accuracy of final calibrations were better than 5%.

Uranium was not included in the above calibration (Potts et al., 1981). In view of the difficulties encountered in the standard additions method, it was decided to calibrate U by comparison of corrected peak areas for AC(OURS) with those of selected international and synthetic standards irradiated in the same batch, by ENAA.

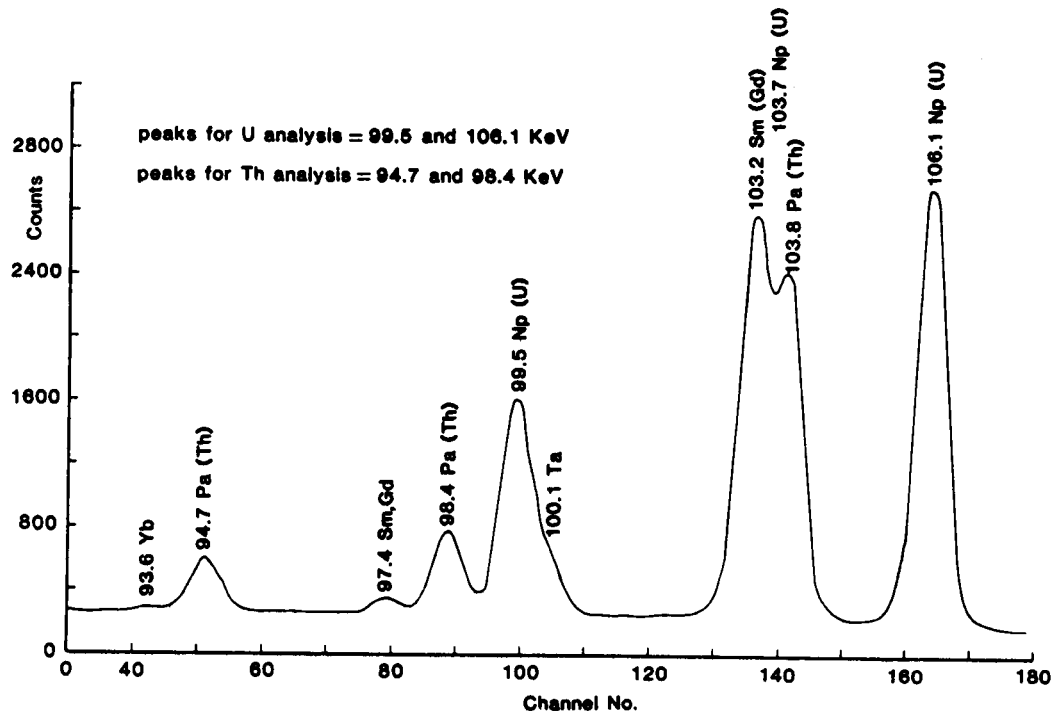

Figure 4.12 Typical energy spectrum for U and Th analysis, counted on the L.E.P.S. Peak energies given in KeV.
Sample is SB23, 10.6 ppm U, 18.1 ppm Th.

Synthetic standards comprised homogenised mixtures of spectrosil and specpure radioelement oxides. Three granitic rock powders, analysed for U by delayed neutron method (see Table 4.7) were also included. Data and references for all standards are presented in Table 4.9. All standards were thoroughly homogenised and dried before use.

Two batches, each comprising one sample of AC(OURS) and 9 standards were irradiated according to the method described in Section 4.2:2. Corrected 'Sampo' peak areas were calculated for both the 99.5 and 106.1 KeV peaks and plotted against U content; results are presented in Table 4.10 and Figure 4.13. Three samples from batch 1 produced results lying greater than 1σ off the mean (Table 4.10 and Figure 4.13); these were rejected, and the U content of AC(OURS) recalculated with no significant modification.

STANDARD	U CONTENT (ppm)	REFERENCES
USGS BCR-1	1.8 (1.74)	Abbey, 1980; (Flanagan, 1973)
USGS GSP-1	2.0 (1.8 ± 0.5)	Pal and Terrel, 1978; (Flanagan, 1973)
USGS G2	2.0	Govindaraju and Roelandts, 1977
CRPG BR	(3)	Govindaraju and De La Roche, 1977
CRPG GA	(4)	Govindaraju and De La Roche, 1977
CRPG GH	(18)	Govindaraju and De La Roche, 1977
USGS AGV-1	2.0 (1.88)	Govindaraju and Roelandts, 1977; (Flanagan, 1973)
GSJ JG-1	3.3	Govindaraju and Roelandts, 1977; (Flanagan, 1973)
SB23	10.73	This study, analysed by DNM
N240 granitic	4.45	This study, analysed by DNM
N54 rocks	1.17	This study, analysed by DNM
JC1	0	Cassidy, 1980; this study, analysed by DNM
JC2 synthetic	3.5	Cassidy, 1980; this study, analysed by DNM
JC3 powders	7.6	Cassidy, 1980; this study, analysed by DNM
JC4	11.6	Cassidy, 1980; this study, analysed by DNM
JC5	20.3	Cassidy, 1980; this study, analysed by DNM

Table 4.9 U contents of standards used for calibration of AC(OURS). Values in brackets are less reliable.

Results from this calibration and that performed by Potts et al., (1981) are:

ppm Th in AC(OURS) = 18.5 ± 1.2 (2σ error).

ppm U in AC(OURS) = 4.4 ± 0.6 (2σ error).

4.2:4 Precision and detection limits

To assess the precision of results obtained by ENAA sample SB23 was analysed as an unknown in every batch. Th coarse texture of SB23 in hand specimen represents the maximum in homogeneity effects likely to result from sample preparation. U.S.G.S. - AGV-1 was also included in many runs to compare reproducibility of results at lower radioelement concentrations. Means and standard deviations are presented in Table 4.11.

SAMPLE		CORRECTED PEAK AREAS (cps g^{-1}) 99.5 KeV	fit % error	106.1 KeV	fit % error	ppm U in AC(OURS) from peaks: 99.5 KeV	106.1 KeV
	BCR-1	0.6038	5.5	1.3754	2.8	5.1 ± 0.5	4.6 ± 0.2
	GSP-1	0.9639	7.7	2.0888	1.7	*3.6 ± 0.4	*3.5 ± 0.1
	G-2	0.8335	4.9	1.6680	2.3	4.2 ± 0.4	4.3 ± 0.2
	BR	0.9668	4.3	2.0448	2.1	*5.4 ± 0.4	*5.3 ± 0.2
BATCH	AC(OURS)	1.7430	4.1	3.6134	1.7		
1	GA	1.9112	3.4	4.1114	1.4	*3.65± 0.3	*3.5 ± 0.1
	GH	7.1813	2.3	14.9640	0.7	4.4 ± 0.3	4.35± 0.1
	AGV-1	0.6883	5.2	1.4956	2.4	4.9 ± 0.5	4.7 ± 0.2
	JG-1	1.4501	3.3	3.0683	1.5	4.0 ± 0.3	3.9 ± 0.1
	SB23	4.1812	2.2	8.6718	0.9	4.5 ± 0.3	4.5 ± 0.1
						$\bar{x}$ = 4.4	$\bar{x}$ = 4.3
						σ_{n-1} = 0.7	σ_{n-1} = 0.6
	N240	1.4420	2.5	3.1502	1.3	4.6 ± 0.3	4.6 ± 0.1
	SB23	3.7714	2.2	7.6776	1.2	4.2 ± 0.2	4.5 ± 0.1
	JC5	7.0722	1.6	14.1133	0.9	4.2 ± 0.2	4.7 ± 0.1
	N54	0.4071	8.1	0.8882	4.0	4.25± 0.5	4.5 ± 0.2
BATCH	AC(OURS)	1.4780	3.6	3.2588	1.6		
2	JC4	3.9505	2.0	7.8159	1.3	4.35± 0.2	4.85± 0.1
	JC1	0.0323	37.8	0.0500	22.8		
	AGV-1	0.6935	6.8	1.4417	2.9	4.3 ± 0.4	4.5 ± 0.2
	JC-2	1.2578	2.5	2.5722	1.8	4.1 ± 0.3	4.4 ± 0.1
	JC-3	2.6018	11.7	5.1542	1.6	4.3 ± 0.7	4.8 ± 0.1
						$\bar{x}$ = 4.2	$\bar{x}$ = 4.6
						σ_{n-1} = 0.1	σ_{n-1} = 0.2

Summary of data:	$\bar{x}$ (weighted average)	σ_{n-1}	n
ppm U in AC(OURS) =	4.4	0.3	28

Table 4.10 Calculation of U content of AC(OURS) by comparison of Sampo peak areas with international and other standards of known U content (table 4.9). (* = data points > 1σ from mean).

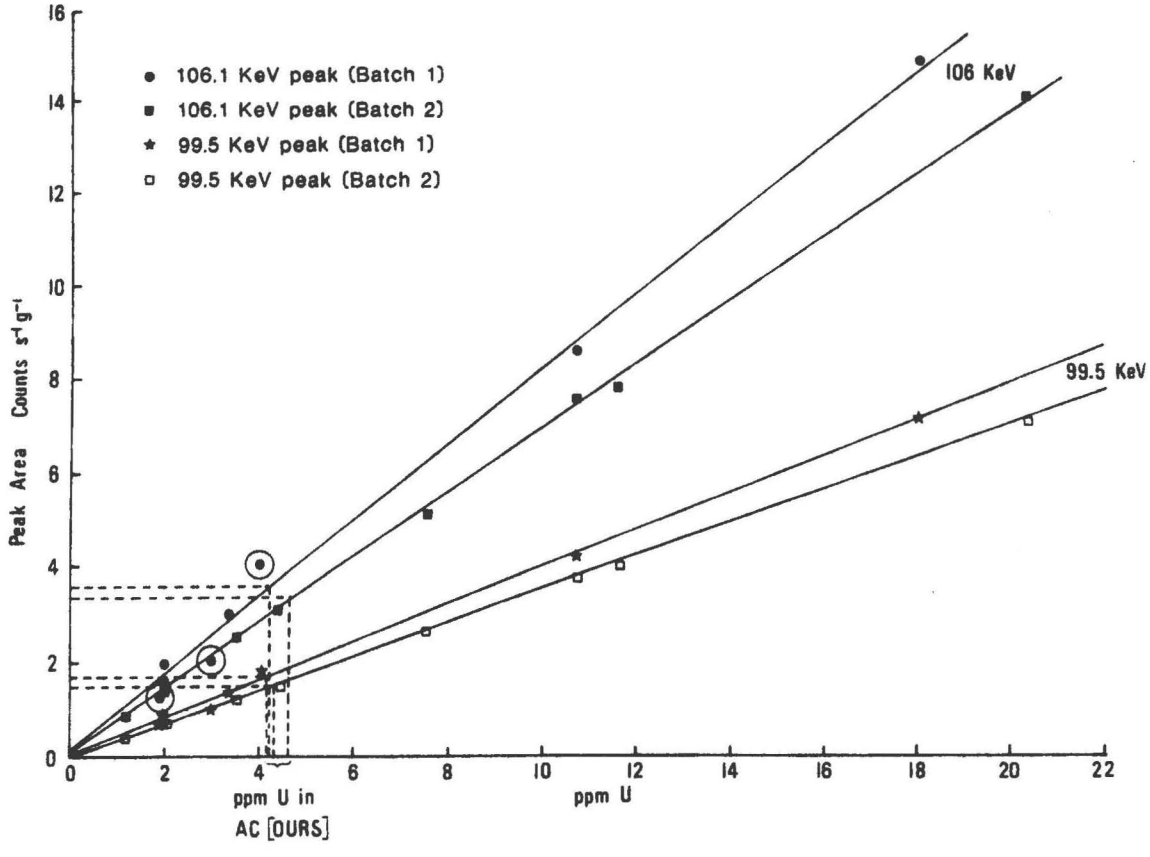

Figure 4.13 Calibration data for U content of AC(OURS)
Ringed data points lie greater than 1σ off the calibration line.
Dotted lines show peak areas and calculated U content of AC(OURS) for each calibration line.

DATA FOR CALIBRATION LINES

BATCH No.	PEAK	Y-INTERCEPT	SLOPE	C.C.	PPM U in AC(OURS)
1	99.5 KeV	0.0355	0.3957	0.9969	4.315
1	106.1 KeV	0.1390	0.8197	0.9965	4.239
2	99.5 KeV	-0.0915	0.3536	0.9985	4.438
2	106.1 KeV	0.0619	0.6899	0.9995	4.634

Detection limits, based on radioelement concentrations that would produce a Sampo peak area of 0.1 cps g^{-1}, at which point the fitting error reaches 10%, are:- U = 0.05 ppm, Th = 0.5 ppm.

SAMPLE	No. of analyses	ppm U			ppm Th		
		$\bar{x}$	σ_{n-1}	% error	$\bar{x}$	σ_{n-1}	% error
SB23	15	10.57	0.36	3.4	18.06	0.71	3.9
AGV-1	11	1.92	0.05	2.9	6.23	0.27	4.3

Table 4.11 Data for secondary standards used for ENAA.

The improved precision and detection limits achieved by this method, compared to those of Cassidy (1980) and Hennessy (1978) are due to more favourable peak: background ratios. These authors used a total neutron flux of 3×10^{12} n cm^{-2} s^{-1}, irradiated for 7.8 hours, cooled for 8 days and counted for 600 s on a coaxial Ge(Li) detector. Under these operating conditions, a typical spectrum contains a maximum of 1000 counts per channel and has a peak: background ratio of approximately 1:2 (see Hennessy, 1978). By comparison, this was the worst ratio encountered in the spectra obtained by the present method.

4.2:5 Possible sources of error

a) Self-shielding effects: These are due to resonance neutron absorption of elements within the sample. Major silicate rock elements show no significant resonance absorption in the epithermal neutron region (Steinnes, 1971). Some heavy elements ($Z>30$), however, do exhibit high absorption properties. Due to their similar geochemistry, these elements tend to occur in high concentrations in the same accessory minerals, causing local concentrations of overlapping resonance absorptions in poorly ground and homogenised samples, thus affecting the neutron energy spectrum.

All samples in this study were ground to -200 mesh in an attempt to eliminate this problem. Steinnes (1971) calculated that self-shielding effects in homogenised samples are insignificant for concentrations of heavy traces below 100 ppm.

b) Detector-sample geometry: The L.E.P.S. is a small detector, sensitive to variations in counting geometry. Hertogen and Gibels (1971) showed that detection efficiency is reduced by ∿2% per mm lateral displacement. Sample and detector mountings were stable, but small errors may be introduced by gravity slumping of some samples (internal diameter of capsules = 16 mm).

4.3 FISSION TRACK RADIOGRAPHY

The fission track method employed in this study has been described in detail elsewhere (Price and Walker, 1963; Kleeman and Lovering, 1967; Wollenberg, 1971) and is summarised briefly: Polished thin sections, approximately 25 x 30 mm, were cleaned and secured to 40 mm diameter 'Lexan' polycarbonate discs with adhesive tape. These were loaded into aluminium canisters (∿41 mm diameter), glass to glass and Lexan to Lexan to avoid inter-contamination, and irradiated in a total thermal neutron flux of approximately 6×10^{16} n cm^{-2}. ^{235}U is the only isotope to fission readily under thermal neutron bombardment, producing massively charged particles which impregnate and damage the Lexan plastic. After a cooling period of 2-3 weeks the Lexan overlays were etched to enhance the damage tracks to optical dimensions using 6N NaOH at 80 ^{o}C as an etchant. The discs were immersed for 2-3 minutes or until track concentrations were visible as small white specs. This subjective approach allowed for temperature and concentration variations in the etchant, avoiding under or over etching and the consequent loss of tracks.

The maximum range of fission fragments in the detector is ∿10 μm giving a matching precision between the U source in the polished thin section and tracks in the Lexan overlay of ∿50 μm (Bowie, Simpon and Rice, 1972), see for example Plate 4.1.

Quantitative analysis of U is possible using fission track techniques (see for example Wollenberg, 1972). However, the detection limit required for this study needed to encompass the low U concentrations ($\sim 10^{-1}$ ppm) which sometimes occur along microfractures and within the structure of major rock-forming minerals, requiring a high neutron flux. This results in track saturation for U levels > 100 ppm (Tieh and Ledger, 1981), as typically occurs in U-bearing accessory minerals. Additionally, track densities may contain a contribution derived from Th fission caused by a small percentage of fast neutrons in the irradiating flux (see Wollenberg, 1971). A semi-quantitative appraisal is possible by observing density contrasts (see Plate 4.1), although the degree of Th contamination cannot be assessed.

4.4 ENERGY DISPERSIVE ELECTRON MICROPROBE ANALYSIS

The energy dispersive electron microprobe technique was used for analysis of complex U- and/or Th-bearing accessory minerals such as sphene, zircon, allanite, monazite, xenotime, thorite and Nb-Ta-oxides. Data were obtained using a Link Systems Si(Li) energy dispersive detector and analyser system, coupled with a Cambridge Instruments M9 Electron Microprobe. A detailed explanation of electron microprobe analysis is given by Read (1975); the basic principals are outlined below.

A focussed beam of electrons is used to excite atomic electrons in the unknown mineral, which, on returning to their ground state, emit

Plates 4.1 Photomicrographs and corresponding fission track prints showing:

a) Low density tracks over sphenes, with some higher density tracks along rims of the crystal. High density tracks also correspond with zircon, z, and apatite, A, gives rise to very low density tracks.

b) High density tracks occurring predominantly along the rims and cleavages of a partially altered biotite, where secondary opaques are present. High density tracks also correspond with pleochroic haloes produced by primary accessory inclusions in the biotite.

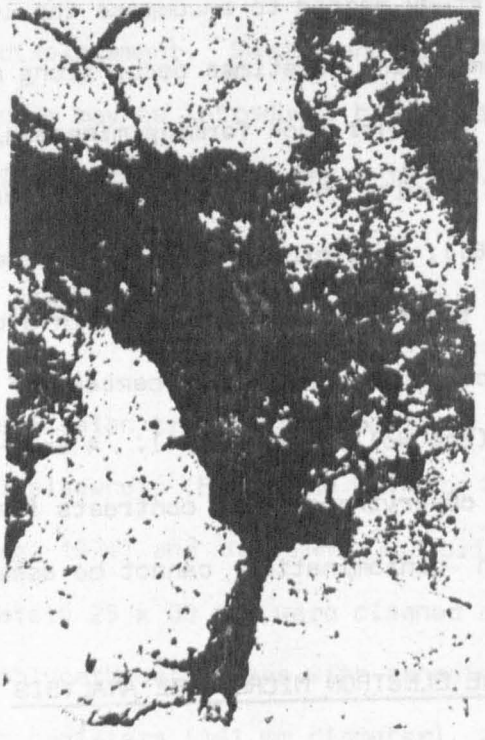

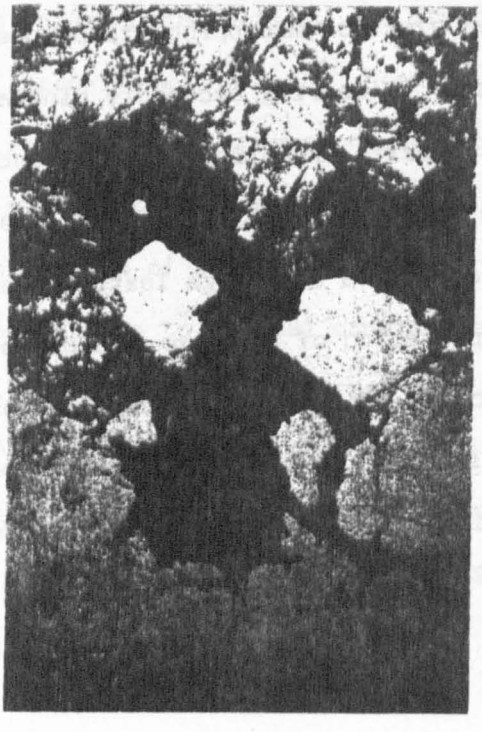

X-rays of characteristic energies according to the elements present. Electrical pulses, proportional in voltage to X-ray energies are processed by a multichannel analyser and accumulated as a 1024 channel spectrum (0-20 KeV) by the Link computer. The energy spectra must be corrected for matrix effects: the attenuation of incident electrons or characteristic X-rays through inelastic collision with atomic particles and secondary excitation of atomic electrons by primary X-rays (fluorescence). These corrections are dependent on sample composition.

An accelerating potential of 30 kV, a beam current of 2.5 ηA with a diameter of 2 μ, and a count time of 200 seconds were used. These operating conditions allowed optimum excitation of U and Th M series and REE L series X-ray lines, while avoiding channel overflows and specimen decomposition. Instrumental corrections were obviated by counting spectra for the unknown and polished cobalt under identical conditions and standardising elemental peak areas to the cobalt K peak. The system was calibrated for elements listed in Table 4.12 (see Tindle, 1982). Calculation of matrix corrections and composition of the unknown by comparison of recorded spectra with standard profiles is an iterative process and is performed by the Link Systems ZAF4/FLS deconvolution software.

Figures 4.14 and 4.15 show the U and Th metal profiles used as standards in the ZAF4/FLS deconvolution program. Although the L are more clearly resolved it was found that the superior counting statistics of the M-line profiles produced more accurate and consistent results (see Figures 4.16, 17 and 18). The computer output contains a 'Fit index', which is a measure of the fit of the standard profiles to the unknown spectra, and an error on the apparent concentration of individual elements before matrix corrections. This error is a conservative (2 sigma) estimate of the standard deviation for the background to the fitted areas and represents the effective detection

Element	Calibration Standard	Conc. of element in Standard	Lines Fitted ( ) not used for ZAF	Standard used for profile (if different from calib.std)
Mg	Syn. MgO	60.31	K	
Al	Syn. Al_2O_3	52.92	K	
Si	Quartz	46.75	K	
P	Apatite	18.00	K	Syn. Na $P_2O_4(OH)$
S	Pyrite	53.45	K	
Cl	Syn. K Cl	47.55	K	Syn. NaCl
K	Syn. K Cl	52.45	K	Syn. K Br
Ca	Wollastonite	34.16	K	Calcite
Ti	Rutile	59.95	K	
V	Metal	100.00	K	
Cr	"	100.00	K	
Mn	"	100.00	K	
Fe	"	99.50	K	
Co	"	100.00	K (L)	
Ni	"	100.00	K (L)	
Cu	"	100.00	K (L)	
Zn	"	100.00	K (L)	
As	"	100.00	K (L)	
Sr	Celestine	47.27	K (L)	
Y	Drake & Weill Syn.	3.21	K (L)	Oxide Powder
Zr	Metal	97.50	(K) L	
Nb	"	100.00	(K) L	
Sb	"	100.00	L	
Ba	Barite	57.11	L	
La	Drake & Weill Syn.	3.65	L	Oxide Powder
Ce	"	3.42	L	"
Pr	"	3.79	L (M)	"
Nd	"	3.65	L (M)	"
Sm	"	3.67	L (M)	"
Eu	"	3.80	L (M)	"
Gd	"	3.87	L (M)	"
Tb	"	3.78	L (M)	"
Dy	"	3.80	L (M)	"
Ho	"	3.81	L (M)	"
Er	"	3.81	L (M)	"
Tm	"	3.81	L (M)	"
Yb	"	3.74	L (M)	"
Lu	"	3.75	L (M)	
Hf	Metal	98.80	L (M)	
Ta	"	100.00	L (M)	
Pb	"	100.00	L (M)	
Th	"	100.00	(L) M	
U	"	100.00	(L) M	

Table 4.12 Standards used for electron microprobe calibration (Dr. A. Tindle, Open University) and element profiles.

limits. Due to the differences in characteristic element abundances and resulting spectral interferences, detection limits for U and Th (and other elements) vary according to the accessory mineral analysed (see Table 4.13).

The interactive program permits spectrum display manipulation via a T.V. monitor with the facility for displaying X-ray line cursors for any element. Identification of ambiguous or overlapping peaks may thus be confirmed by searching for additional spectral lines. Residual spectra may also be displayed for identification of omitted elements. Due to the limitations of the ZAF/FLS software it

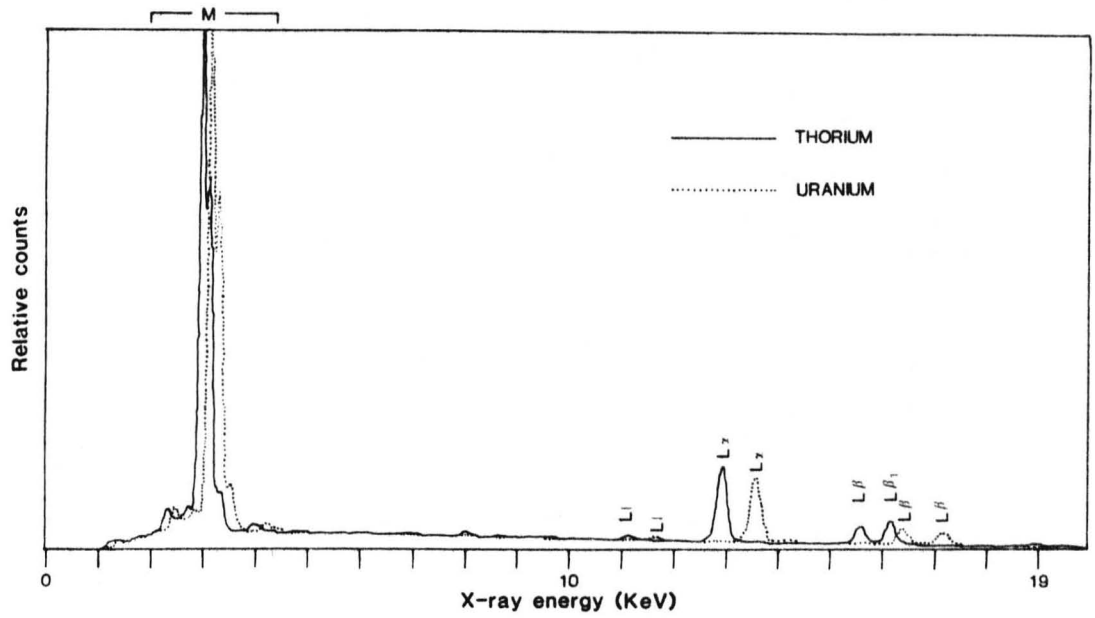

Figure 4.14 Calibration profiles for Uranium and Thorium metals showing relative intensities of major peaks.

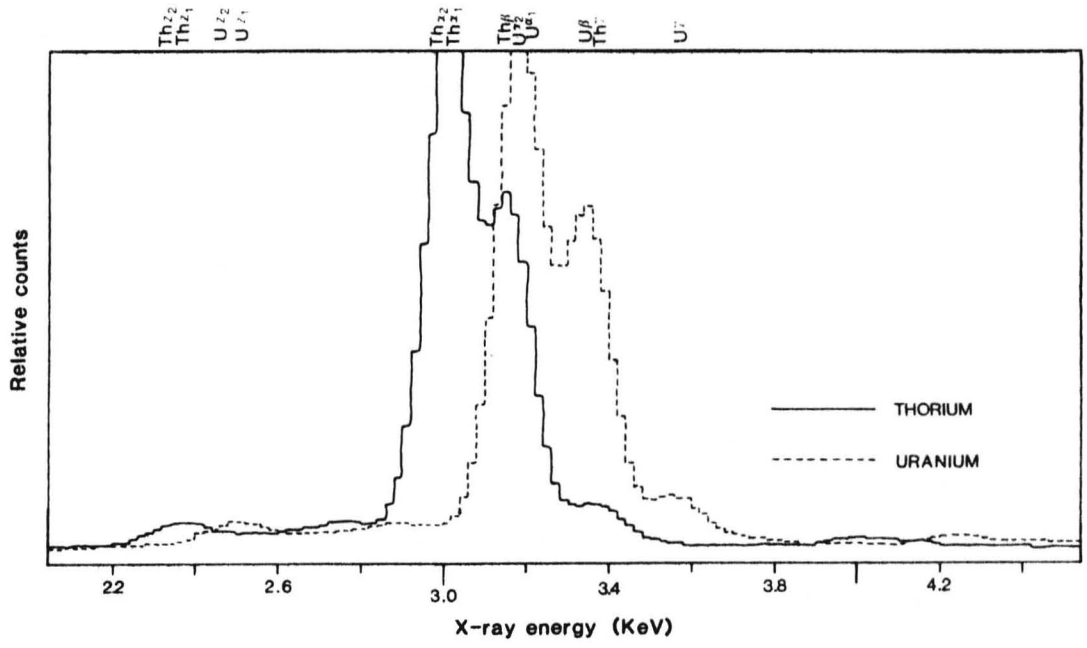

Figure 4.15 Expansion of above spectra between 2 and 4.4 KeV showing resolution of U and Th M lines.

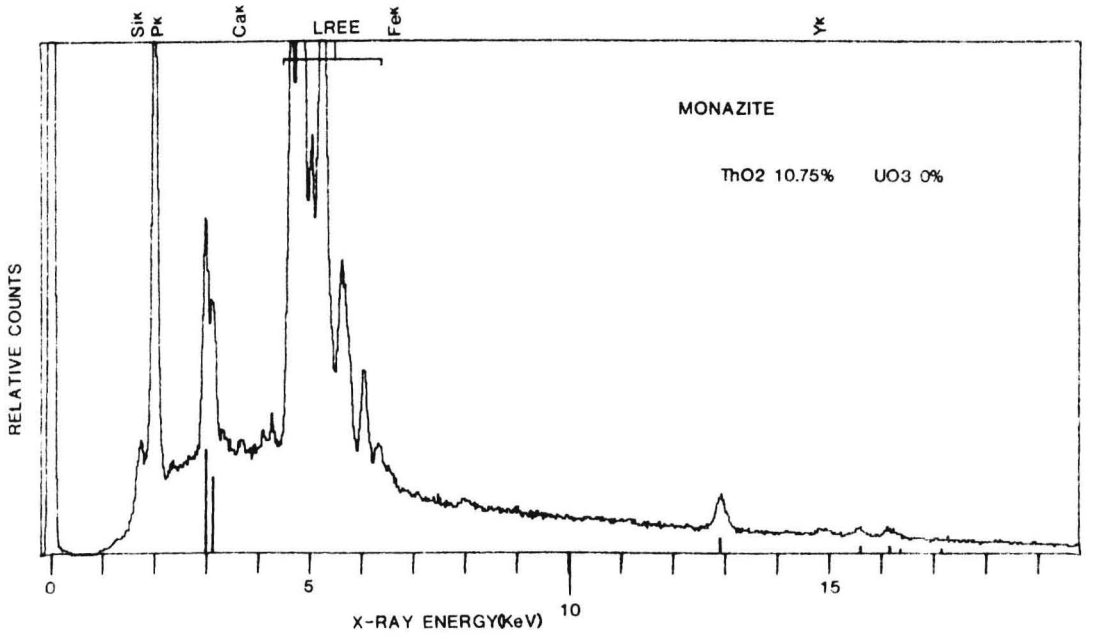

Figure 4.16 Typical electron microprobe spectrum for monazite. Only major peaks are labelled, and lines below profile show relative intensities of visible Th peaks.

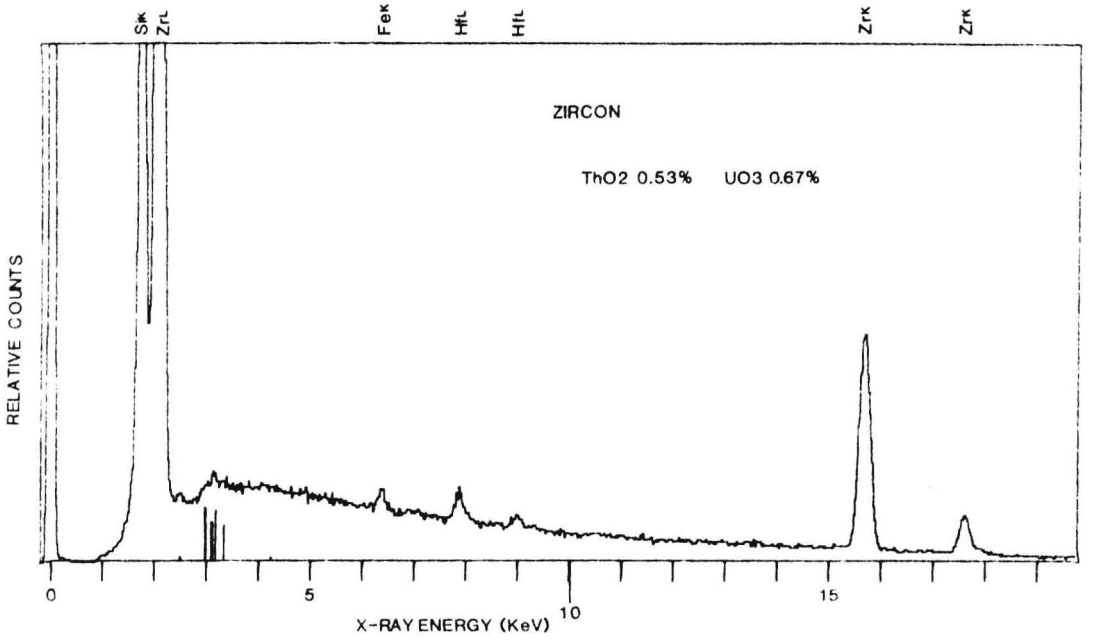

Figure 4.17 Typical electron microprobe spectrum for zircon. Only U and Th M-line peaks are resolvable above background. U and Th contents ≈ detection limits.

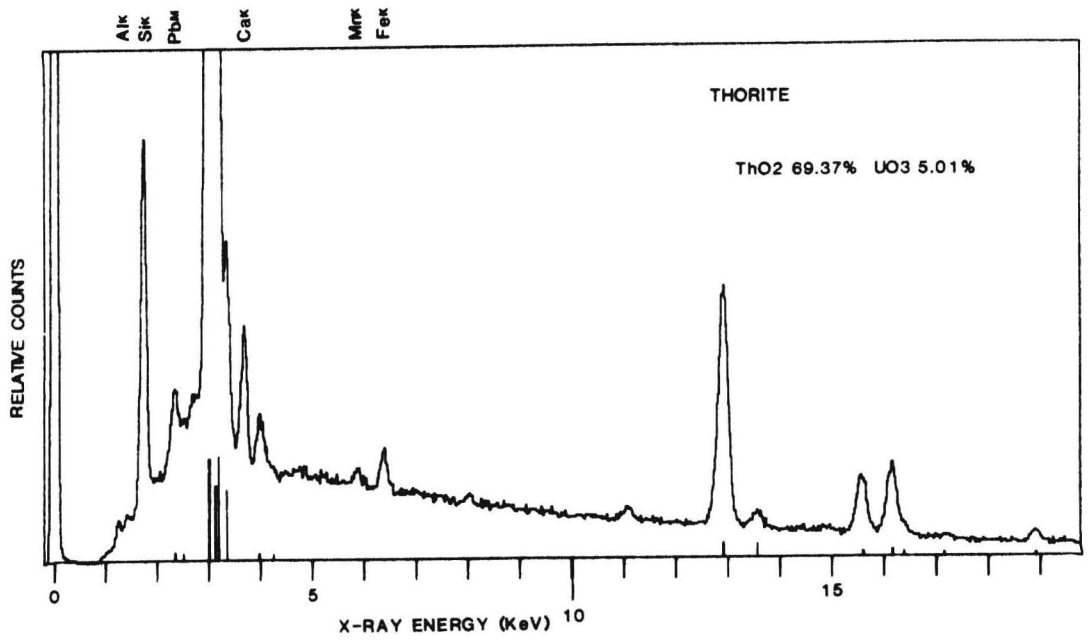

Figure 4.18 Typical electron microprobe spectrum for Thorite. Use of L-line peaks for Th are feasible in this case.

was not possible to analyse more than 18-22 different elements simultaneously. Consequently, for certain minerals such as complex Na-Ta-oxides, some elements, although potentially detectable, could not be analysed.

Certain problems, peculiar to radioelement-rich accessory minerals, limited the effectiveness of microprobe analysis in some cases.

i) The extremely small dimensions of some crystals introduced difficulties in obtaining uncontaminated spectra, even with a highly focussed beam.

ii) Metamictization of these minerals due to radioactive decay produces a 'deficient' surface which does not fully compare with the standard material producing analysed totals below 100% (Bowles, 1978).

iii) Highly radioactive minerals often occur along grain boundaries and are frequently surrounded by amorphous alteration (see

	OXIDE PERCENTAGES (2σ limits)										
	Apatite	Zircon	Sphene	Allanite	Monazite	Xenotime	Thorite	Uraninite	Urano-Niobate		Quartz
La_2O_3	0.27	0.14	0.52	0.45	0.52		0.51	0.41	0.32		0.22
Ce_2O_3	0.27	0.17	0.57	0.46	0.67	0.16	0.48	0.42	0.28		0.17
Pr_2O_3	0.22			0.37	0.47		0.43	0.36			0.16
Nd_2O_3	0.22		0.23	0.34	0.45	0.17	0.43	0.34	0.21		0.14
Sm_2O_3	0.27		0.22	0.32	0.38	0.24	0.29	0.32			0.15
Eu_2O_3	0.26		0.23	0.36	0.44		0.30				0.20
Gd_2O_3	0.21	0.33	0.24	0.34	0.35	0.34	0.33	0.42			0.22
Tb_2O_3	0.30	0.29			0.44	0.34		0.42			0.21
Dy_2O_3	0.28	0.30	0.24	0.28	0.38	0.35	0.37	0.42			0.20
Ho_2O_3	0.24	0.31				0.33					0.20
Er_2O_3		0.29			0.32	0.34	0.33				0.20
Tm_2O_3	0.23	0.28				0.32					0.21
Yb_2O_3	0.23	0.24	0.22		0.31	0.31	0.32		0.24		0.19
Lu_2O_3		0.24				0.34					0.18
HfO_2		0.38									0.20
Ta_2O_5		0.39							0.40		0.20
Y_2O_3	0.50	0.66	0.48	0.59	0.65	1.28	0.86	0.87	0.76		0.43
ThO_2		0.81				1.03	0.45		0.95		0.38
Nb_2O_5		0.75					0.60		1.08		0.23
PbO	0.50		0.53	0.58	0.64		0.42	0.88	0.70		0.29
UO_2	0.32	0.39	0.31	0.36	0.50	0.37	0.76	0.74	0.46		0.23
UO_3	0.36	0.40	0.33	0.36	0.52	0.42	0.72	1.02	0.53		0.18
SiO_2	0.39	0.63	0.51	0.57	0.38	0.54	0.37	0.40	1.32		
TiO_2	0.17	0.11	0.35	0.18	0.21		0.18	0.18	0.15		0.07
Al_2O_3	0.30	0.50	0.37	0.60		0.81	0.61	0.47	0.52		0.28
CaO	0.13	0.11	0.10	0.25	0.14		0.14	0.19	0.21		0.05
MnO	0.12	0.13	0.13	0.19	0.22		0.18	0.19	0.13		0.05
MgO	0.70		0.80	0.98	1.07		0.21	1.24			0.48
FeO	0.24	0.08	0.22	0.13	0.08	0.07	0.09	0.14	0.10		0.06
K_2O		0.13	0.10			0.13	0.19	0.24	0.21		0.07
P_2O_5	0.43	1.01	0.24		0.45	0.62	0.32	0.28	0.64		0.34
Cl	0.07		0.08	0.09	0.11		0.09		0.16		0.04
S							0.12		0.29		0.05

Table 4.13 Energy dispersive electron microprobe detection limits for accessory minerals analysed.

Chapter 6). This renders them susceptible to 'plucking' during preparation of thin sections, again disrupting the ideal geometry of electron/sample interactions.

Despite these problems, the Energy Dispersive Electron Microprobe system proved an invaluable tool for the identification and quantitative analysis of radioactive accessory minerals in the intrusions studied.

CHAPTER 5 THE ETIVE COMPLEX

5.1 GEOLOGICAL SETTING AND STRUCTURE

The Etive Complex is one of the largest of the post-tectonic Caledonian granite complexes in Britain (~400 m.y., Pidgeon et al., 1978). Situated in the south-west Grampian Highlands, it outcrops over an elliptical area of approximately 300 km^2 elongated in a NE-SW direction and forms a region of high relief bounded by the Pass of Brander, Glen Creran, Glen Strae and Glen Coe (Figure 5.1). The Etive 'granites' invade the Old Red Sandstone andesitic lavas of Glen Coe, generally post-dating the Fault Intrusion associated with this caldera but are locally cut by it. The Lorne lavas (Figure 5.1) are contemporaneous with those at Glen Coe (Roberts, 1966, Flett-Brown, 1973), but nowhere are they seen in contact with the Etive Complex due to vertical displacement on the Pass of Brander Fault. The Complex intruded a compositionally diverse sequence of Dalradian and Moine meta-sediments. To the east are pure quartzites which exhibit no thermal alteration at any distance from the contact (Kynaston and Hill, 1908), while the southern and western contacts are bounded by pelitic and semi-pelitic meta-sediments consisting of banded mica-schists, impure marbles and calc-quartzites in the garnet grade of regional metamorphism. The metamorphic aureole in this south-western region extends to approximately 2.5 km from the contact. Thermal effects in the Glen Coe lavas are observed up to 0.8 km from the contact (Anderson, 1937).

The complex probably formed as the result of successive sub-terrainian cauldron subsidences and comprises five distinct, semi-concentric intrusions (Anderson, 1937). These are, in order of

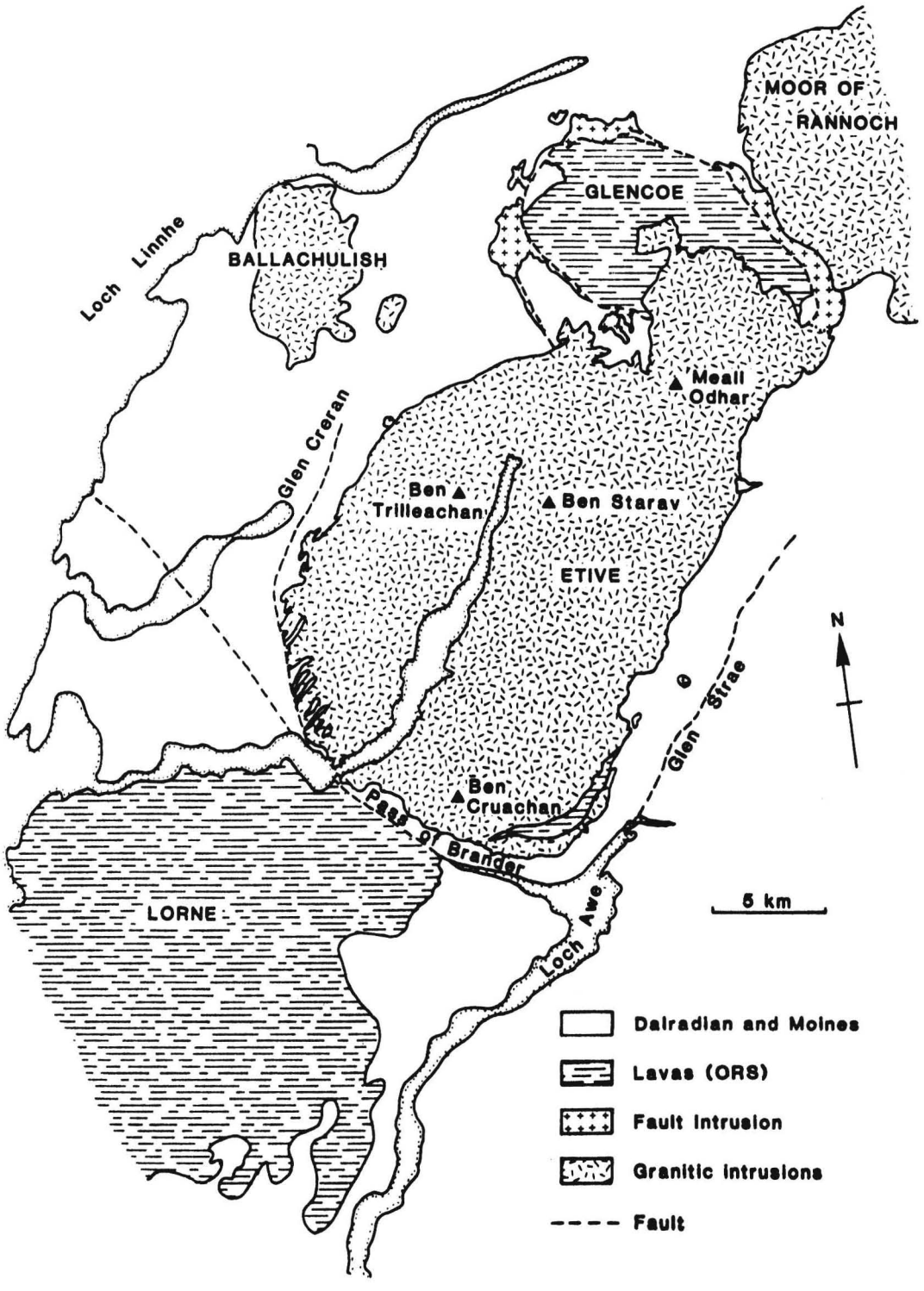

Figure 5.1 Geological setting of the Etive Complex

emplacement, the Quarry Intrusion, the Cruachan 'granodiorite', the Meall Odhar Granite, the outer porphyritic Starav Granite and the inner non-porphyritic Starav Granite (Figure 5.2). The complex is associated with a swarm of NNE-trending dykes (see inset to Figure 5.2).

The close structural and temporal relationship of the Etive Complex with the Glen Coe Fault Intrusion (Figure 5.1) and with the altered lavas of the Bheinn a Bhuiridh Screen (Figure 5.2) suggest that the 'granites' were intruded at a relatively high structural level. Pressures calculated for the contact metamorphic assemblage in the thermal aureole to the south-west of the complex fall in the range 1-2 kb, equivalent to 3-6 km depth (Droop and Trelor, 1981). Flett-Brown (1975) also considered several lines of evidence, including comparison of K-Ar biotite ages from the granites with those of the country rocks, which constrain the depth of intrusion to less than 5 km. A minimum depth of intrusion at the south-west contact may be obtained from the minimum vertical displacement on the Pass of Brander (= height of Ben Cruachan, 1280 m) and the estimated thickness of the Lorne lavas (1250 m, Roberts, 1966), giving a depth of 2.5 km. On the basis of field and geochemical evidence, Flett-Brown (1975) proposed a 20^{o} post-intrusion tilt to the north-east (see below), in which case, the 'granites' exposed in the north-west may represent a higher level at the time of intrusion.

The attitude and nature of the granite-country rock contacts have been studied by several workers (Anderson, 1937; Bailey and Maufe, 1961; Flett-Brown, 1975). In the west, between Loch Etive and Glen Creran (Figure 5.1), the Cruachan unit shows signs of forceful intrusion, with lit-par-lit injection of magma and substantial brecciation of the country rock. Rafts of country rock within the granite are common, sometimes reaching 1 km in length. Although locally variable, the western contact

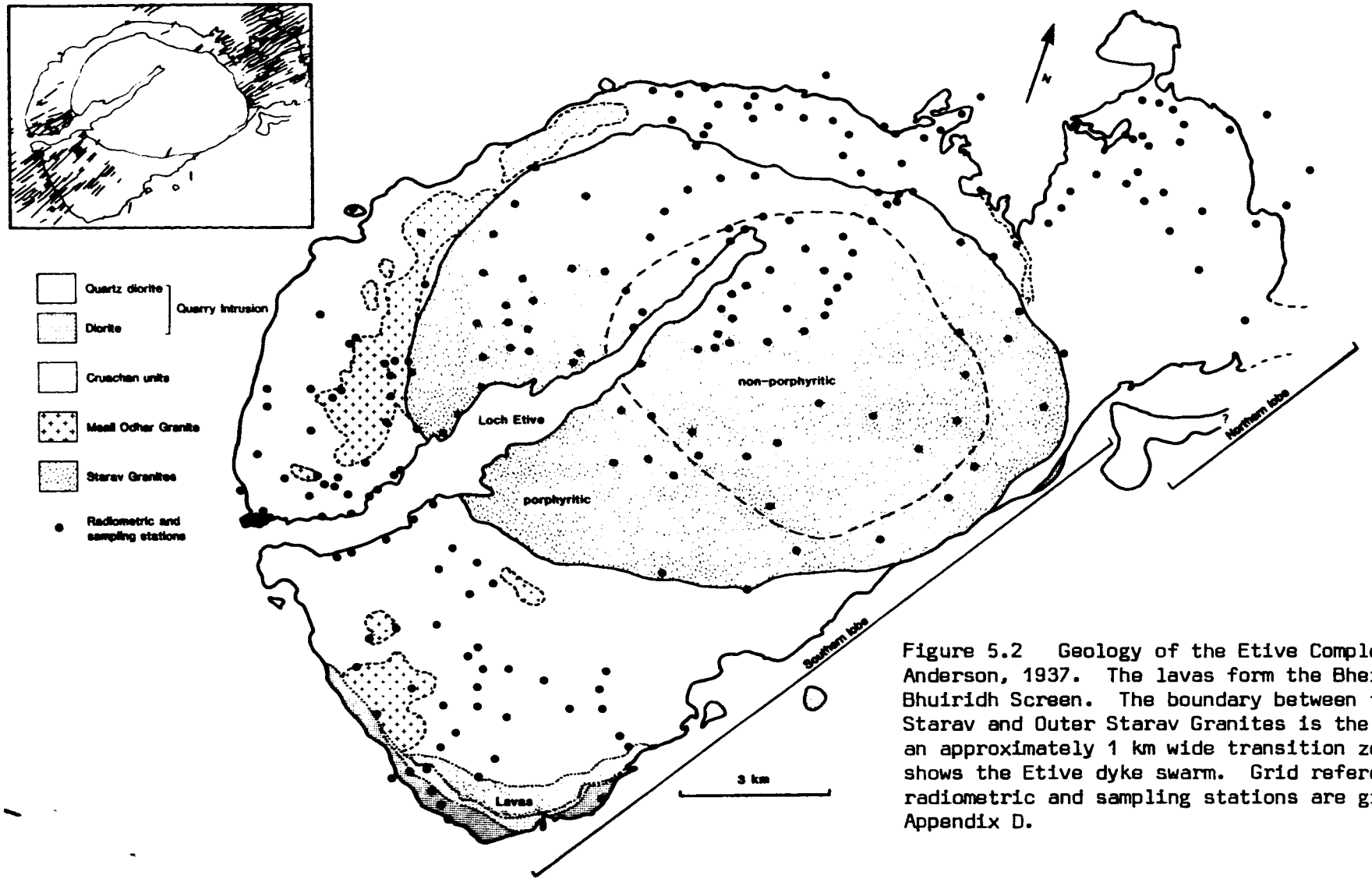

Figure 5.2 Geology of the Etive Complex; after Anderson, 1937. The lavas form the Bheinn à Bhuiridh Screen. The boundary between the Central Starav and Outer Starav Granites is the mean of an approximately 1 km wide transition zone. Inset shows the Etive dyke swarm. Grid references for radiometric and sampling stations are given in Appendix D.

dips to the east and granite overlies schists. North of Glen Creran (see Figure 5.1) country-rock rafts are fewer, the contact is sharper and dips to the north-west at a high angle. Along the eastern margin, the contact is variably vertical to horizontal, with a predominant steep dip to the east, and only minor xenolith contamination has been observed. The contact was recorded at various angles from 60^{o} outwards to 70^{o} inwards in tunnels of the Loch Awe power station (D. Smith, pers. comm.).

Flett-Brown (1975) considered these contact relationships to be consistent with the form of a laccolith dipping approximately 20^{o} to the north-east (Figure 5.3); geochemical and mineralogical arguments for this interpretation will be discussed in Sections 5.2 and 5.3. The present author considers the variable nature of the contacts to be undiagnostic of such an interpretation. Bailey and Maufe (1916) noted that the upper surface of the northern lobe of the Cruachan unit has a steeply domed form, but the overlying lavas were not deformed during intrusion, consistent with a cauldron subsidence mechanism, the magma being accommodated by foundering from below. Figure 5.4 presents an alternative model to Flett-Brown's laccolith which accounts for the arcuate dyke of Meall Odhar granite (Figure 5.2) and the internal relationships of the Starav and Cruachan units. The lit-par-lit type injection and inward dipping contact on the western margin may represent local exploitation of bedding and foliation planes (Figure 5.4) rather than the floor of the magma chamber (Figure 5.3). A post-intrusion dip to the north-east would still be required to explain the apparent migration of intrusive centres; such movement may be associated with the partial ring fault of Glen Creran - Pass of Brander (Figure 5.1). An additional point to note is that the temporally related Fault Intrusion (Figure 5.1) suggests that cauldron

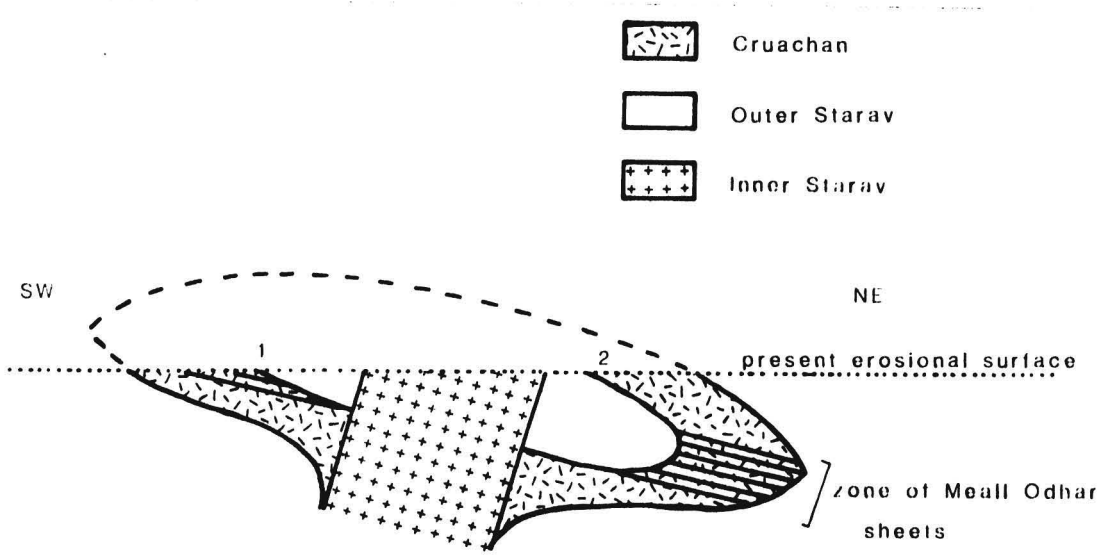

Figure 5.3 Diagrammatic cross-section of the Etive Complex as proposed by Flett-Brown (1972), showing the postulated tilted laccolith with all granites being intruded centrally. Meall Odhar sheets intruded laterally, at the interface between already cool Cruachan tonalite below, and 'crystal mush' above, in a vertically differentiating magma chamber. The dip of the sill-like Meall Odhar granite of 20° NE, and the NE migration of centres of successive units, are artefacts of the tip of the whole laccolith.
The following points are considered by the present author to be inconsistent with this model:

1. (see diagram) The Cruachan-Outer Starav contact here does not conform with field observations: it is vertical to sub-vertical.
2. (see diagram) The position of the arcuate Meall Odhar dyke (Figure 5.2) is not explained.
3. This model does not explain the existence of, and vertical foliation in the Bheinn à Bhuiridh Screen (Figure 5.2).
4. This model does not explain the contrast between the multi-phase intrusion observed in the southern Cruachan lobe, and the lack of this phenomenon in the northern lobe (see Section 5.2:2).

subsidence was active involving at least two blocks at the time of emplacement. The northern lobe of the Cruachan 'granite' may represent a separate intrusive phase, involving a third block (Figure 5.4) rather than the upper portion of a vertically differentiating magma chamber (Figure 5.3). Geochemical and radiometric data from this study support this separation of the two Cruachan lobes (Sections 5.4 and 5.7).

A closed, negative Bouguer anomaly is associated with the Etive Complex (Figure 5.5), indicative of a steep-sided cylindrical or cone-

Caption for Figure 5.4

Simplified cartoon of the possible series of events in the intrusive history of the Etive Complex. Periods of dyke intrusion and emplacement of the Quarry diorites have been omitted for simplicity.

A. Development of a magma chamber at depth forms ring-faults in the surface/subsurface rocks. Blocks 1 and 2 founder into the magma chamber, and magma wells up to form the southern lobe of Cruachan 'granite' and the Fault Intrusion ring dyke. The Cruachan 'granites' exploit weaknesses in the country-rock to the SW showing a locally forceful mode of intrusion.
The Quarry Intrusion is omitted for clarity and the Cruachan developed as successive pulses (see Section 5.2:2).

B. Marginally later the country-rock between the two cauldrons subsides (block 3) permitting a further pulse of Cruachan to invade Glen Coe in the NE (Northern lobe). Movement of block 1, and additional 'pulsing' in the SW is likely.

C. Movement of blocks 1 and 3, probably contemporaneous with the injection of a major dyke swarm permits intrusion of the Meall Odhar sheets and dykes, which exploit cooling fractures in the Cruachan units, the 'type' dyke being positioned between the Northern and Southern lobes. The Meall Odhar Granite may represent intercumulus 'liquid' remobilized by perturbation of the thermal gradient associated with intrusion of the dyke swarm (Flett-Brown, 1975).

D. Complete foundering of block 1 and the Starav Granites are successively intruded (shown as single event here). The present level of erosion is shown after later tilting? Evidence from Glen Coe; (i.e. flat lying lavas) suggests that no tilting occurred in the NE. It is possible that uplift of the S Cruachan lobe was contemporaneous with emplacement of the Starav Granites, movement in the NE being accommodated in the complex zone between the two subsiding blocks.

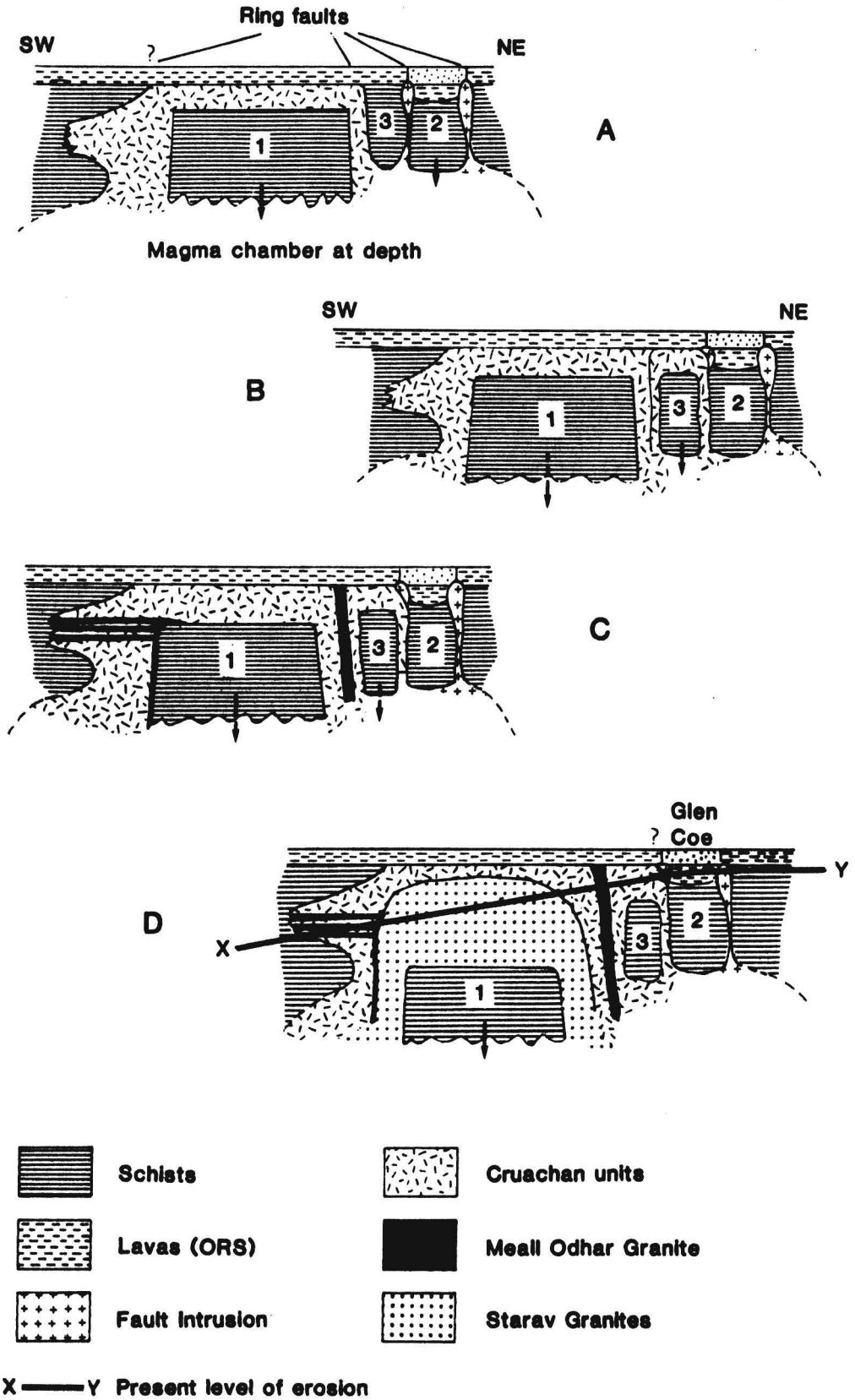
Ring faults
SW
NE
?
1
2
3
A
Magma chamber at depth
SW
NE
B
1
2
3
C
1
2
3
D
Glen
? Coe
X
Y
Schists
Lavas (ORS)
Fault intrusion
Cruachan units
Meall Odhar Granite
Starav Granites
X——Y Present level of erosion

Figure 5.4

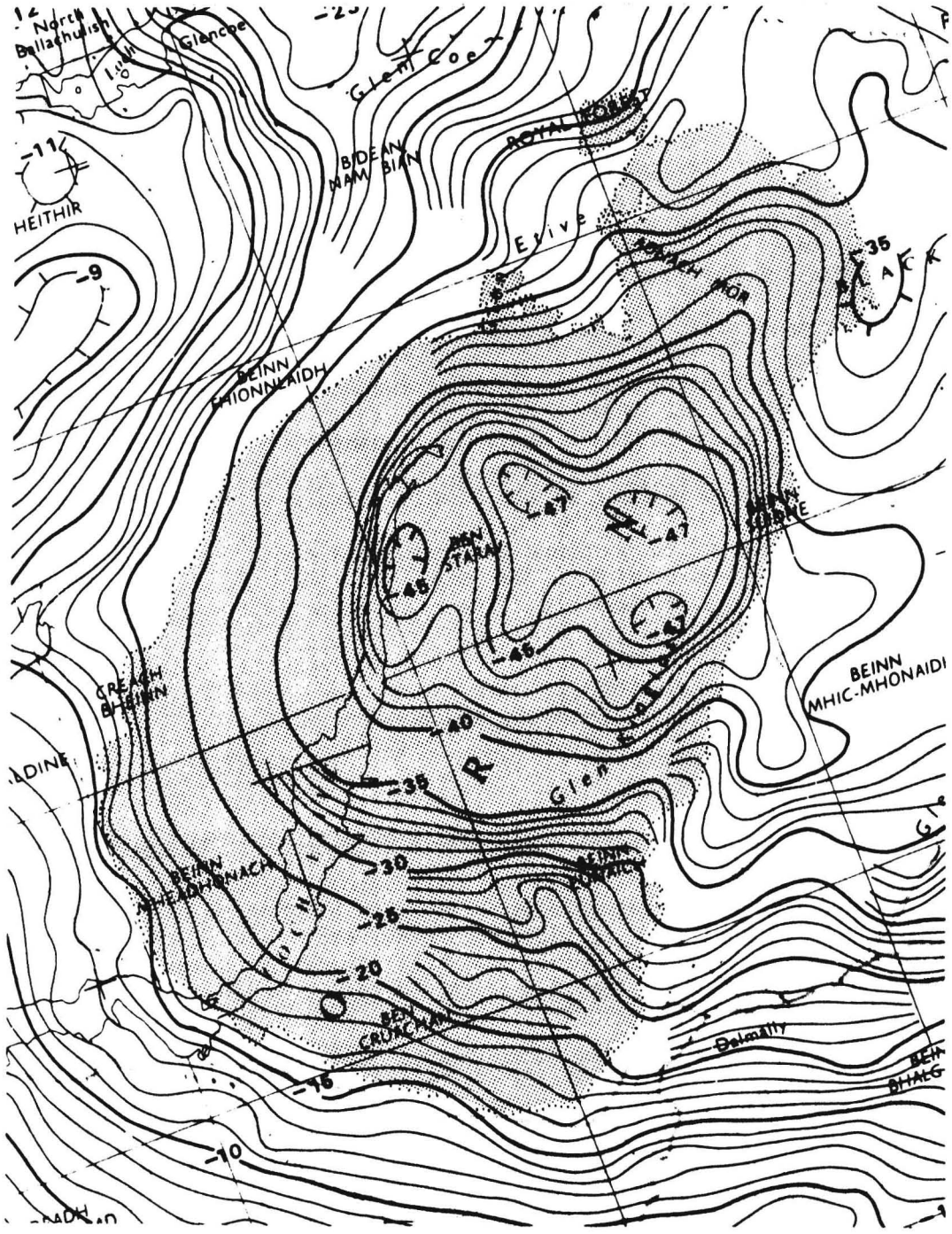

Figure 5.5 Bouguer anomaly associated with the Etive Complex.
From the I.G.S. 1:250000 series map.
Isogal values are in milligals; thick lines at 5 mgal interval,
thin lines at 1 mgal interval.

shaped body. The large negative residual gravity expression (-32 mgals) and positive aeromagnetic expression (+ 650 ηT) of the Etive Complex suggest a voluminous, low density mass at depth (Brown and Locke, 1979). Density contrasts between country rocks and Etive units (Table 5.1) are positive for the Quarry Intrusion, minimal for the bulk of the S Cruachan lobe and increasingly negative for the N Cruachan lobe, Starav Granites and Meall Odhar Granite. The latter may be neglected with respect to its effect on gravity due to its observed discontinuity with depth. Considering the central position of the Bouguer anomaly over the Starav Granites (Figure 5.5) and their large density contrast with both country rocks and other members of the Complex (Table 5.1), it is inferred that these central units continue to some depth and are responsible for the bulk of the gravity anomaly. The distortion of the gravity contours towards the N Cruachan lobe (Figure 5.5) suggests that this unit may also be a significantly voluminous, low density mass.

5.2 INTERNAL RELATIONSHIPS AND MINERALOGY OF THE ETIVE UNITS

5.2:1 The Quarry Intrusion

This unit forms an arcuate outcrop on the south-west margin of the complex. It comprises an outer quartz diorite, contaminated with metasediments up to 10 m from the southern contact, which grades northwards into a more basic, finer grained diorite. The inner margin is bounded by the Beinn à Bhuiridh Lava screen (Figure 5.2). A northerly extension of the quartz diorite has been mapped (S. Perkins, pers. comm.), to include the small outcrop on Eilean Durinnis. This extension, and a continuation of the lava screen, was identified in the tunnels of the Loch Awe Power Station (D. Smith, pers. comm.). Other marginal and satellite diorites have been mapped (Kynaston and Hill, 1908; Anderson,

Unit	Range of densities (kg m^{-3})	Average density (kg m^{-3})	Reference	Density contrast with country rocks (kg m^{-3})
Quarry Intrusion	2770-2790	2780	This study	+80 → +40
Quarry diorite	2850-2860	2850	Anderson, 1937	+150 → +110
Quarry qtz. diorite	2730-2820	2780	Anderson, 1937	+80 → +40
Cruachan (S. lobe)	2600-2780	2700	This study	0 → -40
Cruachan (S. lobe) above 2000'	2670-2720	2680	Anderson, 1937	-20 → -60
Cruachan (S. lobe) below 2000'	2670-2800	2730	Anderson, 1937	+30 → -10
Cruachan (N. lobe)	2630-2720	2670	Anderson, 1937	-20 → -60
Meall Odhar	———	2550	This study	-150 → -190
Outer Starav	2570-2610	2593	This study	-107 → -147
Central Starav	2530-2610	2570	This study	-130 → -170

Table 5.1 Densities of rocks from the Etive Complex.
The method and results of density measurements from this study are presented in Appendix B.
Density contrasts with the surrounding country rocks are calculated using the average 'granite' densities, and limits of country rock densities of 2700 kg m^{-3} (Moines) and 2740 kg m^{-3} (Dalradian). These data are based on density measurements of similar rock types in the NE Grampians. (Locke, 1980).

1937; see Figure 5.2), and may represent parts of this outer phase.

The Quarry diorite is composed of aggregates of augite, hornblende and biotite, separated by plagioclase laths with interstitial K-feldspar (microcline microperthite) and quartz. Accessory minerals, constituting approximately 2.5% of the rock are magnetite, apatite, zircon and pyrite, with minor sphene appearing in the quartz diorite.

5.2:2 The Cruachan units

Detailed mapping in the south-western region of the Etive Complex, has revealed at least six separate intrusive phases of the S Cruachan unit, which are all in sharp contact and define essentially arcuate outcrops (S. Perkins, pers. comm.). Sharp contacts between intrusive phases are a common feature throughout the S Cruachan lobe, but such relationships are absent in the more acidic N lobe (Figure 5.2).

Sporadic thermal alteration of the Cruachan 'granite' has been observed up to 1 km from its contact with the Starav intrusion and a marked foliation is developed in the south-west (Anderson, 1937).

Although in Figure 5.2 outcrops of Meall Odhar Granite are shown as continuous sheets, these are, in fact, intercalated with Cruachan units and the map indicates areas of predominance of one over the other. Dykes and veins of Meall Odhar Granite occur elsewhere in the Cruachan, decreasing in number with altitude and are less frequent in the N lobe.

Modal mineral variations in the S Cruachan units (Table 5.2) show an apparently random, basic-acid-basic-acid trend through the intrusive sequence, suggesting, either a lower chamber (Figure 5.4) open to fresh influxes of magma, or successive tapping of this chamber such that it may or may not have had time to re-establish a vertically stratified nature.

In the more basic S Cruachan rock types K-feldspar is not present as a phenocryst phase but forms interstitially with quartz. Accessory minerals, constituting approximately 2% of the rock, are magnetite, apatite and sulphides, with minor sphene and zircon. Sporadic grains of allanite and epidote occur in some samples.

The rock of the N lobe is a biotite-adamellite, which often contains more hornblende than is usual for its silica content (64-74%). Quartz, plagioclase and K-feldspar are present in approximately equal amounts.

Intrusive units recognized by S. Perkins (pers. comm.)		Modal Percentages				
		Quartz	K-feldspar	Plagioclase	Biotite	Hornblende
OLDEST	Hnbld-qtz monzodiorite I (border facies)	14	12	54	9	7
	Hnbld-qtz monzodiorite I (elsewhere)	10	12	64	10	3
	Hnbld-qtz monzodiorite II	15	20	50	7	6
	Biot-qtz monzodiorite	8	16	65	10	0
	Granodiorite	20	27	45	6	6
	Hnbld-qtz mondodiorite III	8	10	64	14	3
	Hnbld-qtz monzodiorite III (coarse grained)	8	10	60	14	7
YOUNGEST	Monzonite	8	35	45	6	0.5

Table 5.2 Modal analysis of S. Cruachan units. Data from S. Perkins (pers. comm.)

Sphene is an important accessory along with abundant magnetite, minor apatite, zircon and sulphides, and sporadic thorite in the more acidic samples.

5.2:3 The Meall Odhar Granite

The Meall Odhar Granite exhibits marginal chilling at contacts with S Cruachan rocks, but not at contacts with the N Cruachan adamellite, indicating a closer temporal relationship with the latter unit (cf. Figure 5.4). The coincidence of the Meall Odhar intrusion with at least one phase of dykes has been documented by Bailey and Maufe (1961).

The rock is a pink, even-grained granite consisting essentially of perthitic orthoclase and quartz, with approximately 2-8% of resorbed plagioclase (Flett-Brown, 1975). Small biotite and hornblende crystals constitute less than 0.5% of the rock and are frequently altered to chlorite minerals. Accessories are minor magnetite, zircon and apatite, rare sphene and sparsely distributed thorite.

5.2:4 The Starav Granites

The resistant, even-grained Central Starav Granite forms high peaks surrounded by low, boggy terrain over the easily weathered, coarsely porphyritic Outer Starav Granite. There is some evidence of foliation in the mafic minerals of the transitional/hybrid rock (Flett-Brown, 1975).

The Outer Starav is a biotite granite, with large phenocrysts (1-3 cm) of both pink perthitic orthoclase and white oligoclase (Kynaston and Hill, 1908). Quartz, K-feldspar and albite crystallised eutectically in the groundmass and late-stage quartz and K-feldspar form graphic intergrowths. Hornblende is the most abundant mafic mineral in the south-west but becomes scarce to the north-east. Biotite is also

present. Accessory minerals are abundant sphene, although this is less conspicuous than in the N Cruachan adamellite, minor magnetite, apatite and zircon, and sparse thorite.

The Central Starav Granite is generally coarse, but irregular patches of microgranite occur around Ben Starav and are often associated with pockets of pegmatitic material. Quartz, K-feldspar (predominantly microcline) and plagioclase are equidimensional and graphic intergrowth of quartz and K-feldspar appears in the most acidic samples. Mafic minerals, constituting less than 3% of the rock, are dominated by a brown-green, often ragged biotite which is extensively altered to chlorite. Hornblende is minor and similarly altered. Accessory minerals are magnetite, associated with the alteration of mafics, and minor zircon, monazite, thorite and apatite.

Several aplites, often with pegmatitic cores, are associated with the Starav Granites.

5.2:5 Dykes

The swarm of NNE-trending dykes associated with the Etive Complex (inset to Figure 5.2) reflect the regional stress system which prevailed throughout the Caledonian Orogeny. A detailed description of the dykes may be found in Kynaston and Hill (1909), Anderson (1937) and Bailey and Maufe (1961). Four varieties occur; felsites, porphyrites, microdiorites and lamprophyres. Several periods of dyke injection occurred throughout the intrusive history of the Etive Complex, but most post-date or were coincident with intrusion of the Meall Odhar granite. All but two dykes pre-date the Starav granites.

5.3 CRYSTALLISATION HISTORY

A two-stage history of crystallisation involving differentiation

in both upper and lower magma chambers has been proposed to account for field relations, geochemistry and two phases of plagioclase and biotite in the Etive units (Flett-Brown, 1975). The absence of first-generation plagioclases in the Meall Odhar granite is consistent with its origin from intercumulus liquid separated by filter pressing or thermal remobilisation; a conclusion supported by geochemical evidence (Section 5.4).

Flett-Brown (1975) considered the incompatibility of the S Cruachan 'tonalites' with the general trend of modal mineral variations in the Etive Complex (Figure 5.6) to be the result of plagioclase settling; i.e. these represent the bottom of the magma chamber (S lobe) and the N adamellite represents the top. This conclusion was based on limited representation of the Cruachan units and does not account for the observed variation and sharp contacts within the S lobe. In-situ fractionation may have occurred on a local scale, but progressive differentiation in the lower magma chamber, and intermittent removal of magma to higher levels would be more consistent with field evidence.

5.4 GEOCHEMISTRY

Major element variations for the Etive Complex show a sub-alkaline trend (Figure 5.7). The anomalous position of the Meall Odhar granite with respect to its temporal relationship in the Complex is consistent with an intercumulus origin (see below) and Cruachan samples show considerable scatter.

Flett-Brown (1975) considered trace element variations of Cruachan samples with relative height in the upper magma chamber (assuming a post-intrusion dip of $\sim 20^{\circ}$ NE) to show in-situ crystal settling of plagioclase, hornblende, biotite, magnetite and apatite.

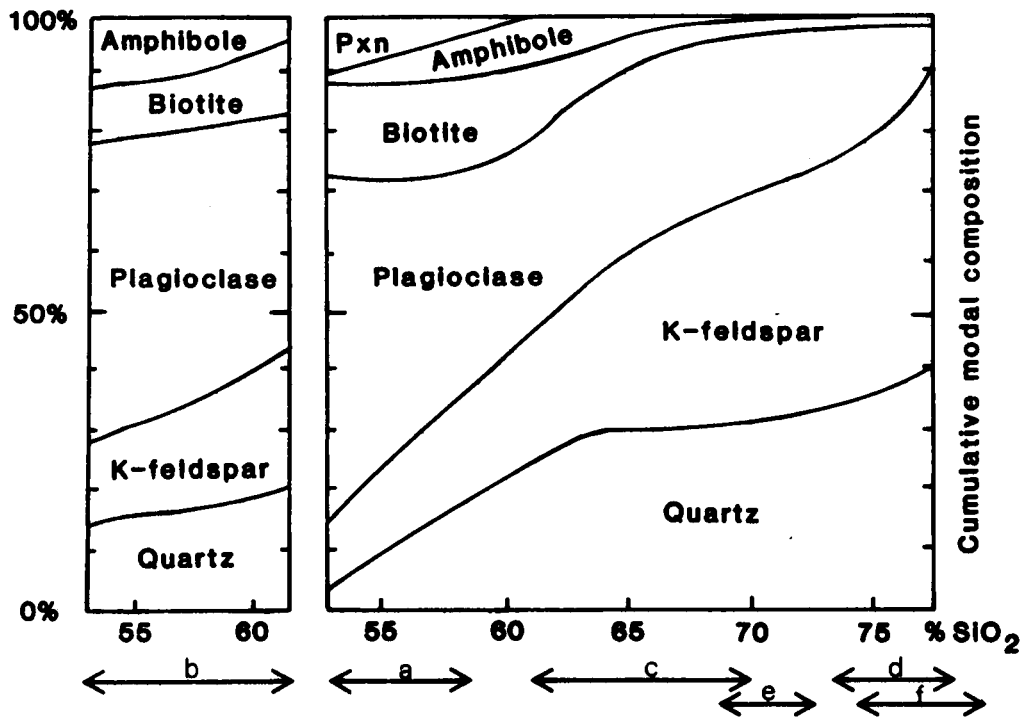

Figure 5.6 Approximate modal compositions of Etive units; from Flett-Brown, 1975. Composition ranges represent: a, Quarry Intrusion; b, S Cruachan 'tonalite' (see text); c, N Cruachan adamellite; d, Meall Odhar Granite; e, Outer Starav Granite; f, Central Starav Granite.

A comprehensive coverage of the distribution of major and trace elements in the Cruachan units (Figure 5.8), however, does not confirm this hypothesis (see caption to Figure 5.8). Although coverage is incomplete over the N Cruachan lobe, the distribution of Rb, Sr, Zr and TiO_2 suggest a concentric zonation in this unit.

Selected interelement plots (Figure 5.9) show that all units except the Central Starav and Meall Odhar granites have trace element characteristics similar to the 'forceful' Newer granites (see Plant et al., 1980, and Chapter 3). The granites lying outside this field, however, never attain the degree of enrichment in incompatible elements (e.g. Rb) or depletion in compatible elements (e.g. Sr) observed in the Cairngorm and other late discordant granites of the

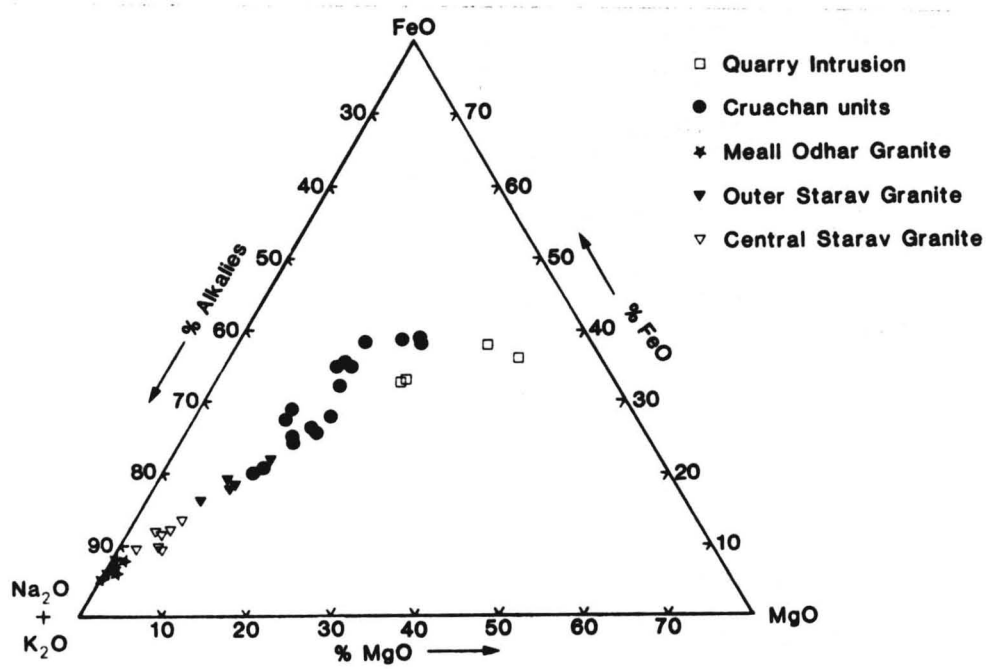

Figure 5.7 AFM diagram for the Etive Complex showing a typical calc-alkaline trend. Data from R. Gallop (pers. comm.).

NE Grampians (Plant et al., 1980; see also Chapter 6). Two samples from the centre of the N Cruachan lobe plot near the Central Starav Granite in all cases (Figure 5.9).

Three component fractionation trends are apparent in Figures 5.9 a and b; the Meall Odhar Granite has anomalously low Rb, Sr and Ba contents (see below). The initial increase in both Sr and Ba indicates fractionation of a mineral with partition coefficients of less than one for both elements, probably pyroxene (see Arth, 1976). The shift to decreasing Sr (at ∿56% SiO_2) and decreasing Ba (at ∿60-64% SiO_2) probably mark the initiation of plagioclase and K-feldspar fractionation respectively (early formed plagioclases tend to have low Sr (Turekian, 1978) and possibly started to nucleate earlier). The later crystallisation of K-feldspar is supported by the absence of this mineral as a phenocryst phase in both the Quarry diorite and the more basic varieties of Cruachan. The scatter on the Ba-Rb plot reflects the fractionation of biotite (see for example McCarthy and Robb, 1978).

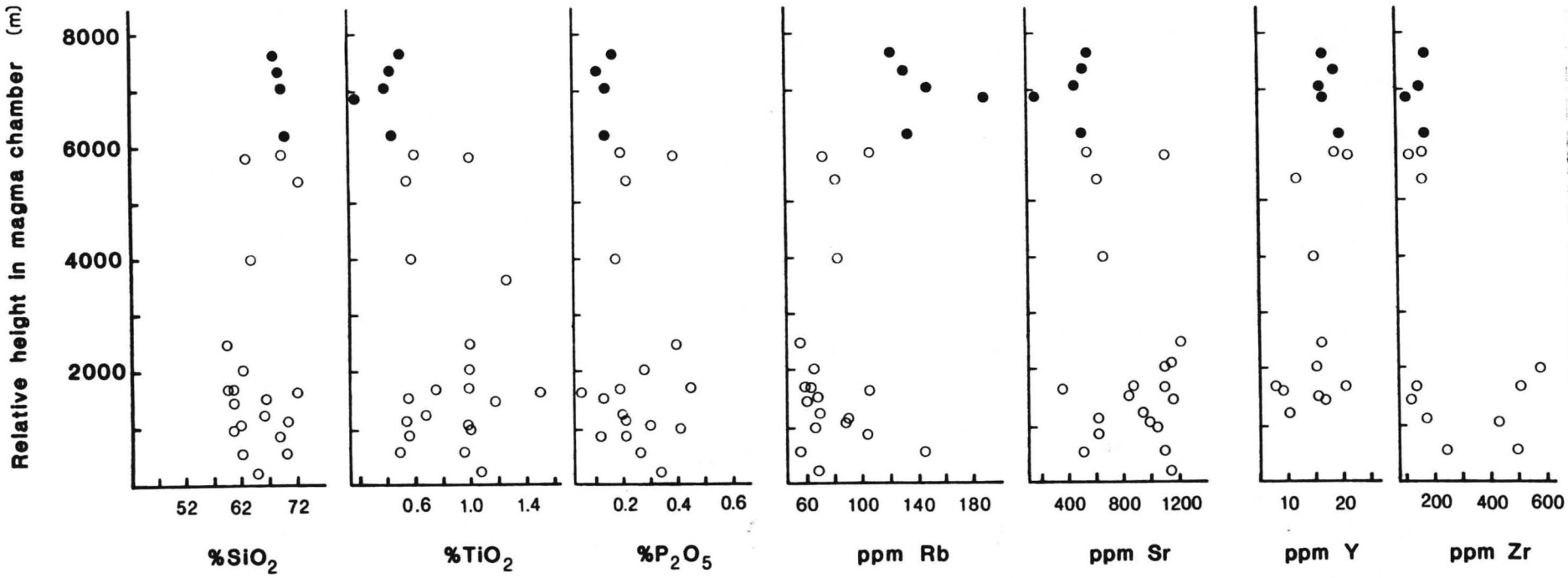

Figure 5.8 Variation of major and trace element contents of Cruachan samples with relative height in Flett-Brown's (1975) postulated upper magma chamber (see Figure 5.3). Open circles, S. Cruachan samples; Closed circles, N Cruachan samples. Analytical data is presented in Appendix C.
The wide range, and non-systematic variation of values for the S Cruachan samples is consistent with a multi-phase intrusion. The generally more restricted ranges shown for the N Cruachan adamellite are compatible with the later intrusion of this more highly differentiated unit (see Figure 5.4), perhaps with simultaneous emplacement of some southern equivalents.

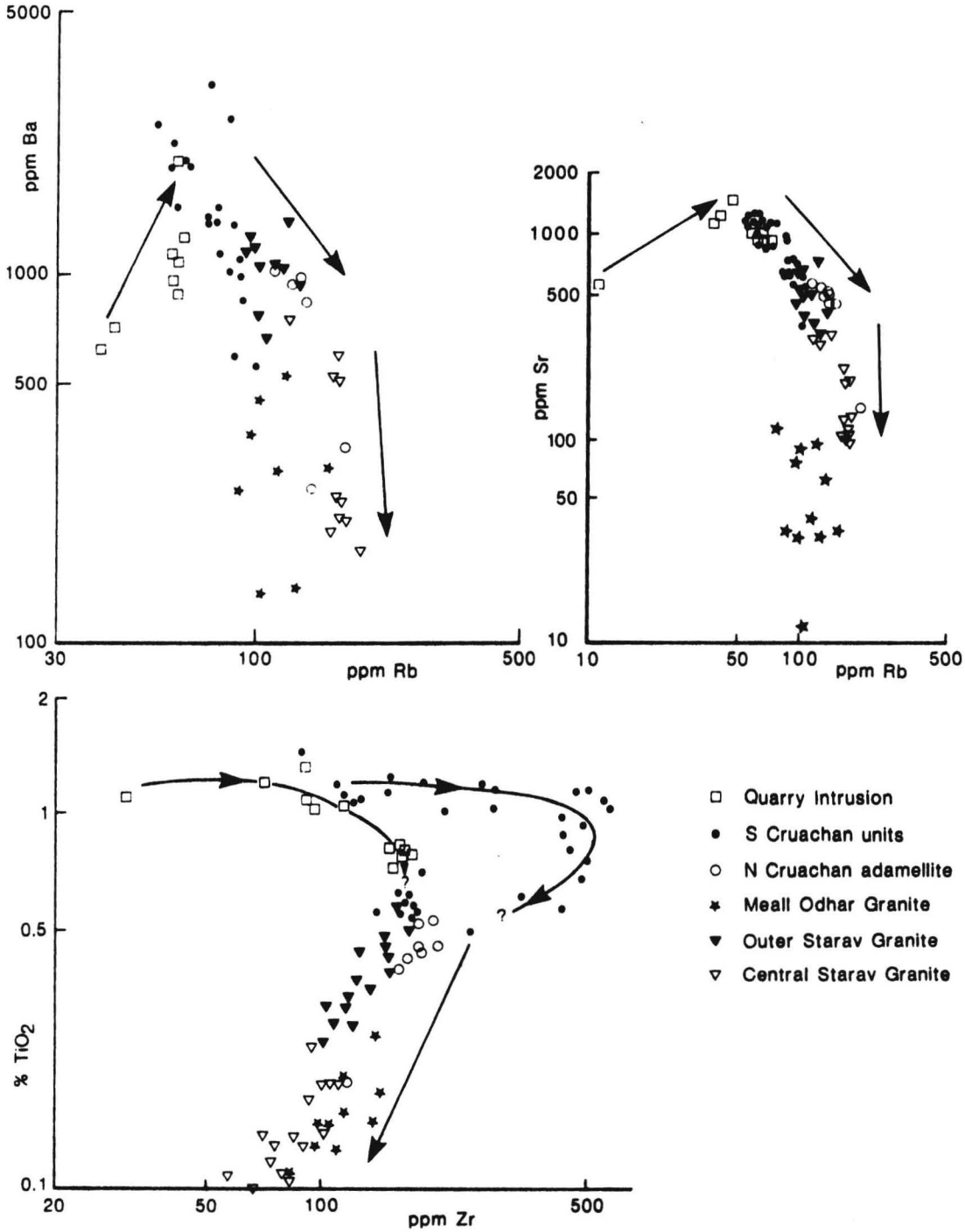

Figure 5.9 Selected interelement plots for the Etive Complex. Data from this study (Appendix C) and R. Gallop (pers. comm.). Arrows indicate direction of increasing SiO_2.

The final trend of depletion in Ba and Sr at approximately constant Rb may be the result of increased feldspar and biotite fractionation and/or the loss of late magmatic fluids enriched in incompatible elements (see for example Tindle and Pearce, 1981).

Figure 5.9c clearly defines separate trends for the Quarry and early Cruachan units. A trend of increasing then decreasing Zr, as zircon crystallises, has been observed for many 'granites' (e.g. Loch Doon, Cassidy, 1981; Tindle, 1982).

All three interelement plots show an overlap of the Outer Starav samples with the later Cruachan units. This may be due to:

i) A relatively short time interval between removal of the upper layers of a differentiating lower magma chamber to form the N Cruachan lobe and emplacement of the Outer Starav unit. The latter would be derived from lower levels in the magma chamber which had insufficient time to attain a higher degree of differentiation.

ii) The Outer Starav Granite being emplaced at a higher level than the N Cruachan unit. In-situ differentiation and subsequent erosion would then account for the geochemical overlap.

iii) A fresh input of magma to the lower magma chamber after emplacement of the Cruachan units and before that of the Outer Starav Granite.

No conclusive evidence is available for any interpretation, but isotopic evidence (Section 5.5) supports proposal (iii).

The position of the Meall Odhar Granite in Figure 5.9a, b and c and Figure 5.7 supports the hypothesis that this unit represents the residual melt or remobilised intercumulus liquid derived from earlier units. Separation from early 'cumulate' phases (plagioclase and biotite) account for depletion in Sr and Ba whilst retaining high SiO_2 and K_2O contents. Depletion in Rb and enrichment in Zr with respect

to the Central Starav Granite indicate that the Meall Odhar Granite was derived from a less evolved melt than this central unit.

Chondrite normalised REE patterns for Etive samples (Figures 5.10 a and b) are all essentially sub-parallel, except for Eu anomalies, and exhibit strong light to heavy REE enrichment. Although successive units overlap, there is a tendency for total REEs to initially increase (cf. sample YR912 to sample SB73, Figure 5.10a) and then to decrease with increasing differentiation. Similar REE trends in the Loch Doon intrusion were controlled initially by crystallisation of major phases (incompatible behaviour of REEs) and subsequently by the crystallisation of REE-rich accessory phases (Tindle, 1982). In the Etive Complex, fractionation of hornblende, biotite and plagioclase which have relatively low REE contents (Figure 5.11) probably accounts for the initial incompatible behaviour of REEs. Subsequent depletion of REEs in the melt probably results from the crystallisation of apatite, sphene, zircon and minor allanite (see Figure 5.11). Crystallisation of monazite (see Table 5.18 for REE contents) in the Central Starav Granite may account for the substantial depletion of REEs in late stage microgranite, sample SB134 (Figure 5.10b).

Negative Eu anomalies are restricted to the N Cruachan adamellite, the Central Starav Granite and the Meall Odhar Granite, suggesting that plagioclase settling only became important during the final stages of crystallisation, perhaps as increasing H_2O concentration decreased viscosity in the magma. The pattern for the Meall Odhar Granite is consistent with previous interpretations of its origin. The absence of a negative Eu anomaly in sample N56 (from the north-east end of the S Cruachan lobe), and of a positive Eu anomaly in samples YR1200 and SB73 (from the south-west end of the S Cruachan lobe) adds weight to

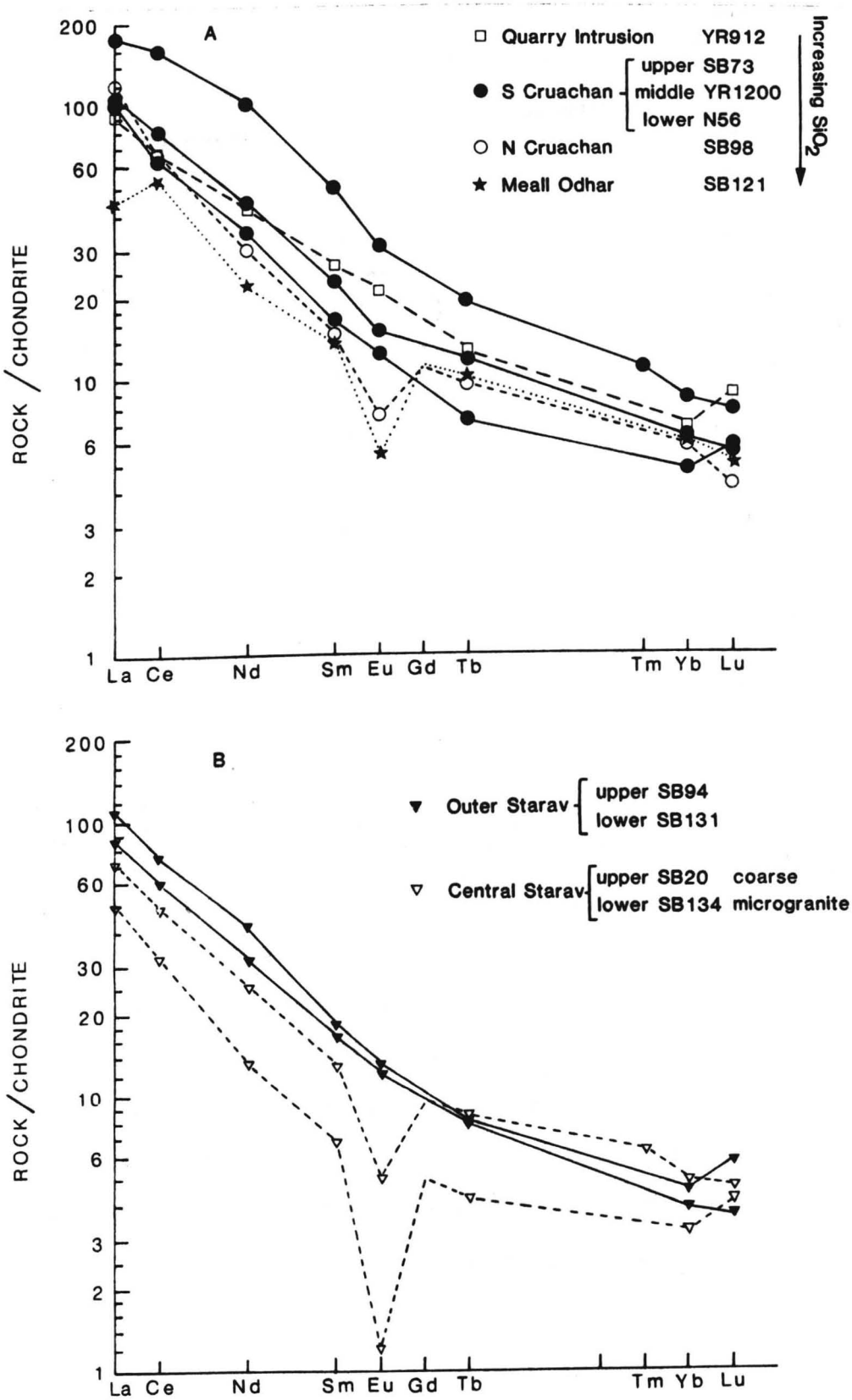

Figure 5.10 Chondrite normalised REE plots for a) Outer Etive units and b) inner Etive units. Analyses are presented in Appendix C.

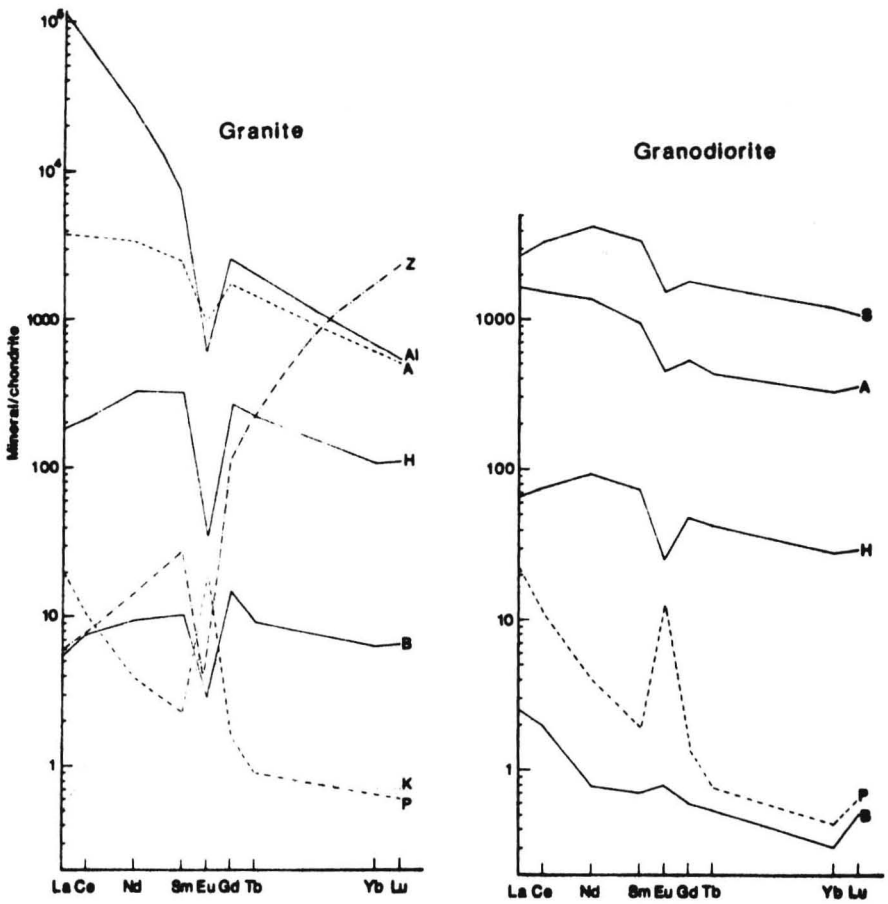

Figure 5.11 Typical chondrite normalised REE patterns for granitic minerals; data from the Querigut Complex, Pyrénées (Fourcade and Allegre, 1981) and Loch Doon, S Uplands (Tindle, 1982). Plots are for; P, plagioclase; K, potassium feldspar; B, biotite; H, hornblende; A, apatite; S, sphene; Z, zircon; Al, allanite.

the argument that in-situ plagioclase settling was not responsible for variations within the S Cruachan unit. The return to a 'flat' REE pattern in the Outer Starav Granite (i.e. SB98 to SB94 and SB131; Figures 5.10a and b) may again be explained in terms of fresh influxes of magma from below or fractionation both in-situ and at lower levels (points i, ii and iii above).

5.5 ISOTOPIC DATA

Biotite K-Ar ages of 399 ± 19 m.y. and 408 ± 18 m.y. were obtained for the Starav Granite (Miller and Bunker, 1965) and 387 ± 6

m.y. and 399 ± 8 m.y. for the Cruachan 'granodiorite' (Brown et al., 1968). Detailed studies of K-Ar mineral ages (Flett-Brown, 1975) produced an age of 415 m.y. for all units except the Central Starav Granite (422 ± 7 m.y.). Flett-Brown attributed the apparent earlier age of the Central Starav to diffusion of excess argon into the lower magma chamber from surrounding country rocks prior to the intrusion of this unit. Recent Rb-Sr whole rock isochron data for the Meall Odhar and Central Starav Granites gave ages of 401 ± 6 m.y. and 396 ± 12 m.y. respectively (Clayburn et al., 1983). A whole rock Rb-Sr isochron for the Quarry Intrusion gave an age of 505 ± 93 m.y. for this unit (Flett-Brown, 1975). It is feasible, on the basis of field evidence, that the Quarry Intrusion represents a precursor to the main cauldron subsidence event.

Comparison of isotopic data for the Etive units (Table 5.3) with the isotopic compositions at 400 m.y. of source regions from which the Etive magmas may have been derived indicates an origin from the melting of both contemporary mantle and lower crust, probably of Grenville age (Clayburn et al., 1983). These authors envisage "a juvenile melt derived from an enriched mantle source overlying the subducted Iapetus slab to initiate melting within the lower crust, and subsequently mix with this melt during prolonged residence in a lower crustal magma reservoir."

There is a clear tendency for the Etive magmas to become enriched in ^{87}Sr and ^{18}O, but depleted in radiogenic Pb with differentiation (Table 5.3). The slight drop in $(^{87}Sr/^{86}Sr)_i$ from the Meall Odhar Granite to at least some of the dykes and the Starav Granites is consistent with the influx of a new batch of mantle derived

Intrusive phase		Age (Myr)	$\delta^{18}O$ SMOW (‰)	$(^{87}Sr//^{86}Sr)_i$	$^{206}Pb/^{204}Pb$	$^{207}Pb/^{204}Pb$	$^{208}Pb/^{204}Pb$
Central Starav	n	402 ± 10	5	5	3	4	3
	r		8.9-9.8	0.7055	16.714-16.860	15.314-15.318	36.276-26.295
	m		9.4		16.798	15.316	36.286
Outer Starav	n	(400)	3	3	3	3	2
	r		9.3-9.7	0.70476-0.70542	16.753-16.765	15.322-15.363	36.266-36.403
	m		9.5	0.70507	16.759	15.343	36.335
Dykes	n	(400)	3	3			
	r		8.6-9.2	0.70480-0.70517			
	m		8.8	0.70501			
Meall Odhar	n	400 ± 4	6				
	r		8.3-9.8	0.7058			
	m		9.0				
Fault Intrusion	n	(400)		1	1	1	1
	r						
				0.70532	16.88	15.395	36.304
	m			0.70532	16.822	15.395	36.304
Cruachan	n	(400)	6	13	2	2	2
	r		7.2-8.7	0.70474-0.70550	16.925-17.178	15.337-15.345	36.466-36.798
	m		8.2	0.70493	17.052	15.341	36.632
Quarry Intrusion	n	(400)	1	1	1	1	1
	r		7.2				
				0.70445	17.185	15.447	36.911
	m		7.2	0.70455	17.185	15.447	36.911

Table 5.3 Summary of age and isotopic relationships within the Etive Complex; from Clayburn et al., 1983.
n = number of samples analysed; r = range of values; m = mean value.

magma into the lower magma chamber before intrusion of the latter units. $\delta^{18}O$ values also show a slight decrease from the Meall Odhar Granites to the dykes, but not in the Starav Granites. However, $\delta^{18}O$ values may reflect fractionation trends (Epstein and Taylor, 1967) or interaction with meteoric and/or magmatic water (e.g. Taylor, 1971), in addition to variations in source regions.

The Nd-isotope data presented by Hamilton et al., (1980) and Frost and O'Nions (1982) also recognize a crustal component in the Etive magmas. T_{CHUR} ages of approximately 840 and 1200 m.y. for the Cruachan and Starav units respectively are consistent with a Grenville component (Hamilton et al., 1980), and $^{143}Nd/^{144}Nd$ ratios indicate an increase in crustal contamination in the Starav Granites relative to earlier units.

5.6 DISCUSSION AND SUMMARY OF SECTIONS 5.1 - 5.5

Chemical, mineral and isotopic variations of the Etive units suggest a complex magmatic history involving crystal fractionation, both at depth and in-situ, coupled with episodic magma mixing in a deep magma chamber. In particular, the reversal in fractionation and isotopic trends after the Meall Odhar Granite indicate a fresh influx of 'basic', mantle-derived, magma into the lower magma chamber before emplacement of the Starav units.

Subterranean cauldron subsidence, involving two to three crustal blocks, is envisaged as the intrusive mechanism; this is consistent with gravity data. The proposed post-intrusion dip to the north-east (Flett-Brown, 1975) is not required to account for geochemical variations in the Cruachan units, which were emplaced by multiple intrusion. It

would, however, still serve to explain the apparent north-east migration of intrusive centres. Phillips et al., (1981) proposed a model of asymmetric convective circulation to explain the offset centre of the Criffel-Dalbeattie pluton; it is possible that such a mechanism was responsible for the asymmetry of the Starav units, with upward movement of the Central Starav magma before solidification producing the 'hybrid' zone between the two units. However, no oscillatory zoning has been recorded in Starav plagioclases (Flett-Brown, 1975) to indicate convective movement (see Phillips et al., 1981). An alternative explanation for offset centres is, perhaps, asymmetric subsidence of country rock blocks due to complex fracturing and faulting in a multiple cauldron model.

5.7 RADIOELEMENT MAPPING OF THE ETIVE COMPLEX

Exposure is generally good over the Etive Complex and ideally suited to in-situ gamma-ray spectrometry, except in a few areas of low-lying boggy ground corresponding to the readily-weathered Outer Starav Granite. Field surveys were completed during the course of three seasons from 1978-1980, employing a 3-channel gamma-ray spectrometer (see Section 4.1). An attempt was made to maintain a maximum station spacing of 1 km, but inaccessibility and some lack of exposure prevented the execution of such an ideal coverage.

The method adopted for data equisition was essentially that followed by Cassidy (1980); i.e. five two minute readings were taken at each station over an area of approximately 20-25 m^2. This ensured a statistically meaningful number of counts in each channel and a more realistic determination of the average radioelement contents than that afforded by a single measurement. Where suitable exposure (i.e.

approximate 2π geometry) was not extensive, fewer, longer readings were taken. At several stations, particularly in the S. Cruachan lobe, a significant variation in channel counts was observed between individual readings. These generally correspond with variations in petrology and further readings were taken to obtain average contents for each intrusive type.

Five base stations were established during the course of field-work to monitor daily and longer term changes in spectrometer performance. Critical variations in base station readings were only observed prior to complete systems failure, which unfortunately occurred on three occasions. Due to the considerable time involved in acquiring replacement units for the spectrometer, it was necessary to cover much of the area by collecting approximately 2 kg samples for radioelement analysis by ENAA (Section 4.2) and XRF (Appendix A). In addition to these, fresh samples were collected at several spectrometer stations for Lexan studies. A total of 303 stations were covered (see Figure 5.2 and Appendix D).

5.8 REDUCTION OF DATA AND PRODUCTION OF RADIOELEMENT MAPS

Raw field data were reduced to radioelement concentrations using the stripping ratios and sensitivity constants calculated in Section 4.1:3. Individual readings were reduced separately and, where appropriate, the resulting U, Th and K_2O contents averaged to give mean analyses for each station (see Appendix D). The data from all stations, except those for aplites, dykes and country rocks, were used as a basis to produce radioelement distribution maps (Figures 5.12-5.15). Where possible these maps were hand contoured, but where data required 'smoothing' to emphasize general radioelement trends, a computer gridding

Caption for Figures 5.12, 13, 14 and 15. Radioelement distribution maps for the Etive Complex.

Internal geological boundaries shown in dotted lines, are as i Figure 5.2. Means and ranges of radioelement contents refer to: (1), the whole of the Quarry Intrusion; (2), the SW region of the S Cruachan lobe; (3), the NE region of the S Cruachan lobe; (4) the whole of the Meall Odhar Granite, including the type dyke and minor outcrops.

Figure 5.12 Distribution of Th. Thorium levels in the Starav Granites and the N Cruachan unit were hand contoured. Dashed contours are estimated where control points are sparse, or data are locally variable.

Figure 5.13 Distribution of U. Uranium levels in the Starav Granites and the N Cruachan unit were hand contoured. Dashed contours are estimated.

Figure 5.14 Distribution of $^{Th}/_{U}$. $^{Th}/_{U}$ ratios in the Starav Granites were computer contoured.

Figure 5.15 Distribution of K_2O. Potassium levels in the N Cruachan lobe were hand contoured. Computer contours were used for the Starav Granites.

Computer Contouring routine A weighted average gridding routine (described in Davis, 1973) was used to derive some radioelement distribution contours. The program obtains a regular grid of values from input control points by calculating weighted averages from an optional number of nearest observations. Anomalous points (only a few were encountered) were omitted from the data set. Specified contours are then constructed from these grid values. After trial, an option of the nearest four control values to calculate weighted averages, was chosen to produce the most representative distribution contours, and eliminate edge effects. The success of this method is evident in the sympathetic trends obtained for hand and computer contoured distribution maps.

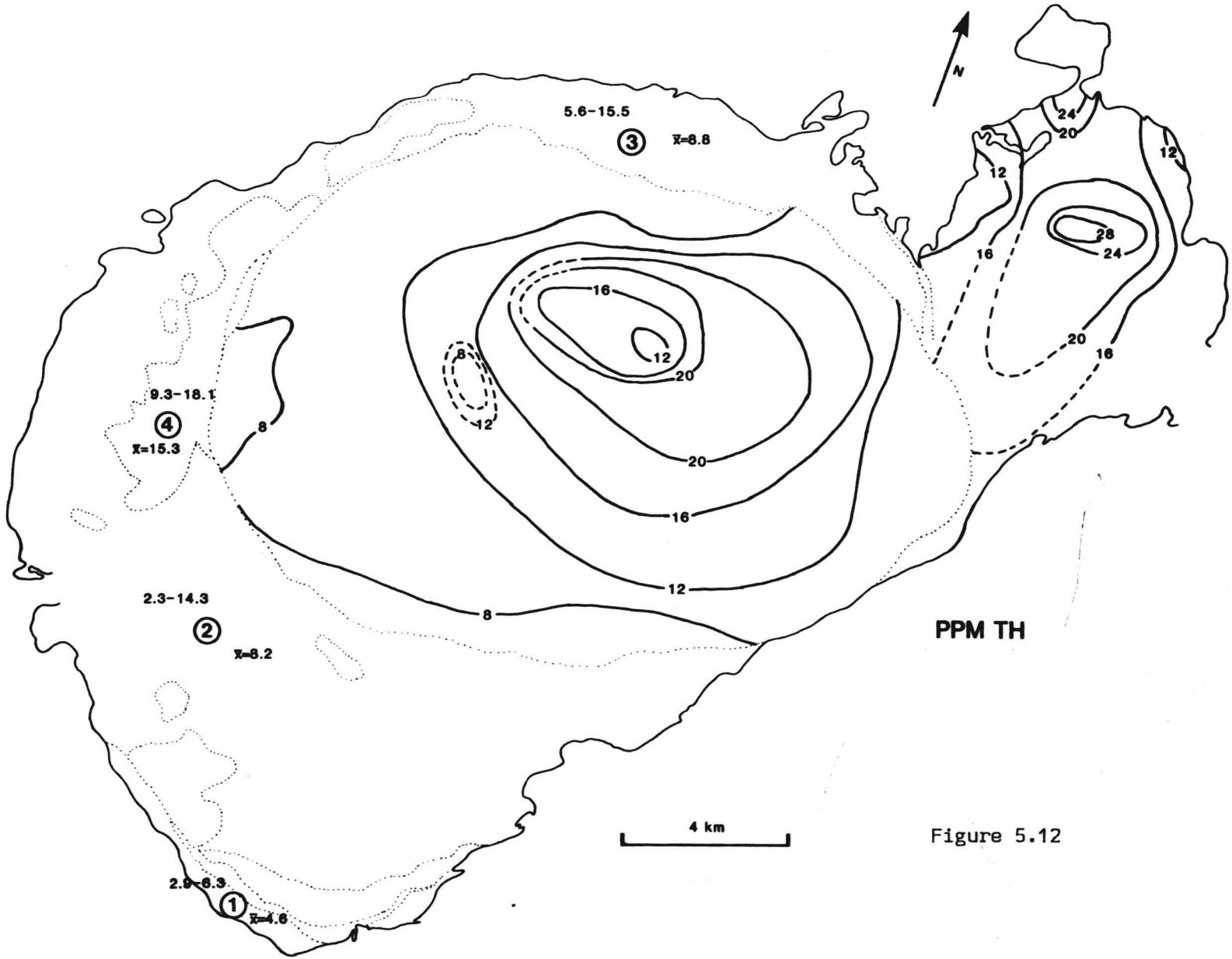

Figure 5.12

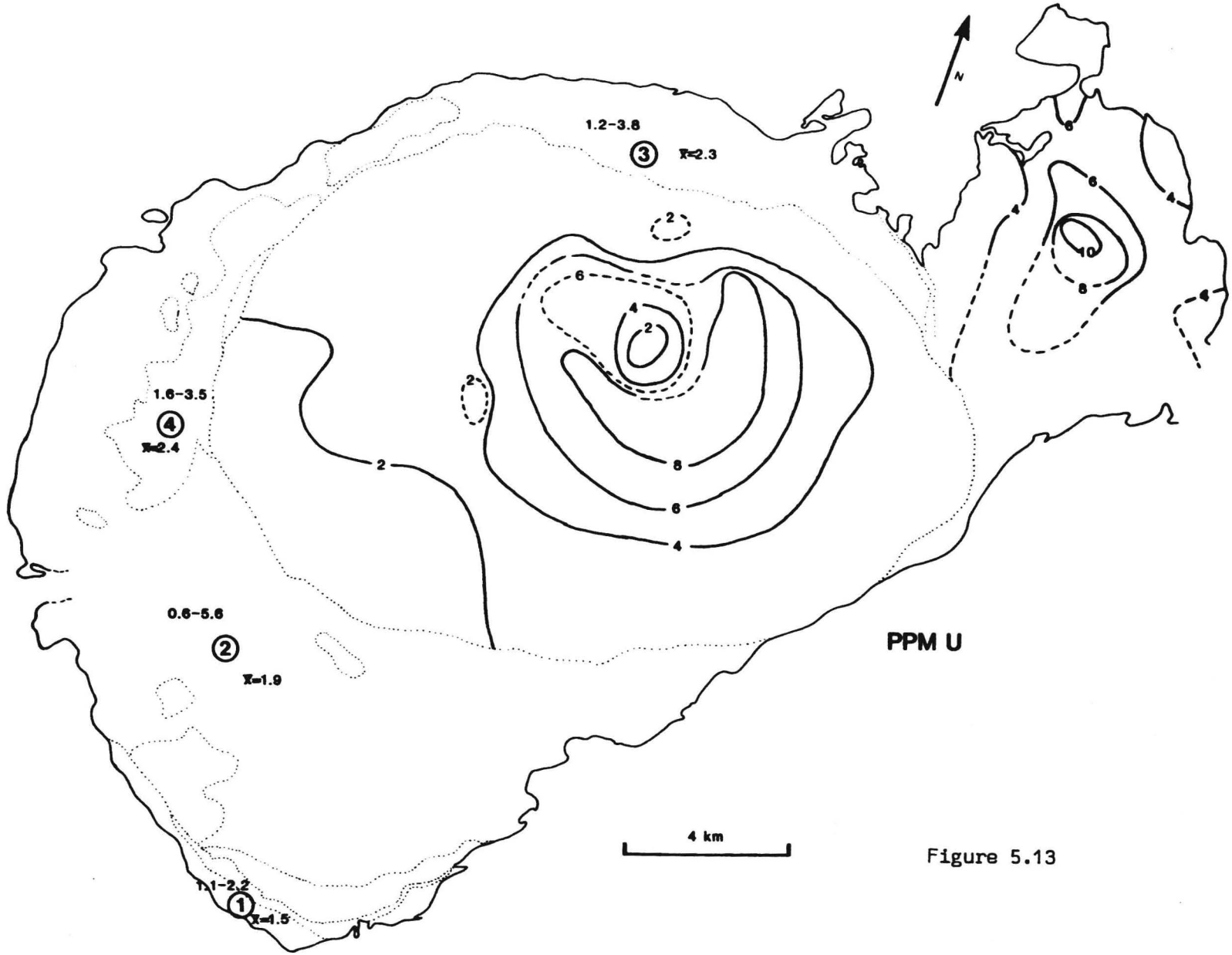

Figure 5.13

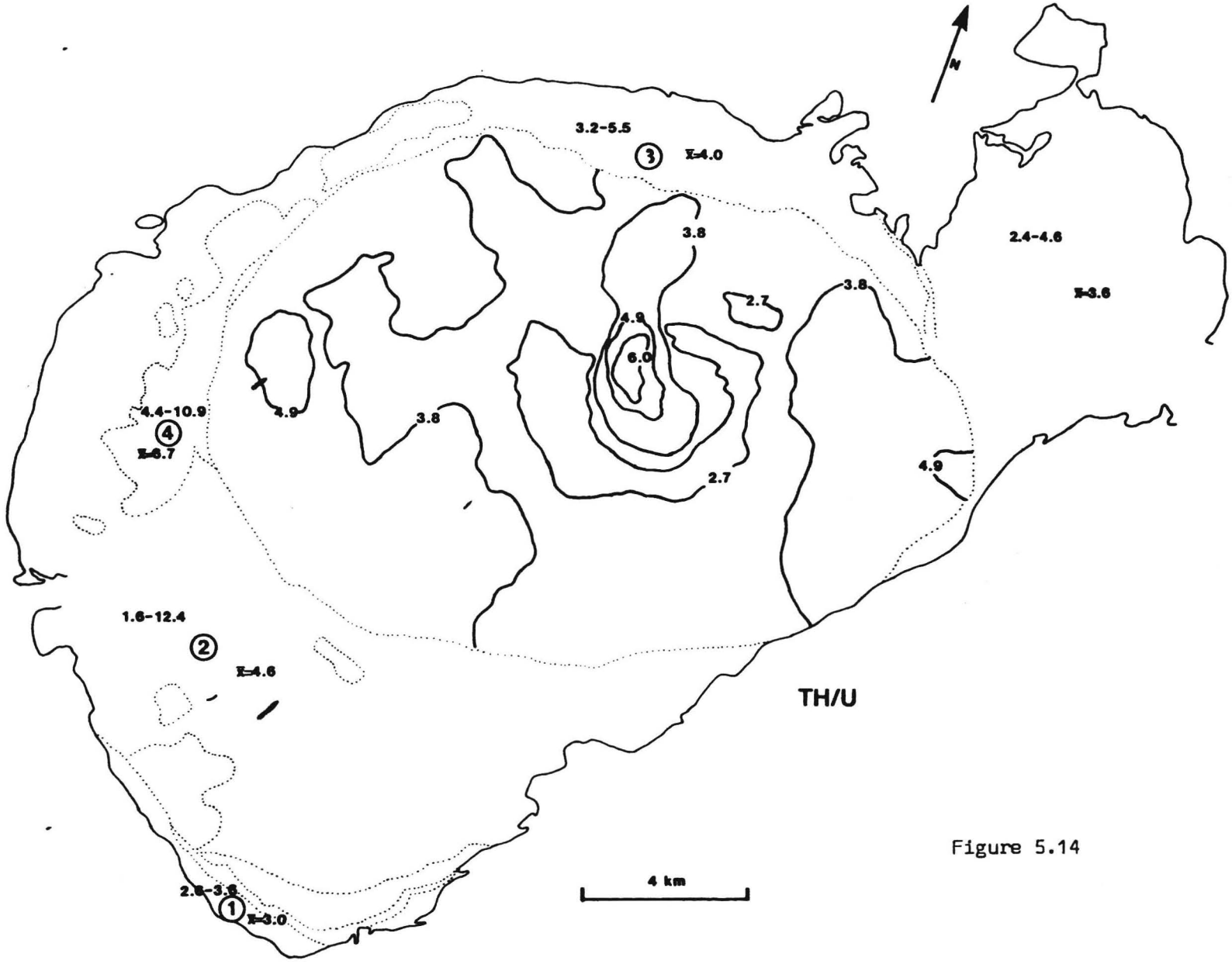
N
3.2-5.5
3
X=4.0
3.8
2.4-4.6
X=3.6
2.7
3.8
4.9
6.0
4.4-10.9
4
X=6.7
4.9
3.8
2.7
4.9
1.6-12.4
2
X=4.6
TH/U
4 km
2.8-3.8
1
X=3.0

Figure 5.14

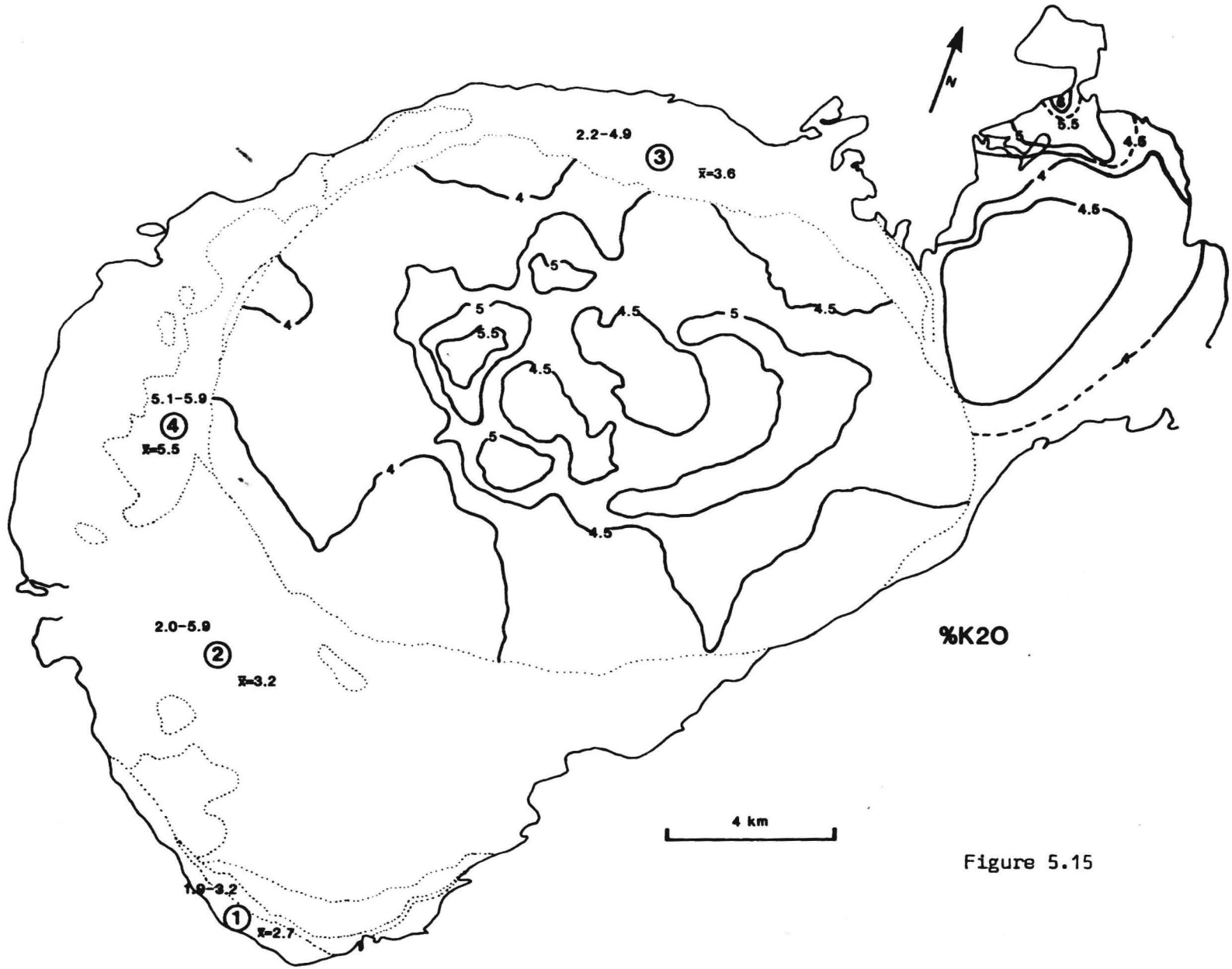

Figure 5.15

and contouring routine was used (see caption to Figures 5.12-5.15). The S Cruachan lobe could not be contoured due to the complex distribution of intrusive phases with different characteristic radioelement contents. The Quarry Intrusion and the Meall Odhar Granite are volumetrically and aerially of minor importance and show no geographical variation in radioelement content.

5.9 DISCUSSION OF RADIOELEMENT DISTRIBUTIONS

Thorium. In the outer units of the Complex mean Th contents (Table 5.4) increase from Quarry Intrusion - S Cruachan units - Meall Odhar Granite - N Cruachan adamellite. The concentric zonation in the N Cruachan lobe is consistent with earlier proposals that this unit represents a separate intrusive phase exhibiting in-situ differentiation; no data were acquired for the northerly protrusion into the Glen Coe cauldron, and it remains uncertain whether the contours close around this local 'high' (Figure 5.12).

As observed for other elements (Figure 5.8), there is no geographical trend of Th contents in the S Cruachan lobe and the highest values, equivalent to Th levels in the perimeter zones of the N Cruachan lobe, were obtained from the more acidic, pink granodiorite units.

The Meall Odhar Granite has a lower mean and narrower range of Th contents than the earlier N Cruachan unit. Two explanations may account for this anomaly:

i) due to the almost hyperbyssal nature of Meall Odhar unit, resulting in relatively rapid cooling, in-situ enrichment processes were not active,

ii) if this unit represents remobilised intercumulus liquid or residual melt, the separation from early formed Th-bearing phases would reduce its whole rock Th content relative to a magma retaining

Unit	No. Spectrometer stations	No. sample stations	Th (ppm)		U (ppm)		*Th/U		K_2O(%)	
			$\bar{x}$	σ	$\bar{x}$	σ	$\bar{x}$	σ	$\bar{x}$	σ
Quarry Intrusion	2	10	4.6	1.7	1.5	0.5	3.1	0.2	2.7	1.0
S Cruachan lobe	51	46	8.4	2.7	2.0	0.8	4.4	1.7	3.4	0.8
N Cruachan lobe	19	9	18.7	5.4	5.2	2.0	3.7	0.6	4.6	0.6
Meall Odhar Granite	12	9	15.5	2.8	2.6	1.2	6.6	2.0	5.6	0.5
Outer Starav Granite	25	24	10.4	2.1	2.6	0.6	4.1	0.9	4.2	0.4
Central Starav Granite	29	16	15.9	4.7	5.1	2.7	3.5	1.2	4.8	0.5
Aplites	2	3	21.4	5.5	4.9	1.6	4.9	1.8	5.4	0.3
Dykes	11	4	9.9	2.8	2.8	0.8	3.6	0.5	3.9	0.8
Country rocks	11	-	7.9	2.0	2.1	0.7	3.7	1.6	3.4	0.8
Average for Etive Complex weighted according to areal extent of units			12.7		2.9		4.2		4.1	

Table 5.4 Radioelement contents for the Etive Complex.
*Mean $^{Th}/_{U}$ ratios are calculated from individual station values

liquidus minerals.

A combination of (i) and (ii) is most likely.

Thorium contents increase towards the offset centre of the Starav units (Figure 5.12), but gradients are noticeably greater in the Central Starav Granite, particularly in the north-east where they coincide with the steep slopes of Ben Starav and Ben Trilleachan. The central decrease in Th content may represent the roof zone of an irregularly domed intrusion (see Section 5.10:5) and does not necessarily imply a depletion in Th as differentiation proceeded.

The overlap in Th contents between the Starav Granites and earlier units is consistent with other trace element trends (Section 5.4).

Uranium. Uranium varies sympathetically with Th in the Etive Complex (Table 5.4 and Figures 5.12 and 5.13); a well documented trend for magmatic differentiation series (see Chapter 2). One notable exception to this trend is the relative depletion of U in the Meall Odhar Granite ($^{Th}/U = 6.6$). This may be due to preferential partitioning of U into early crystallising phases, resulting in a high $^{Th}/U$ ratio in the 'separated melt', or mobilisation and removal of U with late magmatic fluids. Lexan studies (Section 5.10) do not unambiguously resolve these two possibilities.

$^{Th}/U$ ratio. Only the Starav units could be contoured with respect to this parameter (Figure 5.14) revealing a pattern similar to those for U and Th. The decrease of $^{Th}/U$ from the perimeter inwards may be primary or secondary in origin, i.e. caused by:

i) preferential partitioning of Th (with respect to U) into early crystallising phases, or

ii) limited outward mobilisation and redeposition of U with late stage hydrothermal fluids.

Lexan studies show that some U resides in secondary sites in Starav samples, but do not preclude (i) as a contributory factor (Sections 5.10:4 and 5). Although the central anomaly may represent a roof zone, its exceptionally high $^{Th}/U$ ratio (cf. perimeter zones, Figure 5.14) suggests removal of U, in keeping with (ii) above.

In the outer Etive units, mean $^{Th}/U$ ratios (Table 5.4) initially increase from the Quarry Intrusion to the S Cruachan units and then decrease in the N Cruachan adamellite. These trends are controlled by crystallisation of primary accessory phases (Section 5.10:1 and 2).

Potassium. Although K_2O trends (Figure 5.15) essentially parallel those of U and Th, certain contrasts are apparent in the detail of its distribution.

i) The centre of the N Cruachan lobe is not well defined but the northerly 'high' is distinct.

ii) The decrease in U and Th at the centre of the Starav units is not precisely matched by K_2O. This is partly a function of the 'smoothing' performed by the contouring routine and the narrow range of K_2O contents in the Starav Granites.

iii) The mean K_2O content of the Meall Odhar granite is higher than for most other samples.

Variations between K_2O distributions and U and Th distributions are due primarily to their incorporation in major and accessory mineral phases respectively.

Figure 5.16 summarises U and Th data for the Etive Complex, showing the considerable overlap between earlier outer units and the Starav Granites. The dykes define a relatively narrow linear trend, probably representative of differentiation and/or magma mixing processes in the lower magma chamber. The much broader trends of most other units

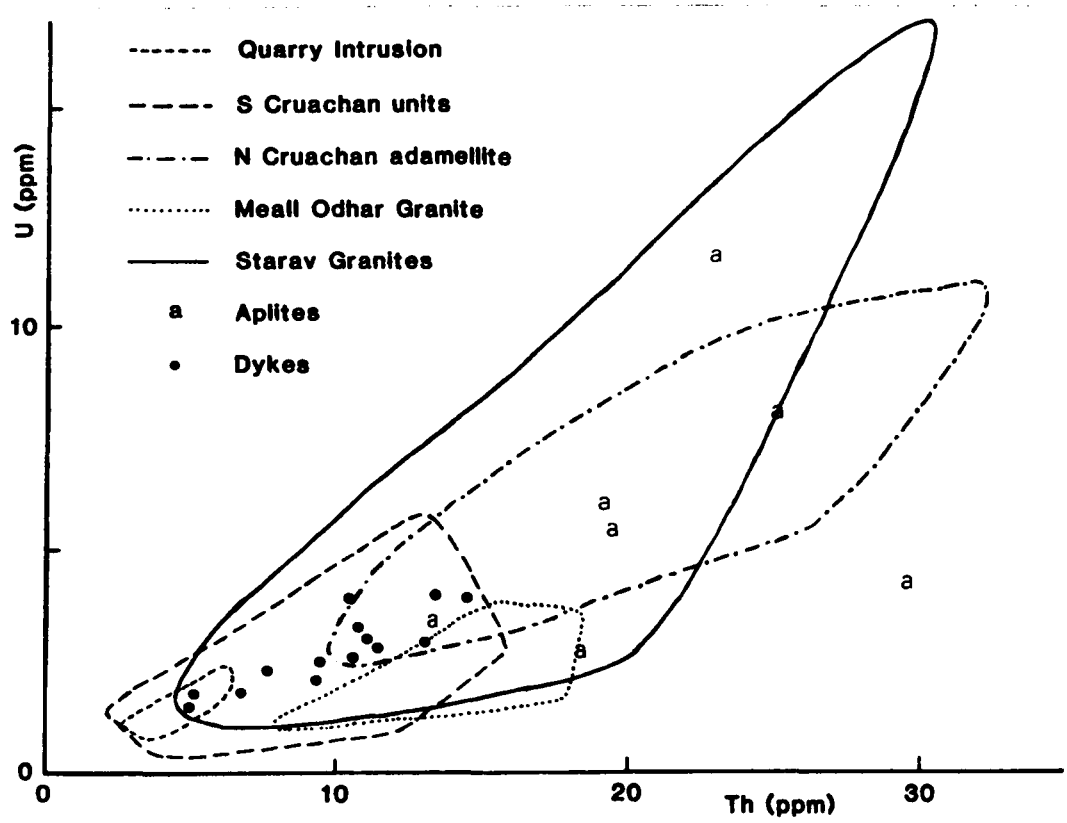

Figure 5.16 Summary of U and Th data for the Etive Complex. The higher limits for the U-Th fields of the N Cruachan and Starav units are defined by relatively few samples, generally from the centres of each intrusion.

probably reflect differentiation and/or post magmatic processes at the level of emplacement. All of the aplites measured are associated with the Starav Granites; two show a slight Th enrichment relative to the parent granites and most show minor U depletion. The relationship between U and Th in the Starav Granites is curvilinear, with a greater increase in U at high Th levels. Uranium contents above 9 ppm were observed at four locations, E131, E130, SB134 (microgranites) and SB23 (coarse grained), all from the Ben Starav area (see Appendix D for grid refs.). The cause of this U enrichment is discussed in Section 5.10. In general, both U and Th continue to be enriched with

differentiation in the Etive Complex.

5.10 MINERALOGY AND MASS BALANCE OF URANIUM AND THORIUM

A combination of Lexan fission track studies (Section 4.3) and electron microprobe analyses (Section 4.4) was used to locate and identify U and Th hosts in the Etive units. Mass balance calculations based on these results and selected whole-rock trace element data were used to quantify the U and Th 'budget' in each rock type. Samples for fission track investigation were selected on the basis of three criteria; spatial distribution within individual intrusions, petrological variations (particularly within the S Cruachan lobe) and range of U, Th and $^{Th}/_{U}$ contents.

5.10:1 The Quarry Intrusion

This intrusion is, volumetrically, of minor importance and was, therefore, studied in relatively little detail. Lexan studies of six samples (Table 5.5) show that U is located predominantly in primary sites. Most sources were too small for identification, but larger crystals revealed high density tracks to be associated with zircon, and low density tracks with apatite.

Sample No.	Rock type	Th (ppm)	U (ppm)	$^{Th}/_{U}$
YR1098	Diorite	6.3	2.0	3.2
YRY.66	Diorite	6.2	2.2	2.8
SB32	Qtz. diorite	6.1	2.0	3.1
YR780	Qtz. diorite	5.3	1.5	3.5
YR786	Qtz. diorite	4.2	1.6	2.6
SB4	Qtz. diorite	6.1	2.7	2.2

Table 5.5 Quarry Intrusion samples used for Lexan studies.

Sphene, yielding low density, evenly distributed tracks, occurs only in quartz-diorite samples.

A minor amount of U is present in all samples as 'background' dispersion in hornblende and biotite. This location is considered primary since no tendency was observed for track concentrations related to crystal boundaries, cleavage traces or alteration products.

Considering track distributions and the typical levels of U and Th in the observed accessory phases (see Table 2.3), it is probable that most U resides in zircon, and both zircon and sphene (when present) are major contributors to whole rock Th contents. Minor quantities of U and Th are held in apatite.

5.10:2 The Cruachan units

Lexan prints were prepared for twenty-two samples, representing the diversity of rock types encountered in these units (see Table 5.6). Results of fission track studies will be discussed in four groups (see Table 5.6): a) S Cruachan samples containing <3 ppm U, b) S Cruachan samples containing ≥3 ppm U, c) N Cruachan samples, d) samples affected by alteration adjacent to the Starav intrusions.

a) Uranium occurs in three primary sites in these samples;

i) Sphene, often present as inclusions in biotite and hornblende, or moulded on opaques, is less abundant in more basic rocks, i.e. diorites and monzodiorites. Typically, fission tracks associated with this mineral are of low density and evenly distributed over the crystal (Plate 5.1A). Higher density tracks are observed over some (Plate 5.1B and C) but these do not predominate in any section and do not correlate with whole rock U and Th contents.

ii) Zircons are conspicuous in all samples, yielding high density tracks (Plate 5.1A, B and C); they are only occasionally

	Sample No.	Rock Type	Th (ppm)	U (ppm)	Th/U	
Southern Cruachan lobe	N54	Dark grey diorite	5.6	1.2	4.7	(a)
	N236	Grey qtz. monzodiorite	6.1	1.4	4.3	
	N53	Grey qtz. monzodiorite	-	1.6	-	
	SB69	Grey qtz. monzodiorite	8.1	1.7	4.8	
	SB60	Grey qtz. monzodiorite	8.2	1.9	4.3	
	N238	Grey qtz. monzodiorite	8.5	1.8	4.7	
	SB9	Grey qtz. monzodiorite	8.6	2.3	3.8	
	SB44a	Pale grey granodiorite	9.1	2.1	4.3	
	N56	Pale grey granodiorite	8.8	2.4	3.3	
	SB73	Pale grey granodiorite	10.8	2.2	4.9	
	N57	Pale grey granodiorite	-	3.6	-	(b)
	SB3	Pale pink granodiorite	13.0	5.6	2.3	
	N55	Pink granodiorite	10.6	3.0	3.5	
	SB138	Foliated at Starav contact	6.9	2.1	3.3	(d)
	SB16	Altered at Starav contact	-	-	-	
	SB18	Altered at Starav contact	-	2.9	-	
Northern Cruachan lobe	E30	Adamellite	18.6	4.3	4.3	(c)
	SB14	Adamellite	-	-	-	
	SB124	Adamellite	18.4	5.0	3.7	
	SB65	Adamellite	19.0	5.3	3.6	
	SB96	Adamellite	21.0	4.6	4.6	
	SB64	Adamellite	25.2	6.4	3.9	

Table 5.6 Cruachan samples used for Lexan studies.

included in biotite and do not give rise to pleochroic halos. A few poorly radioactive zircons were observed, producing only medium density tracks.

iii) Apatite is a relatively abundant accessory mineral, frequently occurring as idiomorphic inclusions in biotite and hornblende. Very low density tracks are associated with apatite (Plate 5.1C) but these probably represent an important contribution to whole rock U (and possibly Th) contents (see Table 5.8).

Some low density, dispersed tracks are observed over biotite and hornblende (e.g. Plate 5.1C) but these are often associated with ubiquitous inclusions of apatite. No secondary U sites were found in these sections.

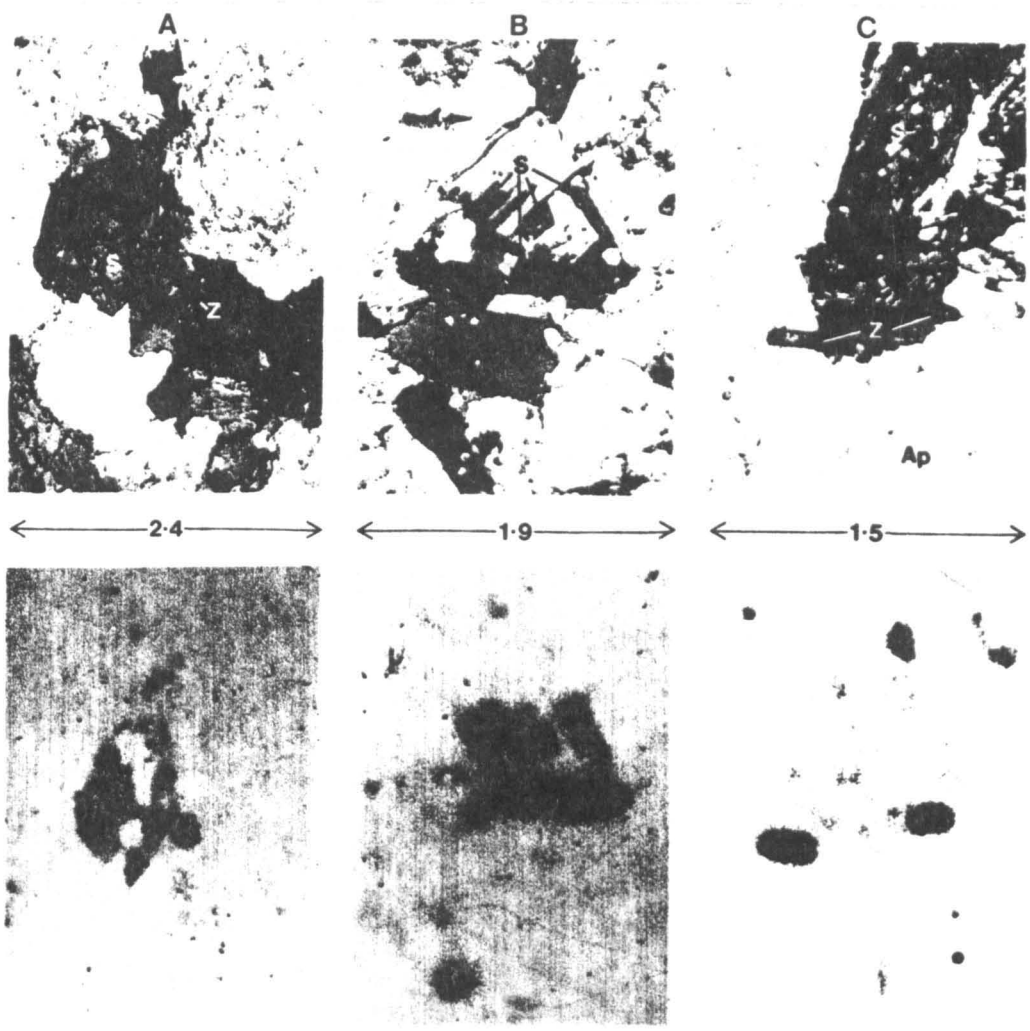

Plate 5.1 Photomicrograph and fission track pairs showing U locations in S. Cruachan samples. Fields of view are given in mm.

A. Sample SB44a. Low density, evenly distributed tracks are associated with sphene, S, included in hornblende. Zircon, Z, produces high density tracks.

B. Sample SB73. High density tracks are associated with sphene, S, in or near biotite. The high density track source in the lower left of the photomicrograph is probably zircon.

C. Sample SB9. High density tracks are associated with two large zircon crystals, Z, and one small sphene crystal, S, included in hornblende. Apatite, Ap, produces low density tracks. Very low levels of 'background' U are dispersed in hornblende and biotite.

b) These samples represent the more differentiated units of the S Cruachan lobe, although none are as coarse or felsic as the N Cruachan adamellite. Uranium is present in apatite and zircon as described for group (a), but sphene is more abundant and yields medium rather than low density tracks. Samples N57 and, particularly SB3 show higher levels of 'background' U in biotite than group (a) samples. Low density tracks are associated with hydrated Fe-oxides lining microfractures and fringing opaques, and with rims and cleavages of partially altered ferromagnesian minerals in sample SB3. These secondary U occurrances probably represent minor remobilisation by late stage hydrothermal fluids.

One, red metamict crystal of chevkinite (identified by microprobe analysis; Table 5.7) was found in sample SB3, the corresponding, high density tracks probably being due largely to Th fission. Two thorite crystals were identified in sample N55, yielding very high density tracks (Plate 5.2A).

c) Sphene is particularly abundant in N Cruachan samples, giving rise to low or medium density, evenly distributed tracks. In one sample, E30, high density tracks were observed over the rims of some sphene crystals. Uranium in zircon and apatite is present as described for group (a). One or two sources of very high density tracks were located in each sample, and positively identified as thorite in two samples (see Plate 5.2B). Some high density 'point' sources are located in feldspar, quartz and grain boundaries, possibly corresponding to submicroscopic thorites. A little U dispersion occurs in biotites, tending to concentrate along crystal boundaries but is sporadic, of very low density and does not represent a significant contribution to whole rock U contents (see Plate 5.2B).

Plate 5.2 Photomicrograph and fission track pairs showing U locations in various Cruachan samples. Fields of view are given in mm.

A. Sample N55. Variable density tracks are associated with sphene, S. Thorite, T, produces very high density tracks, extending to 2-3 times the crystal dimensions. Very low density tracks occur over biotite.

B. Sample SB64. High density tracks occur over a diffuse, yellow thorite crystal, T. Low to medium density tracks correspond to small sphene crystals, S, and very low density tracks are patchily dispersed along the rims of a brown biotite.

C. Sample SB18. Secondary U occurring in rutile pseudomorphing sphene. Track density increases with the degree of alteration. (The Lexan print is a little over-etched).

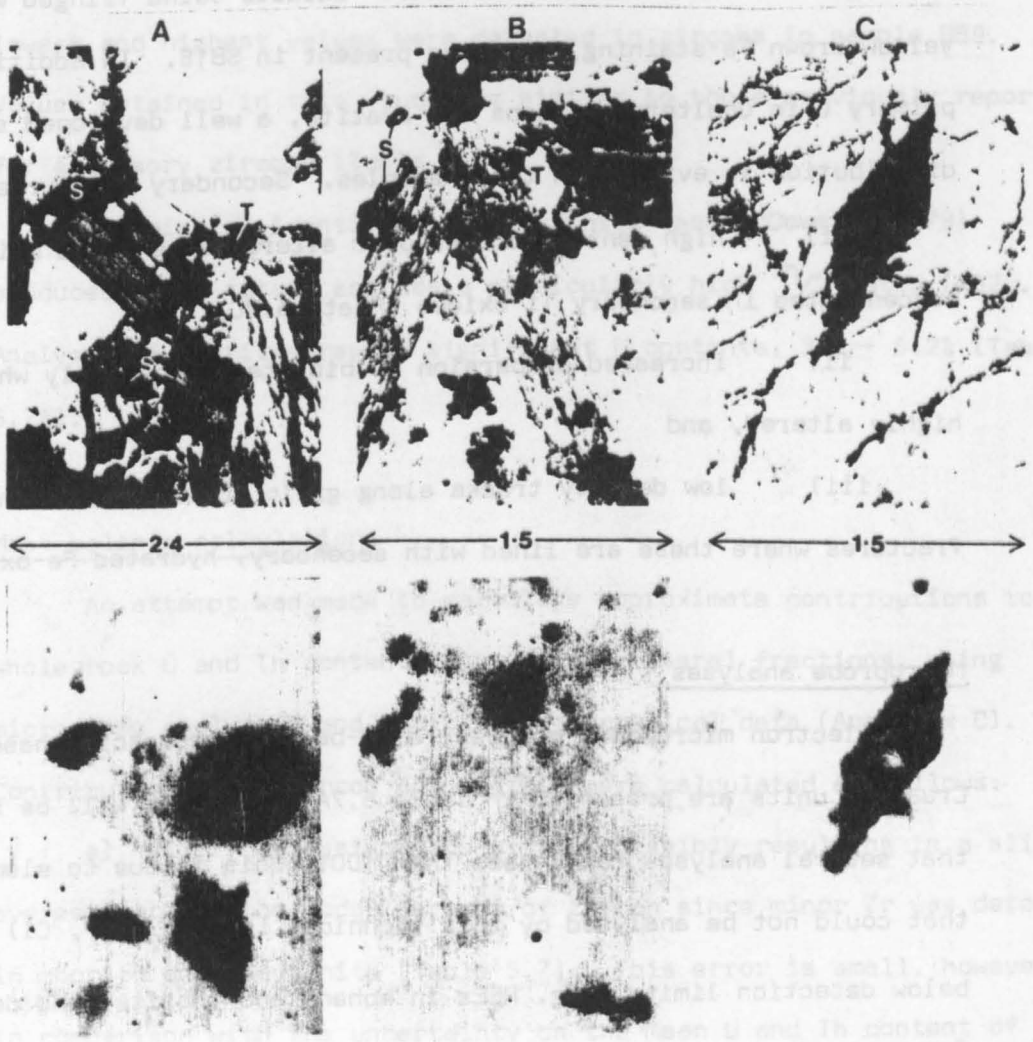

d) The development of a foliation, comprising rough bands of ferromagnesian and felsic minerals is the only apparent alteration in sample SB138. The U distribution is similar to that of group (a) but an increase in the degree of dispersion in ferromagnesian minerals was noted, probably due to the release of U from included accessories during alteration.

Pervasive hydrothermal alteration in samples SB18 and SB16 is probably associated with emplacement of the Starav Granites. In these samples biotites are altered to aggregates of chlorite, muscovite and opaques, and sphene is partially or completely pseudomorphed by secondary Ti-oxides (rutile/anatase). Calcite veins fringed with yellow-brown Fe-staining, are also present in SB16. In addition to primary U in unaltered zircons and apatite, a well developed secondary distribution is evident in these samples. Secondary U occurrences are;

i) high density tracks over altered sphenes, U being concentrated in secondary Ti-oxides (Plate 5.2C),

ii) increased dispersion in biotites, especially where highly altered, and

iii) low density tracks along grain boundaries and micro-fractures where these are lined with secondary, hydrated Fe-oxides.

Microprobe analyses

Electron microprobe analyses of U-bearing accessory phases in the Cruachan units are presented in Table 5.7A and B. It will be noted that several analyses total less than 100%; this is due to elements that could not be analysed by this technique (e.g. H_2O, F, Cl) or are below detection limits (e.g. REEs in sphene and thorite) and decay fragment damage in high U/Th minerals (e.g. thorite). Uranium and Th

contents of sphenes (Table 5.7A) are all below theoretical detection limits (see Table 4.13) but the higher values do correspond to sphenes associated with high rather than low density fission tracks. Analysed Th contents for sphene are within the range reported in the literature, but some U contents appear to be higher (see Table 2.3). Uranium contents of zircon (Table 5.7B) approach detection limits, and Th contents are generally too low for reliable analyses. High U (2.07%) and Th (2.26%) levels, found in one zircon, are accompanied by higher Hf_2O_3 and lower ZrO_2 contents (Table 5.7B); this is typical in high radioelement zircons (Vlasov, 1966). The range of U and Th contents in zircons is relatively large, and non-systematic; for example, the lowest and highest values were detected in zircons in sample SB9. Values obtained in this study are similar to those previously reported for accessory zircons (Table 2.3).

The mineral identified as chevkinite (see McDowell, 1979) produces a low total, and has a particularly high $^{Th}/U$ ratio ($\sim$82). Analyses of thorites reveal significant U contents, 3.9 - 5.2% (Table 5.7A).

Mass balance calculations

An attempt was made to calculate approximate contributions to whole rock U and Th contents for various mineral fractions, using microprobe analyses and whole rock geochemical data (Appendix C). Contributions from zircon and apatite were calculated as follows:

a) All Zr is assigned to zircon, possibly resulting in a slight overestimate of the modal percent of zircon since minor Zr was detected in thorite and chevkinite (Table 5.7). This error is small, however, in comparison with the uncertainty on the mean U and Th content of zircon. Two mean compositions were used for calculations, one

	Sphene						Thorite				Chevkinite
Sample No	SB69	SB44a	SB73	SB73	*SB14	*SB64	N55	N55	*SB65	*SB64	SB3
La_2O_3		(0.42)	(0.40)						1.81		10.65
Ce_2O_3	0.99	1.19	1.17	1.09	0.91	1.19	trace	0.29	1.97		17.68
Pr_2O_3											0.88
Nd_2O_3		0.34	0.69	0.57	0.64				0.58		3.82
Sm_2O_3											(0.33)
Tb_2O_3											(0.32)
Yb_2O_3											(0.24)
Nb_2O_5			(0.16)								
Y_2O_3			(0.21)								(0.18)
ZrO_2										4.55	0.79
P_2O_5							(0.37)	0.46			
ThO_2	(0.10)	(0.19)	(0.28)	(0.26)	(0.09)	(0.32)	77.15	71.89	58.56	69.37	2.46
UO_3	(0.19)	(0)	(0.31)	(0.30)	(0.02)	(0.36)	6.43	4.85	4.86	4.87	(0.03)
SiO_2	28.93	29.38	28.73	28.83	29.45	28.82	9.24	11.57	19.98	8.50	20.96
TiO_2	35.63	35.91	35.99	35.90	34.78	35.66					18.56
Al_2O_3	0.19	1.60	0.56	0.47	1.52	1.44	(0.36)		1.77	1.34	2.59
FeO	1.09	1.53	1.35	1.32	2.51	2.30	0.33	0.45	1.49	0.89	7.53
MnO		0.14	0.13	0.08							(0.18)
MgO								(0.89)		(0.76)	(0.69)
CaO	26.57	25.96	25.56	25.51	26.04	25.76	0.40	0.75	2.01	2.52	5.52
PbO							(0.64)				
Cl							(0.10)	0.14			
TOTAL	93.69	96.68	95.54	94.33	95.96	95.79	95.02	91.29	93.03	92.80	93.39

Table 5.7A Electron microprobe analyses of U-bearing accessory phases in the Cruachan units. All data are in wt. %. Values in brackets indicate concentrations < 2σ error on background (see Section 4.4).

*indicates N Cruachan samples.

	Zircon						
Sample No	SB9	SB9	SB44a	SB73	N55	SB3	*SB14
Yb_2O_3		0.27					
Hf_2O_3	1.11	2.09	1.19	1.19	1.45	1.24	1.36
Nb_2O_5			0.85	(0.79)		(0.30)	
Y_2O_3		(0.55)		(0.43)			
ZrO_2	63.46	47.41	58.47	61.90	66.45	62.84	65.35
P_2O_5			2.69				
ThO_2	(0)	2.73	(0.01)	(0.10)	(0.20)	(0)	(0.02)
UO_3	(0.05)	2.55	(0.24)	(0.09)	(0.12)	(0.15)	0.41
SiO_2	34.52	31.68	31.96	34.53	32.42	34.54	32.86
Al_2O_3	0.63	1.44	0.89	0.94		1.13	
FeO		2.24	0.42	0.37	0.41	0.34	0.30
MnO		(0.09)					
CaO	(0.07)	1.61	2.89				
TOTAL	99.84	93.47	99.61	100.34	101.05	100.54	100.30

Table 5.7B See caption to Table 5.7A.

including, and one omitting the high U/Th zircon;

i) ZrO_2 = 60.85 ± 6.4% U = 0.42 ± 0.7% Th = 0.36 ± 0.8%

ii) ZrO_2 = 63.08 ± 2.8% U = 0.15 ± 0.11% Th = 0.05 ± 0.07%

Standard deviations of ≥100% on the mean U and Th contents will introduce equivalent errors into mass balance claculations.

b) All P_2O_5 is assigned to apatite; overestimates of modal percent arise from P_2O_5 in thorite and zircon (see Table 5.7). In the absence of microprobe analyses for apatite (U and Th contents are well below detection limits) a mean composition of 41% P_2O_5 (Deer et al., 1972), 50 ppm U and 50 ppm Th was used. Although higher radioelement concentrations have been recorded in apatites (see Table 2.3), the very low density fission tracks associated with this phase in the Cruachan units suggests a low U (and probably Th since $^{Th}/_{U} \simeq 1$ for apatite, Table 2.3) content.

Uranium contributions from zircon (Table 5.8) based on mean analysis (i) above frequently exceed whole rock values for S Cruachan samples suggesting that U rich zircons are rare. Calculations based on composition (ii) above also approach or exceed whole rock U values for samples with high Zr content (see Appendix C). It would seem, therefore, that during crystallisation the availability of U(and Th) in the magma determines, to some extent, the radioelement content of zircons. For N Cruachan samples, U contributions from zircon based on either composition are feasible (Table 5.8). A more detailed investigation of zircon compositions would be required to resolve this ambiguity.

For most S Cruachan samples Lexan studies suggest that all remaining U (Table 5.8) is located in sphene (with minor dispersion in ferromagnesian minerals). However, remaining $^{Th}/U$ ratios (Table 5.8) are higher than those of sphene analysed from these rocks (1.5 ± 1.6, Table 5.7) and by other authors (1-3, Table 2.3). Hence, if the mass balance of U is satisfied by sphene, a surfeit of Th remains. Although this anomaly may partially be accounted for by analytical errors, non-representative analyses, or an incorrectly assumed Th content for apatite, the high 'remaining' $^{Th}/U$ ratios obtained still require an alternative site for excess Th. Sporadically distributed, and hence often undetected, high $^{Th}/U$ phases such as thorite, chevkinite (see Table 5.7) and allanite (see Section 5.2:2) would be suitable hosts.

Thorite has been positively identified in sample N55 (S Cruachan) and in the N Cruachan adamellite. It is possible to estimate U and Th contributions from sphene and thorite in these samples by making the following assumptions.

a) A $^{Th}/U$ ratio of approximately 1.5 for sphene is representative

b) The mean composition of thorite is 57.3 ± 6.5% Th, 4.2 ± 0.6%

	Sample No.	Whole rock contents (ppm) Th	U	Contribution from zircon Th (ppm) (i)	(ii)	U (ppm) (i)	(ii)	Contribution form apatite (ppm) Th	U	Remainder to be accounted for (ppm) Th	U	Th/U	Other U/Th sources identified by Lexan and microprobe studies
S Cruachan units	N54	5.6	1.2	1.0	0.1	1.2	0.4	0.5	0.5	5.0	0.3	16.7	Minor sphene
	N236	6.1	1.4	4.8	0.6	5.3	1.7	0.4	0.4	5.1	-0.7	-	Minor sphene
	SB115	6.4	1.6	5.0	0.7	5.6	1.9	0.3	0.3	5.4	-0.6	-	n.d.
	E8	5.3	1.9	4.3	0.6	4.8	1.6	0.3	0.3	4.4	0	-	n.d.
	N238	8.5	1.8	1.0	0.1	1.1	0.4	0.9	0.9	7.5	0.5	15.0	Sphene
	SB9	8.6	2.3	1.2	0.2	1.4	0.5	0.5	0.5	7.9	1.3	6.1	Sphene
	N56	8.8	2.4	1.5	0.2	1.6	0.6	0.3	0.3	8.3	1.5	5.5	Sphene
	SB91	10.7	1.2	4.4	0.6	4.9	1.6	0.2	0.2	9.9	-0.6	-	n.d.
	SB73	10.8	2.2	3.7	0.5	4.2	1.4	0.4	0.4	9.9	0.4	24.7	Sphene
	N55	10.6	3.0	1.5	0.2	1.7	0.6	0.2	0.2	10.2	2.2	4.6	Sphene + thorite
	SB138	6.9	2.1	1.5	0.2	1.7	0.6	0.2	0.2	6.5	1.3	5.0	Sphene + dispersion in biotite and hornblende
N Cruachan unit	SB99	15.7	3.4	1.6	0.2	1.7	0.6	0.2	0.2	15.3	2.6	5.9	n.d.
	E30	18.6	4.3	1.6	0.2	1.8	0.6	0.1	0.1	18.3	3.6	5.1	Sphene + thorite
	SB124	18.4	5.0	1.5	0.2	1.7	0.6	0.2	0.2	18.0	4.2	4.3	+ some minor dispersion
	SB96	21.0	4.6	1.4	0.2	1.6	0.5	0.2	0.2	20.6	3.9	5.3	in biotite
	SB97	31.7	10.6	1.0	0.1	1.1	0.4	-	-	31.6	10.2	3.1	n.d.

Table 5.8 Results of mass balance calculations for Cruachan samples showing the contribution to whole rock U and Th from zircon and apatite. The two calculations for zircon refer to compositions (i) and (ii), see text. The remaining radioelement levels are calculated using results for zircon composition (ii).

(from Table 5.7). $^{Th}/U = 13.3 \pm 5$.

c) No U or Th is located in secondary sites or disseminated in major phases. (From Lexan studies it is clear that minor quantities of U reside in these sites.

d) Calculations for zircon and apatite are correct.

The procedure employed in making these estimates is outlined in Appendix E; results are presented in Table 5.9. The calculated volume density of thorite crystals is in approximate agreement with the observed frequency of 1-2 crystals per thin section. The low TiO_2 content of sample SB97 (from the centre of the N Cruachan lobe) suggests that the calculated U and Th contributions from sphene in this sample are far too high. It is probable that a significant percentage of whole rock U in this sample is held in secondary sites (see for comparison, Central Starav samples, Section 5.10:5) and more Th is located in thorite.

Sample No.	Contribution from sphene		Contribution from thorite		No. thorite crystals required per cm^3
	Th(ppm)	U(ppm)	Th(ppm)	U(ppm)	
N55	2.4	1.6	7.8	0.6	0.9
SB99	2.5	1.7	12.8	0.9	1.5
E30	3.7	2.5	14.6	1.1	1.8
SB124	4.9	3.3	13.1	1.0	1.6
SB96	4.0	2.7	16.7	1.2	2.0
SB97	13.3?	8.9?	18.3?	1.3?	2.2?

Table 5.9 Estimated contributions to whole rock U and Th from sphene and thorite in N Cruachan samples (+N55).

Summary

The errors involved in calculating the U and Th contributions from zircon, apatite and sphene, allow only a semi-quantitative assessment of the importance of these minerals (with respect to whole-rock radioelement contents) in S Cruachan samples. It is clear from Lexan studies that most U is held in these phases; 20-100% in

zircon, 11-50% in apatite, the rest in sphene (from Table 5.8). Contributions from 'background' U in ferromagnesian minerals and secondary distributions is minor, except where U remobilization has occurred, associated with intrusion of the Starav units.

Table 5.10 summarises the distribution of U and Th between observed accessory phases in the N Cruachan adamellite, and its southern equivalent. Zircon and apatite are of less importance than in earlier units, but ubiquitous sphene is a significant host for both U and Th and thorite contributes over 70% of whole rock Th. Uranium attributed to sphene and thorite in Tables 5.9 and 5.10 probably represents an overestimate, since minor quantities of U occur as secondary distributions in biotite.

Sample No.	Zircon		Apatite		Sphene		Thorite	
	Th	U	Th	U	Th	U	Th	U
N55	1.7	18.6	2.2	8.0	22.5	53.3	73.6	20.0
SB99	1.2	17.1	1.3	5.9	15.9	50.0	81.5	26.5
E30	1.1	13.7	0.7	3.0	19.9	58.1	78.5	25.6
SB124	1.1	11.4	0.9	3.4	26.6	66.0	71.2	20.0
SB96	0.9	11.3	0.8	3.7	19.0	58.7	79.5	26.1
SB97	0.4	3.4	-	-	?	?	?	?

Table 5.10 Approximate percentage contributions to whole rock U and Th from accessory phases in the N Cruachan adamellite and its southern equivalent.

5.10:3 The Meall Odhar Granite

Fission track studies of six samples from the Meall Odhar Granite show that the distribution of U in this unit is similar to that in the N Cruachan adamellite but the abundance of host phases differs. Both apatite and sphene are considerably less frequent; only one or two sphenes occur in each thin section. Zircon occurs in association with

Sample No.	Th(ppm)	U(ppm)	$^{Th}/_{U}$
SB10	16.7	2.5	6.7
SB76	8.2	1.1	7.5
SB121	18.1	3.3	5.5
SB12	6.5	1.0	6.5
SB61	13.1	2.6	5.0
SB59	15.3	3.5	4.4

Table 5.11 Meall Odhar samples used for Lexan studies.

clusters of opaques, occasionally as visible inclusions in the few biotites present, or in quartz and feldspar. Fission tracks associated with zircons are of variable density, tending to be of lower density over zircons included in biotite. Thorite was positively identified in samples SB59 and SB121 yielding very high density tracks and causing brown discolouration of the Lexan. Smaller inclusions in quartz and feldspar give rise to similarly high density tracks in all other samples, and high density 'point' concentrations of tracks along grain boundaries are possibly due to submicroscopic thorites. Some minor dispersion of U was observed in a few small biotites.

Microprobe analyses

Analyses of sphene and zircon from the Meall Odhar Granite (Table 5.12) reveal similar compositions and ranges of U and Th content to those in the Cruachan units. Only one thorite was successfully probed (Table 5.12); its $^{Th}/_{U}$ ratio is considerably higher than thorite in the N Cruachan adamellite, reflecting the whole rock $^{Th}/_{U}$ ratio of the Meall Odhar Granite.

Mass balance calculations

Table 5.13 presents the results of mass balance calculations using

	Sphene		Zircon					Thorite
Sample No	SB10	SB121	SB121	SB59	SB10	SB10	SB10	SB59
La_2O_3	0.69	0.23			(0.09)			
Ce_2O_3	1.33	1.62						0.48
Nd_2O_3	0.51							0.37
Gd_2O_3	1.14							
Dy_2O_3	(0.07)							
Yb_2O_3	(0.12)			0.26				
Hf_2O_3	1.48	1.37	3.74	1.25	1.49			
Nb_2O_5	0.58				0.81			
Y_2O_3	0.53				0.28			
ZrO_2			62.13	63.48	51.51	65.51	59.99	
P_2O_5								0.93
ThO_2	(0.19)	(0.15)	(0.10)	(0)	(0.04)	(0.05)	(0.11)	75.57
UO_3	(0.31)	(0.22)	(0.02)	(0)	(0.59)	(0.19)	(0.13)	1.29
SiO_2	28.67	29.53	33.35	34.72	36.52	32.87	36.19	11.10
TiO_2	33.98	33.59						(0.12)
Al_2O_3	0.72	1.01		0.70	3.60			0.75
FeO	2.36	2.77	1.45	0.37	1.58	0.32	0.12	1.63
MnO	0.32	0.36						
CaO	25.52	25.57	0.47		0.19		0.19	0.19
K_2O					0.14			0.36
S								0.19
TOTAL	95.71	95.05	99.00	100.64	99.28	100.19	98.22	94.38

Table 5.12 Electron microprobe analyses of U-bearing accessory phases in the Meall Odhar Granite. All data are in wt. %. Values in brackets indicate concentrations < 2σ error on background (see Section 4.4).

whole rock trace element data (Appendix C), mean mineral compositions from Table 5.12 and the procedure outlined in Section 5.10:2 and Appendix E. The absolute contributions of U and Th from zircon and particularly apatite, are lower than for Cruachan samples due to a decrease in the modal percent of these minerals in the Meall Odhar Granite. On the basis of fission track densities and the observed low abundances of sphene in the Meall Odhar Granite, values calculated for this mineral in Table 5.13 would seem too high (cf. Cruachan samples, Table 5.9, where sphene is abundant). This anomaly may be accounted for by poor radioelement analyses of sphene, the presence of thorites with lower $^{Th}/U$ ratios than the sample

		SB10	SB76	SB121	SB108
Zircon	Th (ppm)	0.17	0.13	0.13	0.16
	U (ppm)	0.50	0.38	0.39	0.50
Apatite	Th (ppm)	0.04	0.07	0.04	0.06
	U (ppm)	0.04	0.07	0.04	0.06
Sphene	Th (ppm)	1.1	0.3	1.7	1.1
	U (ppm)	1.7	0.5	2.6	1.8
Thorite	Th (ppm)	15.4	7.7	16.2	14.1
	U (ppm)	0.3	0.2	0.3	0.2
No thorite crystals required per cm^3		1.7	0.9	1.8	1.6

Table 5.13 Calculated contributions to whole rock U and Th from accessory phases in the Meall Odhar Granite.

probed and the location of minor U in biotites.

The combination of Lexan studies, microprobe analyses and whole rock geochemical data reveal that approximately 90% of whole rock Th in the Meall Odhar Granite is held in thorite, and most whole rock U resides in primary accessory minerals.

5.10:4 The Outer Starav Granite

Fission track studies of fourteen samples from the Outer Starav Granite (Table 5.14) show that U occurs predominantly in primary locations in this unit. However, some secondary sites were noted in several sections, and low density dispersion in biotites may represent minor remobilization of U (see below). Uranium locations are described

Sample No.	ppm Th	ppm U	$Th_{/U}$
SB11	4.8	1.7	2.8
SB15	-	-	-
SB137	7.8	2.4	3.3
SB131	7.5	3.0	2.5
SB125	9.3	2.7	3.4
SB94	9.8	2.6	3.8
SB130	10.3	2.6	4.0
N241	10.9	2.6	4.2
E16C	10.7	2.1	5.1
N239	10.9	2.0	5.5
N59	10.6	1.5	7.1
N240	11.8	4.2	2.8
SB1	11.4	3.0	3.8
SB19	-	3.2	-

Table 5.14 Outer Starav samples used for Lexan studies

in points (a) to (g) below.

a) Apatite is less abundant than in Cruachan units, and yields very low density tracks.

b) Sphene is the most abundant U host in all samples except N241 which is also exceptional in its poorly porphyritic texture, and generally low content of ferromagnesian minerals and opaques. Two types of sphene are distinguished, possibly representing two generations:

i) Larger, well-formed sphenes yielding low to medium density tracks over the bulk of the crystal, but with partial or complete rims of high density tracks (Plate 5.3A and B). This zoning may be due to compositional changes in the magma during a two stage crystallisation history; i.e. the outer rims crystallised later from a magma richer in radioactive elements. Microprobe data for the larger sphene in Plate 5.3B reveal an increase of both U and Th in the rim (Table 5.15A).

ii) Smaller crystals yield high density tracks similar to

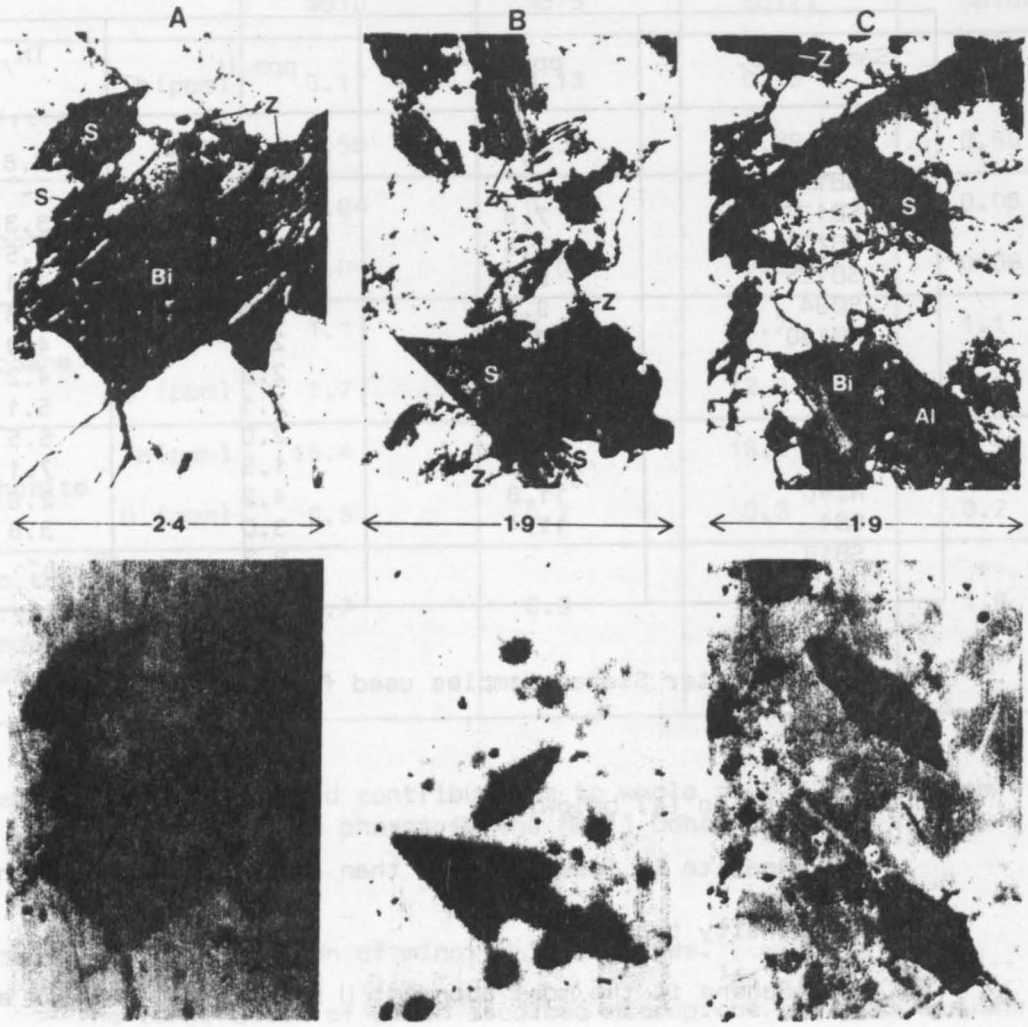

Plate 5.3 Photomicrograph and fission track pairs showing U locations in the Outer Starav Granite. Fields of view are given in mm.

A, Sample SB125; B, Sample E16c; C, Sample SB130.

Larger sphenes, S, show U zonation, with low-medium density tracks over crystal cores and high density tracks over rims. Smaller sphenes in A and B produce uniformly high density tracks. High density tracks are associated with zircons, Z. Allanite, Al, in C shows a complex zonation of U, with high-medium-high density tracks over core-outer zones-rim respectively, suggesting leaching of U from outer zones of the crystal, which migrates towards rims and along anastomosing cracks radiating from the allanite. Secondary U is evident in all three samples. Low density, unevenly distributed tracks over partially chloritised biotites, Bi, are often associated with the development of secondary opaques along rims and cleavage traces. Tracks also occur along grain boundaries and micro-fractures, especially in C.

those observed over the rims of type (i) (Plate 5.3A and B). Crystallisation of these smaller sphenes, may have been contemporaneous with the enriched outer rims of the larger grains.

c) Zircons occur as inclusions in biotites and associated with clusters of opaques and ferromagnesian minerals. Although less abundant than sphene, they always yield high density tracks (Plate 5.3A, B and C).

d) Allanite was located in 2 samples, N59, and SB130; two dark brownish-red metamict grains were found in each section. In N59, both give rise to evenly distributed low-medium density tracks, but those in SB130 show a distinct zonation of radioelements and are associated with secondary U distributions in adjacent biotites and grain boundaries (Plate 5.3C). Remobilisation of U is suggested by the presence of fission tracks in anastomosing cracks radiating from the allanite crystal. Microprobe analysis (Table 5.15C) shows the core of this allanite to be poorer in Th and richer in U than the outer zones, i.e. U has probably been leached from the outer zones.

e) A few small thorite crystals were identified in samples SB125 and SB130, associated with clusters of opaques or biotite and yielding extremely high density tracks. An opaque, thorite-like mineral occurring interstitially between quartz and K-feldspar was found in sample N241 (see Table 5.15).

f) Low density, unevenly dispersed tracks occur over several biotites, many of which are partially chloritised and show incipient development of secondary opaques along rims and cleavage traces. Tracks tend to be concentrated over these alteration products (see Plates 5.3A and C), implying a secondary U distribution.

g) Grain boundaries and microfractures; low density tracks occur locally, associated with primary sources or altered biotites, and are

	Sphene								Fe-Ti-Nb
Sample	N59	N59	E16C(i)		SB130	SB130	SB125	SB125	silicate
number	(i)	(i)	core	rim	(ii)	(i)	(ii)	(ii)	N240
Ce_2O_3	0.63	1.27	1.55	0.95	0.83	(0.25)	1.43	0.70	0.97
Nd_2O_3				(0.21)	0.48				
Nb_2O_5									9.95
ThO_2	(0.34)	(0.05)	(0.05)	(0.21)	(0.29)	(0.05)	(0.33)	(0.31)	(0)
UO_3	(0)	(0)	(0)	(0.16)	(0.25)	(0)	(0.37)	(0.35)	(5.99)
SiO_2	42.92	29.70	29.21	29.34	29.52	30.01	29.09	30.06	13.06
TiO_2	28.53	35.76	36.42	36.92	35.89	37.43	35.74	35.14	15.00
Al_2O_3				0.53	0.95	1.37	0.42	0.62	6.82
FeO	1.53	1.60	1.61	2.01	1.70	1.99	1.52	2.13	23.94
MnO	0.20					0.18		0.18	
MgO									2.50
CaO	22.19	26.45	26.98	26.23	26.27	26.37	26.44	27.47	0.66
K_2O	0.12	0.22	0.18	0.50					0.19
PbO									2.91
TOTAL	96.46	95.05	96.00	97.06	96.18	97.65	95.34	96.96	83.97

	Zircon								Apatite
Sample No	N59	E16C	E16C	E16C	SB130	SB130	N241	SB125	SB130
Yb_2O_3						(0.15)			
Hf_2O_3	3.30	1.37	1.29	1.29	1.65	1.10	1.25	1.53	
Nb_2O_5		(0.41)							
Y_2O_3						(0.30)			
ZrO_2	59.66	61.85	65.02	65.57	63.79	63.73	64.81	64.01	
P_2O_5									40.85
ThO_2	(0)	(0)	(0)	(0.01)	(0)	(0)	(0)	(0.16)	(0)
UO_3	1.01	(0.16)	(0.05)	(0.14)	(0.12)	(0.01)	(0.08)	(0)	(0.08)
SiO_2	32.06	34.31	33.46	33.32	34.83	34.30	33.71	34.54	0.53
Al_2O_3	1.75	1.11							
FeO	0.17	0.45	0.34	0.42	0.25	0.37	0.20	0.26	0.18
CaO	0.51						(0.02)		52.64
K_2O	0.36								
TOTAL	98.82	99.25	100.16	100.75	100.64	99.96	100.07	100.50	94.28

Table 5.15A (above) and B (below) Electron microprobe analyses of U-bearing accessory phases in the Outer Starav Granite. All data are in wt. %. Values in brackets indicate concentrations < 2σ error or background (see Section 4.4). Analyses for sphenes refer to types (i) and (ii) described in the text.

	Allanite				Thorite			Thorogummite	
Sample number	N59	N59	SB130 rim	SB130 core	SB130	SB125	SB125	N241 core	N241 rim
La_2O_3	3.48	8.14	10.52	9.46				1.10	
Ce_2O_3	8.94	9.91	10.52	10.75			0.57	6.84	5.99
Pr_2O_3	0.75	(0.40)	0.59	0.67					
Nd_2O_3	1.91	0.95	1.01	0.99					
Sm_2O_3	0.41								
ZrO_2					(0.50)				
P_2O_5					3.47			2.05	2.33
ThO_2	1.13	1.40	1.05	0.83	61.16	58.44	61.16	51.41	49.05
UO_3	(0)	(0.24)	(0)	(0.21)	1.74	11.39	8.97	4.62	5.53
SiO_2	28.94	31.66	31.85	30.94	11.52	19.18	19.12	14.10	12.50
TiO_2		1.01	1.34	1.97	0.48				
Al_2O_3	10.15	9.68	13.66	14.82	3.92		(0.42)		
FeO	14.83	14.46	12.51	13.97	3.89	0.90	1.15	1.99	1.65
MnO	0.48	0.87	1.02	0.53					
CaO	10.59	11.61	10.51	8.98	0.68	3.94	2.61	0.30	0.35
PbO						(1.15)	1.28		
Cl	0.16	(0.07)	0.19	0.13	0.59		(0.08)		
S			trace	trace					
Mo					0.7				
V					0.2				
TOTAL	81.77	90.40	94.77	94.25	88.92	95.00	95.36	83.32	78.34

Table 5.15C See caption to Table 5.15A.

generally related to Fe-staining. Remobilisation of U from primary sources by late stage hydrothermal fluids, and/or weathering processes is suggested.

One additional source of U, found only in sample N240 is a semi-opaque Fe-Ti-Nb-silicate (see Table 5.15), occurring as inclusions in biotite and yielding very high density tracks. Sample N240 has the highest U content recorded for this unit and exhibits a well developed secondary distribution.

Microprobe analyses

Electron microprobe analyses of accessory phases in the Outer Staray Granite are presented in Table 5.15A, B and C. Although radioelement contents of sphene are below theoretical detection limits

there is a detectable increase of both U and Th in small, second generation crystals. Allanites produce low totals, probably due to metamictisation and incorporation of water. Uranium contents of thorites are highly variable, probably due to leaching and remobilisation of primary U. The opaque, thorite-like mineral in sample N241, has a lower Th content, and higher levels of REEs, particularly Ce; in this respect it may be termed a thorogummite (Frondel, 1958). Appreciable amounts of U and Th are held in the unidentified Fe-Ti-Nb-silicate mineral found in sample N240.

Mass balance calculations

Uranium and Th contributions from zircon and apatite were calculated as described in Section 5.10:2, using the relevant whole rock geochemical data (Appendix C) and mean compositions from Table 5.15B. Results are presented in Table 5.16. Any attempt to quantify the amounts of U and Th held in sphene, allanite and thorite was considered futile in view of their variable radioelement contents, the sporadic distribution of thorite and allanite, and the obvious location of significant quantities of U in secondary sites.

The $^{Th}/U$ ratio of the 'remainder' (Table 5.16) is higher than that of sphene (see Table 2.3), and would be increased if secondary U is subtracted. This suggests that minor phases such as allanite and thorite, with high $^{Th}/U$ ratios may be important hosts for Th.

5.10:5 The Central Starav Granite

Details of samples used for fission track studies are presented in Table 5.17. Samples SB135 to SB23 in Table 5.17 have similar U distributions. A preliminary, low magnification investigation of the

Sample No.	Zircon		Apatite		Remainder		Th/U	Other U/Th sources identified by Lexan and microprobe studies
	Th(ppm)	U(ppm)	Th(ppm)	U(ppm)	Th(ppm)	U(ppm)		
SB130	0.06	0.5	0.2	0.2	10.0	1.9	5.3	Sphene, allanite, thorite
SB131	0.05	0.5	0.2	0.2	7.2	2.3	3.1	Sphene
SB1	0.06	0.6	0.3	0.3	11.1	2.1	5.3	Sphene
N239	0.06	0.6	0.2	0.2	10.8	1.3	8.3	Sphene
N241	0.04	0.4	0.1	0.1	10.8	2.1	5.1	Sphene, thorite
N240	0.04	0.4	0.2	0.2	11.6	3.7	3.1	Sphene, Fe-Ti-Nb-silicate

Table 5.16 Results of mass balance calculations for Outer Starav samples. In addition to accessory phases, some U is located in secondary sites in all samples.

Sample No.	Granite type	Th(ppm)	U(ppm)	Th/U
SB135	Coarse grained	16.3	6.1	2.7
SB133	Coarse grained	17.9	6.3	2.8
SB22	Coarse grained	-	6.7	-
N58	Coarse grained	15.2	7.3	2.2
SB20	Coarse grained	17.2	7.1	2.4
SB21D	Coarse grained	21.3	6.2	3.4
SB21B	Medium grained	-	7.1	-
SB21C	Coarse grained	22.5	8.0	2.8
SB23	Coarse grained	19.5	10.7	1.8
SB179	Coarse grained from *central 'low'	10.5	1.6	6.6
SB134	Microgranite	24.1	9.8	2.6
SB186	Microgranite	30.2	16.8	1.8

Table 5.17 Central Starav samples used for Lexan studies.
*refer to Figures 5.12 and 13.

Lexan prints reveals a track distribution dominated by clusters of high density sources (see for e.g. Plate 5.4C). A small but significant number of these sources produce discolouration of the plastic. Solitary sources also occur but are subordinate to clusters. The clusters correspond to;

a) primary accessory minerals associated with opaques, and

b) primary accessory minerals included in or associated with biotite. A feature which distinguishes biotites in the Central Starav granite from those in earlier units of the Etive Complex is the number and generally submicroscopic size of uraniferous inclusions.

The most abundant U-bearing accessory mineral is zircon, yielding high density tracks (Plate 5.4A). Monazite is less frequent but yields similar density tracks. Thorite, of approximately the same abundance as monazite, gives rise to very high density tracks (Plate 5.4B).

Uranium dispersion associated with primary clusters is related to partially altered biotites, and tracks tend to be concentrated over rims and cleavage traces. The development of secondary opaques enhances such U accumulation, but track densities are always low. Secondary U is also present in some biotites devoid of inclusions or associated accessories suggesting that late stage U remobilisation was a pervasive, rather than just a 'local' process.

Tracks are also associated with alteration fringes of some primary opaques. This appears to be restricted to opaques exhibiting magnetite-ilmenite exsolution textures and one or two pyrite crystals (see Plate 5.5A). Track densities vary from low to high depending on the degree of alteration. Such reactions in Fe-Ti-oxides and Fe-sulphides are indicative of an increase in oxygen fugacity subsequent to the magmatic stage of crystallisation (see Rumble, 1977). Mobile U^{6+}

Plate 5.4 Photomicrograph and fission track pairs showing U locations in the Central Starav Granite. Fields of view are given in mm.

A. Sample SB133. High density tracks associated with zircon, Z.

B. Sample SB133. Very high density tracks associated with thorite, T.

C. Sample SB23. Clusters of high density fission track sources associated with opaques, and included in biotite. Low density tracks occur over grain boundaries and microfractures, and sericitised centres of feldspars (lower right of photomicrograph).

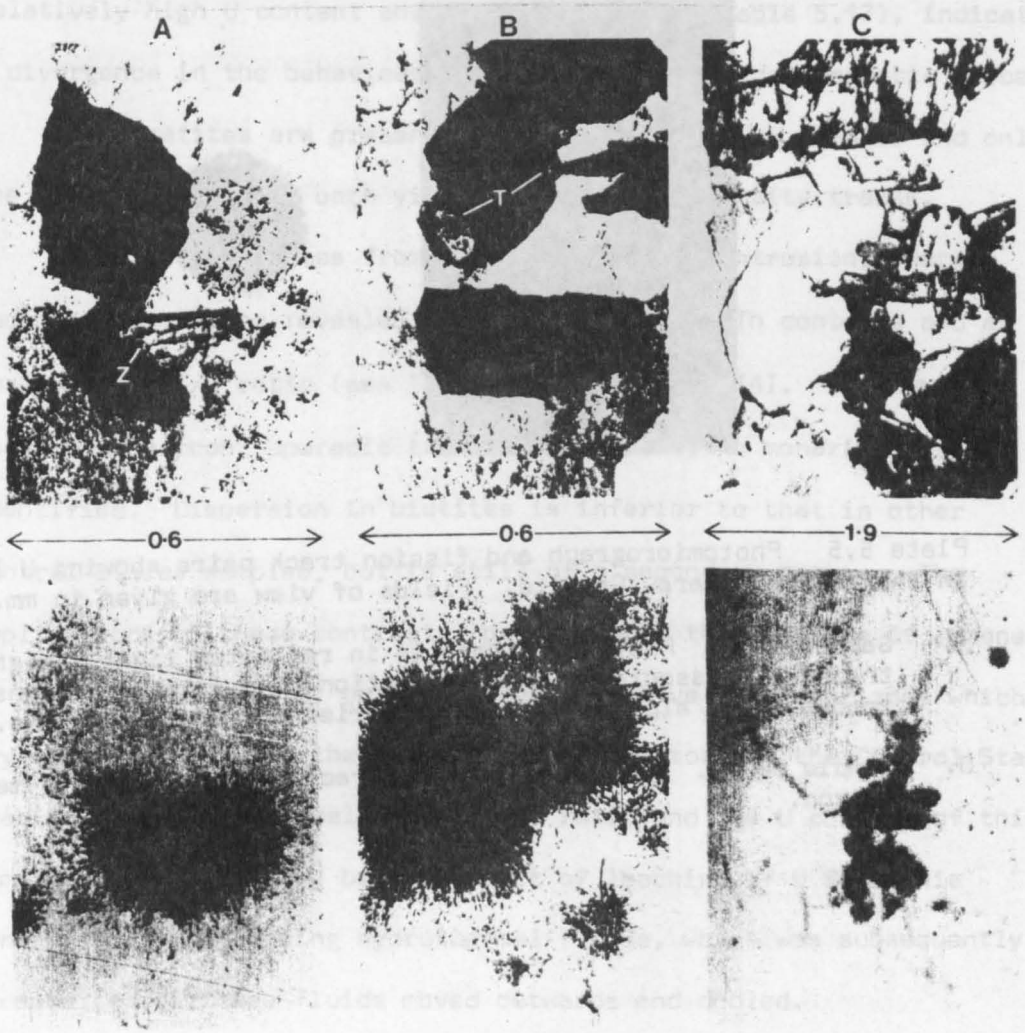

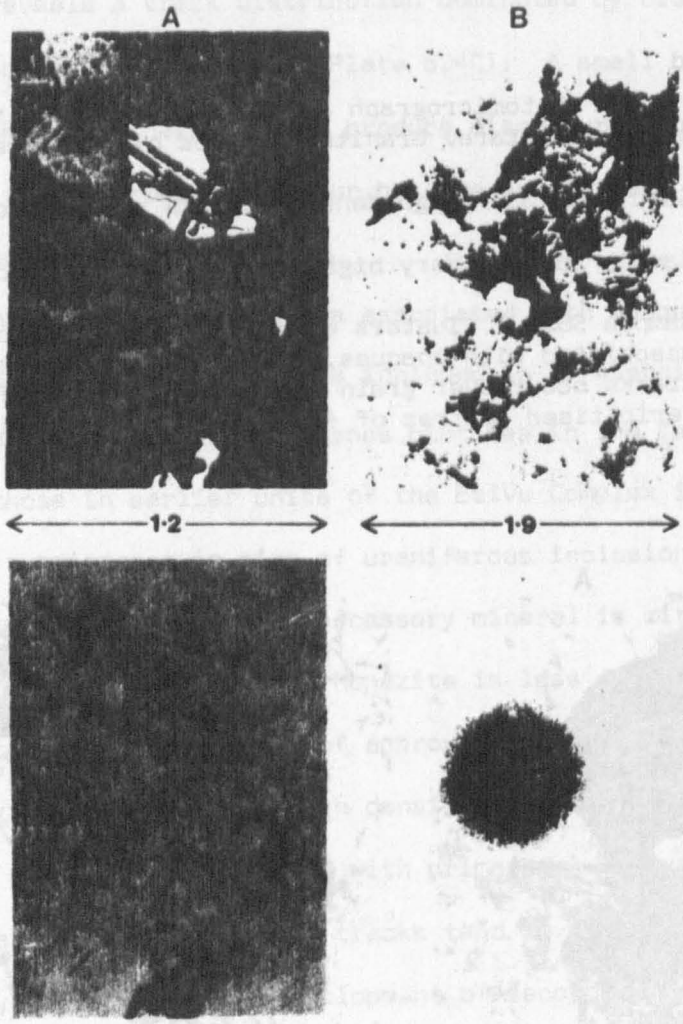

Plate 5.5 Photomicrograph and fission track pairs showing U locations in the Central Starav Granite. Fields of view are given in mm.

A. Sample SB22. Photomicrograph is in reflected light. High density tracks are associated with alteration of pyrite. Low density tracks occur along adjacent boundaries and microfractures.

B. Sample SB134. Very high density tracks associated with metamict zircon.

circulating in late-magmatic hydrothermal fluids is reduced to U^{4+} on the oxidation of sulphides and Fe-Ti-oxides, and is adsorbed in the alteration products.

Low density tracks along grain boundaries and microfractures occur in most samples, but are generally restricted to spatial association with primary sources or denser concentrations of secondary U (see Plates 5.4C and 5.5A). Sample SB23 is particularly enriched in secondary U along grain boundaries, and dispersed in sericitised centres of feldspars (Plate 5.4C). Notably, this sample has a relatively high U content and a low $^{Th}/U$ ratio (Table 5.17), indicating a divergence in the behaviour of U and Th during post-magmatic processes.

Few apatites are present in the Central Starav Granite and only one sphene was found; both yield extremely low density tracks.

Sample SB179 comes from the centre of the intrusion, where radiometric mapping revealed a decrease in U and Th contents and an increase in $^{Th}/U$ ratio (see Figures 5.12, 13 and 14). Uranium is located in zircon, sporadic thorite and sphene; no monazite was identified. Dispersion in biotites is inferior to that in other Central Starav samples, but is still of a secondary nature. The implications of these contrasts, particularly the presence of sphene, is that this sample is, perhaps, representative of a roof zone which crystallised early in the differentiation history of the Central Starav Granite. The exceptionally high $^{Th}/U$ ratio and low U content of this sample (Table 5.17) may be the result of leaching of U from this central region by rising hydrothermal fluids, which was subsequently redeposited as these fluids moved outwards and cooled.

Samples SB134 and SB186 are microgranites and are the most radioelement rich samples in the Etive Complex. Both are conspicously

diminished in biotite and opaques. No tracks were observed along grain boundaries, but a low density secondary U distribution occurs in sericitised centres of feldspars and alteration fringes of opaques. The most prominent source of fission tracks are metamict zircons (see Plate 5.5B) and a few monazites. No thorites were positively located.

Microprobe analyses

Uranium and thorium contents of zircons are again variable (Table 5.18A) and are notably higher in microgranite samples (SB134 and SB186). These high radioelement zircons show increased levels of Hf, detectable Yb and Y, and produce low totals, probably due to their metamict nature. Two mean zircon compositions were used for mass balance calculations:

i) for samples SB186 and SB134

ZrO_2 = 49.19 ± 4.0% U = 1.35 ± 0.91% Th = 0.63 ± 0.69%

and ii) for all other samples

ZrO_2 = 61.61 ± 2.5% U = 0.29 ± 0.21% Th = 0.13 ± 0.16%

Monazites are particularly variable in their radioelement content (Table 5.18B) and have U contents at the lower end of reported ranges for this mineral (see Table 2.3). Thorites have a similar composition to those in the N Cruachan adamellite.

Mass balance calculations

Uranium and Th contributions from zircon were calculated as described in Section 5.10:2 using relevant whole rock Zr contents (Appendix C) and mean zircon compositions (i) and (ii) above. Although an upper limit to the modal percentage of monazite may be

	Zircon										
Sample No	SB135	SB135	SB133	SB21D	SB21D	SB23	SB23	SB134	SB186	SB186	SB186
Ce_2O_3									(0.09)		0.48
Nd_2O_3				(0.16)							
Yb_2O_3	(0.10)								0.24	0.92	0.42
Hf_2O_3	1.23	1.50	1.14	3.18	1.77	1.54	1.92	2.95	3.38	2.73	2.52
Nb_2O_5			(0.55)								
Y_2O_3	(0.41)	(0.25)		(0.71)					(0.44)	(0.19)	0.94
ZrO_2	62.73	62.50	63.51	56.08	62.06	61.66	62.71	50.75	49.53	52.87	43.59
ThO_2	(0)	(0.16)	(0.27)	(0.17)	(0)	(0)	0.53	1.99	0.47	(0.15)	0.48
UO_3	(0.15)	0.50	(0.04)	0.65	(0.39)	(0.12)	0.67	1.73	0.66	1.06	3.18
SiO_2	34.41	34.42	34.16	32.42	34.19	33.89	34.16	29.88	33.01	33.44	30.02
Al_2O_3	(0.50)	(0.39)	0.55					3.59	3.39	3.02	4.13
FeO	0.54	0.56	0.15	5.40	0.79	0.54	0.33	3.09	1.77	1.03	1.74
MnO				0.18					0.13	0.13	0.16
CaO	0.06			1.01		2.25		1.58	0.97	1.59	2.38
K_2O								0.34			
TOTAL	100.13	100.28	100.37	99.96	99.20	100.00	100.32	95.90	94.08	97.23	90.04

Table 5.18A Electron microprobe analyses of U-bearing accessory phases in the Central Starav Granite. All data are in wt. %. Values in brackets indicate concentrations < 2σ on background.

	Monazite					Thorite			
Sample No	SB135	SB21D	SB22	SB23	SB186	SB133	SB22	SB23	N58
LA_2O_3	13.43	21.98	16.87	16.99	16.48	(0.10)			
Ce_2O_3	27.26	29.60	29.72	30.24	30.29		0.33		(0.07)
Pr_2O_3	2.99	1.42	2.47	1.94	3.57				
Nd_2O_3	10.49	5.64	8.07	7.85	9.30				
Sm_2O_3	1.80	0.40	0.54	0.44	1.43				
Gd_2O_3	0.18				0.77				
Yb_2O_3	0.37								
Nb_2O_5					1.94				
Y_2O_3	0.88	(0.20)	(0.78)						
P_2O_5	27.69	27.46	27.57	28.53	26.67				
ThO_2	9.08	5.75	10.70	2.97	2.65	73.55	69.37	69.98	68.64
UO_3	(0.39)	(0.10)	(0)	(0)	(0)	4.98	5.01	5.46	4.27
SiO_2	2.78	1.96	2.80	4.82	2.24	12.73	19.37	15.72	12.19
TiO_2									0.07
Al_2O_3						1.03			2.23
FeO	0.19	(0.09)	0.52	0.26	0.81	1.55	0.93	0.65	0.44
MnO							0.34		
MgO	0.97								
CaO	0.33	0.13	0.20	0.99	0.46	0.65	2.58	1.87	1.05
K_2O						(0.29)			(0.38)
S						0.22		1.09	
TOTAL	98.83	94.73	100.24	95.03	96.61	95.10	97.93	94.77	89.34

Table 5.18B See caption to Table 5.18A.

calculated on the basis of whole rock Ce contents, estimates of radio-element contributions from this accessory phase incur large errors due to variations in Th content; estimates were made using an upper limit of 10.7% Th and lower limit of 2.6% Th in monazite (see Table 5.18). A mean U content of 0.1% was used for mass balance calculations.

With the exception of sample SB134 (microgranite), the absolute contributions of U and Th from zircon (Table 5.19) are similar to values calculated for earlier units of the Etive Complex. The upper limit of Th contribution from monazite exceeds whole rock values in two samples, and a realistic value in all cases probably lies somewhere between the upper and lower limits. Whichever limit is considered, the 'remaining'

	Zircon		Monazite			Remainder				
Sample No.	Th (ppm)	U (ppm)	Th (ppm) upper limit	Th (ppm) lower limit	U (ppm)	Th (ppm) lower limit	Th (ppm) upper limit	U (ppm)	$^{Th}/_{U}$ lower limit	$^{Th}/_{U}$ upper limit
SB133	0.2	0.5	19.3	5.4	0.2	-1.7	12.3	5.6	-	2.2
N58	0.2	0.5	17.4	4.8	0.2	-2.5	10.1	6.6	-	1.5
SB20	0.3	0.6	16.3	4.5	0.2	0.6	12.4	6.3	0.1	1.9
SB23	0.2	0.5	18.2	5.1	0.2	1.1	14.2	10.0	0.1	1.4
SB134	1.3	2.6	10.8	3.0	0.1	12.1	19.9	7.1	1.7	2.8

Table 5.19 Results of mass balance calculations for the Central Starav Granite. Calculations for monazite were made using an upper limit for the modal percent of monazite based on whole rock Ce contents and upper and lower limits for Th contents (see text).

Sample No.	Zircon		Monazite		Thorite		U (%) residing in secondary locations
	Th (%)	U (%)	Th (%)	U (%)	Th (%)	U (%)	
SB133	1.4	8.4	29.9-100	3.2	<68.7	<13.5	>74.9
N58	1.5	6.8	31.8-100	2.5	<66.6	< 9.6	>81.1
SB20	1.7	9.0	26.2-94.5	2.4	<72.0	<11.6	>76.7
SB23	1.2	4.7	25.9-93.2	1.8	<72.9	< 9.1	>84.4
SB134	5.2	26.0	12.4-44.6	1.1	<82.4	<13.9	>59.0

Table 5.20 Summary of the approximate percentage distribution of U and Th in the Central Starav Granite. Based on data in Table 5.19 and whole rock U and Th contents (Table 5.17). The Th contribution from thorite =100-%Th (zircon)-%Th (monazite; lower limit). The U contribution from thorite is then based on a mean $^{Th}/_{U}$ content for thorite of ≈ 14.5 (from Table 5.18). Remaining U is assumed to reside in secondary sites.

$^{Th}/_{U}$ ratio (Table 5.19) is significantly lower than would be expected if thorite is to account for the surplus U and Th implying that substantial amounts of U are held in secondary sites (as observed from Lexan studies). Percentage contributions to whole rock U and Th from all observed host phases in samples of the Central Starav Granite are summarised in Table 5.20. In all samples except SB134 (microgranite) greater than 70% of whole rock U resides in secondary sites. It is possible that some of this U may be located in apatite, as primary distributions in biotite or in highly uraniferous zircons which were not considered in mass balance calculations. Lexan studies indicate that at least some of the secondary U is derived from leaching of primary sites.

The observed and calculated lower percentages of secondary U in the microgranite samples is probably due to their fine grain size which restricted the passage of hydrothermal fluids.

5.11 SUMMARY: THE DISTRIBUTION OF URANIUM AND THORIUM IN THE ETIVE COMPLEX

Table 5.21 summarises the distribution of U and Th in all units of the Etive Complex, and Figure 5.17 illustrates the relative abundances of U and Th bearing accessory phases throughout the intrusive sequence.

It is clear that in the earlier units of the Complex (Quarry Intrusion and most of the S Cruachan unit) U and Th contents are controlled by the crystallisation of the primary accessory phases apatite, zircon and sphene $\pm$ allanite and chevkinite. The appearance of significant amounts of sphene and sporadic allanite and chevkinite accounts for the increase in $^{Th}/_{U}$ ratio from the Quarry Intrusion to

Unit	Apatite		Zircon		Sphene		Thorite		Monazite		Secondary uranium	Other Th and U hosts
	ppm Th	ppm U	ppm Th	ppm U	ppm Th	ppm U	ppm Th	ppm U	ppm Th	ppm U	ppm	
Quarry Intrusion	3.16-0.68	0.16+0.68	0.13-0.37	0.29-0.56	(0-2)	(0.5)	NOT PRESENT		NOT PRESENT		MINOR	Some Th and U in hornblende and biotite
Southern Cruachan	0.22-0.45	0.22-0.85	0.13-0.65	0.38-1.2	0.52-2.45	0.34-1.6	N55 = 7.8	N55 = 0.6	NOT PRESENT		MINOR BUT INCREASED NEAR CONTACT WITH STARAV	Sporadic thorite, chevkinite and allanite may account for some Th (+ minor U). Minor amounts in biotite and hornblende
Northern Cruachan	0.13-0.20	0.13-0.20	0.12-0.21	0.36-0.58	2.5-4.9	1.7-3.3	12.8-16.0	0.9-1.2	NOT PRESENT		MINOR EXCEPT IN CENTRE OF INTRUSION	
Meall Odhar	0.04-0.07	0.04-0.07	0.13-0.17	0.38-0.53	0.3-1.7	0.5-2.6	7.7-16.2	0.15-0.30	NOT PRESENT		MINOR	
Outer Starav	0.10-0.26	0.10-0.26	0.04-0.06	0.39-0.61	Contributions from sphene and thorite impossible to calculate but both are important, especially for Th.				NOT PRESENT		< 1 ppm	Sporadic allanite + an Fe-Ti-Nb silicate found in one sample
Central Starav	negligible		0.13-0.30 SB134 = 1.3	0.28-0.66 SB134 = 2.6	negligible		3.8-7.6	0.26-0.53	10-13 SB134 =6.9	0.17-0.20 SB134 =0.11	5.2-9.5 SB134 = 6.0	
	% Th	% U	% Th	% U	% Th	% U	% Th	% U	% Th	% U	% U	
Quarry Intrusion	6-18	10-40	5.6-21	10-40	(0-50)	(0-20)	———		———		——	
Southern Cruachan	2.3-10	10-50	2-10	19-90	9-28	20-66	N55 = 73	N55 = 20	———		(≤ 10%)	
Northern Cruachan	0.8-1.3	3-6	0.4-1.2	3.4-17	16-27	50-66	71-82	20-27	———		≤ 20% but ~50% in centre	
Meall Odhar	0.2-0.9	1.2-6.3	0.7-1.6	12-34	3.7-9.4	45-78	89-94	8-14	———		——	
Outer Starav	0.9-2.8	3.8-9.5	0.01-0.67	9-26	Sphene and account for thorite ~60-90% Th, 50-70% U.				———		≤ 30%	
Central Starav	-	-	1.2-1.7 SB134 = 5.2	4.7-9.0 SB134 = 26	-	-	25-40 SB134 = 66	3.6-6.3 SB134 = 11.2	60-73 SB134 = 28	1.8-3.2 SB134 = 1.1	80-90 SB134 = 61	

Table 5.21 Summary of absolute and percentage contributions to whole rock U and Th from accessory phases and secondary distributions in all units of the Etive Complex

Values in brackets are estimated from fission track studies and comparison with other units. Mean Th contents for monazites were used. Data for the Quarry Intrusion was calculated using mean analyses of accessory phases in the S Cruachan units.

the S Cruachan units (see Table 5.4). In later units; i.e. the N Cruachan adamellite and the Starav Granites, Th was sufficiently enriched in the magma to crystallise as a discrete phase, thorite, and as a significant component in monazite in the Central Starav Granite. Although U was still being incorporated in progressively decreasing quantities of apatite, sphene and zircon, and in thorite it was enriched relative to Th as differentiation of the magma proceeded. There is some evidence of higher percentages of U substituting in primary zircon in the Central Starav microgranite, but it is probable that much U was partitioned into residual fluids at the centre of concentrically differentiating units (the Starav Granites and the N Cruachan adamellite), existing as the mobile U^{6+} ion. Expulsion and circulation of these fluids was limited due to the relatively dry nature of the original magma (Clayburn et al., 1983) and to the lack of water in the surrounding country rocks required to enhance large scale hydrothermal systems. Uranium was initially leached from rocks near the centre of the Starav units (i.e. the central 'low' in Figure 5.13) and later deposited as insoluble U^{4+} in alteration products after oxidation of Fe-Ti-oxides and Fe-sulphides, chloritisation of biotites and partial sericitisation of feldspars. The proportion of secondary U initially increases from the zone of leaching to the zone of deposition, and then decreases further outwards, as the limit of hydrothermal alteration is reached, thus accounting for the observed variation in the $^{Th}/U$ ratio of the Starav Granites (Figure 5.14). The presence of secondary U distributions, overprinting primary magmatic trends in the Starav units, accounts for the curvilinear relationship on the U vs. Th plot (Figure 5.16). Similar secondary U enrichment processes were probably active at the centre of the N Cruachan unit, but on an even smaller scale.

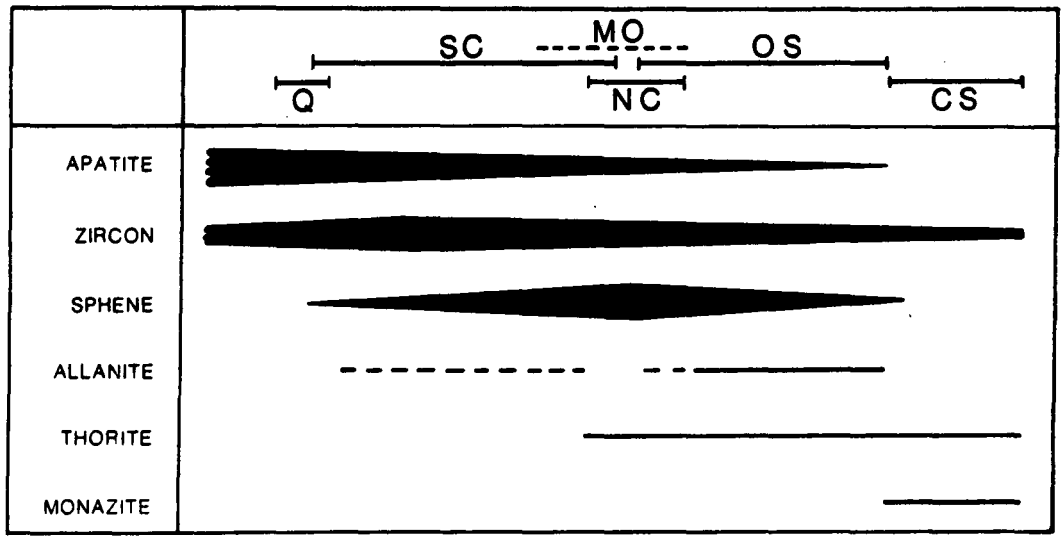

Q Quarry Intrusion
MO Meall Odhar Granite
SC S Cruachan units
OS Outer Starav Granite
NC N Cruachan adamellite
CS Central Starav Granite

Figure 5.18 Relative abundance of accessory phases in units of the Etive Complex.
The Meall Odhar Granite is depleted in apatite, zircon and particularly sphene, relative to its proposed position in the intrusive sequence.

An important consideration with regard to the heat production in these granites (see Chapter 7) is that the aerial limit of U enrichment due to late stage hydrothermal circulation may suggest a similar limit with depth and hence heat productivities calculated for surface samples may not be continuous in the third dimension. Primary zonation of Th also suggests a depletion in heat productivity at depth in the Starav and N Cruachan units.

All data for the Meall Odhar Granite are consistent with its origin as residual magma or remobilised intercumulus liquid from the outer Etive units.

Finally, this study presents the first report of thorite, monazite and chevkinite as accessory phases in the Etive Complex.

CHAPTER 6 THE CAIRNGORM GRANITE

The Cairngorm Granite has been identified as a voluminous (Brown and Locke, 1979), relatively homogeneous intrusion enriched in heat-producing elements (Simpson et al., 1979; Brown, 1979; Watson and Plant, 1979). Hence, two of the factors favouring a high geothermal gradient (see Section 1.2) are potentially satisfied; (i) a large volume of intrusive rocks and (ii) high crustal heat production. To investigate further the distribution, and nature of enrichment of radioelements in this granite a detailed gamma-spectrometry, fission track and petrochemical study was undertaken, using the techniques outlined in Chapter 4. The results of these studies are applied to heat flow models in Chapter 7 in an attempt to assess the 'hot dry rock' potential in the Cairngorm area.

6.1 GEOLOGICAL SETTING AND STRUCTURE

The geology of the Eastern Grampian Mountains is dominated by a group of post-kinematic Caledonian granites extending approximately E-W across the Highlands (see Figure 3.5). The Cairngorm massif constitutes a distinct topographic feature, rising abruptly from the surrounding country rock in the form of a dissected plateau, 160 sq. mls. in area and attaining heights of ∿4200' O.D. Moinian rocks, north, south and west of the granite (Figure 6.1) are uniform micaceous psammites of Pre-Cambrian age known as the Central Highland Granulites (Johnstone, 1975). Those to the east comprise a complex sequence of younger, Dalradian quartzites and schists (Read et al., 1966).

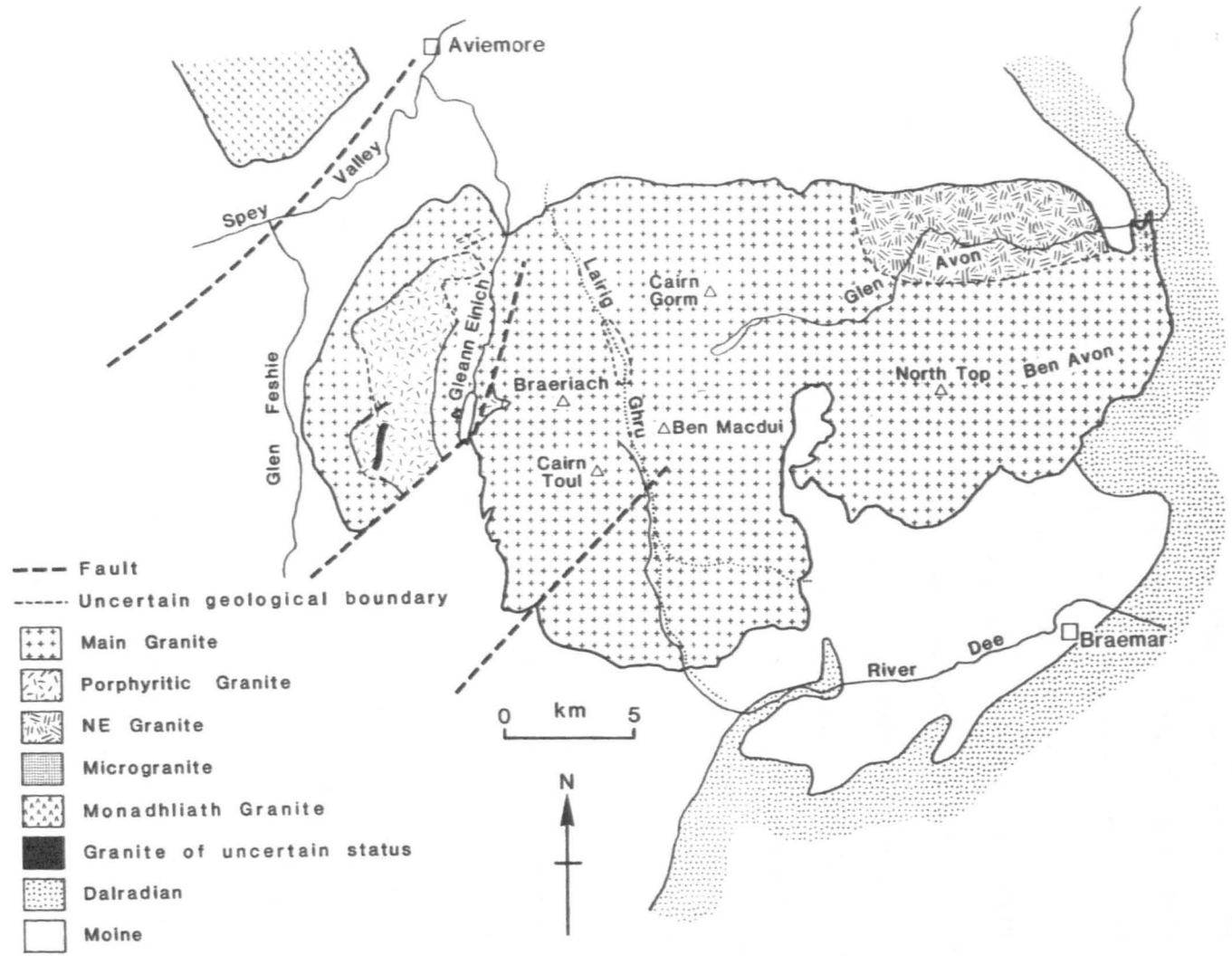

Figure 6.1 Geology of the Cairngorm Granite and surrounding area.

The Cairngorm Granite has previously been considered as a concordant sheet or laccolith (Barrow et al., 1913), but Harry (1965) described it as a stock-like body with sharp, vertical contacts transecting the foilation of the Moine schists (the latter model is more consistent with geophysical evidence; see below). The contact south-west of Loch Einich is marked by a near-vertical fault, characterised by a broad zone of crushing and mineralisation (Figure 6.1). Offset of the granite contact is apparent both here, and along a similar NE-SW fault zone to the south-east (Barrow et al., 1913). A number of sub-parallel, minor crush zones and quartz veins also occur in the southern lobe. Although these structures are, to a large extent, post-granitic in age, the presence of idiomorphic quartz and feldspar crystals in drusy cavities within crush zones suggests that movement along them had ceased before the final stages of consolidation were reached (Barrow et al., 1913).

Xenoliths are scanty and extensive proof of magmatic stoping is lacking, but the Cairngorm Granite appears to have been intruded rapidly, via deep faults and emplaced at a high structural level (Watson and Plant, 1979). Dewey and Pankhurst (1970) considered the NE Grampian granites to be discordant with respect to regional cooling 'chrontours', indicating their generation at a time when regional uplift and cooling were already well advanced. Such characteristics, along with their geophysical expression (see below) classify these granites with Read's later 'permitted', and Brown et al's group 2 intrusions (see Section 3.2).

Geophysically, the NE Grampian granites are characterised by a series of intense negative Bouguer anomalies, reaching minima of approximately -29 to -55 mgal, and pronounced aeromagnetic anomalies

(Locke, 1980). Individual plutons of the Cairngorm-Aberdeen line are not completely resolved on the Bouguer anomaly map and distortion of the negative gravity field results from the proximity of two large positive anomalies (+18 and +41 mgal) associated with basic intrusions north of the granites (Figure 6.2). Locke (1980) produced a residual gravity anomaly map by removing a regional field with a gradient of approximately -0.35 mgal km^{-1} E to W. Calculation of this field involved fitting a low order trend surface to gravity data lying outside the influence of major negative and positive anomalies. The area considered (see Figure 6.2) is relatively small in relation to the area modelled and the gravity field encompasses several 'local' anomalies associated with igneous bodies, the Highland Boundary Fault and the Great Glen Fault. In view of the complexity, and despite the good 'fit' obtained for low-order polynomial surfaces, it is not necessarily valid to extrapolate this 'apparent' regional field across the area of interest. Detailed modelling of all upper crustal metasedimentary, intrusive and structural features in the Grampian region would be required to determine the true regional field across the Cairngorm-Aberdeen line. However, Rollin (1982) also estimates a difference in regional field of approximately -20 mgal between the Aberdeen and Cairngorm intrusions (see Figure 6.3); i.e. -0.2 mgal km^{-1} E to W.

The Cairngorm granite apparently extends to a depth of 12 km, with steep, outward-sloping margins, and is connected to the Monadhliath stock by a granitic 'ridge' at approximately 7 km and to the more easterly plutons at a depth of less than 2 km (Figure 6.3).

An additional feature of the Bouguer gravity map for the Grampian region is a ridge of low gravity anomaly (-30 mgal)

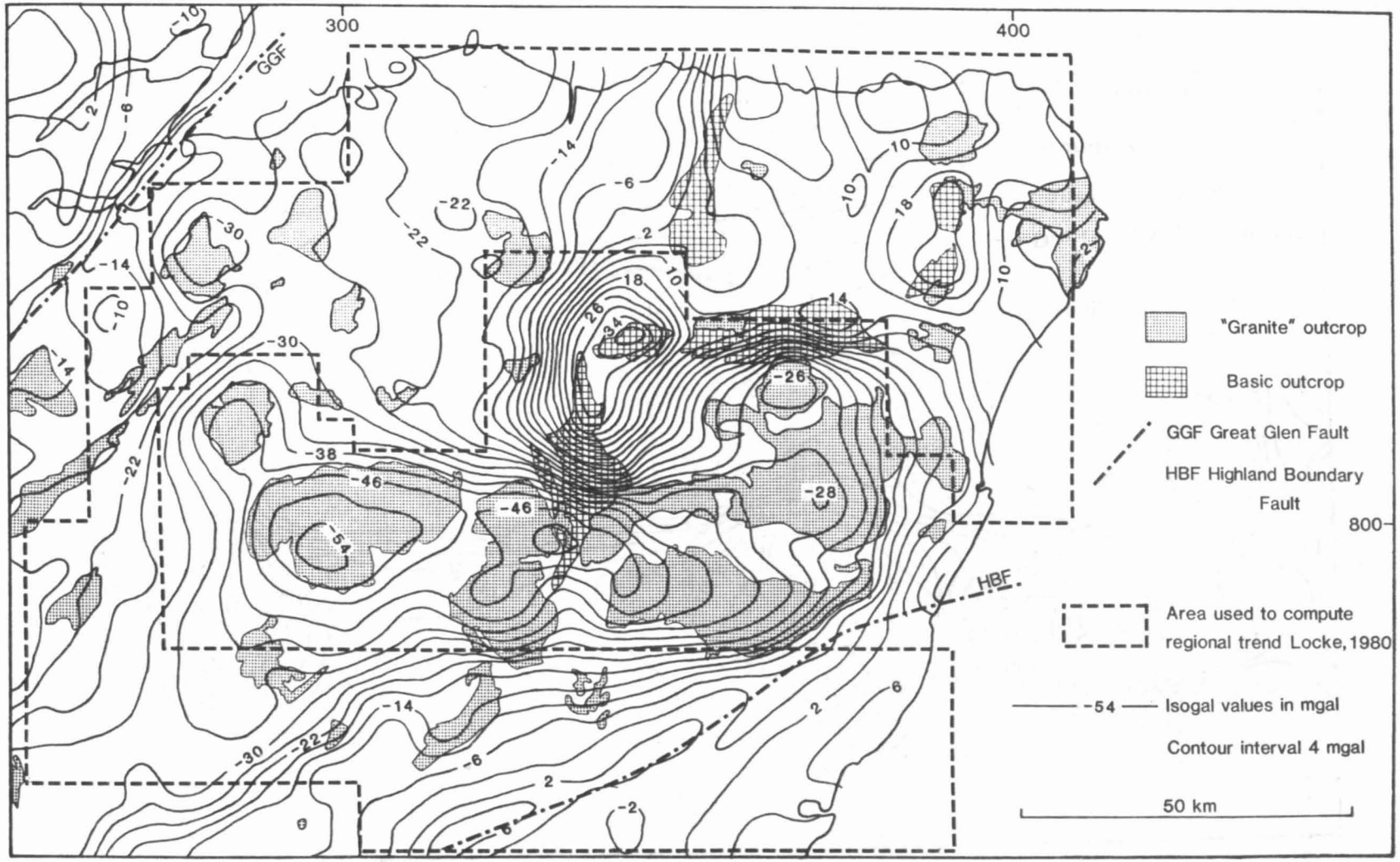

Figure 6.2 Bouguer anomaly map of the NE Grampian Highlands; modified from Rollin 1982. See Figure 6.3 for gravity modelling by Locke (1980).

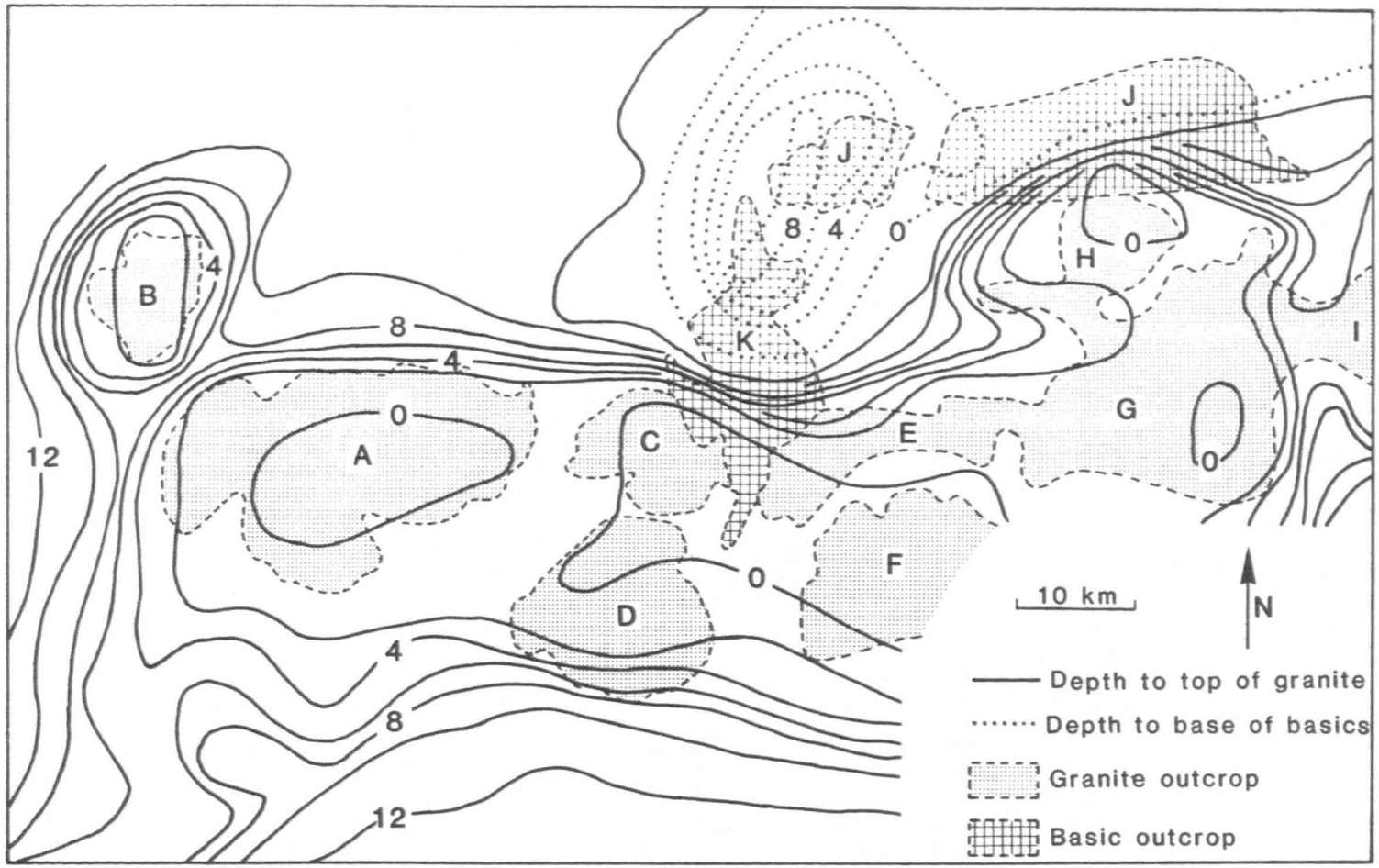

Figure 6.3 Gravity model of the eastern Grampian Highland; after Locke (1980). Contour interval is 2 km. Density contrasts with country rocks used for modelling were -100 kg m^{-3} for the granites and +240 kg m^{-3} for the basic bodies Outcrops are: A, Cairngorm; B, Monadhliath; C, Glen Gairn; D, Lochnagar; E, Ballater; F, Mount Battock; G, Skene; H, Bennachie; I, Aberdeen; J, Insch; K, Morven-Cabrach.

connecting the minima around Cairngorm (-55 mgal) and Etive (-45 mgal) (part of this is shown in the SW corner of Figure 6.2). A possible solution for the anomaly is a shallow granitic ridge linking the Etive and Cairngorm intrusions (Rollin, 1982). Aeromagnetic data, however, do not reflect this anomaly suggesting that if the postulated ridge exists, it is not contemporaneous with these Siluro-Devonian intrusions.

6.2 PETROGRAPHY AND INTERNAL RELATIONSHIPS

From previous work, two units have been recognised in the western Cairngorms, the Main Granite and the apparently later Porphyritic Granite (Harry, 1965; Figure 6.1). Internal contacts between the two are generally sharp, intrusive and vertical. Further east isolated outcrops of Microgranite appear for a short distance (∿3 km) along the Lairig Ghru (Barrow et al., 1913), but temporal relationships between this unit and the Main Granite remain unclear (see later). During this study an extremely coarse, readily weathered granite characterised by the presence of large (1.5-3.5 cm), pink, subhedral feldspars (Plate 6.1a), was found to crop out along Glen Avon and in small exposures on the relatively low, drift covered ground to the north-east (Figure 6.1). This unit has not previously been documented and is hereinafter referred to as the NE Granite. Contacts between the NE Granite and the Main granite were not observed.

Large nests of quartz veins and a number of aplites occur in the vicinity of Cairn Gorm (Harry 1965) and small aplitic dykes are numerous at some localities in the southern lobe (Barrow et al., 1913). Where these exploit vertical joints, the centres are frequently

pegmatitic, often containing drusy cavities. Veins of granite, aplite and pegmatite are seen in several localities invading the country rocks at the granite margins.

6.2:1 The Main Granite

This rock type is predominant in the Cairngorm intrusion at the present level of erosion. It is typically coarse grained (Plate 6.1E), sometimes containing idiomorphic feldspars, 1.5-3 cm in length, occasionally reaching 4 cm. Oligoclase is abundant as early-formed rectangular laths, often enclosed by plentiful, slightly perthitic microcline. Interstitial aggregates of quartz crystals form areas up to 1 cm^2. Disseminated flakes of biotite are sometimes ragged and rimed or partially replaced by muscovite. The development of a secondary magnetite-hematite phase along the rims and cleavage traces of some flakes is thought to be due to the breakdown of biotite. Similar opaques, occurring as fine-grained secondary aggregates in some feldspars, are intimately related to Fe-stained microfractures and alteration of biotites. The above metnioned alterations are particularly well developed in samples near the western margin (N82, N83, SB156, see below), and those near faults and margins at the head of Loch Einich (SB163, N197) and in the southern lobe (SB171) (see Plate 6.5, Section 6.7:2). Incipient alteration, however, occurs in samples from several localities in the Main Granite. Muscovite is also present as secondary areas in partially sericitized plagioclase crystals and occasionally as interstitial flakes.

A marginal phase of the Main Granite within a few hundred metres of the Moine contact near Glen Feshie and Strathspey (Figure 6.1) is

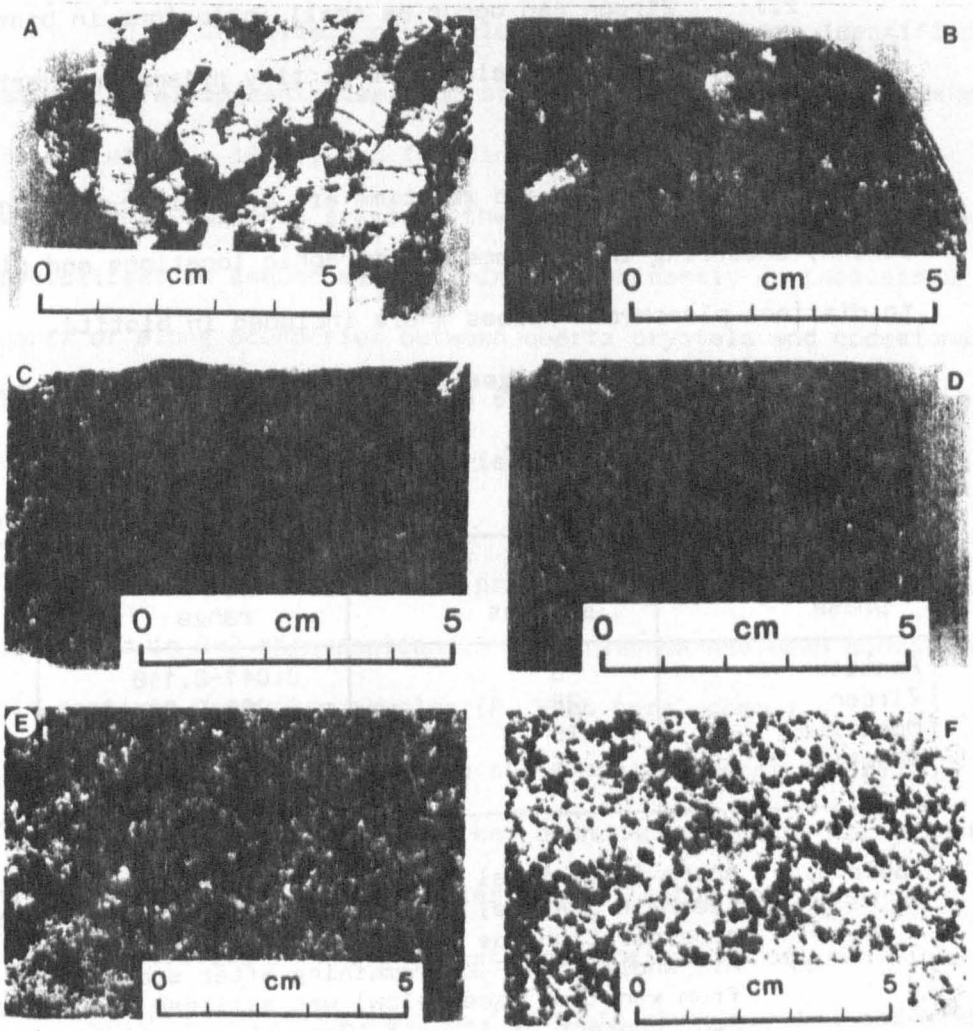

Plate 6.1 Hand specimens of Cairngorm granites

A NE Granite, sample SB170.
B Porphyritic Granite, sample N198.
C Microgranite, sample N193.
D Main Granite, medium grained, sample SB164.
E Main Granite, coarse grained, sample SB177.
F Main Granite, medium grained marginal facies, sample N83.

generally medium grained (Plate 6.1F), porphyritic in places, and fine grained a few metres from the contact (Harry, 1965).

The accessory mineral assemblage of the Main Granite has been studied in detail during this work and comprises:

i) Apatite, which occurs as very small, prismatic or

cubic crystals, usually included in biotite.

ii) Zircon can occur as small inclusions in biotite, surrounded by pleochroic haloes, or as tiny prisms in quartz and feldspar.

iii) Monazite and xenotime are of similar abundance to zircon, occurring in the same petrographic locations and give rise to distinct pleochroic haloes where included in biotite.

Approximate modal percentages of apatite, zircon, monazite and xenotime are presented in Table 6.1.

Accessory phase	No. samples	Modal % range	Modal % mean
Apatite	6	0.041-0.118	0.070
Zircon	25	0.008-0.034	0.022
Monazite	25	0.009-0.050	0.024
Xenotime	25	0.007-0.040	0.017

Table 6.1 Approximate modal percentages of some accessory phases in the Main Granite; calculated from geochemical mass balance considerations as follows.

a) All whole rock P_2O_5 remaining after subtraction of P_2O_5 from xenotime (see below) was assigned to apatite. A P_2O_5 content of 41 wt.% (Deer et al., 1972) was assumed for apatite.

b) All whole rock Zr was assigned to zircon. A mean composition for zircon from microprobe analyses was used (Table 6.10).

c) All whole rock Ce was assigned to monazite. A mean composition of monazite from electron microprobe analyses was used (Table 6.11).

d) All whole rock Y was assigned to xenotime. A mean composition for xenotime from electron microprobe analyses was used (Table 6.12). The P_2O_5 content attributable to xenotime was calculated from modal percentages, and subtracted from modal percentages, and subtracted from whole rock values in order to calculate apatite contents.

Whole rock data are presented in Appendix F and errors incurred in these calculations are discussed further in Section 6.7:2.

iv) Minor thorite is present as orange-red crystals often with semi-opaque rims, either included in biotite or in association with primary opaques. Thorite is more apparent in relatively biotite-

rich samples.

v) A variety of complex Nb-Ta oxides were identified in heavy mineral concentrates from streams draining the Cairngorm mass (Basham et al., 1982), and in thin sections from this study. Petrographic evidence suggests these minerals formed late in the crystallisation sequence, occurring predominantly as inclusions in quartz or along boundaries between quartz crystals and occasionally along microfractures (see Plates 6.3 and 6.4). Their presence as U-bearing phases sometimes gives rise to damage haloes in adjacent crystals.

vi) Minute grains of primary uraninite have been tentatively identified in 2-3 thin sections. Its presence has been confirmed in thin sections from core samples (P. Webb pers. comm.).

vii) Primary magnetite and ilmenite (Mackie, 1925).

viii) Accessory garnet has been documented by Harry (1965) and Barrow et al., (1913). The latter authors noted its presence in fine-grained, muscovite-rich granite at the margin west of Loch Einich. Garnet occurred in three samples from this study; in N82 and N156, both from within 50 m of the western margin in Glen Feshie, and in SB171 collected approximately 40 m from the fault zone in the southern lobe. All three samples exhibit well-developed replacement of biotites by fibrous muscovite and secondary opaques. The garnets are essentially almandine-spessartine, occurring as pale pink, subhedral-anhedral crystals, either interstitially or enclosed in quartz. Garnet has also been reported from a pegmatite invading the country rock in the Dee Valley (Barrow et al., 1913).

h) Sparse fluorite and topaz have been reported (Simpson et al., 1979; Mackie, 1925).

Abundant, late-stage drusy growths on vertical joints, particularly in the Cairn Gorm area, comprise coloured quartz, K-feldspar, biotite, plumose muscovite and, locally, beryl or topaz (Watson and Plant, 1979).

6.2:2 The Porphyritic Granite

Harry (1965) distinguished two textural varieties which differ only in possessing a fine or medium-grained groundmass. Both contain scattered rectangular, perthitic potash feldspar phenocrysts, approximately 1.5 cm long, and rounded quartz aggregates, approximately 0.5 cm in diameter, set in a fine-grained quartz-microcline-plagioclase-biotite groundmass. (Plate 6.1B). Muscovite forms small, ragged crystals rimming or partially replacing biotite. The accessory mineral assemblage is probably similar to that of the Main Granite, with the exception that no garnet or topaz has been observed, and it is unlikely that U-rich Nb-Ta-oxides are present.

6.2:3 The Lairig Ghru Microgranite

This fine, even-grained granite (Plate 6.1C) has a mineral assemblage similar to the Main Granite but biotite and opaques are conspicuously more abundant. Biotites are ragged, extensively chloritized and a few contain rutile needles. Minor muscovite occurs as a secondary alteration product of feldspar and biotite and occasionally, as interstitial plumose growths.

6.2:4 The NE Granite

The large, subhedral feldspars characteristic of this granite (see Plate 6.1A) are perthitic microcline, often well zoned, sometimes twinned and frequently enclose early-formed plagioclase laths. These

are separated by coarse aggregates of quartz, plagioclase, K-feldspar and biotite. Biotite is abundant, generally fresh and often encloses or is associated with, clusters of primary magnetite grains. Pleochroic haloes in biotites are fewer and less distinct than those in the Main Granite, implying a lesser abundance of concentrated radioelement-bearing phases. Muscovite was not observed in the NE Granite. The accessory mineral assemblage differs significantly from other units and comprises:

i) Ubiquitous apatite occurs as abundant, well-formed prismatic crystals. Modal percentages, based on whole rock P_2O_5 contents (see Appendix F) and assuming 41 wt.% P_2O_5 in apatite (Deer et al., 1972) are 0.195-0.366% (3 samples).

ii) Zircon is often included in biotite or associated with clusters of opaques, but occurs in all major phases. Modal percentages are 0.031-0.44%.

iii) Sphene is conspicuous and probably crystallised simultaneously with biotite.

iv) Sparse allanite is present; only two well-formed crystals were found in four thin sections.

v) Magnetite is an abundant, early-formed phase frequently found as inclusions in biotite.

The mineralogical characteristics of each unit of the Cairngorm mass are summarised in Table 6.2. Although genetic relationships have not been unequivocally confirmed, the consanguinity of all four units is implied from geochemical trends (see Section 6.3), spatial associations and similarities in mineralogy. An evolutionary trend is apparent from the NE Granite to the Main Granite involving a decrease in biotite and primary Fe-Ti-oxides and the appearance of

	N.E. GRANITE	PORPHYRITIC GRANITE	MICROGRANITE	MAIN GRANITE
APPROX. ORDER OF CRYSTALLISATION ↓ PLAGIOCLASE	Early-formed, often enclosed in K-feldspar	In groundmass. Often partially sericitized	Often partially sericitized.	Oligoclase - early formed rectangular laths. Often partially sericitized.
BIOTITE	Abundant, generally fresh. Fewer, less distinct pleochroic halo's than in Main Granite	Some large flakes, but mainly in groundmass. Sometimes rimmed by muscovite.	Extensively chloritized. More abundant than in Main Granite. A few contain rutile needles.	Disseminated flakes. Sometimes ragged and rimmed or partially replaced by muscovite. Secondary opaques, along rims and cleavage traces where altered. Pleochroic halos, abundant and distinct.
POTASSIUM FELDSPAR	Abundant large (1.5-3.5 cm) subhedral perthitic microcline;- characteristic.	Rectangular, perthitic microcline phenocrysts ~1.5 cm long and in groundmass.	Microcline, sometimes perthitic.	Perthitic microcline, sometimes forming large (1.5-3.0 cm) idiomorphic crystals.
QUARTZ	Coarse aggregates	Rounded aggregates, ~0.5 cm in diameter and in groundmass.	Interstitial aggregates	Interstitial aggregates up to 1 cm in diameter.
MUSCOVITE	Absent	Small ragged crystals rimming or partially replacing biotite.	Minor, as secondary alteration of biotite and plag. Occasionally as interstitial plumose growths.	As alteration products of biotite and feldspar. Sometimes as larger, apparently primary, interstitial flakes.
ACCESSORY MINERALS	Magnetite - abundant. Apatite - abundant, well-formed crystals Zircon - more abundant than in Main Granite Sphene - conspicuous Allanite - sparse	As Main Granite, except no garnet, fluorite, topaz or uraninite observed. Is unlikely that Nb-Ta-oxides are present.	Magnetite and ilmenite - more abundant than in Main Granite. Apatite Zircon Possibly some monazite and xenotime.	Magnetite + ilmenite - less abundant than in other units. Apatite - small, often submicroscopic crystals Zircon, Monazite, Xenotime } approx. equal abundance Thorite - sparse, most apparent in relatively biotite rich samples Uranium - Only 2-3 grains tentatively identified
LATE MAGMATIC CRYSTALLISATION				Garnet - Only in 3 'marginal' samples. Nb-Ta-oxides - probably present in most samples. Fluorite and topaz } minor

Table 6.2 Major and accessory phase mineralogy of the Cairngorm granites.

muscovite as a secondary alteration product or as interstitial flakes. Early crystallisation of K-feldspar is suggested by the abundance of subhedral, probably partially resorbed crystals of this phase in the NE Granite and its occurrence as phenocrysts in the Porphyritic Granite. A significant contrast is noted in the accessory mineral assemblage which changes from apatite + zircon + sphene ± allanite in the NE Granite to apatite + zircon + monazite + xenotime + Nb-Ta-oxides ± thorite ± uraninite in the Main Granite. Modal percentages of apatite and zircon are lower in the Main Granite. Uncertainties in the accessory mineral assemblage of the Microgranite and the Porphyritic Granite arise from their fine grain-size and the attendant difficulties in optical and microprobe analyses. However, the absence of sphene, as in the Main Granite, was confirmed by high magnification optical scans.

6.3 GEOCHEMISTRY

Thirty-two samples were analysed for selected trace elements by XRF (Appendix A) using pressed powder pellets, and fifteen for major elements using glass beads. All analyses are presented in Appendix F.

6.3:1 Major elements

A summary of major element analyses for all units is presented in Table 6.3.

The NE Granite has significantly lower SiO_2 contents and higher TiO_2, Al_2O_3, Fe_2O_3, MgO, CaO and P_2O_5 contents in comparison with other units. A differentiation trend from the NE Granite to the Main Granite, which parallels that of the inner units of the Etive Complex, is apparent

UNIT	No. SAMPLES	SiO_2		TiO_2		Al_2O_3		Fe_2O_3		MnO		MgO		CaO		Na_2O		$*K_2O$		P_2O_5	
		$\bar{x}$	σ	$\bar{x}$	σ	$\bar{x}$	σ	$\bar{x}$	σ	$\bar{x}$	σ	$\bar{x}$	σ	$\bar{x}$	σ	$\bar{x}$	σ	$\bar{x}$	σ	$\bar{x}$	σ
N.E. GRANITE	3	70.7	0.3	0.34	0.03	15.2	0.5	2.1	0.2	0.04	0	0.4	0.2	1.28	0.03	3.8	0.1	4.6	0.5	0.12	0.03
PORPHYRITIC GRANITE	1	74.7	-	0.21	-	13.9	-	1.5	-	0.05	-	0.2	-	0.84	-	3.2	-	4.6	0.5	0.06	-
MICROGRANITE	2	74.6	0.08	0.17	0.01	13.8	0.3	1.2	0.01	0.03	0	0.08	0.01	0.44	0.1	3.4	0.3	5.5	0.2	0.06	0.01
MAIN GRANITE	9	76.2	1.5	0.12	0.04	13.1	0.7	1.0	0.3	0.05	0.01	0.12	0.09	0.38	0.06	3.7	0.3	4.7	0.4	0.04	0.01

Table 6.3 Major element concentrations in units of the Cairngorm intrusion. All data are in wt.%. K_2O values are from gamma-ray spectrometry survey (Appendix G).

on an AFM plot (Figure 6.4) suggesting a co-magmatic origin for all Cairngorm units involving fractional crystallisation of major phases. All units are mildly peraluminous; i.e. molecular proportions of $Al_2O_3 > Na_2O + K_2O + CaO$ (Shand, 1927), and are alkali-calcic in terms of silica saturation.

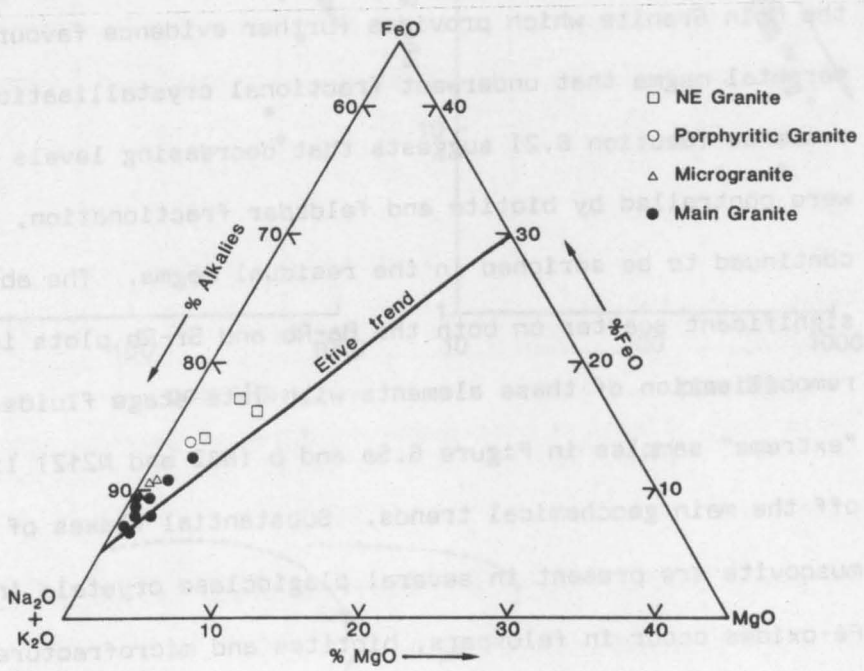

Figure 6.4 AFM plot for the Cairngorm Granite

6.3:2 Trace elements

The Cairngorm granite is characterised by anomalous concentrations of several trace elements relative to most other Caledonian granites and the metamorphic country rocks; it has high levels of the LIL elements (U, Th, K, Rb, and Cs) and other incompatible elements (Li, Be and Mo), enrichment in Sn and REEs, a low K/Rb ratio and low levels of Zr, Ti and Sr (Plant et al., 1980; Johnstone, Plant and Watson, 1979; Watson and Plant 1979; Simpson et al., 1979). Stream sediment and bedrock analysis also reveal low levels of transition elements; Cu, Vi, Ni, Cr and Co (Johnstone, Plant and Watson, 1979). Trace element analyses from this

study (Appendix F) confirm the high concentrations of Rb and Y and low concentrations of Zr, Ti and Sr. Additionally, they reveal a high Nb content for granitic rocks, particularly in the Main Granite.

Selected inter-element plots (Figure 6.5) show an evolutionary trend from the NE Granite, through the Porphyritic and Microgranite, to the Main Granite which provides further evidence favouring a common parental magma that underwent fractional crystallisation. Petrological evidence (Section 6.2) suggests that decreasing levels of Ba and Sr were controlled by biotite and feldspar fractionation, whilst Rb continued to be enriched in the residual magma. The absence of significant scatter on both the Ba-Rb and Sr-Rb plots indicates little remobilisation of these elements with late stage fluids. The two "extreme" samples in Figure 6.5a and b (N82 and N212) lie slightly off the main geochemical trends. Substantial flakes of secondary muscovite are present in several plagioclase crystals in N212 and secondary Fe-oxides occur in feldspars, biotites and microfractures. N83 exhibits well developed replacement of biotite by muscovite and Fe-oxides in addition to sericitisation of feldspars. It is possible that some Ba and Sr was removed during these alteration processes but the dominant trends appear to be magmatic, as substantiated by the linear relationship between the high field strength elements, Zr and Ti (Figure 6.5c).

6.3:3 The significance of garnets

Electron microprobe analyses (Table 6.4) show these to be essentially almandine-spessartine (i.e. Fe-Mn) solid-solutions, with no evidence of zoning. Such garnets are typical of both low temperature aureoles and highly differentiated peraluminous granites (Deer et al.,

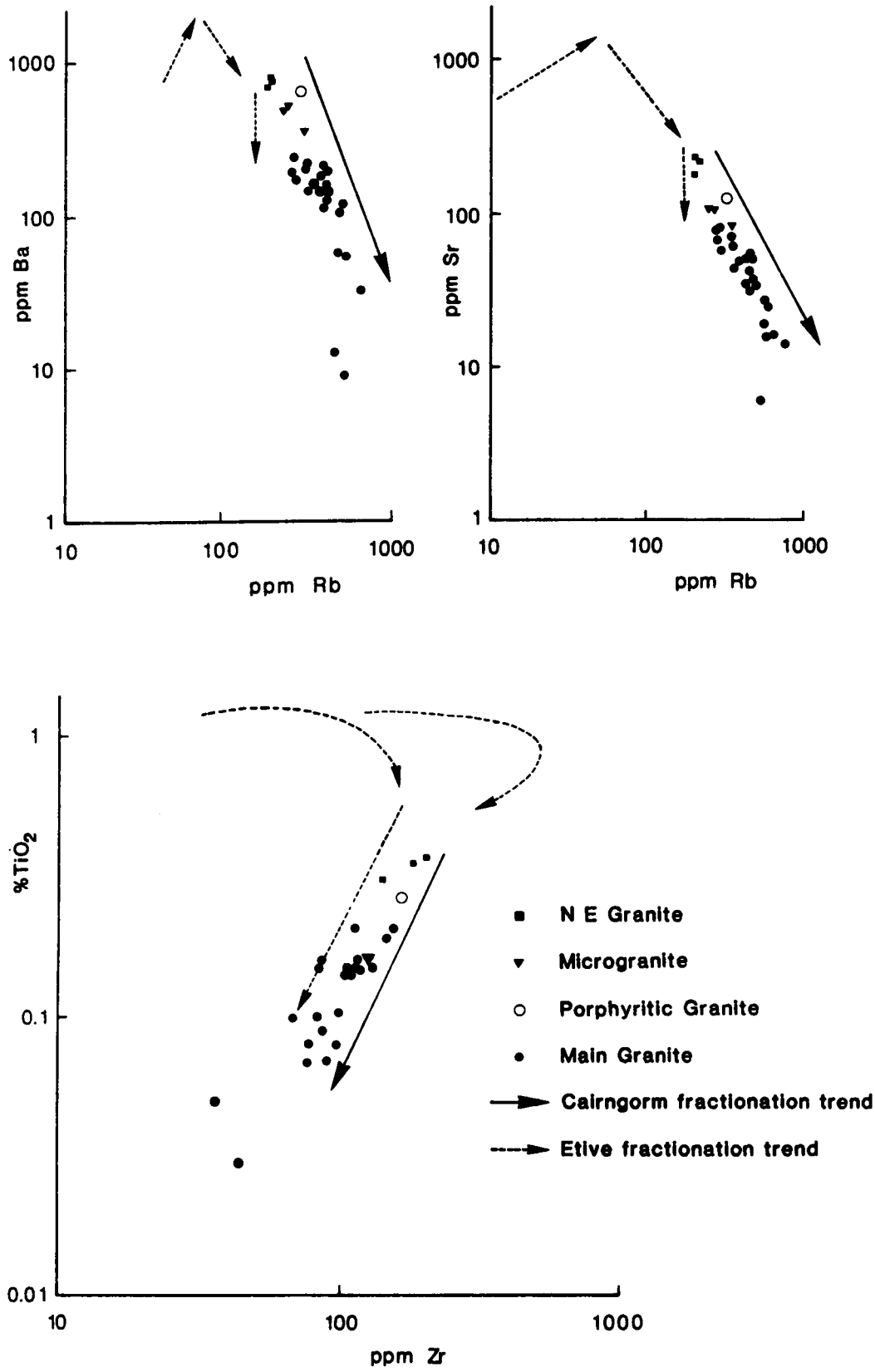

Figure 6.5 Selected trace element plots for the Cairngorm Granite.

1972; Clarke, 1981).

Sample No.	N82 Rim	N82 Core	N82	N82	SB171
SiO_2	36.39	36.42	36.16	36.31	35.93
TiO_2	0.05	0.05	0.05	0.05	0.05
Al_2O_3	21.26	20.66	20.52	20.98	20.69
FeO	24.96	25.03	25.13	25.48	24.01
MnO	17.99	17.86	17.74	17.91	18.75
MgO	0.08	0.17	0.12	0.10	0.17
CaO	0.20	0.50	0.60	0.22	0.54
TOTAL	100.93	100.69	100.32	101.05	100.14

Table 6.4 Electron microprobe analyses of garnets from the Cairngorm Granite. All data in wt.%. Analysed by A. Tindle.

The mechanisms that may have been important in the appearance of garnet in these Cairngorm samples are:

i) Reaction between magma and digested pelitic xenoliths rich in Al and Mn relative to the melt (Clarke 1981). All garnet bearing samples were located near the granite margin or fault zones, although no country rock xenoliths were seen.

ii) Nucleation directly from the melt as late stage differentiation increases the $Mn/(Mn + Fe^{2+} + Mg)$ ratio sufficiently to stabilize spessartine-rich garnet (Clarke, 1981). The MnO content of sample N82 is marginally higher (0.09 wt.%, P. Webb pers. comm.) than in other Cairngorm samples (mean MnO = 0.05 wt.%).

iii) Reaction between early formed phases and the residual silicate melt; for example, Biotite + Liquid → Muscovite + Garnet (Miller and Stoddard, 1981). All three garnet bearing samples exhibit

replacement of biotite by muscovite, though garnet itself was not observed in reaction relationship with biotite. Garnet may, however, be produced indirectly, via the melt in such reactions (Miller and Stoddard, 1981).

Without further investigation, the paragenesis of these garnets remains unclear. However, the reported presence of pale pink garnet in pegmatite from the Cairngorm intrusion (Barrow et al., 1913) suggests that late stage volatiles may be important.

6.3:4 Rare Earth elements

Six samples were analysed for REEs by INAA (Appendices A and F). Chondrite normalised REE plots (Figure 6.6) show a strong enrichment in heavy REE's and a slight depletion in light REE's (with the exception of sample N187) from the NE Granite to the Main Granite. Considerable enhancement of the negative Eu anomaly accompanies this trend. High total REE contents (Appendix F) and the relatively incompatible behaviour of heavy REE's (Figure 6.6) contrast with trends in the Etive Complex and certain other Caledonian granites that have been analysed, for example Foyers and Strontian (Pankhurst, 1979). The development of a Eu anomaly with increasing differentiation is, however, similar to trends in the Etive Complex and may result from feldspar fractionation or residual feldspar during melting in the source region.

Several authors have documented the dominance of accessory phases in controlling the REE geochemistry of granitic rocks (e.g. Fourcade and Allegre, 1981; Pagel, 1982; Tindle, 1982). High REE contents have been found in several accessory phases in the Cairngorm Granite (see Tables 6.11 to 6.14) and the trend towards increasing whole rock heavy REE contents with evolution (Figure 6.6) may result from the change in

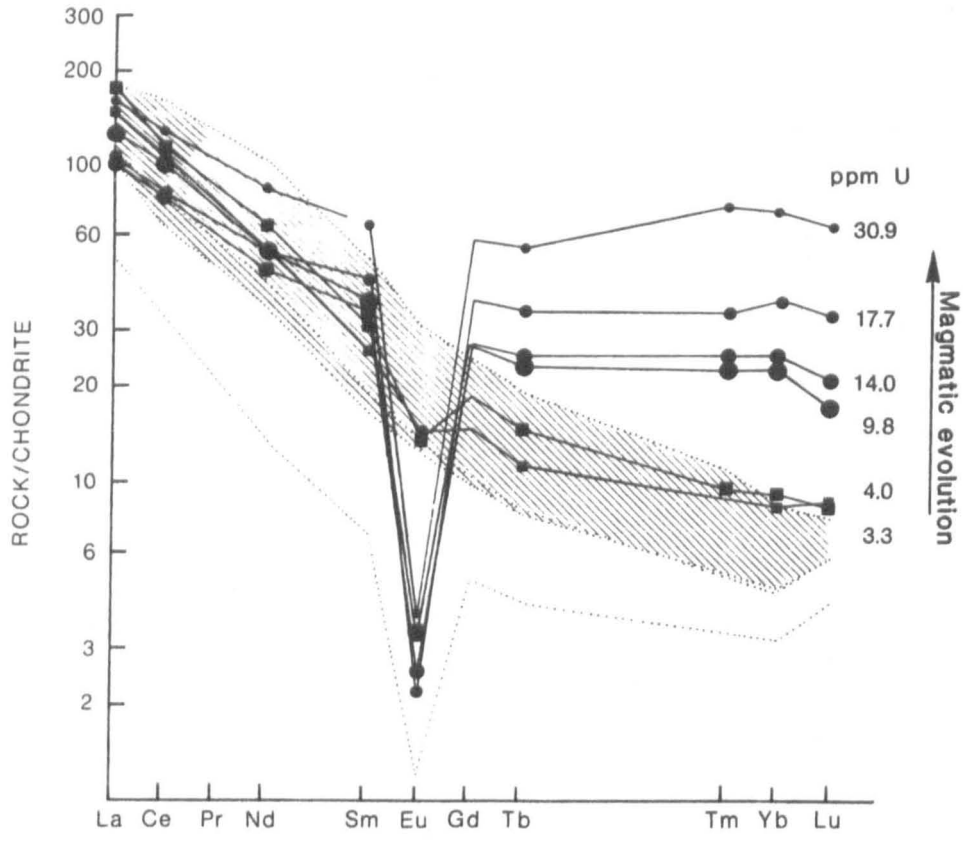

Figure 6.6 Chondrite normalised REE plots for the Cairngorm Granite. Symbols represent: squares, NE Granite, large - SB161, small - SB170 circles, Main Granite, in decreasing order of size, SB177, SB162, N190, N187. Lined area, field of outer Etive units; shaded area, field of Starav units.

accessory mineral assemblages from the NE Granite to the Main Granite (see Section 6.3:5). The effects of this change can be appreciated by studying chondrite normalised REE patterns for typical accessory minerals in NE and Main Granite samples (Figure 6.7). The high LREE/ HREE ratio in the NE Granite may be accounted for by the presence of abundant apatite and sphene and minor allanite (Figure 6.7a). In contrast, the light REE budget in Main Granite samples may be accounted for predominantly by monazite (Figure 6.7b), with contributions from apatite, thorite and Nb-Ta-oxides (Figure 6.7d). The most significant phase which accounts for the enrichment of heavy REE's in the Main

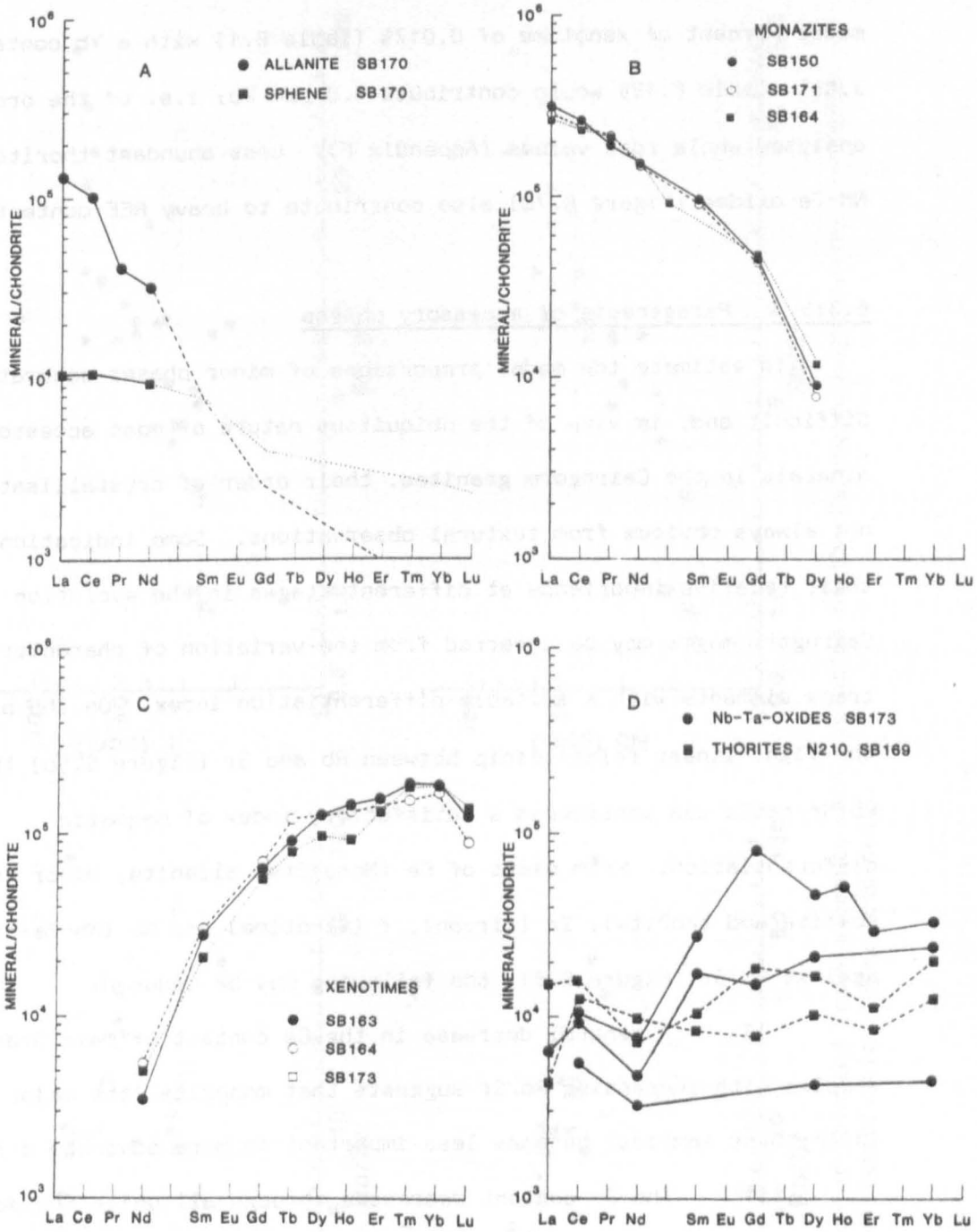

Figure 6.7 Chondrite normalised REE patterns for typical accessory phases in the NE Granite (a) and the Main Granite (b, c and d). Data from electron microprobe analyses (Tables 6.10 to 6.14) and Tindle (1982). Only elements marked by symbols were above electron microprobe detection limits. Intermediate values are interpolated. See Figure 5.11 for zircon and apatite.

Granite, however, is xenotime (Figure 6.7c). For example, a mean model percent of xenotime of 0.017% (Table 6.1) with a Yb content of 3.68% (Table 6.12) would contribute 6.3 ppm Yb; i.e. of the order of analysed whole rock values (Appendix F). Less abundant thorite and Nb-Ta-oxides (Figure 6.7d) also contribute to heavy REE contents.

6.3:5 Paragenesis of accessory phases

To estimate the modal proportions of minor phases accurately is difficult and, in view of the ubiquitous nature of most accessory minerals in the Cairngorm granites, their order of crystallisation is not always obvious from textural observations. Some indication of their relative importance at different stages in the evolution of the Cairngorm magma may be inferred from the variation of characteristic trace elements with a suitable differentiation index. On the basis of the tight linear relationship between Rb and Sr (Figure 6.5b) the Rb/Sr ratio was considered a satisfactory index of magmatic differentiation. From plots of Ce (Monazite, allanite, minor in sphene, apatite and thorite), Zr (zircon), Y (xenotime) and Nb (Nb-Ta-oxides) against Rb/Sr (Figure 6.8), the following may be deduced:

i) A general decrease in the Ce content of Main Granite samples with increasing Rb/Sr suggests that monazite (the major host for Ce in these samples) becomes less important in more advanced differentiates.

ii) The Zr content decreases through all units indicating a decline in zircon abundances with evolution.

iii) A general increase of Y content with Rb/Sr in the Main Granite implies that xenotime may have become more important as differentiation advanced.

iv) The positive relationship between Nb and Rb/Sr supports

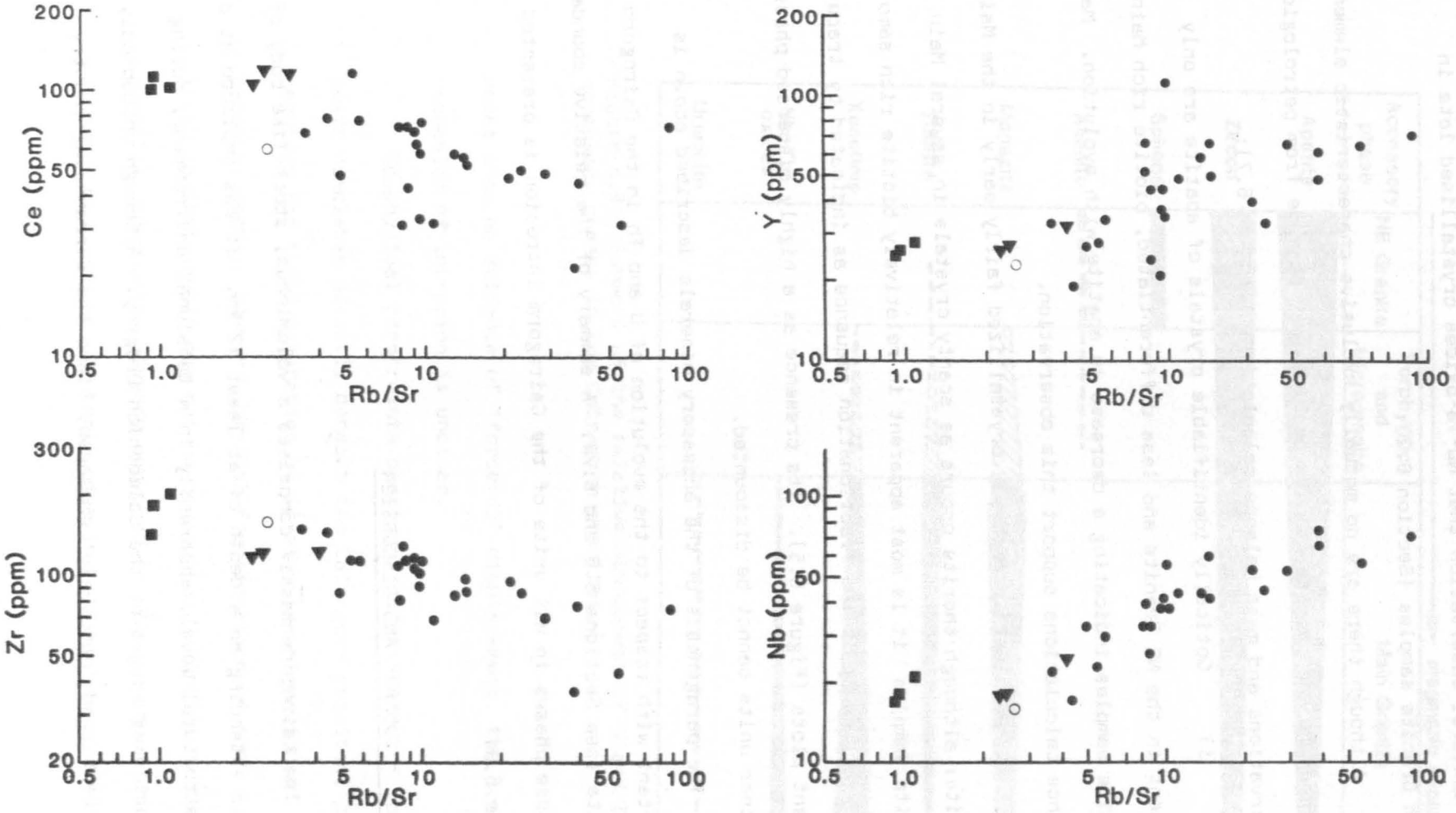

Figure 6.8 Variation of selected trace elements with evolution of the Cairngorm magma, using the Rb/Sr ratio as a magmatic differentiation index (see text).

the textural observation that Nb-Ta-oxides crystallised late in Main Granite samples (Section 6.2).

Although there are no mutually exclusive characteristic elements for apatite and thorite, some deductions may be made from petrological observations and mass balance calculations (Section 6.7):

i) Optically identifiable crystals of apatite are only present in the NE Granite and less differentiated, biotite rich Main Granite samples indicating a decrease in apatite with evolution. Mass balance calculations support this observation.

ii) Thorite probably crystallized fairly early in the Main Granite; although thorite occurs as scanty crystals in several Main Granite samples it is most apparent in relatively biotite rich samples which fall early in the fractionation sequence as indicated by trace element plots (Figure 6.5). Its presence as a highly dispersed phase in other units cannot be discounted.

The paragenesis of the accessory minerals described above is important with respect to the evolution of U and Th in the Cairngorm Granite (see Sections 6.6 and 6.7). A summary of the relative abundances of these phases in all units of the Cairngorm intrusion is presented in Figure 6.9.

6.4 SUMMARY AND DISCUSSION

The Cairngorm massif comprises a voluminous, stock-like body of granite extending to a depth of at least 12 km. It was emplaced at a high structural level, apparently in a tensional environment, during the declining stages of the Caledonian Orogeny. Although undoubtedly discordant and 'passively' emplaced, since the surrounding country

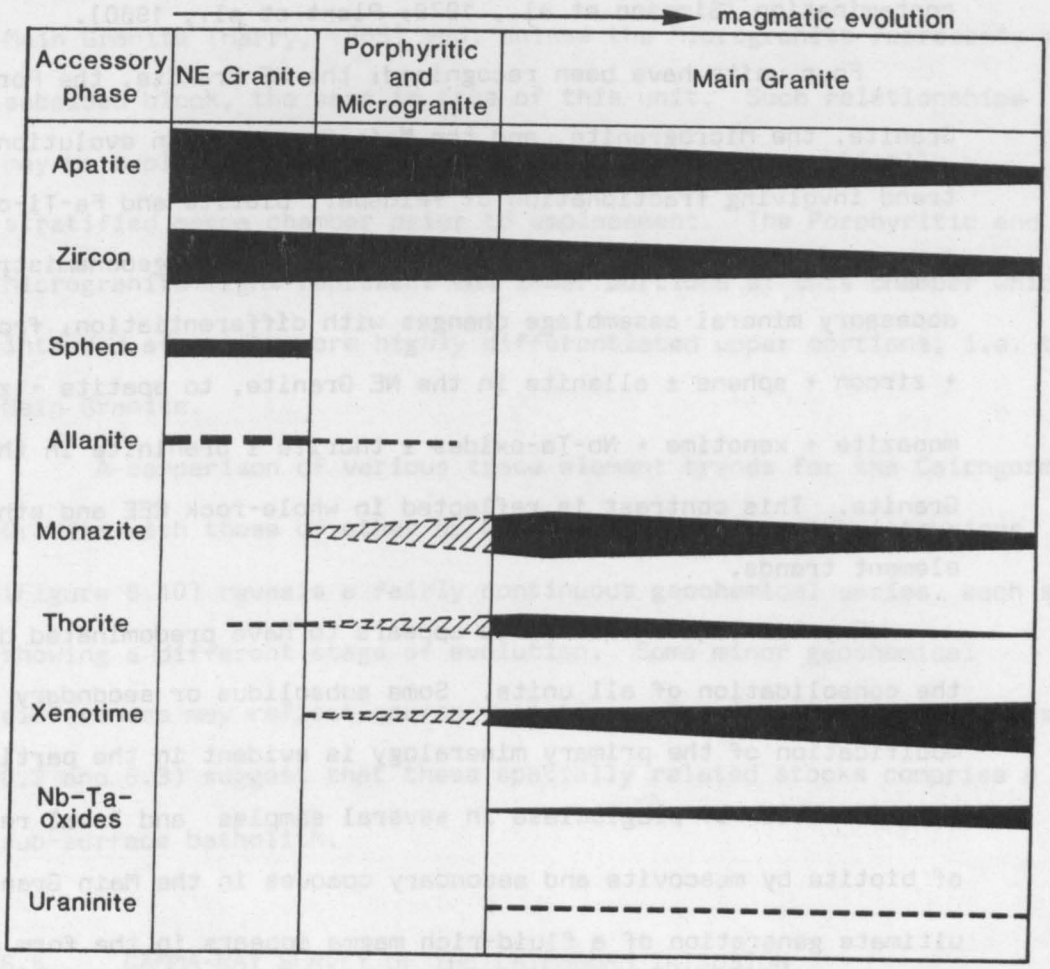

Figure 6.9 Summary of the relative abundances of U and Th bearing accessory phases in the Cairngorm granites.

rocks show no evidence of 'forceful' displacement, the precise mechanism of intrusion is unclear.

Geophysical constraints preclude the existence of voluminous basic cumulates directly beneath the Cairngorm granites, as would be required for their generation by in-situ fractionation of a basaltic parental magma. However, crystal fractionation of such a magma at lower crustal levels may not be discounted. Partial melting of juvenile underplate already enriched in LIL and other incompatible elements may account for their high levels in the magma, levels which

may have been enhanced by fractionation and limited crustal contamination (Simpson et al., 1979; Plant et al., 1980).

Four units have been recognised; the NE Granite, the Porphyritic Granite, the Microgranite, and the Main Granite. An evolutionary trend involving fractionation of feldspar, biotite and Fe-Ti-oxides is evident from petrology, major and trace element geochemistry. The accessory mineral assemblage changes with differentiation; from apatite + zircon + sphene ± allanite in the NE Granite, to apatite + zircon + monazite + xenotime + Nb-Ta-oxides ± thorite ± uraninite in the Main Granite. This contrast is reflected in whole-rock REE and other trace element trends.

Crystal-liquid equilibria appears to have predominated during the consolidation of all units. Some subsolidus or secondary modification of the primary mineralogy is evident in the partial sericitization of plagioclase in several samples and local replacement of biotite by muscovite and secondary opaques in the Main Granite. The ultimate generation of a fluid-rich magma appears in the form of pegmatites and quartz veins invading the surrounding country rocks and exploiting vertical joints in the granite. Locally, the passage of late stage fluids through solidified granite has resulted in the deposition of secondary, hydrated Fe-oxides along microfractures but, in general, the primary magmatic mineralogy and geochemistry has been maintained.

No field evidence is available to clarify the temporal relationship between the NE Granite and the Main Granite, but geochemical and petrological trends suggest that the former unit represents a precursory phase to the major intrusive episode. Differentiation of a magma of NE Granite composition to generate later units is consistent with both geochemistry, mineralogy and geophysics.

Intrusion of the Porphyritic Granite post-dates that of the Main Granite (Harry, 1965) and, unless the Microgranite represents a subsided block, the same is true of this unit. Such relationships may be explained by the existence of a high-level, vertically stratified magma chamber prior to emplacement. The Porphyritic and Microgranite might represent the lower portions of this chamber which intruded after the more highly differentiated upper portions, i.e. the Main Granite.

A comparison of various trace element trends for the Cairngorm Granite with those of other NE Grampian Siluro-Devonian intrusions (Figure 6.10) reveals a fairly continuous geochemical series, each stock showing a different stage of evolution. Some minor geochemical differences may reflect source variation. Gravity data (see Figures 6.2 and 6.3) suggest that these spatially related stocks comprise a sub-surface batholith.

6.5 GAMMA-RAY SURVEY OF THE CAIRNGORM INTRUSION

6.5:1 Field work

The survey was conducted during Spring 1980 following the procedure outlined in Section 5.7. Exposure is good on the steep slopes over high ground and on the numerous buttresses overlooking glens which transect the plateau. Extensive drift cover on valley floors, particularly along Glen Einich and Glen Avon (Figure 6.1) prevented complete coverage in these areas. The flat tops of the plateau offer little outcrop except for abundant, loose blocks of granite weathered in-situ; readings were taken on these where fresh outcrop was limited or absent. Access to the area is poor, particularly in the south,

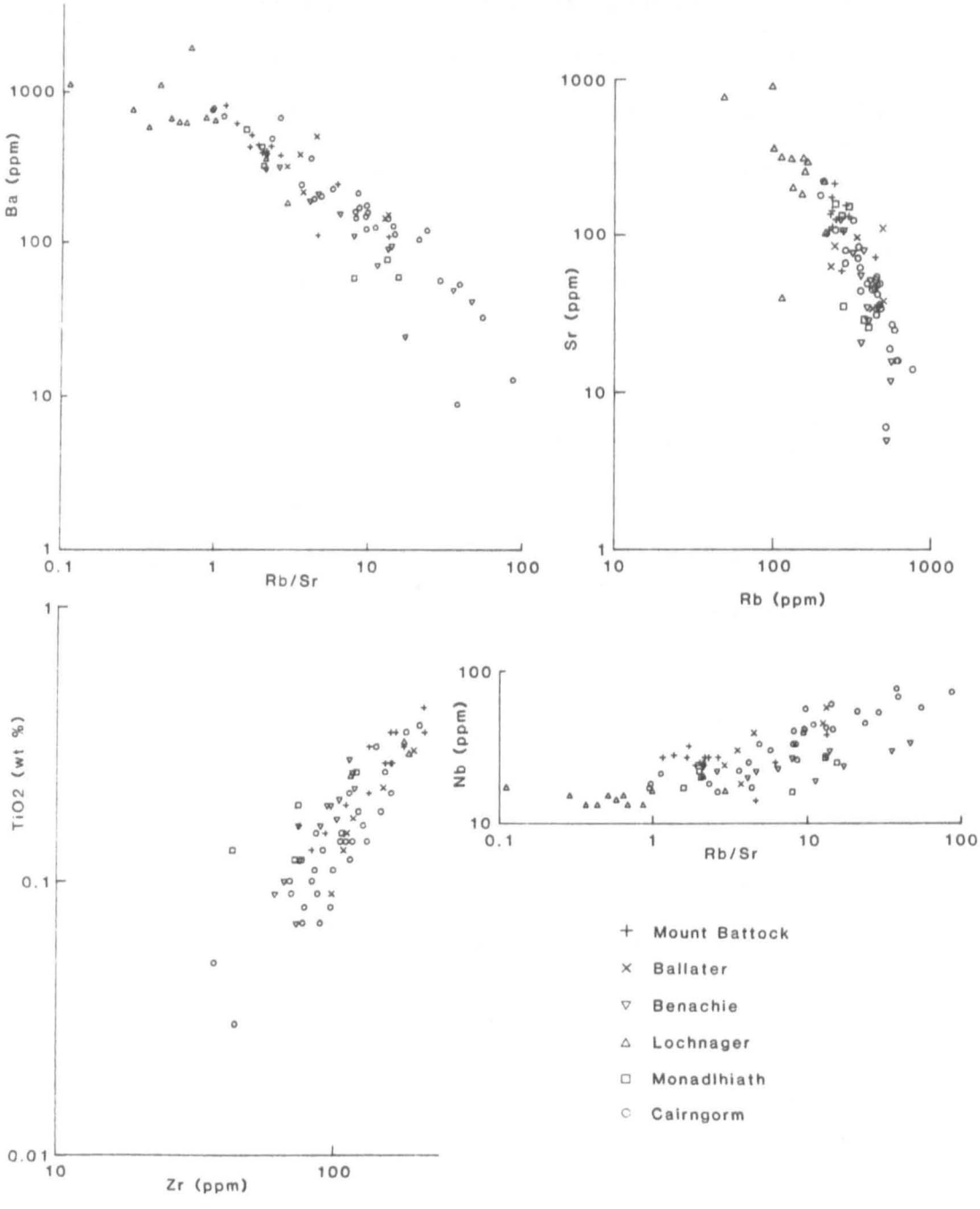

Figure 6.10 Comparison of selected trace element trends from the Cairngorm Granite and other NE Grampian intrusions. Data for other intrusions from P. Webb (pers. comm.).

resulting in incomplete coverage of remote regions requiring longer than one day traverses.

A total of 121 gamma-ray stations were covered, supplemented by a further 25 radioelement analyses of samples collected by G. Brown and J. Cassidy and analysed for this study by ENAA and XRF (Section 4.2 and Appendix A). Grid references for all stations and sample locations are presented in Appendix G.

6.5:2 Results

Raw field data were reduced using the relevant calibration equations for spec III (Section 4.1:3) and averaged to yield mean radioelement concentrations at each station (results are tabulated in Appendix G). The range and maximum value of U(2-30 ppm) and Th(10-59 ppm) contents are considerably higher than those observed for the Etive Complex, and indeed for any Caledonian granite yet surveyed

ROCK TYPE	No. γ-ray stations	No. Lab analysed samples	Th (ppm) mean ± 1σ	U (ppm) mean ± 1σ	Th/U mean ± 1σ	K_2O (%) mean ± 1σ
NE GRANITE	9	0	26.5 ± 7.5	4.3 ± 1.6	6.7 ± 2.0	4.6 ± 0.5
PORPHYRITIC GRANITE	5	1	25.8 ± 6.0	6.1 ± 2.0	5.0 ± 2.4	4.6 ± 0.5
MICROGRANITE	0	3	20.7 ± 0.6	4.4 ± 0.7	4.8 ± 0.7	5.5 ± 0.2
MAIN GRANITE	99	21	32.3 ±10.7	10.1 ± 4.0	3.5 ± 1.5	4.7 ± 0.4
APLITE	1	0	32.8	10.3	3.2	6.6
MOINIAN SCHISTS at or near contact	5	0	21.0 ± 7.6	5.7 ± 1.5	3.7 ± 0.8	4.3 ± 0.4
MONIAN SCHISTS elsewhere	4	0	10.4 ± 2.1	2.3 ± 0.8	4.6 ± 0.9	3.4 ± 0.6

Table 6.5 Radioelement contents of Cairngorm units and surrounding country rocks. Mean Th/U ratios were calculated from individual sample ratios.

(Simpson et al., 1979; Cassidy, 1980). The Th and U contents (Table 6.5) of less evolved units are significantly lower than values for the Main Granite but the K_2O content remains approximately constant (with the exception of the Microgranite). A decrease in the mean Th/U ratio from the NE Granite, through the Porphyritic and Microgranite, to the Main Granite indicates a preferential enrichment of U over Th with differentiation. A plot of U against Th for individual stations (Figure 6.11) reveals a general positive correlation between these two elements but with a high degree of scatter, suggesting that some remobilisation of U has occurred.

Aplites are poorly represented at outcrop, and are seldom wide enough for effective analysis by in-situ gamma-ray spectrometry. One successful analysis (Table 6.5) gave U and Th values close to the mean for the Main Granite. There is no evidence, therefore, that radio-elements are enriched any further in the dry residual melt.

Moinian schists, at or near the granite contact appear to be enriched in both U and Th relative to similar rocks elsewhere (Table 6.5). Numerous aplitic and granitic veinlets were observed at three of these locations and may account for this enrichment. The presence of granite just below the surface or permeation of U-rich fluids into the country rock may be the cause of enrichment at other locations. Areal distribution maps (Figures 6.12 to 6.15) could not be contoured due to the absence of systematic radioelement trends and the lack of control points in remote or drift-covered regions. Although there are no smooth areal trends, several general points may be noted from the radioelement distribution maps.

i) Thorium (Figure 6.12). Within the Main Granite, high Th values predominate in the eastern half of the intrusion and low values

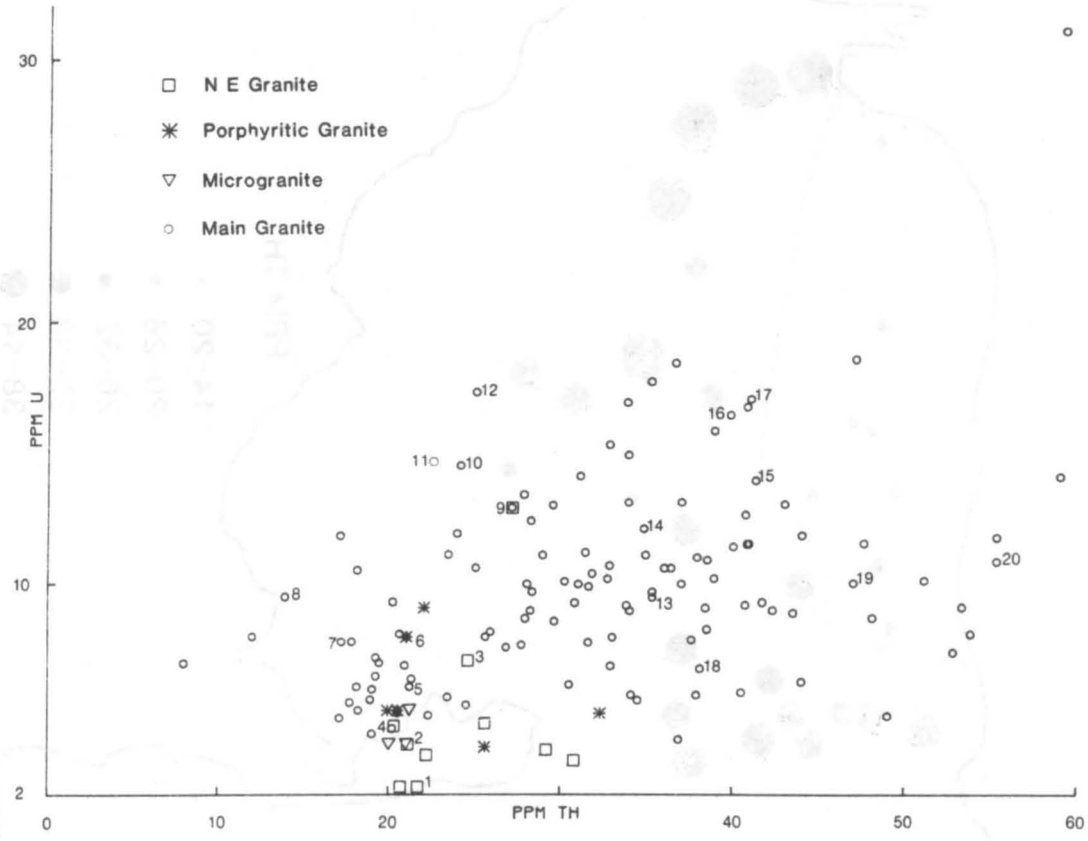

Figure 6.11 Variation of U and Th in the Cairngorm granites. Data points represent mean station values. Numbered points are samples used for fission track studies:
1, SB160; 2, SB161; 3, SB170, 4, SB175; 5, SB163; 6, N197; 7, SB156; 8, SB171; 9, SB166; 10, N188; 11, SB178; 12, SB176; 13, SB173; 14, SB164; 15, SB162; 16, SB150; 17, N211; 18, SB177; 19, N210; 20, SB169.

in the west and south-west.

ii) Uranium (Figure 6.13). The highest U values in the Main Granite tend to lie in the central portion of the intrusion. Values in the east, west and south-west are variably low-medium.

iii) Th/U ratio (Figure 6.14). Th/U values are generally high in the NE Granite and in the eastern lobe of the Main Granite. Elsewhere in the Main Granite the ratio tends to be medium-low. Although some anomalously high Th/U values may reflect depletion in U through post-magmatic hydrothermal processes or surficial weathering, it is felt that much of the control on Th/U ratios is magmatic (see Section 6.7).

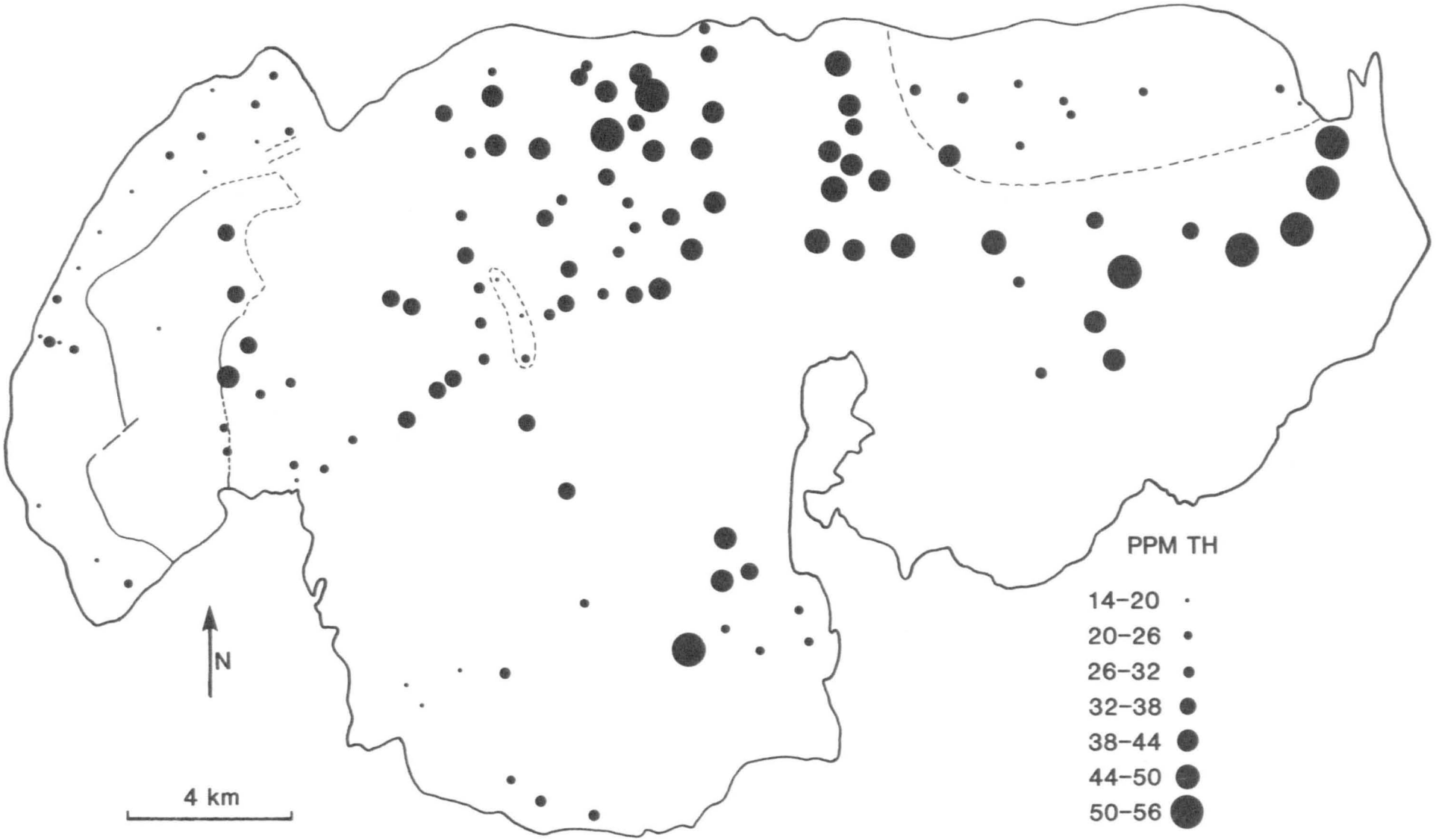

Figure 6.12 Thorium distribution map for the Cairngorm Granite. Geological boundaries as in Figure 6.1.

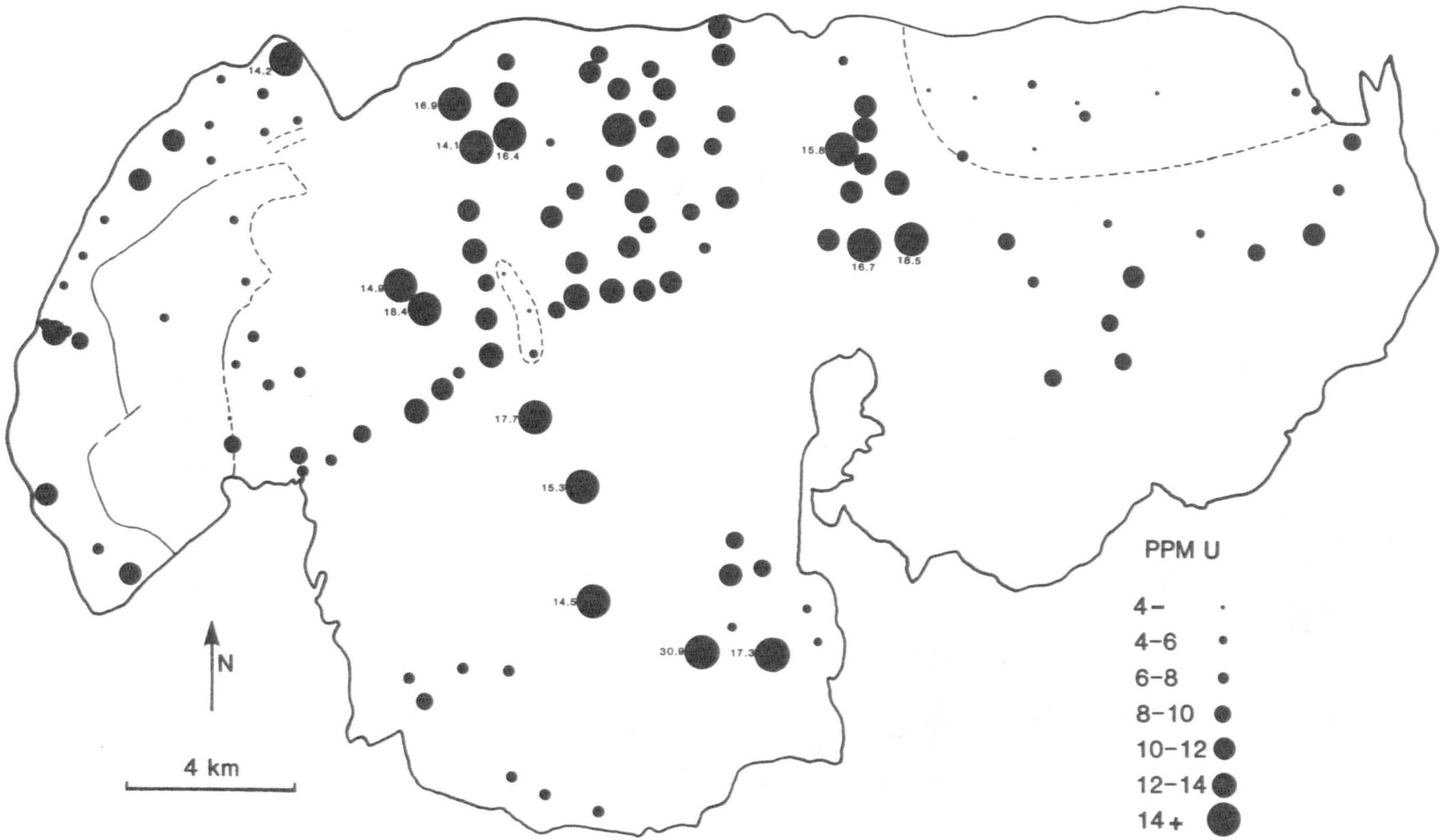

Figure 6.13 Uranium distribution map for the Cairngorm Granite. Geological boundaries as in Figure 6.1.

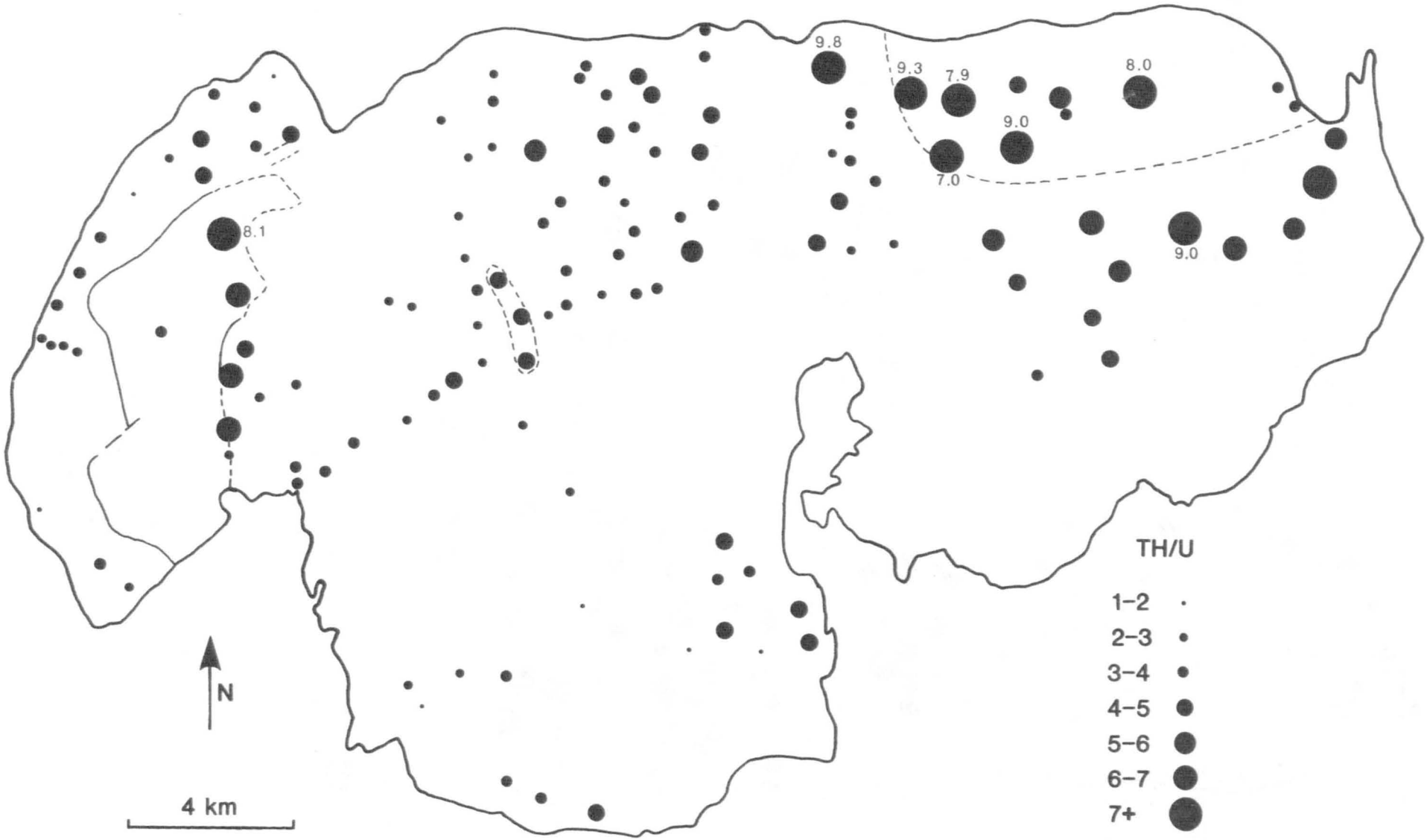

Figure 6.14 TH/U distribution map for the Cairngorm granite. Geological boundaries as in Figure 6.1.

Figure 6.15 Potassium distribution map for the Cairngorm Granite. Geological boundaries as in Figure 6.1.

iv) K_2O (Figure 6.15). Unlike U and Th, the K_2O distribution is essentially uniform throughout all units.

Points (i) and (ii) above, suggest that the factors controlling the enrichment of U and Th within the Cairngorm granites may be, to some extent, independent.

6.6 TRACE ELEMENT EVIDENCE FOR MAGMATIC URANIUM AND THORIUM VARIATION

The variation of U, Th and Th/U with differentiation, as indexed by Rb/Sr is shown in Figure 6.16. Samples N82 and N83 appear to be anomalous, with exceptionally low Th contents and relatively low U contents (reasons for this depletion are discussed in Section 6.7:2). Sample N187 is anomalously high in U. In general, all plots show a high degree of scatter, but the following trends are apparent from Figure 6.16.

i) Uranium content increases with differentiation, even within the Main Granite.

ii) Although Th contents in the Main Granite are generally higher than in less evolved units, there is no obvious tendency for Th to increase with differentiation within the Main Granite. However, there are no low Th values (except N82 and N83) where Rb/Sr $>$ 20.

iii) Th/U decreases with differentiation, although if anomalous samples are omitted, there is little variation in Th/U where Rb/Sr $>$ 20.

Some decoupling in the behaviour of U and Th in the Main Granite is indicated. Many of the highest Th contents are found in samples with Rb/Sr $<$ 10, whilst most of the highest U contents are found in samples with Rb/Sr $>$ 10.

The variation of U and Th with other trace elements (Figure 6.17) again shows the anomalous nature of samples N82 and N83, and to some extent

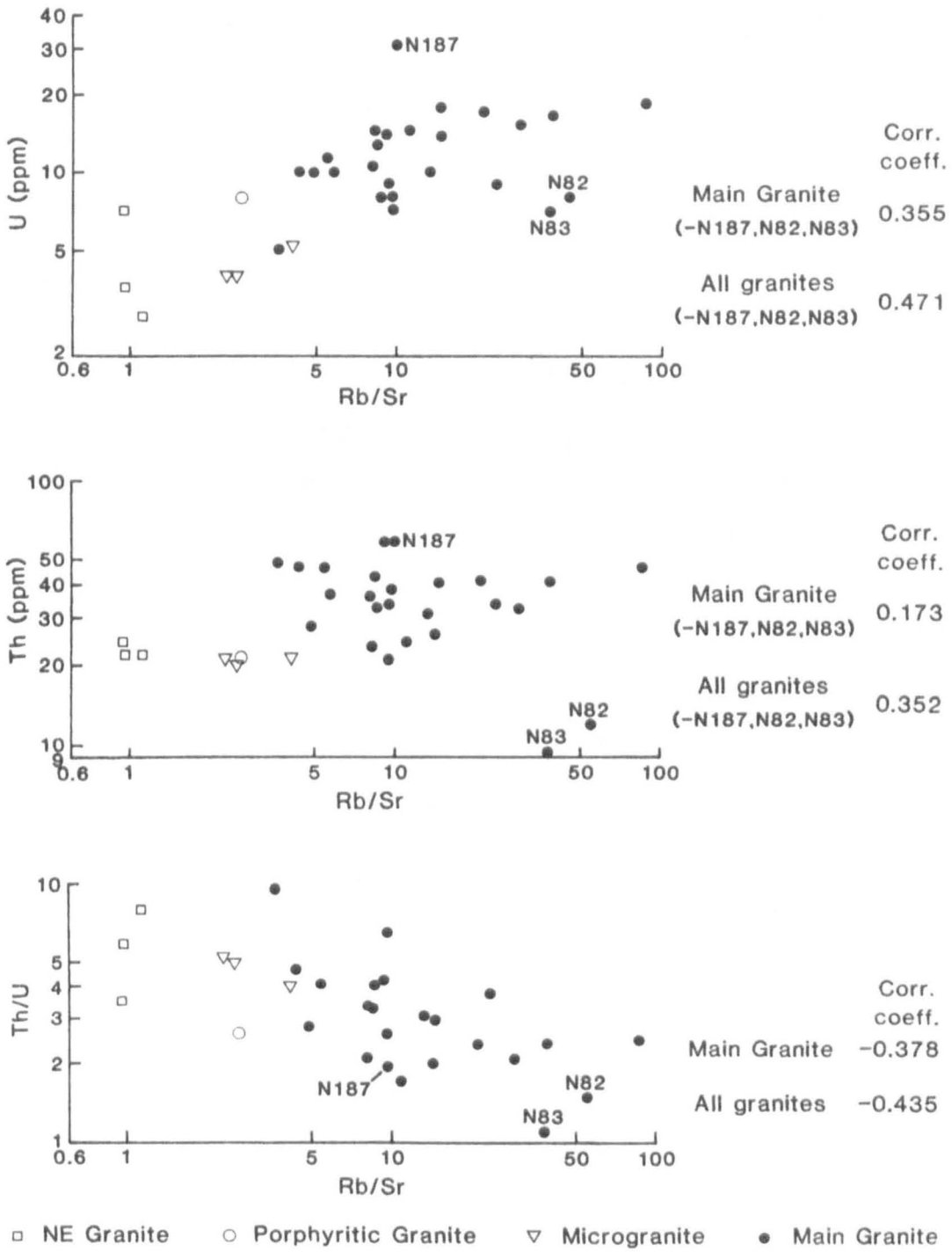

Figure 6.16 Variation of U and Th with Rb/Sr ratio in the Cairngorm Granite.

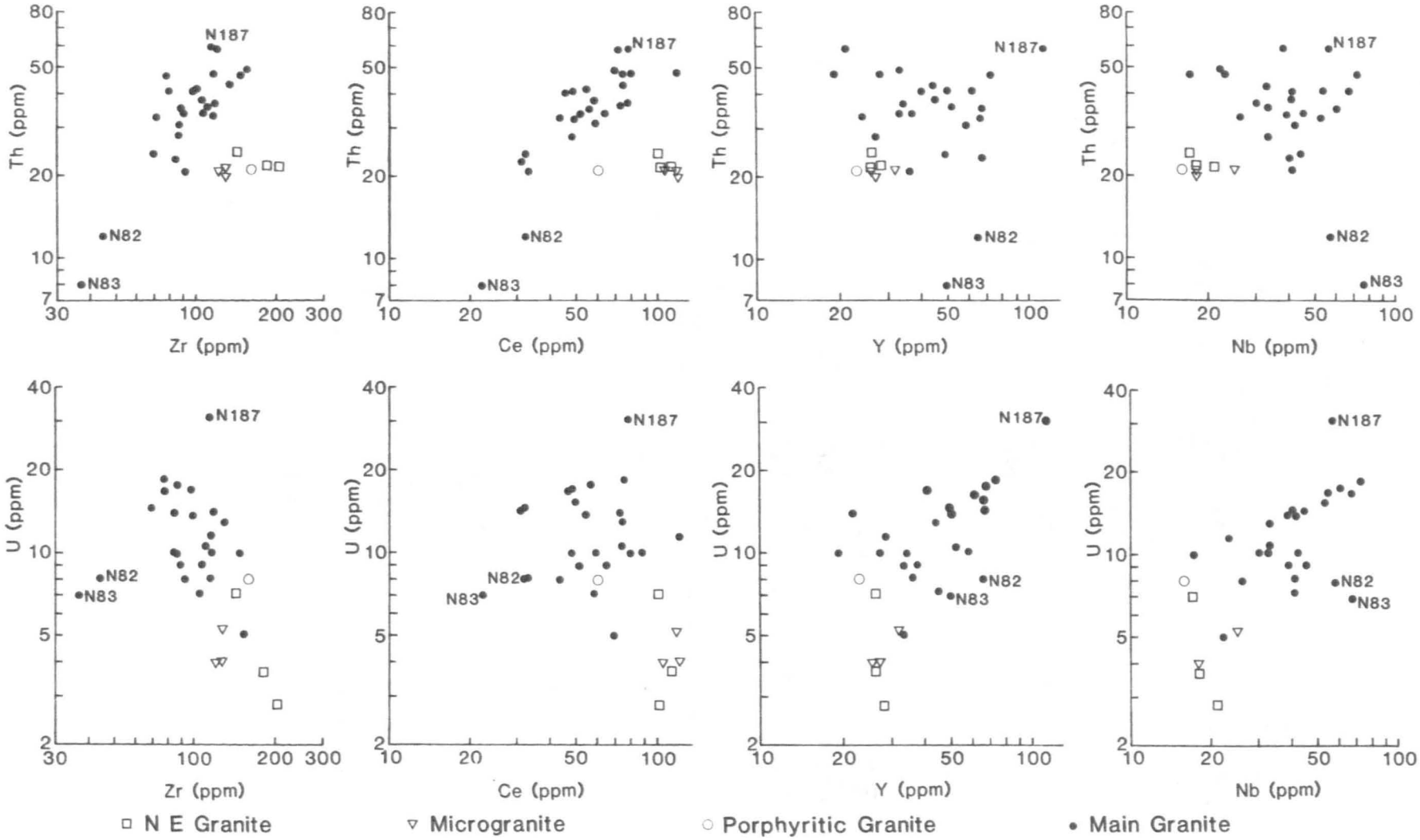

Figure 6.17 Variation of U and Th with selected trace elements in the Cairngorm Granite.

N187. The significance of these plots with respect to 'host' accessory phases is summarized below.

i) The antipathetic relationship between U and Zr indicates that zircon is not a major host for U; the apparent correlation is coincidental, reflecting only the trends of each element with differentiation. Th contents within the Main Granite show a vague tendancy to increase with Zr, but zircon is again not a major host for this element (see Section 6.7:2).

ii) There is a marked positive correlation between Th and Ce in the Main Granite which is unrelated to Rb/Sr trends. This suggests that a Ce-bearing phase, probably monazite which is ubiquitous in the Main Granite (see Figure 6.9), may be a major host for Th. However, the isolated position of the less evolved units on this plot would suggest that the same phase is not a significant Th host in these units. Indeed, little monazite occurs in these units and more probable Th hosts are sphene and allanite (see Figure 6.9). There is little correlation between U and Ce.

iii) Y plots are highly scattered but show a slightly positive correlation with U. The role of xenotime as a U and Th host is discussed further in Section 6.7:2 but it is clear from these plots that it is unlikely to be the major host for either element, especially Th.

iv) If anomalous samples are omitted, there is a positive correlation between U and Nb in the Main Granite. The presence of significant quantities of U in late magmatic Nb-Ta-oxides (see Section 6.7:2) would explain this trend. However, there is a marked scatter of points lying on the low U side of this trend indicating that either not all Nb-minerals are rich in U, or that U has been remobilised and

depleted from several samples. Some scatter is due to U held in other phases.

6.7 MINERALOGY AND MASS BALANCE OF URANIUM AND THORIUM

A combination of 'Lexan' fission track studies, electron microprobe analyses of minor phases and mass balance calculations was employed to locate and identify U and Th hosts, and to quantify, as far as possible, the whole-rock U and Th budget for all units of the Cairngorm Intrusion.

6.7:1 The NE Granite

Three samples with different U contents and Th/U ratios were selected for fission track studies (Table 6.6). Primary U host phases are present in approximately the same abundance in all three samples, but the amount of secondary U distribution increases with whole rock U contents. The characteristics of radioelement-bearing phases in the NE Granite are summarised below.

Sample No.	No. in Fig. 6.11	Th (ppm)	U (ppm)	Th/U
SB160	1	21.8	2.8	8.0
SB161	2	21.8	3.7	5.9
SB170	3	24.6	7.1	3.5

Table 6.6 NE Granite samples used for fission track studies

i) Apatite, although relatively abundant, does not represent a significant contribution to whole rock U levels; fission tracks associated with this mineral are of very low density compared with other U-bearing phases.

ii) Fission tracks associated with zircon vary from medium to high density (Plate 6.2a) reflecting an inter-crystal variation in U (and possibly Th) content, as confirmed by microprobe analyses (Table 6.7).

iii) Sphene yields high density, evenly distributed tracks. (Plate 6.2a). Both U and Th contents of sphene are below the detection limits of the electron microprobe (Table 4.13) but the presence of saturated fission tracks related to this mineral indicates U contents $\geq$ 100 ppm. Microprobe analysis (Table 6.7) does, however, suggest that Th contents are higher than U.

iv) One crystal of allanite was found in a section of sample SB170, and one in three standard thin sections of sample SB160. Electron microprobe analysis (Table 6.7) suggests that many of the high density tracks associated with allanite (Plate 6.2b) are due to Th fission. The presence of tracks in microfractures and boundaries adjacent to allanite crystals, which decrease in concentration with distance (Plate 6.2b) indicate some remobilisation of U, possibly related to incipient metamictisation.

v) Secondary U occurrences. In sample SB170, low density fission tracks occur over biotite, particularly along grain boundaries, partially sericitised feldspar, and microfractures, where they are associated with Fe-staining (Plate 6.2a and b). In samples SB160 and SB161 secondary U locations are restricted to low density dissemination in biotite.

Approximate contributions to whole rock U and Th contents from zircon and apatite were calculated as follows.

a) All whole-rock Zr (see Appendix F) was assigned to zircon, and a mean analysis of zircon from data in Table 6.7 was used. Although these analyses are considerably different with respect to U and Th, the

Plate 6.2 Photomicrograph and fission track pairs showing U locations in the NE Granite. Fields of view are given in mm.

a) Sample SB170. High density fission tracks are associated with sphene (S) and zircon (Z). Low density tracks occur over microfractures through feldspar, quartz and biotite. Dispersed tracks over feldspar increase in density with the degree of alteration; U probably occupies interstitial sites between sericite nuclei. Unevenly dispersed tracks also occur over biotite.

b) Sample SB170. Thorium fission probably accounts for a significant proportion of the high density tracks over allanite (A1). Tracks along microfractures and over biotites (especially along crystal boundaries) represent secondary U remobilisation. Track densities in microfractures/grain boundaries decrease with distance from allanite and may indicate remobilisation of U from the crystal structure of allanite.

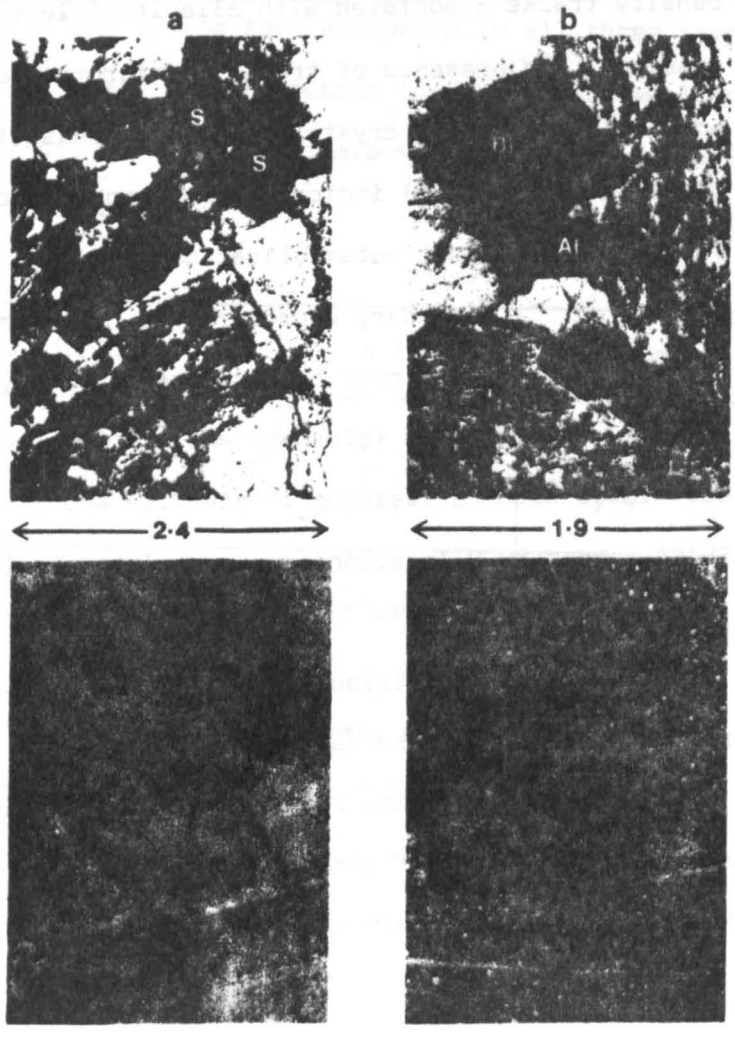

Sample No. MINERAL	SB170 ZIRCON (h.d.t.)	SB170 ZIRCON (m.d.t.)	SB170 SPHENE	SB170 ALLANITE
La_2O_3			(0.39)	4.66
Ce_2O_3			1.03	11.01
Pr_2O_3				1.33
Nd_2O_3			0.68	3.04
Hf_2O_3	1.61	1.28		
Nb_2O_5			0.49	
Y_2O_3	0.70		1.39	
ZrO_2	60.13	63.61		
P_2O_5	1.03			
ThO_2	(0.15)	(0.09)	(0.19)	1.78
UO_3	1.33	(0.04)	(0)	(0)
SiO_2	34.01	34.03	29.58	28.75
TiO_2			32.94	2.84
Al_2O_3	0.59	0.53	2.12	14.79
FeO	0.28	0.18	2.53	12.57
MnO			0.11	0.40
CaO			25.50	5.96
TOTAL	99.83	99.76	96.95	87.13

Table 6.7 Electron microprobe analyses of accessory phases in the NE Granite. All abundances are in wt.%. Values in brackets indicate concentrations < 2σ error on background. The low total for allanite is due to the presence of unanalysed elements (e.g. F, H_2O) and those below detection limits (e.g. other LREEs, P_2O_5, Cl). (h.d.t. = high density tracks, m.d.t. = medium density tracks).

observed variation in fission track densities over zircons in all three samples, suggests that a mean analysis is appropriate for mass balance calculations.

b) Uranium and Th contents of apatite are below electron microprobe detection limits. A mean content of 50 ppm U and Th (see Section 5.10) was considered appropriate, being consistent with the low fission track density associated with this mineral phase. A P_2O_5 content of 41% (Deer et al., 1972) was assumed and all whole rock P_2O_5 assigned to apatite.

Sample No.	Apatite U ppm	Apatite U %	Apatite Th ppm	Apatite Th %	Zircon U ppm	Zircon U %	Zircon Th ppm	Zircon Th %	Remainder U ppm	Remainder U %	Remainder Th ppm	Remainder Th %	Th/U
SB160	0.2	5.4	0.2	0.7	2.6	91	0.5	2.2	0.1	3.6	21.2	97	212
SB161	0.2	4.9	0.2	0.8	2.3	62	0.4	1.9	1.2	32	21.2	97	17.7
SB170	0.1	1.4	0.1	0.4	1.8	25	0.3	1.3	5.2	73	24.2	98	4.6

Table 6.8 Approximate contributions to whole rock U and Th from apatite and zircon in the NE Granite.

It is clear from Table 6.8 that most of the Th in the NE Granite is not accounted for by apatite and zircon and is probably located in sphene and allanite. Estimates of the modal percentages of sphene and allanite may be made by assigning all whole rock Ce and Nd (see Table 6.7 and Appendix F) to these minerals and solving simultaneous equations. This will overestimate abundances of sphene and allanite due to the presence of light REEs in other mineral phases, particularly apatite. Using Th analyses from Table 6.7 and estimated modal percentages of sphene and allanite the contribution to whole rock Th from these minerals is 25.5 ppm in sample SB161 and 16.1 ppm in sample SB170. Bearing in mind that these are probably overestimates and that uncertainties arise from the lack of data on Ce/Nd ratios in other minerals, these results suggest that in sample SB170, at least, a deficit of Th still remains to be accounted for. Low concentrations of Th in other phases would remain undetected by the present fission track method and it is possible that sporadically distributed minor phases such as thorite are present.

The remaining percentage of U (Table 6.8) increases with whole rock U content and with the observed increase in secondary U distribution and alteration of the samples. Post-magmatic remobilisation and/or addition of U by hydrothermal fluids, possibly related to the later? Main Granite, is suggested.

6.7:2 The Main Granite

Seventeen samples, representing the range of whole-rock U, Th, and Th/U values for this unit, were studied using the "Lexan" fission track technique (Table 6.9 and Figure 6.13).

No. in Fig. 6.13	Sample No.	ppm Th	ppm U	Th/U
20	SB169	55.3	10.8	5.1
19	N210	47.6	11.5	4.1
15	SB162	41.3	13.9	3.0
17	N211	40.8	16.7	2.4
16	SB150	39.8	16.4	2.4
18	SB177	38.2	7.1	5.6
13	SB173	35.3	9.7	3.6
14	SB164	34.8	12.1	2.9
9	SB166	27.1	12.9	2.1
12	SB176	25.0	17.3	1.4
10	N188	24.1	14.5	1.7
11	SB178	23.1	14.2	1.7
5	SB163	21.2	6.1	3.5
6	N197	21.0	8.0	2.6
4	SB175	20.2	4.5	4.5
7	SB156	17.8	7.8	2.3
8	SB171	13.9	9.5	1.5

Table 6.9 Main Granite samples used for fission track studies.

A complex U distribution is evident for most samples, comprising both primary and secondary modes of occurrence. The various observed radioelement bearing phases are discussed briefly below, and a summary of the fission track distribution in individual samples presented in Table 6.16.

Primary U-Th hosts

i) Zircon. Fission tracks associated with zircon are of medium to high density and tend to be variable within any one thin section.

Microprobe analyses (Table 6.10) reveal a wide range of U and Th contents, which do not correlate with whole-rock values. High U-Th zircons tend to be slightly red and partially metamict.

ii) Monazite gives rise to high density fission tracks. Thorium and U contents vary between 6.2 - 12.2 wt.% and ∿0.07 - 0.9 wt.% respectively (Table 6.11) and no correlation was found with whole rock values. In comparison with monazites from the Central Starav Granite (Table 5.18) those from the Cairngorm Main Granite are relatively enriched in middle-heavy REEs, reflecting whole-rock geochemical contrasts.

iii) Xenotime yields high density fission tracks. Vlasov (1966) reported a marked predominance of U over Th impurities in most xenotimes but analyses from the Main Granite (Table 6.12) show U and Th abundances to be approximately equal, ranging between ∿0.3 - 2.6 wt.%.

iv) Xenotime/zircon. Xenotime (YPO_4) is isostructural and isomorphous with silicates of Zr, U and Th. The isomorphism accounts

$$Y^{3+} + P^{5+} \rightleftarrows (Zr, U, Th)^{4+} + Si^{4+}$$

for the invariable presence of U and Th in xenotime and, in this case, for the xenotime-zircon series (Table 6.13). Uranium contents are similar to those in xenotime but Th contents are much more variable; 0.5 - 5.6 wt.%. This phase has only been identified in two samples from the Main Granite and has not previously been reported in British granites.

v) Thorite is less abundant than zircon, xenotime and monazite and yields very high density tracks (Plate 6.3a and b). From its textural relationship (Section 6.2+1) it is inferred that thorite crystallised relatively early in the Main Granite. Microprobe analyses (Table 6.13) show U contents to be low compared to thorites in the Etive Complex (Tables 5.7, 12, 15, 18). They are also rich in REEs

SAMPLE NO	SB177	SB177	SB177	SB169	SB169	SB173	SB163	SB163	SB150	SB150	SB166	SB166	SB166
Ce_2O_3							(0.09)			0.20			
Nd_2O_3										0.20			
Dy_2O_3										0.65			
Er_2O_3									(0.17)	(0.21)			
Yb_2O_3			0.34				(0.16)	0.36		0.76	(0.14)		0.58
Hf_2O_3	1.63	1.93	2.23	3.21	2.00	1.79	1.17	1.12	1.29	1.95	0.98	1.22	3.62
Nb_2O_5						(0.27)				0.82			
Y_2O_3	1.58					(0.20)	0.77	(0.21)		3.05			
ZrO_2	57.83	62.03	57.56	54.90	64.38	62.07	59.31	63.10	61.51	43.35	63.05	61.06	56.74
P_2O_5	2.55	2.75	2.51										
ThO_2	(0.03)	(0.19)	(0.02)	3.25	(0.26)	(0)	(0.18)	(0.02)	(0.22)	1.58	(0)	(0)	0.50
UO_3	0.68	0.91	0.56	1.30	0.77	0.48	(0.04)	(0.20)	(0.14)	1.25	(0.08)	(0.22)	2.59
SiO_2	29.97	30.78	29.93	26.87	31.49	34.14	32.95	34.48	33.25	25.52	33.35	32.68	33.69
TiO_2									(0.08)	0.32			
Al_2O_3				0.63	(0.15)	0.73	1.23	0.60		2.06			
FeO	1.71	0.45	2.25	2.71	0.33	0.26	2.92	(0.10)	0.57	1.20	0.13	0.82	
CaO	0.36	0.12	0.88	1.10		0.09			0.22	2.01	(0.03)	0.10	(0.05)
K2O				0.12	(0.03)		(0.16)			(0.10)			
TOTAL	96.34	99.16	96.28	94.09	99.41	100.03	98.98	100.19	97.45	85.23	97.76	96.10	97.77

Table 6.10 Electron Microprobe analyses of zircons in the Main Granite. All abundances are in wt.%. Data in brackets indicate concentration < 2σ error on background. The mean analysis of zircon ($ZrSiO_4$) used for mass-balance calculations is:

	ZrO_2	Zr	ThO_2	Th	UO_3	U
wt.%	60.52	44.8	0.35	0.3	0.67	0.6
± 1σ	±2.9		±0.9		±0.6	

The U and Th contents of zircon are highly variable, but do not correlate with whole rock values; nor are they consistent within any one sample. A mean zircon analysis was, therefore, considered most appropriate for mass balance calculations.

SAMPLE NO	SB177	SB169	SB173	SB164	SB164	SB150	SB171
La_2O_3	10.62	9.99	10.79	10.16	10.94	11.82	10.83
Ce_2O_3	23.49	24.95	26.99	23.57	26.52	26.14	24.45
Pr_2O_3	2.25	2.82	2.86	3.16	3.39	2.72	3.00
Nd_2O_3	9.70	10.72	11.10	11.31	10.76	10.70	10.63
Sm_2O_3	1.30	2.31	2.10	2.06	2.50	2.27	2.10
Gd_2O_3		1.21	1.49	1.45	1.34	1.41	1.34
Dy_2O_3				0.48		(0.34)	(0.30)
Nb_2O_5						(0.09)	
Y_2O_3	1.72		1.02	2.66		1.38	2.00
P_2O_5	23.88	24.87	27.81	24.17	26.58	28.12	25.68
ThO_2	11.85	10.21	7.69	13.89	9.79	9.31	12.34
UO_3	1.06	(0.45)	(0.46)	0.96	(0.36)	(0.09)	0.56
SiO_2	4.98	2.68	2.25	4.15	2.39	2.00	3.38
FeO	1.92	2.07		(0.09)		(0.15)	0.35
CaO		0.31	0.19	0.17	0.65	0.70	0.42
K_2O				(0.09)		(0.14)	(0.19)
PbO							(0.34)
S				(0.04)		(0.08)	
TOTAL	92.77	92.59	94.75	97.41	95.22	97.46	97.91

Table 6.11 Electron microprobe analyses of monazites in the Main Granite. All abundances are in wt.%. Data in brackets indicate concentrations < 2σ error on background.
The mean analysis for monazite ((Ce, La, Th)PO_4) used for mass-balance calculations is:

	Ce_2O_3	Ce	ThO_2	Th	UO_3	U
wt.%	25.16	21.4	10.73	9.4	0.56	0.5
± 1σ	±1.4		±2.1		±0.3	

and contain significant quantities of Nb, Y, Zr and P.

vi) Nb-Ta-oxides. A variety of complex, U-bearing Nb-Ta-oxides were located from fission track studies, and identified by microprobe analysis (Table 6.14). They occur predominantly as inclusions in quartz, or along boundaries adjacent and between quartz crystals (see Plates 6.3C and 6.4B and C). Several were noted along microfractures where they tend to be opaque or semi-opaque and associated with secondary Fe-oxides (see Plate 6.4A). Fission tracks associated with these minerals are generally of very high density, often causing thermal discolouration

SAMPLE NO	SB175	SB173	SB173	SB163	SB164	SB164	SB166	SB166	SB171	SB171
Nd_2O_3		0.37	0.32	0.28	0.59	0.42	0.38	0.25	0.45	0.44
Sm_2O_3			0.94	0.69	0.52	0.72	0.93	0.63	0.86	0.71
Gd_2O_3	0.73	1.76	2.55	2.09	1.65	2.19	2.31	2.40	2.51	2.30
Tb_2O_3		0.47	0.56	0.56	(0.37)	0.75	0.74	0.64	0.99	0.70
Dy_2O_3	4.42	3.84	6.06	5.12	4.07	5.02	4.87	6.04	5.55	5.39
HoO_3	1.52	0.83	1.31	1.29	1.00	1.26	0.97	1.46	1.04	1.30
Er_2O_3	4.07	3.48	4.13	3.99	3.59	3.89	3.33	3.98	3.53	3.80
Tm_2O_3	0.69	0.70	(0.41)	0.78	0.87	0.58	0.62	0.51	(0.39)	0.74
Yb_2O_3	5.23	4.65	4.24	4.63	3.53	4.56	4.48	3.88	3.40	3.36
Lu_2O_3	1.21	0.54	0.54	0.51	(0.30)	(0.35)	0.69	0.47		
Y_2O_3	39.07	35.26	34.56	35.70	36.96	36.58	35.82	34.38	32.21	34.65
ZrO_2							0.89		(0.67)	(0.41)
P_2O_5	36.93	35.10	34.96	34.01	34.28	35.61	37.29	37.46	33.82	33.57
ThO_2	(0.35)	1.41	1.22	0.43	1.84	1.02	0.74	0.72	2.61	1.87
UO_3	1.47	2.46	1.70	0.84	2.72	0.93	1.21	0.87	2.38	1.94
SiO_2				0.59	1.27	(0.08)	0.17		1.71	2.54
TiO_2					(0.46)					
Al_2O_3									(0.29)	0.67
FeO		(0.09)		0.55		(0.14)	(0.15)	1.34	0.34	
MnO									(0.09)	
CaO			(0.03)	(0.07)	0.13				0.19	0.13
PbO										0.56
TOTAL	95.69	89.55	93.53	92.13	94.15	94.10	95.59	95.03	93.03	95.08

Table 6.12 Electon microprobe analyses of xenotime in the Main Granite. All abundances are in wt.%. Data in brackets indicate concentrations < 2σ error on background. The mean analysis of xenotime (YPO_4) used for mass-balance calculations is:

	Y_2O_5	Y	ThO_2	Th	UO_3	U
wt.%	35.52	28.1	1.22	1.1	1.65	1.4
± 1σ	±1.8		±0.7		±0.7	

	XENOTIME/ZIRCON					THORITE	
SAMPLE NO	SB166	SB171	SB171	SB171	SB171	N210	SB169
La_2O_3						0.59	(0.15)
Ce_2O_3		(0.41)	(0.70)	0.61		1.63	1.37
Pr_2O_3						(0.11)	(0.09)
Nd_2O_3	0.29	0.31			0.44	0.53	0.72
Sm_2O_3	0.29				0.95	0.25	0.20
Eu_2O_3	1.08				(0.19)		
Gd_2O_3	1.04		0.65		1.96	0.60	0.25
Tb_2O_3	(0.47)				0.66		
Dy_2O_3	2.74	1.15	1.55	0.42	4.59	0.67	0.40
Ho_2O_3	0.66	0.42			1.08		
Er_2O_3	1.52	0.75	1.31	(0.15)	2.85	0.29	0.22
Tm_2O_3	(0.27)				0.56		
Yb_2O_3	2.21	1.58	2.65	0.62	3.35	0.51	0.31
Hf_2O_3		1.89	1.46	2.35			
Ta_2O_5		0.79	0.78				
Nb_2O_5		0.87	0.78			0.85	1.28
Y_2O_3	19.53	7.19	13.79	2.95	25.48	3.82	2.90
ZrO_2	24.41	32.52	22.26	40.59	7.93	2.00	1.52
P_2O_5	18.88	5.97	12.33	1.86	26.42	2.37	2.94
ThO_2	0.62	2.82	4.50	0.85	6.37	61.40	57.62
UO_3	1.05	0.95	1.50	1.41	1.36	0.93	(0.20)
SiO_2	13.88	21.86	19.62	23.27	6.09	14.75	15.32
TiO_2		(0.16)	0.47	0.24	0.15	0.35	0.98
Al_2O_3		2.97	3.32	3.29	0.78	1.13	2.10
FeO	3.21	3.83	2.50	2.39	1.16	1.50	2.53
MnO			(0.08)	0.25	0.42		0.04
CaO	1.65	2.29	1.66	2.06	0.55		0.41
K_2O			0.16	(0.12)		1.31	0.55
BaO		1.13					
V						(0.27)	(0.31)
TOTAL	93.80	88.73	92.07	83.43	93.43	95.35	92.41

Table 6.13 Electron microprobe analyses of xenotime/zircon minerals and thorite in the Main Granite. All abundances are in wt.%. Data in brackets indicate concentrations < 2σ error on brackground. All crystals analysed were inclusion-free and probably result from solid solution between xenotime and zircon.

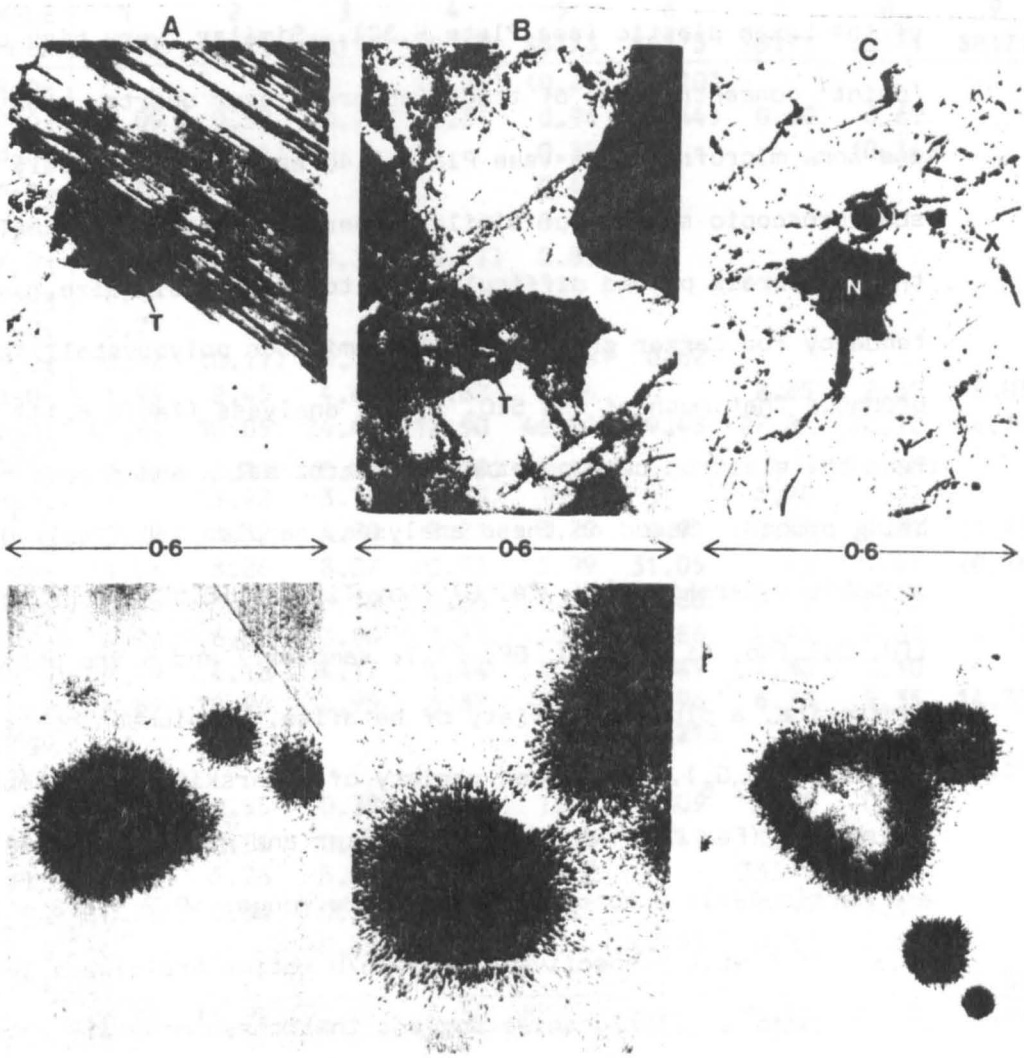

Plate 6.3 Photomicrograph and fission track pairs showing U locations in the Main Granite. Fields of view are given in mm.

A Sample N210. Thorite, T, gives rise to very high density fission tracks. Two unidentified primary U sources are included in biotite.

B Sample SB177. Thorite, T, included in feldspar, again yields very high density tracks. Lower density tracks are associated with a partially altered opaque mineral.

C Sample SB171. Primary Nb-Ta-oxide, N, included in quartz yields extremely high density tracks, causing thermal discolouration of the Lexan plastic. Smaller U sources, X and Y, give rise to similarly high density tracks.

of the Lexan plastic (see Plate 6.3C). Similar, very high density 'point' concentrations of tracks observed over quartz, quartz boundaries and some microfractures (see Plate 6.4B and C) are probably related to submicroscopic sources of similar minerals. Microprobe analyses of these minerals proved difficult, due to their small size, and the tendency for larger grains to be metamict or polycrystalline. It is probable that much of the SiO_2 in the analyses (Table 6.14) results from the electron beam penetrating quartz below and around the crystals being probed. Based on these analyses, samples 1-6 (Table 6.14) are probably samarskite [(Y, Fe, U) (Nb, Ti, Ta)$_2$(O, OH)$_6$] or betafite [(U, Ca)$_2$(Nb, Ti, Ta)$_2$(O, OF, F)$_7$]; samples 7 and 8 are possibly samiresite, a plumboan variety of betafite, or plumboniobate [(Ca, Pb, Fe, Y, U) Nb_2O_6), a plumboan variety of samarskite, and sample 9 is columbite [(Fe, Mn) (Nb, Ta)$_2O_6$] (Parker and Fleischer, 1968). Th, and particularly U contents show a wide range; ∿0.2 - 6.8 wt.% and ∿0.3 - 25.8 wt.% respectively, but Th/U ratios are always less than one.

Textural relationships suggest that these minerals crystallised late in the evolution of the Main Granite liquid; those occurring along quartz boundaries possibly crystallised from trapped residual fluids/ magma during the final stages of magmatic solidification. Those along microfractures may have crystallised from expelled U and Nb rich residual fluids, and are probably contemporaneous with the observed late-stage alteration of some biotites and deposition of secondary Fe-oxides.

vii) Uraninite has not been positively identified in these samples, but four or five probable uraninites were noted in quartz and feldspar. These were extremely small (of the order of 10^{-4} - 10^{-5} mm), opaque cubes, yielding very high density fission tracks extending to approximately ten times the dimensions of the grains. Uraninite has been

SAMPLE NUMBER	1 SB173	2 SB173	3 SB173	4 SB173	5 SB173	6 SB173	7 SB171	8 SB171	9 SB171
La_2O_3				(0.24)	(0.25)	(0.10)			
Ce_2O_3	1.09	0.58	(0.25)	0.31	0.94	(0.44)	0.60	0.69	
Nd_2O_3	0.56	(0.23)			0.35			(0.14)	
Sm_2O_3	0.68				0.42				
Gd_2O_3	0.71				0.48				
Dy_2O_3	1.82	(0.17)	0.35	(0.11)	0.85				
Ho_2O_3	0.44								
Er_2O_3	0.75								
Yb_2O_3	0.82	(0.11)	(0.11)	(0.21)	(0.05)	0.62			
Ta_2O_5	1.95	2.45	4.62	2.62	3.54		2.85	2.65	8.03
Nb_2O_5	47.64	30.05	24.46	12.50	46.31	29.43	27.85	24.12	64.14
Y_2O_3	2.62	0.80	(0.29)	(0.19)	1.44			(0.66)	
P_2O_5		3.42	3.75	3.13	1.23		1.20	1.42	
ThO_2	3.22	6.37	4.78	3.21	3.29	6.91	0.85	0.83	(0.25)
UO_3	4.03	8.26	8.07	20.93	5.99	31.05	5.69	4.41	(0.34)
SiO_2	5.64	3.65	3.19	10.86	6.18	4.86	8.53	18.33	
TiO_2	4.26	6.58	3.86	3.82	3.62	1.86	0.57	0.61	4.32
Al_2O_3	1.79	4.18	4.17	5.44	1.81	3.49	4.55	5.10	
FeO	4.89	14.96	6.93	6.67	6.23	3.96	6.78	9.35	14.35
MgO						(0.21)			
MnO							0.51	0.75	5.67
CaO	1.60	0.93	0.38	0.35	1.21	1.09	0.44	0.91	
K_2O	0.26	0.59	0.46	0.69	0.19	0.47	1.27	1.07	
PbO	1.43	1.26	5.99	2.99	3.22		33.95	22.34	
Cl	0.26	0.33	0.56	0.39	0.21		1.59	1.12	
S			0.29			0.80	0.85	0.82	
W									1.87
TOTAL	86.46	84.92	72.61	74.50	88.38	84.67	98.08	95.32	98.97

Table 6.14 Electron microprobe analyses of Nb-Ta-oxides in the Main Granite. All abundances are in wt.%. Data in brackets indicate concentrations < 2σ error on background. Low totals probably arise from the metamict nature of several crystals, and the possible presence of other volatiles (e.g. H_2O, F).

identified in core samples from the Main Granite (P. Webb pers. comm=.

Secondary Distribution

Significant amounts of U are present in several samples as accumulations in secondary alterations of major minerals or adsorbed in hydrothermal Fe-oxides along grain boundaries and microfractures. A

Plate 6.4 Photomicrograph and fission track pairs showing U locations in the Main Granite. Fields of view are given in mm.

A Sample SB173. A primary Nb-Ta-oxide mineral, N, occurring along a quartz-feldspar boundary, gives rise to high density tracks. Low density tracks indicate a secondary U distribution along grain boundaries, microfractures and in altered feldspars. Higher density tracks may relate to submicroscopic inclusions of primary accessory minerals, but some correlate with increased concentrations of secondary Fe-oxides.

B Sample N211. Very high density tracks are associated with a Nb-Ta-oxide, N, small inclusions in quartz, X and Y (probably Nb-Ta-oxides), and in biotite, Bi. Although some low density tracks occur over biotite, especially along crystal boundaries and over partially altered feldspar (bottom left), the U distribution in this sample is predominantly primary.

C Sample N188. Predominantly primary U distribution with very high density tracks over abundant inclusions in biotite, Bi, and unidentified minerals along boundaries between quartz crystals, W, X and Y (probably Nb-Ta-oxides).

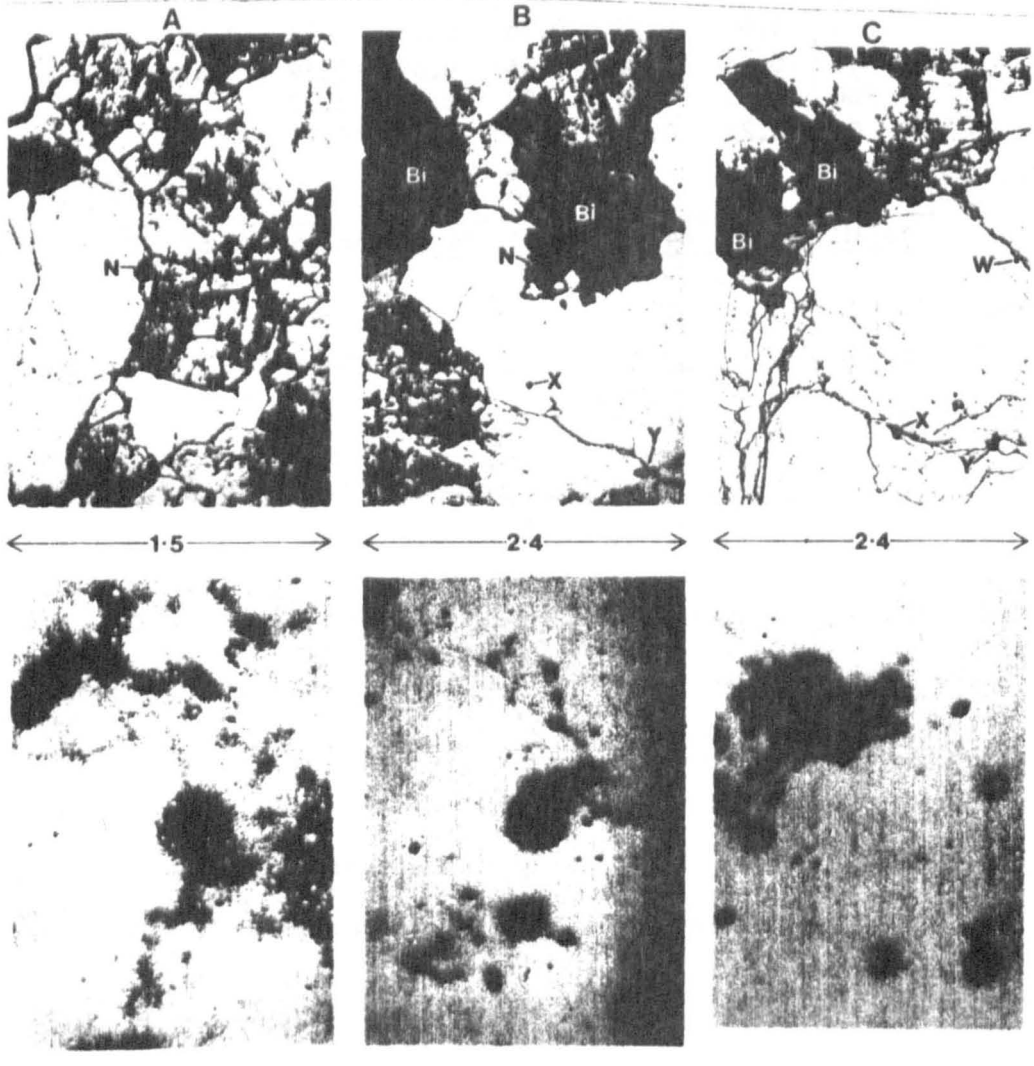

brief summary of secondary modes of occurrence is given below.

i) Biotites. Where these are intensely altered to muscovite and opaques (magnetite/hematite), low-medium density fission tracks are concentrated over the secondary opaques (Plate 6.5A). Microprobe analysis of this phase met with limited success but revealed low levels of U, very low levels of Th and no detectable Nb. (Table 6.15). Variable density tracks are present over rims and cleavages of many biotites exhibiting incipient development of secondary opaques and some 'ghosting' occurs. Such secondary U distributions may occur in isolation, i.e. restricted to biotite crystals (e.g. Plate 6.4B) or may be intimately related to U mobilization and precipitation along grain boundaries and microfractures (e.g. Plate 6.5C).

ii) Feldspars. Low density fission tracks are associated with partially sericitised feldspars. Track concentrations increase considerably where secondary opaques are developed (Plate 6.5B); these are often related to secondary U along microfractures (e.g. Plates 6.4A and 6.5C).

iii) Magnetite. Primary magnetite often exhibits alteration fringes yielding low-medium density tracks. Attempted electron microprobe analyses (Table 6.15), although giving low totals, revealed higher U, Th and Nb contents in the alteration product than in primary magnetite.

iv) Microfractures and grain boundaries. The presence of U along grain boundaries and microfractures is a feature of several samples from the Main Granite. The associated fission track density is variable and increases with the presence of Fe-staining and secondary Fe-oxides (Plates 6.5C and 6.4A). Microprobe analysis of these secondary products was generally unsuccessful due to their amorphous and hydrated nature.

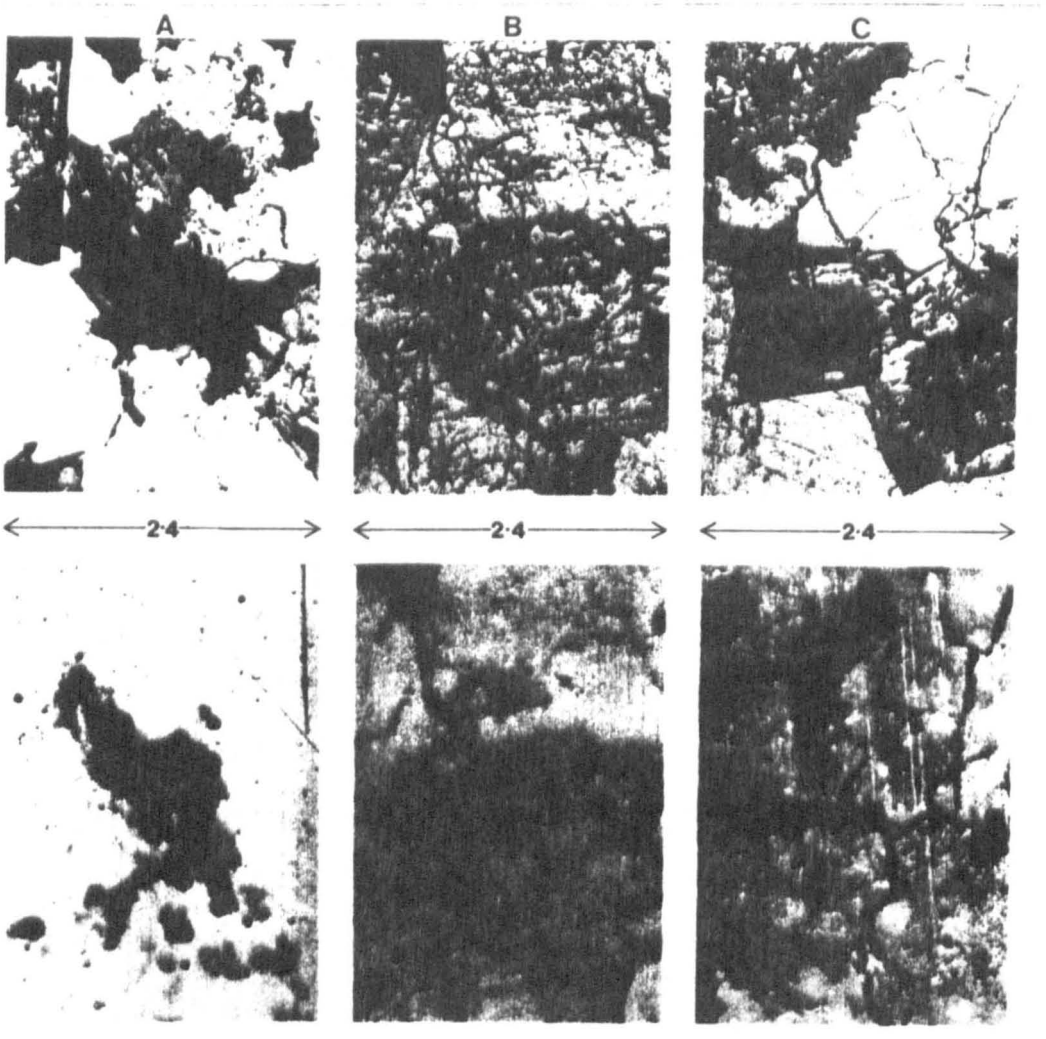

Plate 6.5 Photomicrograph and fission track pairs showing U locations in the Main Granite. Fields of view are given in mm.

A Sample SB163. Photomicrograph taken in crossed-polars. Biotite has been altered to secondary opaques and muscovite. Muscovite also occurs as secondary flakes in feldspar (top left). Low density tracks are associated with secondary opaques replacing biotite. High density tracks correspond to original inclusions of primary accessory minerals.

B Sample SB166. Fission tracks occur of secondary alteration products in feldspar, associated predominantly with secondary Fe-oxides.

C Sample SB150. Fission tracks of various densities occur over partially altered biotites, concentrating particularly along cleavage traces where secondary opaques are present, feldspars, and along grain boundaries and microfractures.

SAMPLE NO U-bearing phase	SB163 Magnetite/ hematite after biotite	SB166 Primary magnetite	SB166 Secondary alteration of primary magnetite	SB173 Secondary opaque along microfractures
Nb_2O_5		0.59	2.46	(1.47)
ThO_2	(0.09)	(0)	(0.19)	(0.20)
UO_3	(0.16)	(0)	0.47	1.20
SiO_2	[12.88]	[1.56]	[5.86]	[28.39]
TiO_2	0.63	8.73	2.46	0.18
Al_2O_3	[6.33]		[10.17]	[16.34]
FeO	64.64	75.49	30.78	28.87
MnO	0.14		0.10	0.55
MgO				1.95
CaO				[0.32]
K_2O	[2.29]	[0.18]	[0.13]	[0.39]
Cl			0.30	
TOTAL	87.16	86.55	53.12	80.62

Figure 6.15 Attempted electron microprobe analyses of secondary U-hosts in the Main Granite. All abundances are in wt.% Round brackets indicate concentrations < 2σ error on background. Square brackets indicate probable contamination from surrounding major minerals. Poor total are due to contamination, the granular nature of these alteration products, and hydration.

One analysis, however, revealed significant U and low levels of Nb (Table 6.15); associated fission tracks were of high density.

The frequent association of U along microfractures with sericitisation and the development of secondary opaques in feldspars suggests that this 'mode of occurrence' represents remobilisation of U during late-stage hydrothermal processes, rather than redistribution by surficial weathering.

A summary of the results of fission track studies on individual samples is presented in Table 6.16. Zircon, monazite and xenotime were located in all samples, as described earlier, and have been omitted from Table 6.16; their relative abundance in individual samples is discussed later. Several important points arise from Table 6.16:

SAMPLE No	U ppm	Th ppm	Th/U	PRIMARY DISTRIBUTION			SECONDARY DISTRIBUTION			
				Thorite	U-Nb-Ta-Oxides	Uraninite	Biotites	Feldspars	Grain Boundaries & Microfractures	Others
SB177	7.1	38.2	5.6	HD, VHD	None identified	VHD, 1 v. small opq cube in qtz.	LD, some rims & cleavages assoc minor 2ry opqs.	None	None	LD, 1ry opqs where assoc U accessories.
SB169	10.8	55.3	5.1	Several VHD	3-4 Sub-microscopic sources of HD & VHD, between qtz crystals. Some with opq rims.?		LD-MD some rims & claevages, some 2ry opqs	LD where partially sericitized	LD-MD along many, spatially assoc 1ry sources & 2ry Fe-oxides	LD, altered 1ry opqs
N210	11.5	47.6	4.1	VHD	3-4 VHD sources in qtz. ?	None	LD,rims & cleavages + around included 1ry opqs.	VLD where sericitized	None	LD, apatites assoc bts.
SB162	13.9	41.3	3.0	1-2 VHD in bt. ?	1-2 VHD sources along microfractures. ?	None	MD assoc 2ry opqs along rims & cleavages	LD-MD over 2ry opqs,assoc microfractures	HD along many assoc 2ry Fe-oxides. LD along others	LD-MD, altered 1ry opqs.
SB150	16.4	39.8	2.4	1-2 VHD in bt. ?	Several VHD sources in qtz, + along microfractures.?	VHD, 1 in qtz, 1 in fsp. V. small	HD over 2ry opqs + LD-MD dispersion in most.	LD where sericitized	HD along several assoc 2ry Fe-oxides. LD-MD along others.	HD-MD, altered 1ry opqs
N211	16.7	40.8	2.4	VHD, in bt. ?	Several sub-microscopic sources of HD & VHD in & between qtz crystals. Probably U-Nb-Ta-oxides. ?		Little VLD dispersion.	VLD over few 2ry opqs.	None	None
SB173	9.7	35.3	3.6	1 VHD, in bt. ?	VHD, in qtz. 2-3 VHD unidentified opqs along microfractures. ?		MD-HD rims & cleavages, some ghosting.	None	HD where assoc 2ry Fe -oxides & 1ry sources. LD elsewhere.	None
SB164	12.1	34.8	2.9	VHD, reddish crystals, some with opq rims. ?		None	HD, rims & cleavages, some ghosting	None	LD locally over Fe-staining assoc 1ry sources.	LD-MD, altered 1ry opqs.
SB166	12.9	27.1	2.1	None	Several HD - VHD in & between qtz crystals	None	MD-HD rims & cleav-ages, + ghosting, assoc 2ry opqs.	MD over 2ry opqs.LD where sericitized.	MD-HD assoc 2ry Fe-oxides, esp around 1ry sources & qtz.	MD-HD, most 1ry opqs altered
SB178	14.2	23.1	1.7	None	Several VHD, submicroscopic sources in qtz. ?	VHD, v.small opq at qtz/fsp boundary.?	little LD along rims & cleavages	VLD where sericitized	HD in some qtz boundaries.	None
N188	14.5	24.1	1.7	None	Several VHD sources in & between qtz crystals. ?		LD, few rims & cleavages, some 2ry opqs.	None	None	None
SB176	17.3	25.0	1.4	None	Several VHD in qtz. VHD, submicroscopic sources in qtz & 1-2 in fsp. ?		LD - some rims & cleavages, MD where 2ry opqs.	LD over few 2ry opqs.	None	None
SB175	4.5	20.2	4.5	None	None	VHD, 1 v. small opq cube in qtz. ?	None	None	None	None
N197	8.0	21.0	2.6	None	Few VHD sources in qtz boundaries. ?	None	LD-MD rims & cleavages, esp where 2ry opqs.	LD, 2ry opqs related to microfractures	LD, assoc with 2ry Fe-oxides	None
SB163	6.1	21.2	3.5	None	1-2 VHD sources in qtz & fsp. ?	None	Highly altered to opqs + musc,LD-MD over 2ry opqs.	LD over few 2ry opqs	Some VLD in boundaries near bts. None in microfractures.	None
SB156	7.8	17.8	2.3	None	Few VHD submicro-scopic in qtz. ?	None	Highly altered to opqs + musc, HD ghosting of most.	MD-HD, 2ry Fe -oxides, assoc microfractures.	HD in most, assoc 2ry Fe-oxides.	None
SB171	9.5	13.9	1.5	None	VHD, in qtz. HD, opq/columbite in qtz.	None	HD ghosting of many, often assoc 2ry opqs.	LD, assoc 2ry opqs.	LD-MD, generally assoc 1ry sources	None

Table 6.16. Summary of fission track studies on Main Granite samples. Abbreviations: VHD, very high density tracks; HD, high density tracks; MD, medium density tracks; LD, low density tracks; VLD, very low density tracks; qtz, quartz; bt, biotite; fsp, feldspar; opq, opaque; musc, muscovite; assoc, associated with; esp, especially; v, very; 1ry, primary; 2ry, secondary.
Where primary U sources have not been positively identified probable sources are indicated with a question mark, based on similarities in optical properties, location and fission track signatures with identified phases.

NB. Zircon, monazite and xenotime are present in all samples as described in the text. These have been omitted from the table

i) Optically identifiable thorite is only present where whole rock Th contents are high, suggesting that thorite is a major host for Th.

ii) Uranium (and Th) bearing Nb-Ta oxides appear to be present in most samples, and are notably abundant in SB150, N211, SB166, SB178, N188 and SB176, which all have greater than 12 ppm whole rock U. Sample SB175, with only 4.5 ppm whole rock U does not appear to contain U-rich Nb-Ta-oxides (the presence of uraninite in this sample is anomalous).

iii) The degree of U distribution in secondary alteration products and microfractures is not positively correlated with whole rock U contents.

For example, samples N211, N188 and SB176 have high U contents but show no U in boundaries and microfractures, and very little dispersion in biotite and feldspar (see Plate 6.4B and C). The predominantly primary distribution of U in these samples, coupled with their position in Figure 6.11 (high U content for a given Th content) suggests that U may have been lost from other samples which exhibit secondary remobilisation of U.

iv) The observed abundance of Nb-Ta-oxides shows a general positive correlation with whole rock U contents, suggesting that these minerals may be a major host for U. With reference to Figure 6.17, this would indicate that samples lying below the presumed magmatic trend have suffered U depletion.

Evidence from combined fission track and electron microprobe studies show that Th variations in the Main Granite are controlled by magmatic differentiation, and that early crystallising thorite is an important host for Th. Primary Nb-Ta-oxides, which crystallised late

in the differentiation history of the Main Granite, appear to be a major host for U. Although uraninite is not abundant it hosts significant quantities of U. Secondary redistribution and probably depletion of U is evident in many samples, resulting from late-stage hydrothermal processes. Hydrothermal mobilisation of U is supported by field gamma-rays surveys which indicate high U levels in country rocks close to the granite contact.

Mass-balance calculations

Approximate contributions to whole rock U and Th contents from zircon, monazite and xenotime have been calculated using partial whole rock trace element analyses (Appendix F) and the mean compositions of accessory phases from electron microprobe analyses (Tables 6.10, 11 and 12), and assigning all Zr to zircon, 90% of whole rock Ce to monazite and all Y to xenotime. Contributions from thorite and Nb-Ta-oxides could not be calculated directly due to the absence of uniquely characteristic elements and the wide range of Th and U contents respectively (Tables 6.13 and 6.14). Possible sources of error in these calculations are described below.

i) Minor Zr was detected in xenotime and thorite; Zr in xenotime/zircon minerals (Table 6.13) is proportional to the zircon component, and hence is incorporated in the calculations. Observed ranges of U and Th in zircon are greater than ± 100% on the mean (Table 6.10) but do not vary systematically either within or between samples. Maximum possible errors in the calculation of U and Th contributions from zircon due to this variation are ± 2.2 ppm and ± 0.8 ppm respectively (see Table 6.17).

ii) Estimates of Th contributions from monazite involve the

greatest error. Ce has been detected in xenotime/zircon minerals, Nb-Ta-oxides, thorites and zircons (Tables 6.10, 13 and 14). It may also be present in apatites (Deer et al., 1972; Tindle, 1982), and as low concentrations in major minerals (Alderton et al., 1980). An upper estimate of 90% whole rock Ce was, therefore, assigned to monazite, but modal percentages may still be overestimated. Maximum errors arising from the observed range of U and Th contents in monazite (Table 6.11) are presented in Table 6.17.

iii) Yttrium is present in some zircons, monazite, thorites and Nb-Ta-oxides (Tables 6.10, 11, 13 and 14). Yttrium in xenotime/zircon minerals is incorporated in the calculations as xenotime. Errors due to the observed variation of U and Th in xenotime (Table 6.12) are presented in Table 6.17.

Accessory phase	Average[1] modal %	U (ppm)[2] upper limit	U (ppm)[2] lower limit	Th (ppm)[2] upper limit	Th (ppm)[2] lower limit	Possible error on[3] values in Table 6.18 ppm U	Possible error on[3] values in Table 6.18 ppm Th
ZIRCON	0.020	2.32	0.12	0.78	0	± 2.2	± 0.8
MONAZITE	0.025	1.80	0.55	28.08	19.08	± 1.2	± 9.0
XENOTIME	0.015	2.93	1.19	2.52	0.69	± 1.7	± 1.8

Table 6.17 Maximum probable errors on calculations of radioelement contributions from zircon, monazite and xenotime in the Main Granite.

[1]Approximate average modal % of mineral in Main Granite samples.

[2]Upper and lower limits calculated using ± 1σ on mean microprobe analyses for U and Th contents of accessory phases.

[3]Taking range of U and Th contents as ± 2σ on mean analyses.

Note that errors are also incurred in assuming mean Zr, Ce and Y contents for zircon, monazite and xenotime in the Main Granite.

Results of mass balance calculations are presented in Table 6.18. Uranium contributions from each of the three primary accessory phases show fairly narrow limits (excluding sample N187 which has anomalously high Y and U contents) when compared with the variation in whole rock U contents: zircon, 0.5 - 1.9 ppm U; monazite, 0.4 - 2.3 ppm U; xenotime, 0.9 - 3.3 ppm U. The total contribution from all three phases (3.3 - 5.9 ppm U) does not vary systematically with whole rock U contents (Figure 6.18). Thorium contributions from zircon (0.3 - 1.1 ppm) and xenotime (0.8 - 2.7 ppm) generally represent less than 10% of whole rock Th, but monazite accounts for more than 40% of whole rock Th in all samples, although there is some evidence in the data for samples N210, N82 and N83 of over-estimated modal percentages of monazite (see Table 6.18). A sympathetic trend of estimated Th from monazite and whole rock Th content is evident in Table 6.18 and is refelcted in Figure 6.18.

The remaining U and Th to be accounted for (Table 6.18) is plotted against whole rock values for these elements in Figure 6.19. The excellent positive correlation in Figure 6.19a shows that enhanced U contents (i.e. above the range 3-6 ppm) are due to hosts other than zircon, monazite and xenotime. Evidence from Lexan, electron microprobe and trace element studies (Figure 6.17) suggest that these are most likely to be Nb-Ta-oxides (± uraninite) with lesser contributions from thorite, alteration products of major minerals and secondary hydrated Fe-oxides along grain boundaries and microfractures. Figure 6.19b shows a much weaker positive correlation for Th, since over 50% of whole rock Th is concentrated in the phases which have been subtracted (particularly monazite; Tablt 6.16). But, the persistence of a weak positive correlation suggests that enhanced Th levels (i.e. $\gtrsim$ 25-35 ppm) are due to the presence of another high Th phase. Fission track and electron microprobe studies

Sample number	Whole rock contents U ppm	Th ppm	Contribution from zircon U ppm	Th ppm	Contribution from monazite U ppm	Th ppm	Contribution from xenotime U ppm	Th ppm	Total from zir mon and xen U ppm	Th ppm	Remainder to be accounted for by other hosts U ppm	%	Th ppm	%
N187	30.9	59.2	1.4	0.8	1.5	30.6	5.5	4.3	8.4	35.7	22.5	72.7	23.5	39.7
N168	14.0	59.0	1.5	0.8	1.4	28.2	1.0	0.8	3.9	29.8	10.1	72.1	29.2	49.5
N208	5.0	49.0	1.9	1.1	1.4	27.4	1.6	1.3	4.9	29.7	0.1	2.6	19.3	39.4
N209	10.0	47.0	1.8	1.0	1.6	31.4	0.9	0.7	4.3	33.1	5.7	56.7	13.9	29.5
N210	11.5	47.6	1.5	0.8	2.3	46.9	1.4	1.1	5.2	48.7	6.3	55.1	---	---
N212	18.5	47.1	1.0	0.5	1.5	29.4	3.5	2.7	5.9	32.7	12.6	67.9	14.4	30.7
SB162	13.9	41.3	1.2	0.7	1.1	21.4	2.44	1.9	4.8	24.0	9.2	65.8	17.3	41.8
N167	17.0	41.0	0.5	0.3	1.0	19.5	1.9	1.5	3.4	21.3	13.6	79.9	19.7	48.1
N211	16.7	40.8	1.0	0.5	0.9	18.3	3.0	2.4	4.9	21.2	11.8	70.6	19.6	48.1
SB177	7.1	38.2	1.3	0.7	1.2	23.0	2.2	1.7	4.7	25.5	2.5	34.5	12.7	33.3
N184	10.0	37.0	1.5	0.8	1.5	30.6	1.7	1.3	4.6	32.7	5.4	53.7	4.3	11.7
SB167	10.6	36.0	1.4	0.8	1.4	29.0	2.5	2.0	5.3	31.7	5.3	49.6	4.3	11.9
N190	17.7	35.2	1.1	0.6	1.1	22.3	3.3	2.6	5.5	25.4	12.2	69.2	9.8	27.8
N166	9.0	34.0	1.1	0.6	1.0	20.3	1.6	1.3	3.7	22.1	5.3	58.7	11.9	34.9
N164	9.0	34.0	1.3	0.7	1.3	25.4	1.8	1.4	4.4	27.6	4.6	51.1	6.4	18.9
N169	8.0	33.0	1.4	0.8	0.9	17.1	1.2	0.9	3.4	18.8	4.6	57.1	14.2	43.1
N189	15.3	32.8	0.9	0.5	1.0	19.5	3.2	2.5	5.1	22.5	10.2	66.9	10.4	31.6
N170	10.0	31.0	1.1	0.6	1.2	23.4	2.9	2.3	5.1	26.3	4.9	48.9	4.7	15.3
N186	10.0	28.0	1.1	0.6	0.9	19.1	1.3	1.0	3.3	20.7	6.7	66.7	7.3	26.1
N188	14.5	24.1	0.9	0.5	0.6	12.7	2.4	1.9	3.9	15.1	10.6	73.3	9.1	37.6
SB178	14.2	23.1	1.0	0.6	0.6	12.8	3.3	2.6	4.9	15.9	9.3	65.2	7.2	31.0
N197	8.0	21.0	1.14	0.6	0.7	13.1	1.8	1.7	3.5	15.4	4.5	55.8	5.6	26.7
N82	8.0	12.0	0.6	0.3	0.6	12.7	3.2	2.5	4.3	15.5	3.7	45.8	---	---
N83	7.0	8.0	0.5	0.3	0.4	8.7	2.4	1.9	3.3	10.9	3.7	53.1	---	---

Table 6.18 Results of mass balance calculations for the Main Granite.

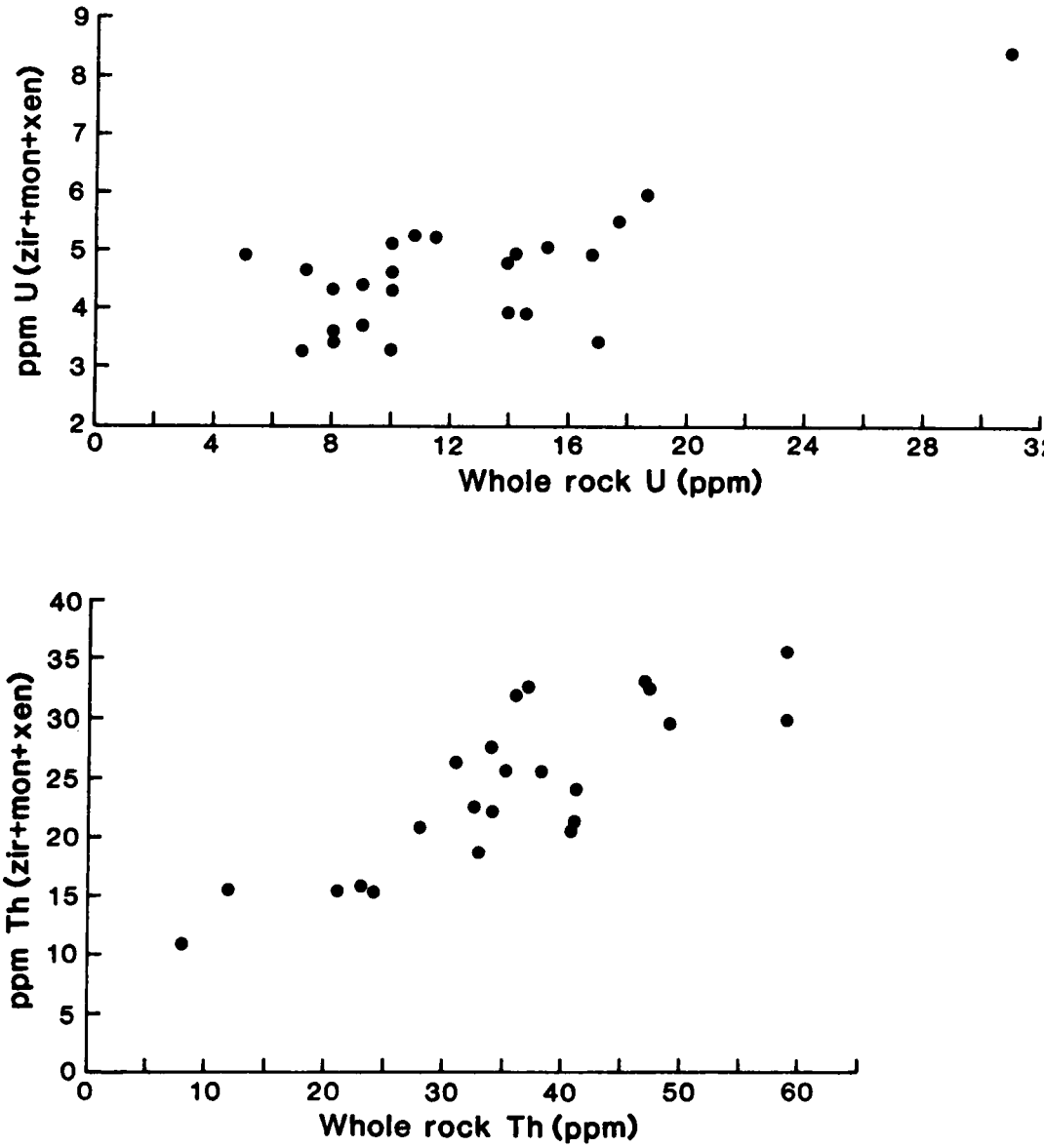

Figure 6.18 Variation of U (a) and Th (b) contributions from zircon, monazite and xenotime with whole rock U and Th contents.

have identified this phase as thorite and some Th is located in Nb-Ta-oxides and as very low concentrations in some secondary products (Table 6.15). The conclusion that thorite, rather than Nb-Ta-oxides is the major host for excess Th is supported by the lack of any

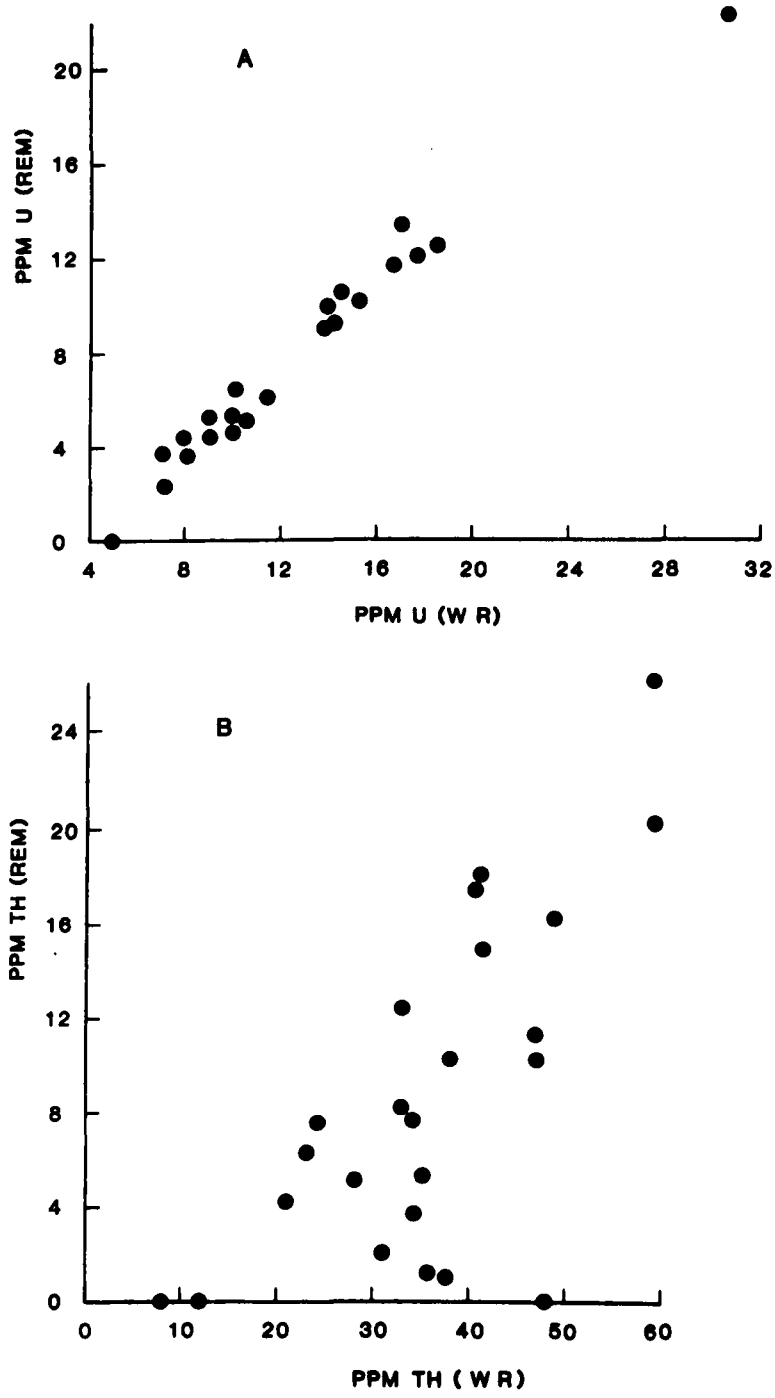

Figure 6.19 Remaining U and Th contents to be accounted for after subtraction of contributions from zircon, monazite and xenotime (RRM) plotted against whole rock U and Th values for Main Granite samples.

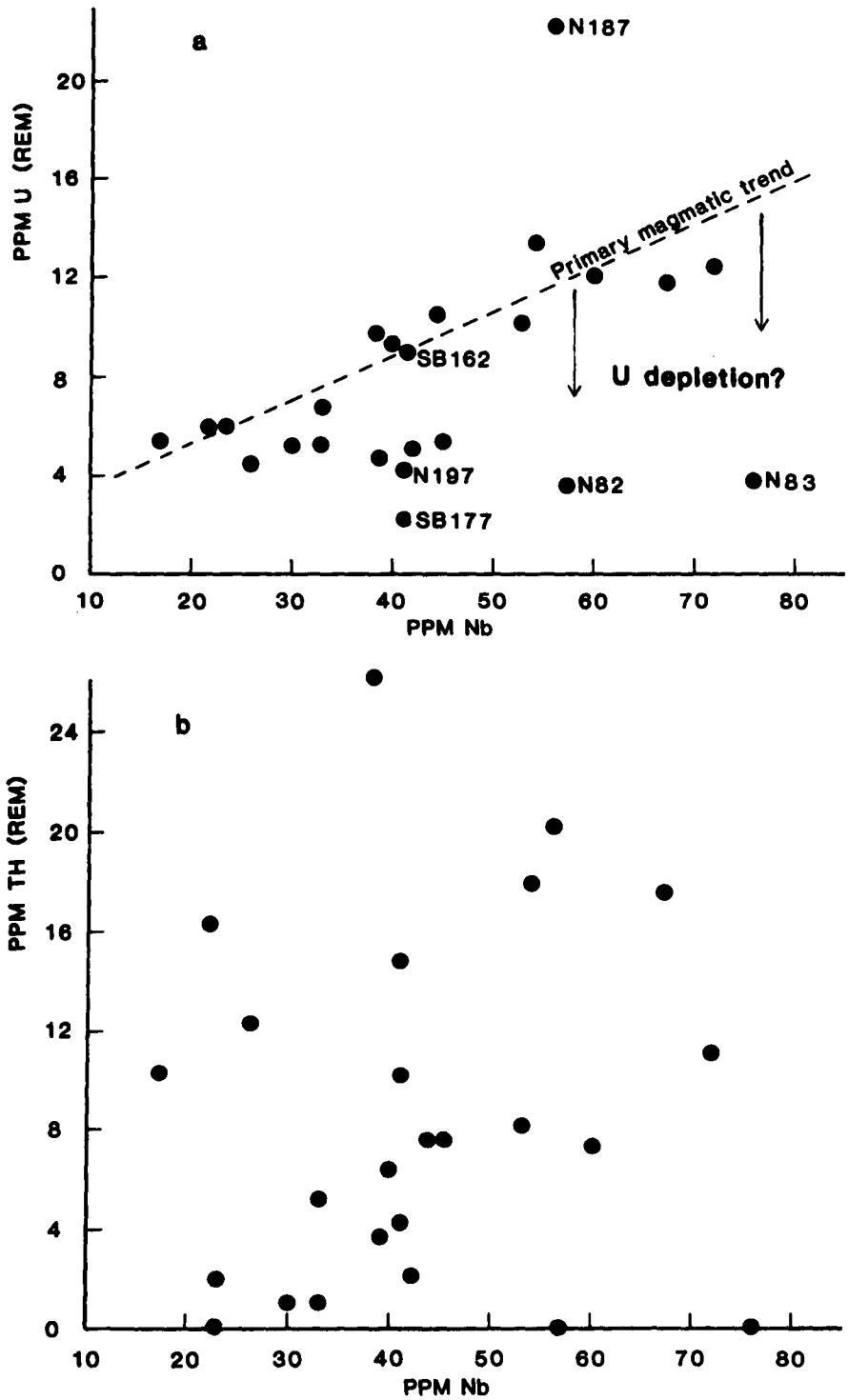

Figure 6.20 Remaining U and Th contents to be accounted for after subtraction of contributions from zircon, monazite and xenotime, plotted against whole rock Nb values for Main Granite samples.

correlation between Th remainder (from Table 6.18) and whole rock Nb contents (Figure 6.20b).

There is a good, although somewhat scattered correlation between U remainder (Table 6.18) and whole rock Nb (Figure 6.20a). Samples lying well off this trend are N187 which has an anomalously high U content, SB177 which contained no U-rich Nb-Ta-oxides (Table 6.16) and N82 and N83 which have anomalously low Th contents and are extensively altered (see Section 6.2:1). Sample N197 also exhibits extensive alteration associated with U in secondary locations and lies below the main trend. Sample SB162, however, although exhibiting a well developed secondary U distribution lies on the main trend. These results support the conclusions that much of the U excess from Table 6.18 is held in primary Nb-Ta-oxides and that in several samples some U has been remobilised and/or depleted by late-stage hydrothermal processes.

Figure 6.21 gives an estimate of the percentage distribution of

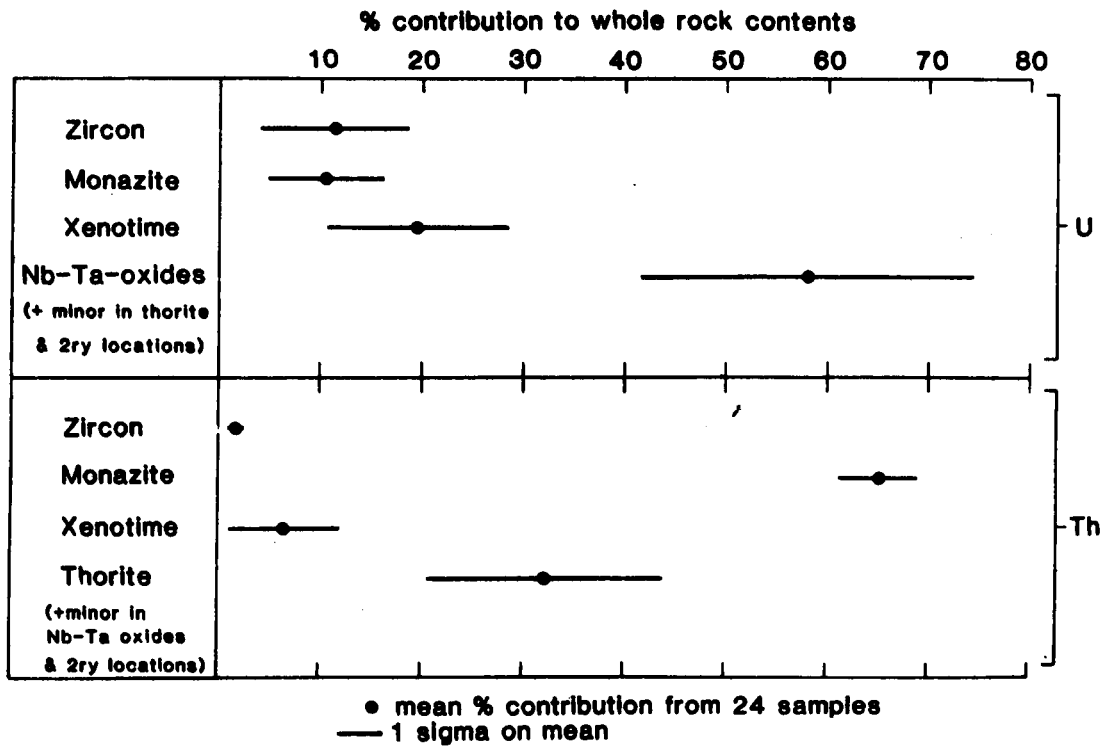

Figure 6.21 Approximate percentage distribution of U and Th between observed host phases in the Main Granite. Based on Lexan studies, microprobe analyses, trace element data and mass balance calculations.

U and Th between the various observed radioelement-bearing phases in the Main Granite. The conclusion that U is held predominantly in primary, refractory minerals (zircon, monazite, xenotime and Nb-Ta-oxides) is consistent with the absence of U in stream waters, and the high U content of stream sediments in the Cairngorm area (Watson and Plant, 1979).

Low Thorium contents in the Main Granite

Figure 6.12 shows a predominance of low Th values in the west and south-west areas of the Main Granite. Fission track studies of samples from these areas (SB178, SB156, SB171, SB163 and N197) reveal an absence of thorite (Table 6.16), and the low Ce content of analysed samples (SB178, N82, N83; Appendix F) indicate low contents of the major Th-bearing mineral, monazite. Samples SB156, SB171, SB163 and N171 have mineralogies similar to N82 and N83, with highly altered biotites and SB171 also contains garnet but SB178 is unaltered. The possibility exists that contamination with assimilated country rock may have caused this alteration, including the local presence of garnet (see Section 6.3:3) and this might help to explain the low Th contents (i.e. dilution). However, sample SB178 has a low Th content and a high U content (14.5 ppm) and, since contamination would dilute both radioelements, this does not appear to be the cause of Th depletion. The U distribution in the unalaltered sample, SB178, is predominantly primary (Table 6.16) but other samples (e.g. SB156, SB171, SB163 and N197) show a well developed secondary distribution associated with alteration. The lower U content of altered samples suggests that U has been depleted during hydrothermal alteration; the proximity of these samples to granite margins and fault

zones would allow easy access to late stage hydrothermal fluids. The problem of low Th contents, however, still remains, since Th is generally less mobile than U. Depletion in Th with advanced differentiation cannot be confirmed on the basis of Rb/Sr ratios (cf. N82 and N83 have Rb/Sr ratios of 38 and 55 respectively) since high Rb levels may be associated with hydrothermal muscovite. Additionally, high Rb/Sr ratios are found in samples elsewhere in the Main Granite which do not exhibit low Th contents (Figure 6.16). The reason for Th depletion, therefore, remains unclear and may only reflect local trace element (Ce and Th) variations in the magma.

6.8 SUMMARY AND DISCUSSION

Uranium and Th contents in the Cairngorm intrusion increase with differentiation from the NE Granite to the Main Granite. This increase is controlled by a change in the primary accessory mineral assemblage from apatite + zircon + sphene ± allanite in the NE Granite to apatite + zircon + monazite + xenotime + Nb-Ta-oxides ± uraninite in the Main Granite. Due to the fine grained nature of the Porphyritic and Microgranite units, Lexan and electron microprobe studies could not be used to identify radioelement host minerals, but on the basis of trace element analysis (Figures 6.16 and 6.17) they appear to be intermediate between the NE Granite and the Main Granite.

In the NE Granite, sphene and allanite are the major hosts for Th and zircon the major primary host for U; some U is also located in apatite, sphene and allanite. Enhanced U levels in at least one sample of the NE Granite appear to be related to a secondary distribution, possibly connected with permeation of U-enriched hydrothermal fluids

from the Main Granite. The possible presence of other primary U-bearing phases, however, cannot be dismissed. In the Main Granite, monazite and thorite are the predominant Th hosts and Nb-Ta-oxides are a major host for U. High U levels are magmatic in origin but primary distributions are often overprinted by secondary, hydrothermal remobilisation/depletion of U. Some of the observed U depletion may be due to subsequent removal by weathering processes from easily leachable sites.

Since most of the U and Th in the Main Granite (the dominant rock type in the Cairngorm intrusion) is held in primary, refractory accessory minerals and gravity modelling indicates a large volume of low density granite beneath the Cairngorm Mountains, it is likely that the high radioelement levels observed at the surface continue with depth. It has been shown, however, that U tends to increase with differentiation in the Main Granite which may suggest a decrease of U with depth if in-situ fractionation was active during the consolidation of the Cairngorm magma. Conversely, the identification of sporadic uraninite in outcrop samples (mainly in quartz; Table 6.16), a mineral which is often easily weathered, suggests the possibility of significantly more grains of uraninite in unweathered rocks below the surface. Uraninite was found to be the source of high U levels in core samples of several Hercynian granites (Barbier et al., 1967; Ball and Basham, 1979; Cuney, 1978). Recent borehole data show a higher average U content for the Main Granite than observed in surface samples (G. Brown, pers. comm) and uraninite has been positively identified in core samples (P. Webb, pers. comm).

Finally, the change in accessory mineral assemblage with differentiation in the Cairngorm intrusion reflects that which was shown, to a

lesser extent, in the Etive Complex (Chapter 5). Sphene and allanite, which are important U and Th hosts in early Etive units are replaced by monazite and thorite in the most evolved unit, the Central Starav Granite. If the Etive and Cairngorm 'granites' represent similar parental magmas at various stages of evolution, then further differentiation of the Etive-Starav magma might have resulted in xenotime and U-rich Nb-Ta-oxide crystallisation

CHAPTER 7 HEAT PRODUCTION AND HEAT FLOW MODELS

7.1 INTRODUCTION

The empirical linear correlation between surface heat flow, q_o, and surface heat production, A_o, observed for tectonically stable regions, viz

$$q_o = q^* + A_o D \qquad (i)$$

is generally interpreted as implying a fractional distribution of heat producing elements in the crust over a characteristic depth, D (e.g. Lachenbruch, 1970; Roy et al., 1968; Richarson and Oxburgh, 1979). The contribution from mantle and/or deep crustal sources, q^*, is considered to be constant for any 'heat flow province' and variations in the total surface heat flow, q, are attributed to lateral and vertical variations in crustal heat production.

Any distribution of heat production with depth, z, will lead to a one-dimensional, steady-state interpretation of equation (i) if it satisfies the relation.

$$\int_0^\infty A_z \, dz = DA_o$$ where z = 0 represents the present surface

Three possible solutions are shown in Figure 7.1. However, if equation (i) is to be preserved in regions of differential erosion then the distribution of heat production with depth must satisfy the condition

$$\int_0^\infty A_z \, dz = DA_z$$ where $z \geq 0$ and D is independent of z.

This is satisfied uniquely by model C in Figure 7.1 (Lachenbruch, 1968). In addition, Jampart et al., (1980) proposed a solution to equation (i) involving different depth scales for each of the three radioelement distributions.

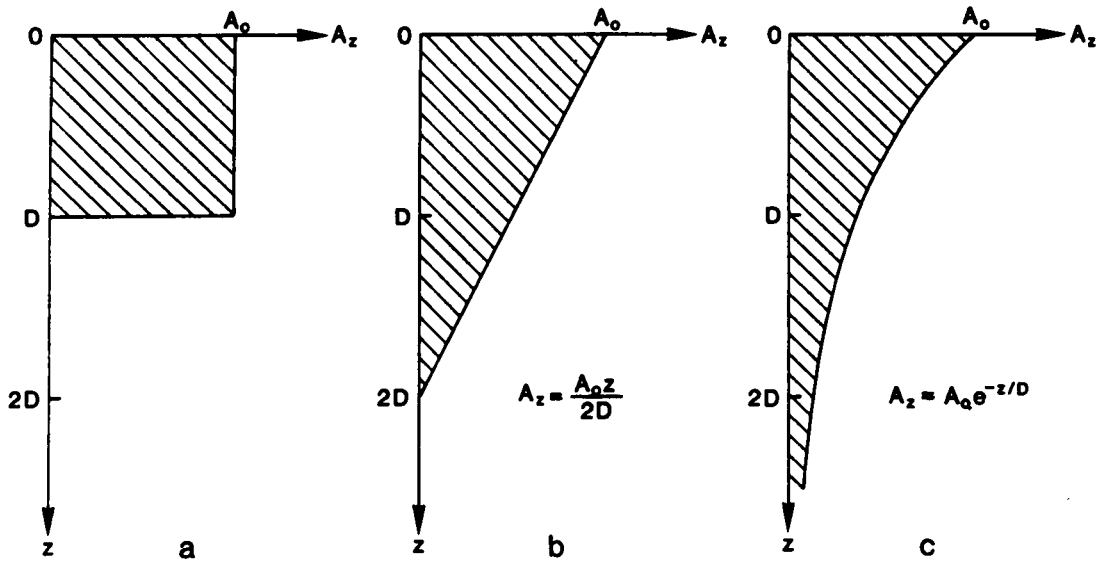

Figure 7.1 Three heat-production models consistent with the linear heat-flow relation; a, step function; b, linear function; c, exponential function.
Adapted from Lachenbruch, 1971.

The physical significance of the characteristic depth, D, calculated from the correlation between q_o and A_o is not easily defined. Costain et al., (1977) considered the role of microcracks in facilitating the migration of U and Th within the upper 7-10 km of the Earths crust, in which case D would be defined by the zone of microcrack porosity. A single process for crustal fractionation of heat producing elements is, however, unlikely and at any location, the quantity A_oD may comprise several horizons within which A_z may vary as function a, b or c (Figure 7.1) or some other function. Radiogenic bodies such as granitic plutons may be considered as one such horizon, with the additional constraint of finite lateral extent.

In this chapter the enhancement of surface heat flow due to the excess of radioelements (relative to surrounding country rocks) in the Etive and Cairngorm intrusions is estimated. Results are expressed in terms of the 'heat flow anomaly', defined as;

heat flow anomaly = heat flow produced by the anomalous body - heat flow that would be observed in the absence of the body.

By analogy with gravity anomalies, which are calculated from the density contrast between the causative body and the surrounding country rocks, the heat flow anomaly is calculated from the corresponding heat production contrast.

7.2 THE DISTRIBUTION OF HEAT PRODUCTION IN THE ETIVE AND CAIRNGORM GRANITES

The relationship between heat production and the elemental concentrations of U, Th and K is given by Rybach (1976):

$$A = 0.1326\rho\ (0.718U + 0.193\ Th + 0.262\ K)\ \mu W\ m^{-3}$$

where ρ is the rock density ($g cm^{-3}$), U and Th are in ppm and K is in wt.%. The densities used for calculation of heat production are given in Table 7.1, and U, Th and K contents in Appendices D and G. Where U, Th or K values were unavailable for any sample, the mean value for the

Intrusion	Unit	Density g cm^{-3}	References
Etive Complex	Quarry Intrusion	2.80	Anderson (1935) and this study (Ch.5)
	Cruachan (southern lobe)	2.70	
	Cruachan (northern lobe)	2.67	
	Meall Odhar	2.55	
	Outer Starav	2.60	
	Central Starav	2.60	
Cairngorm	All units	2.60	Locke 1982
Country rocks	Dalradian	2.74	Locke, 1982
	Moines	2.70	

Table 7.1 Densities used for heat production calculations

relevant unit was assumed (see Tables 5.4 and 6.5). The average heat productivities for all units of the Etive and Cairngorm intrusions are presented in Table 7.2 and areal distributions are shown in Figure 7.2.

			Heat production $\mu W\ m^{-3}$		
Intrusion	Unit	No. Stations	For unit $\bar{x}$	σ	Contrast with country rocks
Etive	Quarry Intrusion	12	0.89	0.27	-0.50
	Cruachan (S)	96	1.36	0.36	-0.03
	Cruachan (N)	25	2.96	0.35	1.57
	Meall Odhar	12	1.97	0.30	0.58
	Outer Starav	49	1.76	0.64	0.37
	Central Starav	41	2.85	0.99	1.46
	Country rocks	12	1.39	0.35	-
Cairngorm	N E Granite	10	3.09	0.74	1.55
	Porphyritic Granite	7	3.49	0.52	1.95
	Microgranite	3	2.94	0.22	1.40
	Main Granite	110	4.93	1.44	3.39
	Country rocks:				
	at contact	5	3.26	0.81	-
	away from contact	4	1.54	0.34	-

Table 7.2 Heat production in units of the Etive and Cairngorm intrusions

7.2:1 The Etive Complex

There is no significant contrast in heat production between the S Cruachan granites which dominate the outer margins of the southern lobe of the Etive Complex (Figure 5.2) and the surrounding country rocks (Figure 7.2 and Table 7.2). This portion of the Complex, therefore, will not produce a heat flow anomaly. Although the Meall Odhar granite shows a positive contrast of 0.58 mW m^{-3} (Table 7.2), it is of limited vertical extent (Section 5.1) and is unlikely to enhance surface heat

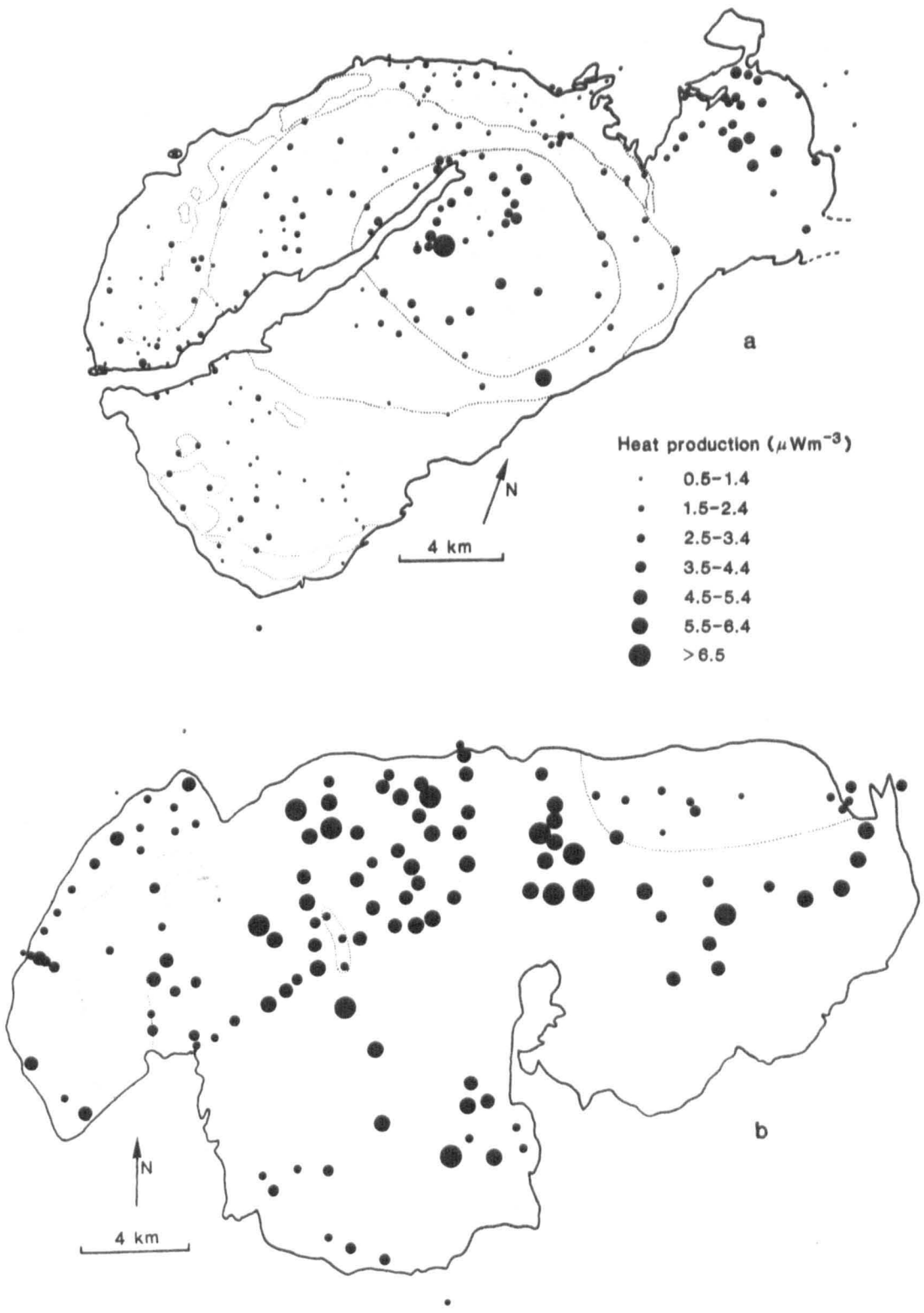

Figure 7.2 Areal distribution of heat production in the Etive Complex (a) and the Cairngorm Granite (b).
Geological boundaries as in Figures 5.2 and 6.1.

flow significantly.

The N Cruachan adamellite and the Starav Granites all have positive heat production contrasts with the country rocks (Table 7.2) and heat production increases towards the centre of each unit (Figure 7.2). The low values at the very centre of the Starav Granites represent a zone of U depletion, probably due to leaching by late stage hydrothermal fluids (see below). The overall increase in heat production arises from two processes:

a) The enrichment of Th and to a lesser extent K and U as in-situ differentiation of the magmas progressed inwards.

b) The deposition of U from enriched residual fluids in limited hydrothermal systems. Uranium was initially leached from the very centre of the Starav Granites and deposited in alteration products and micro-fractures as the hydrothermal fluids moved outwards and cooled. Lexan studies (Section 5.10) show that process (b) was of limited extent at the present level of erosion and suggest that U enrichment is unlikely to continue to any depth. The in-situ differentiation of radioelements observed in surface samples is probably similarly expressed in the third dimension and also suggests a decrease in heat production with depth in the Starav and N Cruachan units. The scale of the lateral decrease in heat production is approximately -2.5 $\mu W\ m^{-2}$ over 8 km in the Starav Granites and -2.0 $\mu W\ m^{-2}$ over 4 km in the N Cruachan adamellite. These general trends are, however, too poorly-defined to assign a linear, exponential or step function to the variation.

7.2:2 The Cairngorm Granite

Heat production values for the Cairngorm Granites are high compared with those observed for the Etive Complex and for country rocks away

from the immediate vicinity of the contact (Table 7.2 and Figure 7.2). No systematic trends of heat production values are apparent on the areal distribution map (Figure 7.2). A general low ($<4.0\ \mu W\ m^{-3}$) in the north-east corresponds to the N E Granite and areas of below average heat production in the west and south-west correlate with areas of Porphyritic Granite and Main Granite with low Th content (see Figure 6.12).

Geochemical, mineralogical and fission track studies (Chapter 6) indicate that radioelement concentrations in the Main Granite are controlled predominantly by primary magmatic processes. In contrast with the Etive Complex, there is no systematic variation of radioelement contents at outcrop level (Figures 6.12 to 6.15) suggesting that in-situ differentiation was not extensive and radioelement concentrations do not diminish with depth. The observation that some U may have been removed from secondary sites by weathering processes in surface samples and the identification of minor primary uraninite preserved in host minerals resistant to weathering (Section 6.7:2) suggests that heat production may, in fact, initially increase with depth. Recent evidence from shallow boreholes supports this conclusion (G Brown, pers. comm.).

For the purposes of heat flow anomaly calculations, the most representative model of heat production distribution in the Cairngorm massif was considered to be a homogeneous production rate equivalent to the mean value for the Main Granite. This may be a conservative estimate for the Main Granite, but allows for the lower heat production rates in the N E Granite, Porphyritic Granite and Microgranite.

7.3 METHOD USED TO CALCULATE HEAT FLOW ANOMALIES

The method used to calculate the heat flow anomalies produced by

the Etive and Cairngorm granites is based on the theory given by Simmons (1967). This method calculates the enhancement of vertical heat flow due to the contrast in heat production between the causative body and the surrounding rocks for the steady state case of heat conduction. Calculations rely on the following assumptions:

a) All heat transfer is by conduction; i.e. convection of ground water is negligible

b) Thermal conductivity is constant, isotropic and the same in both the radiogenic body and the surrounding medium; the effects of thermal conductivity contrasts between granite and country rocks and the probable decrease of thermal conductivity with depth are considered later.

Because both gravity and temperature are potential fields which satisfy Laplaces equation, $\Delta^2\psi = 0$ (where ψ = potential), the same techniques used to calculate gravity anomalies may be applied to thermal anomalies and, for the same causative body,

$$F = \frac{-\delta V}{\delta r} \propto Q = \frac{-K\delta T}{\delta r} \qquad \text{(ii)}$$

where F = gravitational field; V = gravitational potential; Q = heat flow field; T = steady state temperature field; K = thermal conductivity (independent of T); r = distance between the point of observation and the source.

The gravitational field, F, is continuous in all directions but the heat flow field, Q, is dependent on the properties of the medium between the source and the observation point and must, therefore, satisfy boundary conditions. Simmons (1967) considered the case where the source is in a semi-infinite medium, $z > 0$ (where z = depth), of conductivity K. The solution to this problem must satisfy Laplaces equation, $\Delta^2 T = 0$ for all $z > 0$ and, at $z = 0$ (i.e. the Earths surface),

the temperature must be zero. Simmons (1967) derived the solution to the proportionality in equation (ii) in terms of the vertical field components, giving;

$$Q_z = \frac{F_z A'}{2\pi G\rho'} \qquad \text{(iii)}$$

where A' = contrast in heat production per unit volume; ρ = density contrast and G = gravitational constant.

Application of equation (iii) to methods used to calculate gravity anomalies permits calculation of the theoretical heat flow anomaly due to the same body. Two methods were used in this study, a simple calculation of the surface heat flow field along the axis of a vertical cylinder and a computational method for calculation of the surface heat flow field due to more complex shapes.

a) Considering the model shown in Figure 7.3, the surface

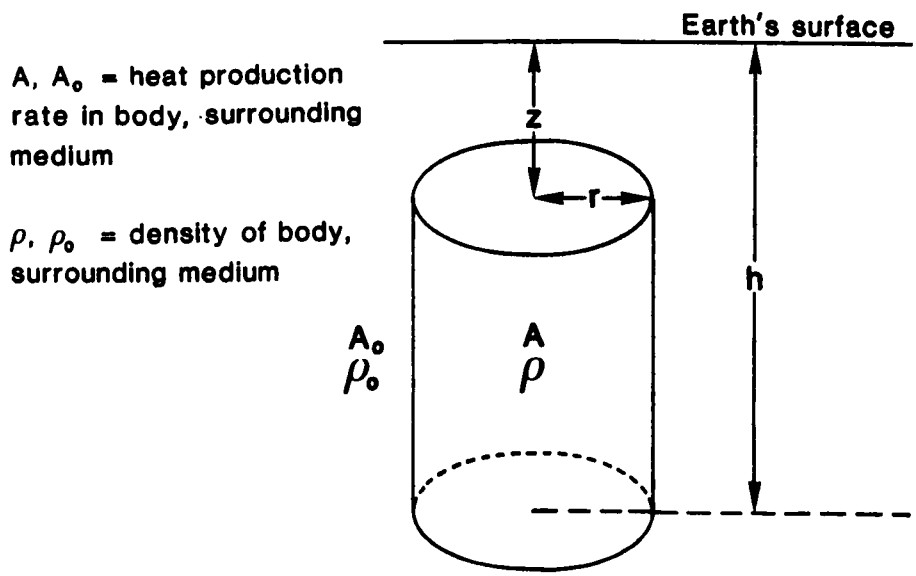

Figure 7.3 Parameters of vertical cylinder model used for heat flow anomaly calculations.

gravitational anomaly along the axis of the cylinder is given by;

$$F_z = 2\pi G\rho' \left\{ h - z + \sqrt{r^2 + z^2} - \sqrt{r^2 + h^2} \right\}$$

where $\rho' = \rho - \rho_0$

Modification using equation (iii) gives;

$$Q_z = A' \left\{ h - z + \sqrt{r^2 + z^2} - \sqrt{r^2 + h^2} \right\} \quad \text{(iv)}$$

where $A' = A - A_o$

Equation (iv) was used to estimate heat flow anomalies due to units of the Etive Complex (Section 7.4:1).

b) Talwani and Ewing (1960) developed a method to compute the surface gravity anomaly, F_z, due to a three dimensional body by numerical integration of horizontal, polygonal laminae that approximate the shape of the causative body. Modification of their method through equation (iii) gives an expression for the surface heat flow anomaly;

$$Q_z = \int_{\text{z = bottom of body}}^{\text{z = top of body}} Q_i \, dz$$

where $Q_i = \frac{A'}{2\pi} \sum_{i=1}^{n} v_i$ and v_i is a function of the geometry of the horizontal polygonal lamina and the relative position of the observation point (see Talwani and Ewing, 1960).

This technique was used to estimate the surface heat flow anomaly due to the Cairngorm Granite (Section 7.4:2).

7.4 CALCULATION OF HEAT FLOW ANOMALIES

7.4:1 The Etive Complex

The only units of the Etive Complex which may give rise to heat flow anomalies are the N Cruachan adamellite and the Starav Granites (Section 7.2:1). Although a three-dimensional model of the Etive Complex is not available, the position and shape of the negative Bouguer anomaly associated with this intrusion (Figure 5.5), together with density

measurements (Table 5.1) suggest that the anomaly is produced predominantly by the above mentioned units (Section 5.1). The amplitude of the residual anomaly (∿37 mgal) and steep gradient of the contours imply that these units are steep-sided, cone-shaped or cylindrical bodies extending to approximately 10 km depth. Heat flow anomalies for each unit were estimated using equation (iv) and the parameters listed in Table 7.3.

Unit	Mean radius (km) (from surface outcrop)	Depth (km)	Heat production contrast ($\mu W\ m^{-3}$)
N Cruachan	3.7	10	1.57
Outer Starav	7.3	10	0.37
Central Starav	4.7	10	1.46

Table 7.3 Parameters of vertical cylinder models used to estimate surface heat flow anomalies.

The total anomaly along the central axis of the Starav units is given by;

Q_z(total) = Q_z(Central Starav) + Q_z(Outer Starav calculated with r = 7.3 km) - Q_z(Outer Starav calculated with r = 4.7 km)

Results are: Q_z at centre of Starav units ≈ 5.8 mW m^{-2}

Q_z at centre of N Cruachan unit ≈ 4.8 mW m^{-2}

Considering the evidence for depletion of heat production with depth in both the Starav and N Cruachan units (Section 7.2:1) these estimates probably represent maximum values. However, both an increase in radius with depth and the proximity of the two anomalies (causing mutual enhancement) would tend to offset the error due to assuming constant heat production with depth and the order of magnitude of the above estimates is considered realistic; doubling the radius, for example, would only increase the anomalies by 25% (i.e. they would still be low).

The above calculations consider only the situation where thermal conductivity remains constant, both laterally (i.e. it is the same in both granite and country rock) and vertically. Granitic bodies generally have higher thermal conductivities than their host rocks but the resulting refraction of heat into the intrusion may be offset by lateral conduction out of the body due to the higher radiogenic heat production in the granite (England et al., 1979). Thermal conductivity measurements have not been recorded for the Etive granites but values for other granites, for example S W England (Wheildon et al., 1977) and Cairngorm (J. Wheildon, pers. comm.) range between approximately 3.1 - 3.6 W m^{-1} $^{o}C^{-1}$. Preliminary studies on the thermal conductivity of Dalradian hornfels and garnet-mica schist in the vicinity of Ben Nevis give values of 2.6 - 2.9 W m^{-1} $^{o}C^{-1}$ perpendicular to banding and 2.8 - 3.9 W m^{-1} $^{o}C^{-1}$ parallel to banding (P Webb, pers. comm.). Assigning a value to thermal conductivity is particularly difficult in the case of metamorphic rocks which comprise layers of different compositions alternating on scales varying from millimeters to tens of metres and large numbers of measurements would be required to characterise the thermal conductivity of country rocks around Etive. However, these preliminary results suggest that there will be little contrast in the thermal conductivity between the Etive granites (assuming K ≈ 3.3 - 3.4 W m^{-1} $^{o}C^{-1}$) and their metamorphic host rocks (which dip NW at variable angles) and perturbations of the vertical heat flow due to refraction are likely to be low.

Thermal conductivity is a function of temperature and pressure as well as composition and, for the temperature/pressure gradients normally encountered in the upper crust, the effect of temperature dominates. For a temperature increase of approximately 100 ^{o}C conductivity falls by about 10% (Oxburgh et al., 1977). Since this effect has been ignored

in calculations the resulting heat flow anomaly values may be slightly, but not significantly low.

While appreciating the errors inherent in the method used to calculate heat flow anomalies and the uncertainties in the parameters assumed, the results indicate that the heat flow anomaly produced by the Etive Complex is of low magnitude and is unlikely to enhance the local geothermal gradient significantly.

7.4:2 The Cairngorm Granite

The surface heat flow anomaly due to the Cairngorm Granite was calculated using the gravity modelling program of Talwani and Ewing (1960) adapted for heat flow (Section 7.3). Because other intrusions in the N E Grampians have been shown to possess high heat productivities (e.g. Rollin, 1982) it is possible that the surface heat flow over Cairngorm is enhanced by their presence. Heat flow models were, therefore, also developed for neighbouring intrusions in order to assess the degree of enhancement. Since each intrusion modelled has a different mean heat production contrast with the country rocks (see below) separate anomalies were calculated and summed to give the total surface anomaly. Polygonal laminae models approximating the three-dimensional geometry of the intrusions were based on the gravity model of Locke (1982) and modified to obtain finite bodies as described in Figure 7.4. Uncertainties in the gravity model arising from uncertainties in density contrasts and removal of the regional gravity field (Section 6.1) will be reflected in errors on the value of Q_z.

Heat production contrasts used to model heat flow anomalies for each intrusion are listed in Table 7.4.

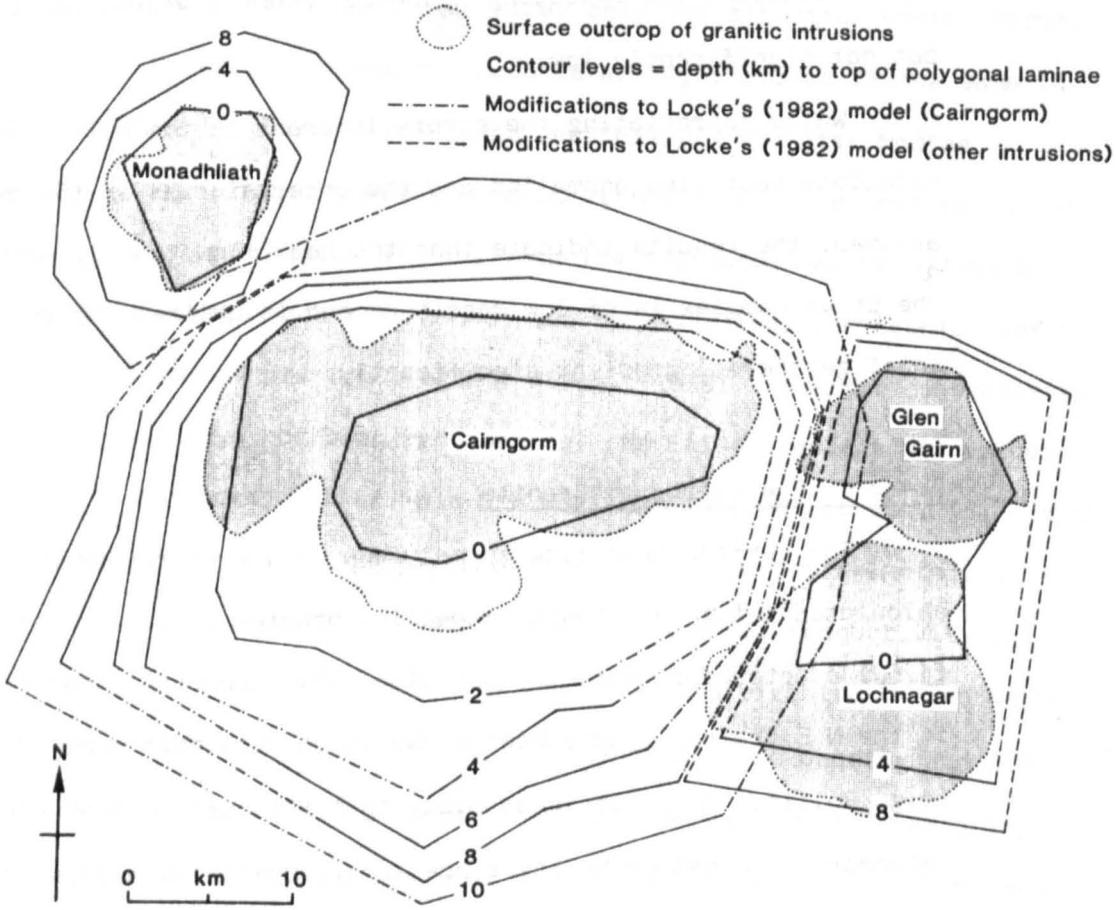

Figure 7.4 Polygonal laminae model used to estimate the heat flow anomaly due to 'excess' heat production in the Cairngorm and neighbouring intrusions; modified from the gravity model of Locke (1982), see Figure 6.3 Modifications in the north-west and east were necessary to obtain finite bodies for each intrusion allowing separate calculations based on the mean heat production contrasts in the Cairngorm, Monadhliath and Glen Gairn + Lochnagar granites (see text). Truncation of the contours in the extrame east (cf. Figure 6.3) does not affect the calculation of the total heat flow anomaly in the area of interest (see text). The elongation of structure contours to the south-west in Locke's model (Figure 6.3) are probably due to the presence of an older granitic ridge (Section 6.1) and do not represent an extension of the Cairngorm intrusion; contours were, therefore, closed in this area.

Intrusion	Mean heat production $\mu W\ m^{-3}$		Reference
	In granite	Contrast with country rock	
Cairngorm	4.9	3.4	This study
Monadhliath	4.6	3.0	Hennessey, 1981
Glen Gairn	2.6	1.0	Hennessey, 1981
Lochnagar	3.1	2.5	P. Webb, pers. comm.
Glen Gairn + Lochnagar	2.8	1.7	

Table 7.4 Mean heat production values used for calculation of heat flow anomalies due to the Cairngorm and neighbouring intrusions. Glen Gairn and Lochnagar were modelled as a single intrusion with a heat production contrast of 1.7 $mW\ m^{-3}$.

Results are presented in Figures 7.5 and 7.6. It is clear from these Figures that although the lateral extent of the surface heat flow anomaly over Cairngorm is increased by the presence of other radiogenic bodies in close proximity, the amplitude of the maximum anomaly is not significantly enhanced. This observation justifies the truncation of structure contours to the east in Figure 7.4.

The relatively high heat production contrast for Cairngorm (cf. Etive, Section 7.4:1) increases the probability of heat refraction at the granite - country rock contact. Assessment of the deviation in vertical heat flow due to refraction is made difficult by the lack of reliable constraints on the thermal conductivity of the surrounding country rocks, and the non-ideal geometry of the Cairngorm intrusion. An estimate is possible by taking a mean aspect ratio for the Cairngorm Granite of approximately 2:1 (radius : depth, based on the radius at 6 km depth; Figure 7.4), a heat production contrast of 3.4 $mW\ m^{-3}$, a depth of approximately 10 km, a minimal conductivity contrast with country rocks (see Section 7.4:1) and using the calculations of England et al., (1979) shown in Table 7.5. The implication is that the net

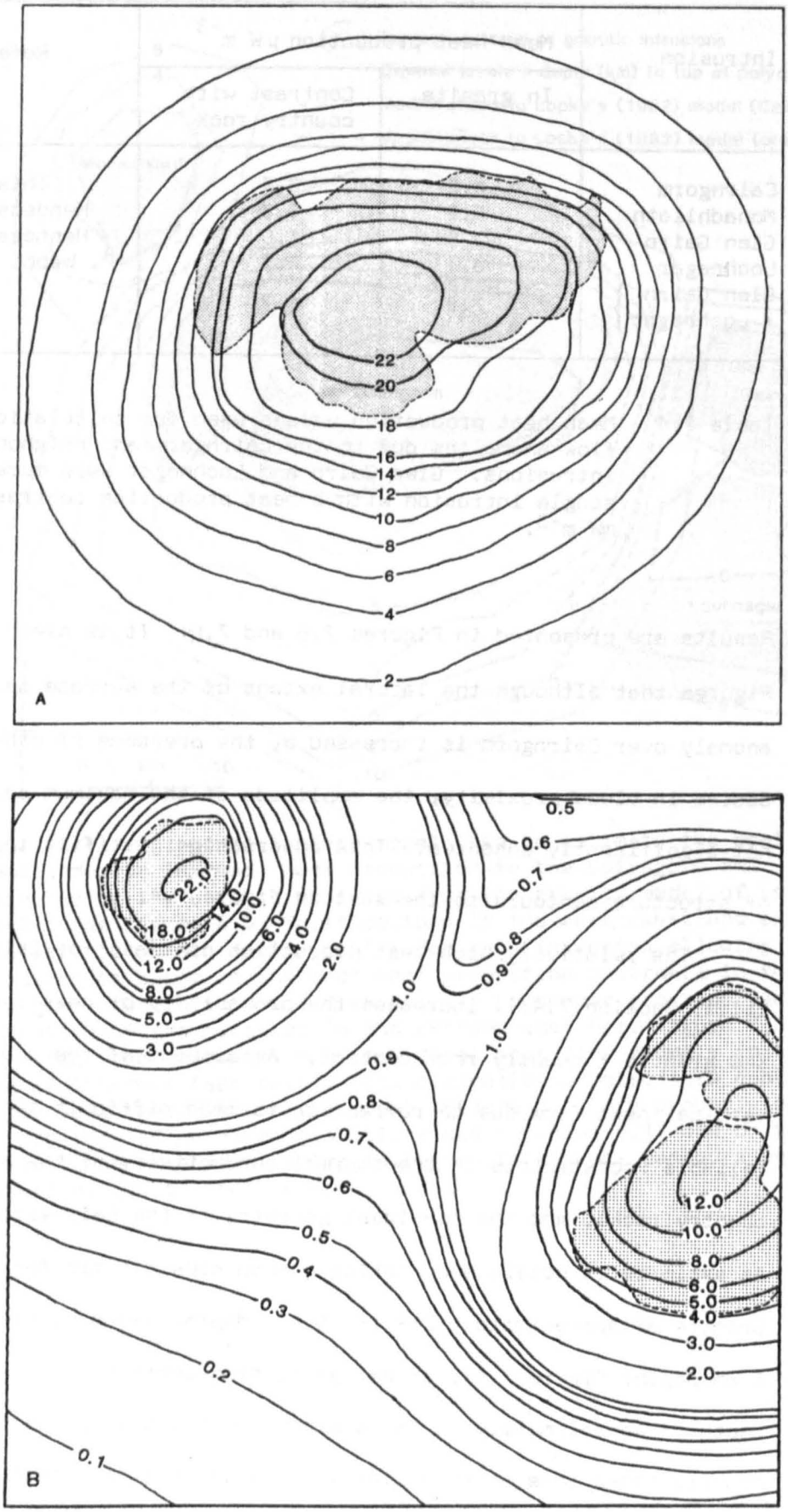

Figure 7.5 Surface heat flow anomalies due to 'excess' radiogenic heat production in the Cairngorm (a) and neighbouring (b) intrusions. Contour levels are in mW m^{-2}.

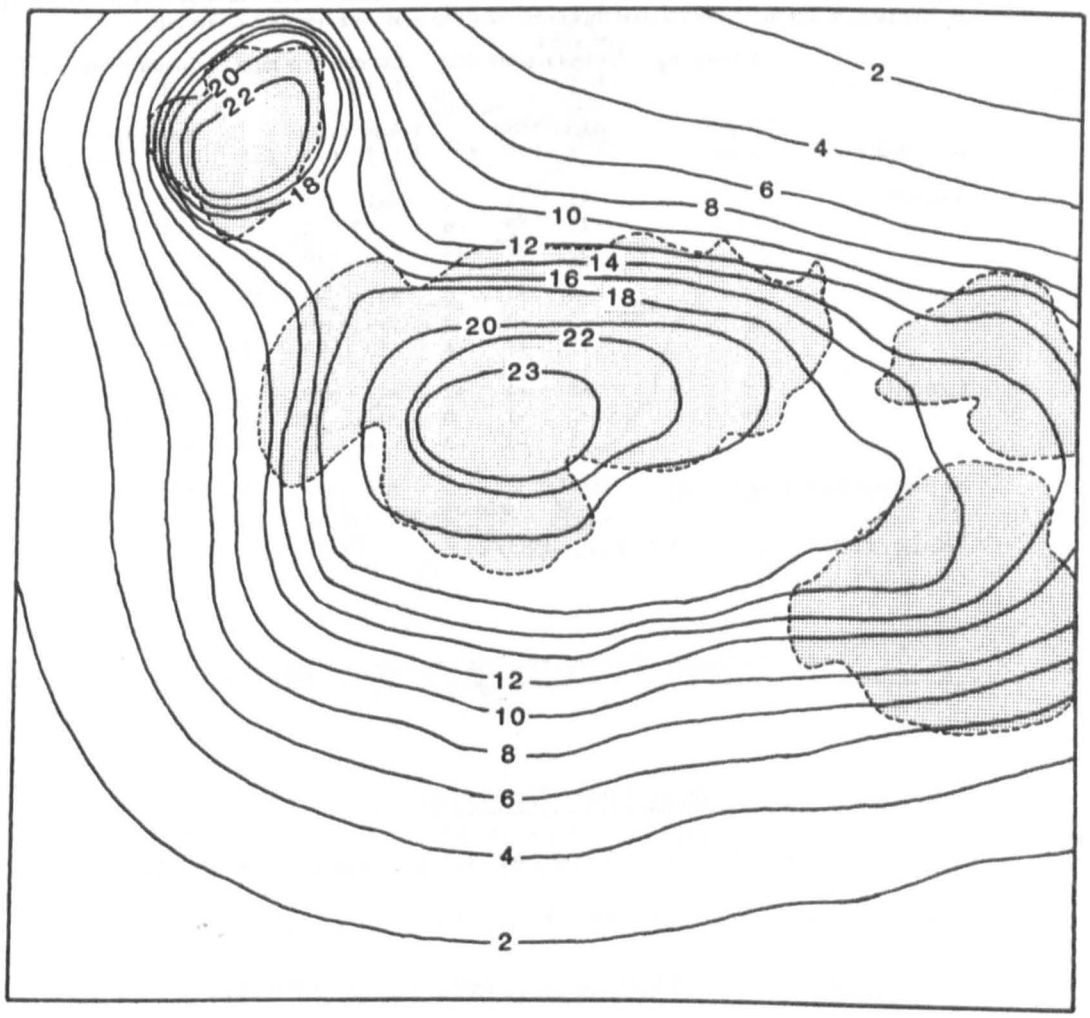

Figure 7.6 Resultant surface heat flow field derived from summation of the anomalies in Figure 7.5a and b. Contour levels are in mW m^{-2}.

refraction of heat probably takes place away from the intrusion and is of the order of -6 to -10 mW m^{-2}. However, subsurface connections with other granites at less than 2-3 km depth, as indicated by gravity models (Figure 6.3) will tend to reduce this refraction effect. Errors due to the uncertainties in the amount of heat refraction and to the possible increase in thermal conductivity with depth must be considered in the assessment of results shown in Figure 7.6.

Surface heat flow expected on the axes of idealized cylindrical plutons of differing aspect ratios, depths, heat productivity and conductivity contrast with the country rock. The heat flows are expressed as deviations in $mW\,m^{-2}$ from the heat flux expected if the heat were transferred vertically.

	$K^* = k_c : k_p$	Conductivity ratio 1 : 1.25			Conductivity ratio 1 : 1.5			Conductivity ratio 1 : 2		
	Depth	Aspect ratio			Aspect ratio			Aspect ratio		
Heat production	(km)	1 : 2	1 : 1	2 : 1	1 : 2	1 : 1	2 : 1	1 : 2	1 : 1	2 : 1
$3\,\mu Wm^{-3}$	5	−1	−1	−1	+7	+5	+1	+23	+16	+8
	10	−12	−9	−6	−3	−2	−2	+14	+9	+2
	20	−33	−24	−14	−23	−18	−12	−6	−5	−5
$2\,\mu Wm^{-3}$	5	+2	+1	0	+11	+8	+3	+27	+19	+7
	10	−5	−3	−3	+4	+3	0	+20	+14	+5
	20	−19	−13	−8	−10	−7	−5	+7	+4	0
$1\,\mu Wm^{-3}$	5	+5	+4	+2	+14	+10	+4	+30	+20	+8
	10	+2	+1	0	+11	+8	+2	+27	+19	+7
	20	−5	−3	−3	+4	+3	0	+20	+14	+5
No heat production	All	+10	+7	+3	+18	+13	+6	+33	+24	+10

Table from England et al., (1979)

7.5 PRELIMINARY ESTIMATES OF TEMPERATURE GRADIENTS

7.5:1 The regional heat flow field

In order to calculate vertical temperature gradients in the Etive and Cairngorm granites the total heat flow must be known;

i.e. heat flow anomaly (Q_z) + regional heat flow ($q^* + A_c D$)

where q^* = heat flow from below the intrusion; A_c = heat productivity in the upper crustal country rocks;

D = depth of the intrusion; Q_z = heat flow anomaly calculated in Section 7.4:2

Regional heat flow measurements available for Scotland are shown in Figure 7.7. Not all holes were drilled specifically for heat flow measurements and depths vary from approximately 170-920 m (Oxburgh et al., 1977). No regional heat flow measurements are available

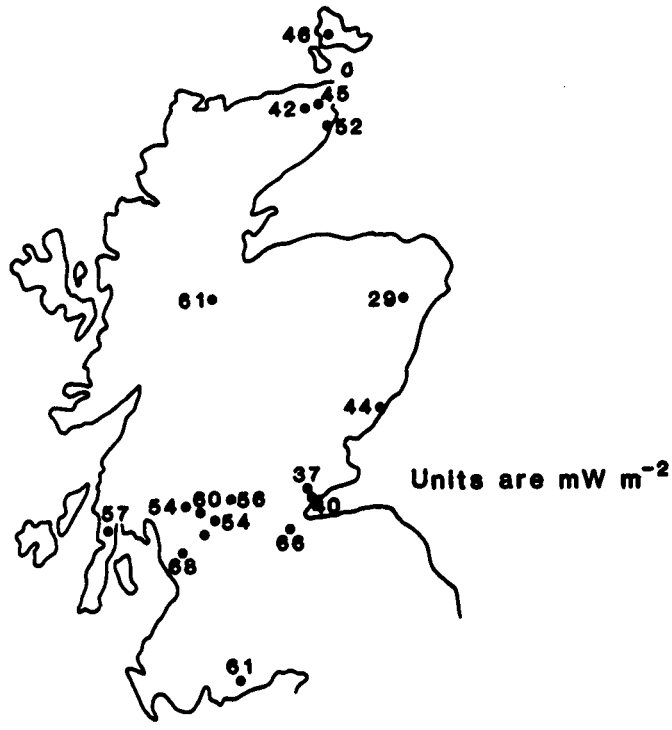

Figure 7.7 Heat flow measurements for Scotland; from Oxburgh et al., 1977 and Rollin, 1982. All holes were drilled in country rocks ranging from Dalradian and Moines to Devonian and Carboniferous sediments.

in the immediate area of interest, but the region north of the Caledonian suture (Figure 7.7) is considered to be a single heat flow province (G. Brown, pers. comm.) and a mean value of approximately 50 mW m^{-2} was assumed, based on the data in Figure 7.7.

7.5:2 Temperature gradients in the Etive and Cairngorm intrusions

Addition of a regional surface heat flow of 50 mW m^{-2} to the anomalies calculated in Section 7.4:1 and 2 gives maximum surface heat flows of approximately 56 mW m^{-2} and 73 mW m^{-2} over Etive and Cairngorm respectively. Temperature gradients at the surface are given by;

$$\frac{\delta T}{\delta z} = \frac{Q_s}{k}$$ where Q_s = the total vertical surface heat flow

and is approximately 16 ^{o}C km^{-1} for Etive and 21.5 ^{o}C km^{-1} for

Cairngorm. Preliminary measurements in a shallow borehole at Cairngorm give a near surface temperature gradient, uncorrected for topography, of 20.5 $^{o}C\ km^{-1}$ (J. Wheildon, pers. comm.); in good agreement with the predicted value. Geochemical analyses of Main Granite samples removed from the 300 m borehole indicate that U values are higher at depth than in surface samples (mean U content from borehole samples ≈15 ppm; P. Webb, pers. comm.). Taking this into account, the agreement between the measured and calculated near-surface temperature gradients may imply that the heat flow anomaly due to radioelements in the Cairngorm granite is higher than predicted and the assumed regional heat flow is overestimated. Extending this argument, if the northern Caledonides represent a single heat flow province, then some of the higher values in Figure 7.7 may be associated with enhanced heat production in upper crustal rocks.

Assuming that both the thermal conductivity and heat production in the Central Starav Granite (Etive) and Main Granite (Cairngorm) remain constant with depth, the sub-surface temperatures may be calculated from the expression;

$$T_z = \frac{1}{K} \left(Q_s z - \tfrac{1}{2} A_o z^2\right) + T_s$$

where Q_s = total surface heat flow; A_o = surface heat production; z = depth; K = thermal conductivity; T_s = mean annual surface temperature, assumed to be approximately 10 ^{o}C.

Calculated temperature profiles are presented in Figure 7.8

7.6 SUMMARY

A detailed study of the areal distribution and mineral location of radioelements in granitic rocks gives a reasonable indication of the probable variation of heat production with depth in an intrusion.

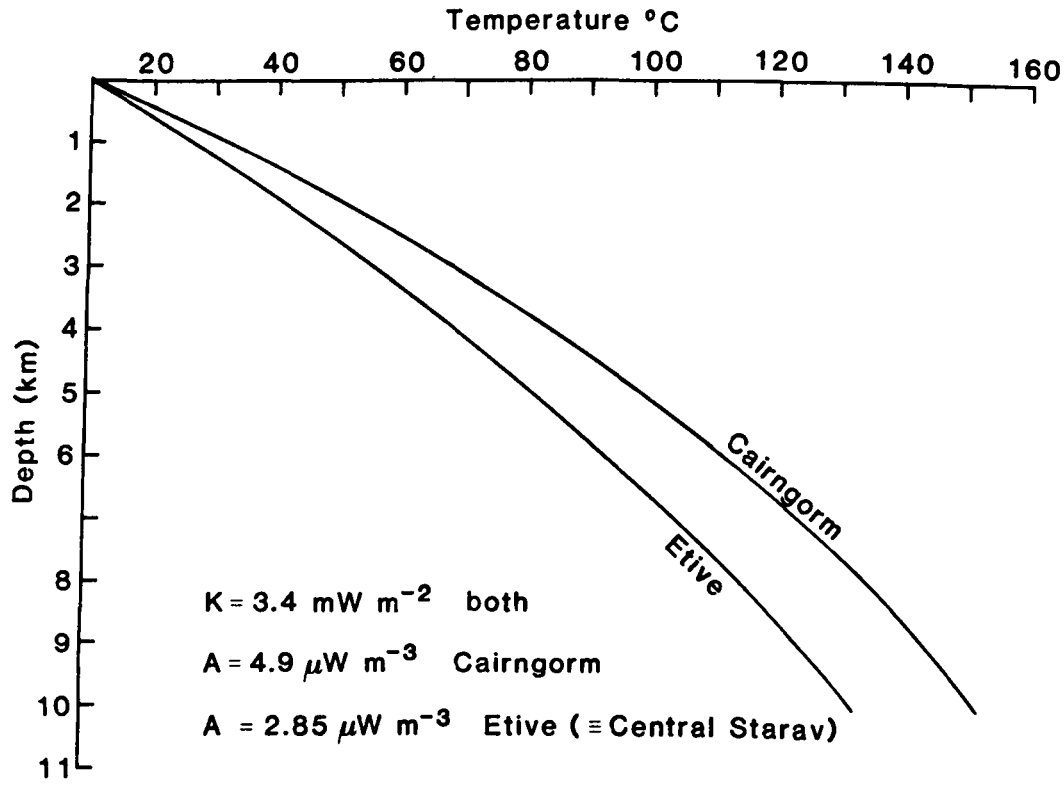

Figure 7.8 Predicted temperature profiles beneath the Starav Granites (Etive) and the Cairngorm Granite. The Etive profile would be even steeper (i.e. lower temp. gradient) if an exponential decrease in A with depth were used in all calculations.

Application of this information, combined with three-dimensional gravity models and a knowledge of the regional heat flow, to heat flow anomaly modelling procedures leads to prediction of the sub-surface temperature profile.

The economic application of hot dry rock geothermal energy requires crustal temperatures in excess of 150 ^{o}C to be reached within accessible drilling depths, 4-5 km (Rollin, 1982). However, it is reasonable to consider extractions between 2-4 km at temperatures above approximately 64 ^{o}C for low enthalpy applications in space heating projects etc. (Batchelor and Pearson, 1979). Results from this study indicate that temperature gradients below the Etive Complex do not meet either of the above requirements but that those below Cairngorm may satisfy the second. The recognition of a granite with enhanced radioelement contents and

geometric dimensions similar to the Cairngorm granite and buried beneath a low conductivity sedimentary cover would prove a more ideal target for hot dry rock geothermal exploitation. Although the presence of low density, large volume granitic masses may be interpreted from high amplitude, negative Bouguer anomalies, this characteristic is, of course, not diagnostic for high heat production values. As shown in this study, both the Etive Complex and the Cairngorm Granite are associated with large negative Bouguer anomalies but the corresponding heat productivities and heat flow anomalies differ considerably. Thus such anomalies which are thought to represent buried, low density granites elsewhere in the Caledonides would need to be tested by drilling before the geothermal resource could be evaluated.

CHAPTER 8 CONCLUSIONS AND DISCUSSION

Radioelement levels and heat production in the Cairngorm Granite are two to three times higher than those in the Etive Complex and are comparable with those observed in the Hercynian Granites of S.W. England. The contrast in U and Th contents of the Cairngorm Granite and the Etive Complex is reflected in the accessory mineral assemblages of these intrusions.

In the Etive Complex the U-, Th-bearing accessory mineral assemblage changes with progressive differentiation; from apatite + zircon + sphene → apatite + zircon + sphene ± allanite ± chevkinite ± thorite → apatite + zircon + sphene + thorite ± allanite → zircon + thorite + monazite ± apatite. For all units of the complex, mass balance calculations show that all Th in a rock sample may be accommodated in apatite, zircon, sphene and, in particular, in thorite, allanite and monazite. However, these primary accessory phases never account for more than 4-5 ppm U. Where whole-rock U values are ≥4-6 ppm, in the Central Starav and N. Cruachan units, enhanced U levels are held, predominantly, in secondary locations following hydrothermal alteration of primary biotite and Fe-Ti oxides and sulphides. The limited areal extent of this late-stage/post-magmatic U-enrichment suggests that large-scale hydrothermal convection systems were not established in the Etive Complex; the secondary alteration results from expulsion of relatively small volumes of magmatic fluids during the final, water-saturated stages of differentiation.

The least evolved unit of the Cairngorm massif, the N E Granite, exhibits the same apatite + zircon + sphene ± allanite association observed in much of the Etive Complex. Enhanced U levels in the N E Granite (≥4-6 ppm) are also accommodated, predominantly, in secondary

locations. In the more evolved, Main Granite the U-, Th-bearing accessory mineral assemblage changes to apatite + zircon + monazite + xenotime + Nb-Ta-oxides ± thorite ± uraninite. Although most of these minerals are primary accessory phases, which crystallised during the magmatic stages of evolution, textural relationships indicate that many of the U-rich Nb-Ta-oxides are of post-consolidation age, crystallising along microfractures which may represent escape channels for residual fluids. Most of the whole-rock Th in the Cairngorm Granite may be accounted for by the observed accessory minerals, especially monazite and thorite. Apatite, zircon, monazite and xenotime account for no more than 4-6 ppm U. Although there is a well-developed secondary U distribution in several Main Granite samples, Lexans studies, microprobe analyses and whole-rock trace element correlations indicate that much of the enhanced U content resides in refractory Nb-Ta-oxides. The importance of uraninite to the U budget in the Cairngorm Granite is difficult to assess since this mineral is unstable in the surface environment and was not unambiguously identified during this study. A detailed study of the U-, Th-bearing accessory minerals in core samples is, at present, being undertaken and is partly aimed at determining the relative importance of Nb-Ta-oxides and uraninite with respect to whole-rock U levels in fresh samples.

The transition from a sphene-allanite association to a monazite-xenotime-Nb-Ta-oxide association within the Cairngorm Granite is partially evident in the Etive Complex; sphene and allanite disappear and monazite appears in the Central Starav Granite. There is, however, no evidence for the appearance of xenotime or Nb-Ta-oxides; whole-rock Y levels do not increase and Nb levels only increase marginally with differentiation in the Etive Complex. These contrasts are also apparent in the HREE

element contents of each intrusion.

It is instructive to consider the trace element variations of the Etive and Cairngorm intrusions in terms of their tectonic setting and possible magma source regions. Both intrusions post-date final Caledonian subduction, with ages of ∿410 and 408 m.y. respectively, and were intruded during a period of tectonic relaxation and uplift associated with major shears and low angle faults (see for example, Pitcher 1983). The calc-alkaline/alkali-calcic nature of these intrusions is consistent with this 'mature-arc' association (see Brown, 1982). Recently, several authors (e.g. Harris, Pearce and Tindle, in prep; Brown, Thorpe and Webb, in press) have applied trace element data to the discrimination of siliceous plutonic rocks from various arc and anorogenic origins. Important variations have been observed in the levels of LIL and HFS elements, and related to contributions from dehydrated, subducted slab, crustal contamination and within-plate mantle; LIL enrichment is associated with the downgoing slab and crustal sources, while HFS enrichment is associated with greater contributions from within-plate mantle. Source-related trace element contrasts between highly evolved plutonic rocks are difficult to identify due to the influence of crystal fractionation and late-stage fluid interactions. However, the problem may be overcome by plotting discriminatory elements against a suitable differentiation index and only making comparisons at the same degree of differentiation. Using this method, Brown, Thorpe and Webb (in press) distinguish late (post-subduction) Caledonian Granites of the Southern Province from those of the E Grampian Highlands (see Figure 8.1). Those in the south are subduction enriched (high in LIL elements) while those in the E Grampian Highlands are both

rich in LIL elements and HFS elements indicating both a subduction related and/or crustal input and a greater within-plate (HFS) component. These results are consistant with the greater distance of the E Highlands Granites from the former subduction zone than the southern granites (∿200 km as opposed to 100 km; see Figure 3.5). A plot of data from this study on Brown et al's discriminant diagram shows a similar distinction between the Etive and Cairngorm Granites (Figure 8.1).

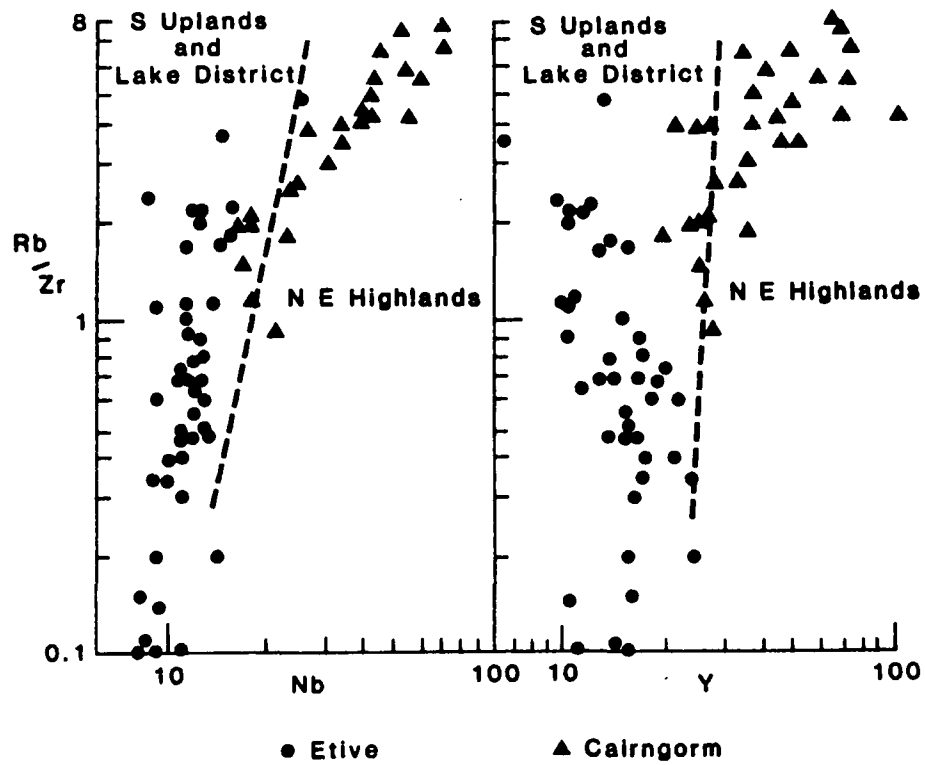

Figure 8.1 Plot of fractionation index (Rb/Zr) against Nb and Y for the Etive Complex and the Cairngorm Granites. Fields for the S Uplands and Lake District granites and N E Highland granites are from Brown, Thorpe and Webb (in press).

This distinction, however, cannot be explained in terms of distance from the proposed Iapetus suture (both intrusions are approximately the

same distance away), or arc maturity at the time of intrusion (both are post-subduction). These differences may be related to E-W variations in mantle characteristics, or to a combination of vertical stratification in the mantle and the depth of magma generation. The latter may in turn be related to E-W variations in crustal thickening and/or oblique closure of the Iapetus ocean, halting subduction earlier in the east. Alternatively, the influence of F^- and Cl^- on the behaviour of U, Th, Nb and Y during partial melting and differentiation may have been over-looked. High F^- and Fl^- levels in the Cairngorm Granite are evident in the presence of fluorite and detectable Cl in biotites (P. Webb pers. comm.)

The present study indicates that highly-evolved, alkali-calcic plutons such as Cairngorm, with high levels of both LIL and HFS elements, of mature arc type, are better candidates for geothermal resources than petrologically diverse, calc-alkaline-alkali-calcic intrusions such as the Etive Complex. Despite the high heat production observed, the predicted and measured heat flow over Cairngorm is sub-economic and probably reflects the low regional background heat flow of N Scotland. The similarity between the Cairngorm massif and other E Highland granites suggests that these may also represent sub-economic prospects. However, similar post-tectonic Caledonian Granites in the S Province, with high radioelement levels and large negative Bouguer anomalies, e.g. Shap and Skiddaw may represent more economic prospects for the following reasons:

a) The degree of erosion is generally lower in the S Province than in the E Highlands and high radioelement concentrations observed at the surface may continue to a greater depth.

b) The background heat flow is known to be higher in the S Province.

c) The lower conductivity country rocks in the S Province would tend to direct heat flow towards rather than away from the granites. The ideal prospect, in fact, would be a high heat production granite buried beneath a low conductivity, insulating sedimentary cover, e.g. Weardale.

To extend this theme, similar post-collision intrusions such as the Hercynian granites of the Iberian Peninsular and the Massif Central, France, or the Caledonian plutons of the Svecofenian orogenic belt, may represent potential prospects worthy of preliminary investigation.

Finally, the mineral locations of U observed in this study have interesting implications regarding granite fertility with respect to U mineralisation. Carrat (1975) recognised granites associated with U mineralisation to be post-tectonic, highly differentiated with fluid-stage alteration effects and containing uraninite. Such characteristics have been recognised in the two-mica leucogranites of the Massif Central, France (e.g. Barbier, 1967; Carrat, 1975; Cuney, 1978) and, to a large extent, in the Cairngorm Granite. However, an important difference may be noted between the Cairngorm Granite the Hercynian plutons of the Massif Central: the latter do not contain xenotime or Nb-Ta-oxides. Models for U-mineralisation associated with these granites are based on leaching of uraninites, either by percolating meteoric waters, or late-stage/post magmatic hydrothermal fluids, and redeposition of U in veins within or close to the plutons. A lack of U mineralisation in some Hercynian granites has been attributed to the non-soluble nature of high-Th uraninite. In Cairngorm, this lack of U-mineralisation may equally be related to the refractory nature of the major, U-bearing accessory

minerals, i.e. Nb-Ta-oxides and xenotime. The accessory mineral assemblage of highly-differentiated, alkali-calcic intrusions, therefore, may be an important indication of fertility with respect to uranium mineralisation. Following this, sediments formed from erosion of granites such as Cairngorm may contain high concentrations of U and Th in heavy mineral fractions.

REFERENCES

Abbey, S., 1980, Studies in "standard samples" for use in the general analysis of silicate rocks and minerals: Geostand. Newslett., 4, 163-190.

Adams, J. A. S., Osmond, J. K. and Rogers, J. J. W., 1959, The geochemistry of thorium and uranium. In: Physics and chemistry of the Earth, vol. III, Pergamon Press.

Alderton, D. M. H., Pearce, J. A., and Potts, P. J., 1980, Rare Earth Element mobility during granite alteration: Evidence from southwest England: Earth Planet. Sci. Letts., 49, 149-165.

Amiel, S., 1962, Analytical applications of delayed neutron emmision in fissionable elements: Anal. Chem., 34, 1683-1692.

Anderson, J. G. C., 1937, The Etive Granite Complex: Quart. J. Geol. Soc. Lond., 93, 487-533

Arth, J. G., 1976, Behaviour of trace elements during magmatic processes- A summary of theoretical models and their application: U. S. Geol. Surv. J. Res., 4, 41-47.

Baedecker, P. A., Rowe, J. J. and Steinnes, E., 1976, Application of epithermal neutron activation in multielement analysis of silicate rocks employing both coaxial Ge(Li) and low energy photon detector systems: J. Radioanal. Chem., 40, 115-146.

Bailey, E. B. and Maufe, H. B., 1916, The geology of Ben Nevis and Glen Coe: Mem. Geol. Surv. Scotland.

Ball, T. K. and Basham, I. R., 1979, Radioactive accessory minerals in granites from S W England: Proc. Ussher Soc., 437-448.

Bamford, D., Nunn, K., Prodehl, C. and Jacob, B., 1978, L.I.S.P.B. IV - Crustal structure of northern Britain: Geophys, J. Roy. Astr. Soc., 54, 43-60.

Barbier, M. J., Carrat, H. G. and Ranchin, G., 1967, Presence d'uraninite en tant que mineral accessoire usuel dans les granites a deux micas uraniferes du Limousin et de la Vendee: C. R. Acad. Sci. Paris, 264, 2436-2439.

Barbier, M. J., 1974, Continental weathering as a possible origin of vein-type uranium deposits: Mineralium Deposita, 9, 271-288.

Barrow, G., Hinxman, L. W., Cunningham, C. E. H. and Kynaston, H., 1913, The geology of Upper Strathspey, Gaick and the Forest of Atholl: Mem. Geol. Surv. Gt. Britain, 64.

Basham, I. R., Vairinho, M. M. B. and Bowles, J. F. W., 1979, Uranium-bearing accessory minerals in Sao Pedro Do Sul Granite, Portugal. In: Vein-type and similar uranium deposits in rocks younger than Proterozoic: Proc. Tech. Comm. Meeting, Lisbon; I.A.E.A., Vienna, 279-298.

Basham, I. R., Ball, T. K., Beddoe-Stephens, B. and Michie, U. McL., 1982, Uranium-bearing accessory minerals and granite fertility: 1, Methods of identification: Symp. Proc., Symp. on uranium exploration methods, Paris.

Batchelor, A. S. and Pearson, C. M., 1979, Preliminary studies of dry rock geothermal exploitation in southwest England: Instn. Mining Metall. Spec. Paper, B51-B56.

Batchelor, A. S., Pearson, C. M., and Halladay, N. P., 1980, The enhancement of the permeability of granite by explosive and hydraulic fracturing. In: Proc. 2nd International Seminar on the results of the EC Geothermal Energy Research (eds. Strub, A. S.and Ungemach, P.), D. Reidel Pub. Co., Dordrecht, Holland, 1009-1031.

Berzina, I. G., Yeliseyeva, O. P. and Popenko, D. P., 1974, Distribution relationships of uranium in intrusive rocks of Northern Kazakhstan: Internat. Geol. Rev., 16, 1191-1204.

Birch, F., Roy, R. F., and Decker, E. R., 1968, Heat flow and thermal history in New England and New York. In: Studies of Appalachian geology: northern and maritime (eds. Zen et al.), Interscience, New York, 437-451.

Blaxland, A. B., Aftalion, M. and Van Breeman, O., 1979, Pb isotopic composition of feldspars from Scottish Caledonian granites and the nature of the underlying crust: Scott. J. Geol., 15, 139-151.

Bohse, H., Rose-Hansen, H., Sorensen, H., Steenfelt, A., Lovborg, L. and Kundzendorf, H., 1976, On the behaviour of uranium during crystallisation of magmas - with special emphasis on alkaline magmas. In: Formation of uranium ore deposits: Proc. of a symp., Athens, 1974, I.A.E.A., Vienna, 49-60.

Bott, M. H. P., 1974, The geological interpretation of a gravity survey of the English Lake District and the Vale of Eden: J. Geol. Soc. Lond., 130, 309-331.

Bowden, P., Bennett, J. N., Kinnaird, J. A., Whitley, J. E., Abaa, S. I. and Hadzigeorgiou-Stavrakis, P. K., 1981, Uranium in the Niger-Nigeria Younger Granite Province: Mineral. Mag., 44, 379-389.

Bowie, S. H. U., Simpson, P. R. and Rice, C. M., 1973, Application of fission-track and neutron activation methods to geochemical exploration. In: Geochemical Exploration (ed. Jones, M. J.): Proc. 4th Internat. Geochem. Exploration Symp. Lond., Instn. Mining Metall., London, 359-372.

Bowles, J. F. W., 1978, Quantitative microprobe analysis of uranium minerals: Microscope, 26, 55-67.

Brown, G. C., and Hughes, D. J., 1973, Great Glen Fault and timing of granite intrusion on the proto-Atlantic continental margins. Nature Physical Science, 244, 129-132.

Brown, G. C., 1979, Some geochemical and geophysical constraints on the origin and evolution of Caledonian granites. In: The Caledonides of the British Isles-reviewed (eds. Harris, A. L., Holland, C. H. and

Leake, B. E.), J. Geol. Soc. Lond. Spec. Issue, Scottish Academic Press, Edinburgh, 645-651.

Brown, G. C. and Locke, C. A., 1979, Space-time variations in the British Caledonian granites: some geophysical correlations: Earth Planet. Sci. Letts., 45, 69-79.

Brown, G. C., Plant, J. A. and Lee, M. K., 1979, Geochemical and geophysical evidence on the geothermal potential of Caledonian granites in Britain: Nature, 280, 129-131.

Brown, G. C., Cassidy, J., Locke, C. A., Plant, J. A. and Simpson, P. R., 1981, Caledonian plutonism in Britain: A summary: J. Geophys. Res., 86, 10502-10514.

Brown, G. C., 1982, Calk-alkaline intrusive rocks: their diversity, evolution and relation to volcanic arcs. In: Andesites (ed. Thorpe, R. S.), J. Wiley and Sons, Chichester.

Brown, G. C., Lee, M. K., Webb, P. C., Wheildon, J. and Cassidy, J., 1982, Development of HDR reconnaissance in the United Kingdom. In: Proc. of the Internat. Conference on Geothermal Energy, Florence, Italy, B.H.R.A. Fluid Engineering.

Brown, P. E., Miller, J. A. and Grasty, R. L., 1968, Isotopic ages of late Caledonian granite intrusions in the British Isles: Proc. York. Geol. Soc., 36, 251-276.

Brune, D. and Jirlow, K., 1964, Optimisation in activation analysis by means of epithermal neutrons: Determination of molybdenum in steel: Nukleonik, 6, 242-244.

Brunfelt, A. O. and Steinnes, E., 1969, Instrumental activation analysis of silicate rocks with epithermal neutrons: Anal. Chim. Acta., 48, 13-24.

Buntebarth, G., 1976, Distribution of uranium in intrusive bodies due to combined migration and diffusion: Earth Planet. Sci. Letts., 32, 84-90.

Cassidy, J., 1980, Gamma-ray spectrometric surveys of Caledonian granites: method and interpretation: Unpublished Ph.D. thesis, University of Liverpool.

Clark, S. P., Peterman, Z. E. and Heier, K. S., 1966, Abundances of uranium, thorium and potassium. In: Handbook of physical constants, Geol. Soc. America Memoir No 97, part 24, 521-541.

Clarke, D. B., 1981, The mineralogy of peraluminous granites: A review: Canadian Mineralogist, 19, 3-17.

Clayburn, J. A. P., Harmon, R. S., Pankhurst, R. J. and Brown, J. F., 1983, Sr, O and Pb isotope evidence for origin and evolution of Etive Igneous Complex, Scotland: Nature, 303, 492-497.

Costain, J. K., Glover, L. and Sinha, A. K., 1977, Evaluation and targetting of geothermal energy resources in southeastern United States: Progress Report VPI-SU-5648-1, U. S. Dept. of Energy.

Costain, J. K., Glover, L. and Sinha, A. K., 1978, Evaluation and targetting of geothermal energy resources in southeastern United States: Progress report VPI-SU-5648-3, U. S. Dept. of Energy.

Costain, J. K., Glover, L. and Sinha, A. K., 1980, Low-temperature geothermal resources in the eastern United States: EOS Trans. American Geophys. Union, 61, 1-4.

Cumming, G. L., 1974, Determination of uranium and thorium in meteorites by the delayed neutron method: Chem. Geol., 13, 257-267.

Cuney, M., 1978, Geological environment, mineralogy and fluid inclusions of the Boirs Noirs - Limouzat uranium vein, Forez, France: Econ. Geol., 73, 1567 -1610.

Darnley, G. A., 1972, Airbourne gamma-ray survey techniques. In: Uranium prospecting handbook (eds. Bowie, S. H. U., Davis, M. and Ostle, D.), . Instn. Mining Metall., London, 174-211.

Davis, J. C., 1973, Statistics and data analysis in geology, Wiley, New York.

Deer, W. A., Howie, R. A. and Zussman, J., 1972, An introduction to the rock-forming minerals, Longman Group Ltd., London.

Dewey, J. F., 1969, Evolution of the Appalachian/Caledonian Orogen: Nature, 222, 124-129.

Dewey, J. F. and Pankhurst, R. J., 1970, The evolution of the Scottish Caledonides in relation to their isotopic age pattern: Trans. Roy. Soc. Edinburgh, 68, 361-389.

Doig, R., 1968, The natural gamma-ray flux: in-situ analysis: Geophysics, 33, No 2, 311-328.

Droop, G. T. R. and Treloar, P. J., 1981, Pressure of metamorphism in the thermal aureole of the Etive Granite Complex: Scott. J. Geol., 17, 85-102.

El-Batrouk, S. I., 1975, Geophysical investigation on the Loch Doon Granite, SW Scotland: Unpublished Ph.D. thesis, University of Glasgow.

England, P. C., Oxburgh, E. R. and Richardson, S. W., 1980, Heat refraction and heat production in and around granite plutons in north-east England: Geophys. J. Roy. Astr. Soc., 62, 439-455.

Epstein, S. and Taylor, Jr. H. P., 1967, Variation of 018/016 in minerals and rocks. In: Researches in geochemistry vol. 2 (ed. Abelson, P. H.), John Wiley, New York, 29-62.

Fehn, U., Cathles, L. M. and Holland, H. D., 1978, Hydrothermal convection and uranium deposits in abnormally radioactive plutons: Econ. Geol., 73, 1556-1566

Fitton, J. G. and Hughes, D. J., 1970, Volcanism and plate tectonics in the British Ordovician: Earth and Planet. Sci. Letts., 8, 223-228.

Flanagan, F. J., 1973, 1972 values for international geochemical reference samples: Geochim. Cosmochim. Acta., 37, 1189-1200.

Flett Brown, J., 1972, Rb-Sr studies and related chemistry on the Caledonian calk-alkaline igneous rocks of north-west Argyllshire: Unpublished Ph.D. thesis, University of Oxford.

Fourcade, S. and Allegre, C. J., 1981, Trace element behaviour in granite genesis: A case study. The calk-alkaline plutonic association from the Querigut Complex (Pyrenees, France): Contribs. Mineral. Petrol., 76, 177-195.

Fowler, M. B., 1981, Uranium content, distribution and migration in the Glendessary syenite, Inverness-shire: Mineral. Mag., 44, 443-448.

Frondel, C., 1958, Systematic mineralogy of uranium and thorium: U. S. Geol. Surv. Bull., 1064.

Frost, C. S. and O'Nions, R. K., 1982, Isotopic constraints from O, Sr, Nd, and Pb on granite petrogenesis - abstract: EOS, 63, 461.

Gableman, J. W., 1977, Migration of uranium and thorium - exploration significance. In: Studies in geology No 3, American Assoc. Petroleum Geologists.

Gallagher, M. J., Michie, U., Smith, R. T. and Haynes, L., 1971, New evidence of uranium and other mineralisation in Scotland: Trans. Instn. Mining. Metall., 80, B150-B173.

Garnish, J. D., 1976, Geothermal energy: the case for research in the United Kingdom: Dept. of Energy Paper No 9, H.M.S.O., London.

Gerasimovsky, V. I., 1974, Trace elements in selected groups of alkaline rocks. In: The alkaline rocks (ed. Sorensen, H.), John Wiley and Sons, New York.

Gorden, G. E., Randle, K., Goles, G. G., Corliss, J. B., Beeson, M. H. and Oxley, S. S., 1968, Instrumental activation analysis of standard rocks with high resolution gamma-ray detectors: Geochim. Cosmochim. Acta., 32, 369-396.

Gorvindaraju, K. and De La Roche, H., 1977, Rapport (1966-1976) sur les elements en traces dans trois roches standards geochemiques du CRPG: Basalte, BR et granites, GA et GH: Geostand. Newslett., 1, 67-98.

Gorvindaraju, K. and Roelandts, I., 1977, Neutron activation analysis of two U.S.G.S. rock reference samples (Granite G-2, Andesite AGV-1) and discussion in the light of compiled data: Geostand. Newslett., 1, 163-179.

Grasty, R. L. and Darnley, A. G., 1971, The calibration of gamma-ray spectrometers for ground and airbourne use: Geol. Surv. Canada, Dept. of Energy, Mines and Resources, Paper 71-17.

Grutt, Jr. E. W., 1971, Prospecting criteria for sandstone-type uranium deposits. In: Uranium prospecting handbook (eds. Bowie, S. H. U., Davis, M. and Ostle, D.), Instn. Mining. Metall. (1972).

Halliday, A. N., 1981, On the sources of uranium in some Scottish Caledonian granites: Mineral. Mag., 44, 437-442.

Hamilton, P. J., Evensen, N. M., O'Nions, R. K. and Tarney, J., 1979, Sm-Nd systematics of Lewisian gneisses: implications for the origin of granulites: Nature, 277, 25-28.

Hamilton, P. J., O'Nions, R. K. and Pankhurst, P. J., 1980, Isotopic evidence for the provenance of some Caledonian granites: Nature, 287, 279-284.

Harmon, R. S. and Halliday, A. N., 1980, Oxygen and strontium isotope relationships in the British, late, Caledonian granites: Nature, 283, 21-25.

Harry, W. T., 1965, The form of the Cairngorm Granite pluton: Scott. J. Geol., 1, 1-8.

Hennessy, J., 1978, Uranium, thorium and Caledonian granite magmatism: Unpublished Ph.D thesis, University of Liverpool.

Hennessy, J., 1981, A classification of British Caledonian granites based on uranium and thorium contents: Mineral. Mag., 44, 449-454.

Hertogen, J. and Gijbels, R., 1971, Instrumental activation of rocks with a low energy photon detector: Anal. Chim. Acta., 56, 61-82.

Hildreth, W., 1979, The Bishop Tuff: Evidence for the origin of compositional zonation in silicic magma chambers: Geol. Soc. America Special Paper 180.

Howarth, R. J., Koch, G. S., Plant, J. A. and Lowry, R. K., 1981, Identification of uraniferous granitoids in the U.S.A. using stream sediment geochemical data: Mineral. Mag., 44, 455-470.

Institute of Geological Sciences, 1979, Bouguer anomaly map of Argyll, 1:250 000 series, sheet 56 N - 06 W.

Ishihara, S. and Mochizuki, T., 1980, Uranium and thorium contents of Mesozoic granites from Peninsular Thailand: Bull. Geol. Surv. Japan, 31, 369-376.

Johnstone, M. R. W., 1975, Morarian Orogeny and Grenville Belt in Britain: Nature Phys. Sci., 257, 301-302.

Johnstone, G. S., Plant, J. A. and Watson, J. V., 1979, Regional geochemistry of the Northern Highlands of Scotland. In: The Caledonides of the British Isles- reviewed (eds. Harris, A. L., Holland, C.H. and Leake, B. E.), Geol. Soc. Lond. Spec. Publ., 117-128.

Kennedy, M. J., 1979, The continuation of the Canadian Appalachians into the Caledonides of Britain and Ireland. In: The Caledonides of the British Isles- reviewed (eds. Harris, A. L., Holland, C. H. and Leake, B. E.), Geol. Soc. Lond. Spec. Publ., 33-64.

Killeen, P. G. and Carmicheal, C. M., 1970, Gamma-ray spectrometer calibration for feild analysis of thorium, uranium and potassium: Canadian J. Earth Sci., 7, 1093-1098.

Killeen, P. G. and Heier, K. S., 1975, Th, U, K and heat production measurements in ten Precambrian granites of the Telemark area, Norway: Norges Geol. Unders, 319, 59-83.

Kleeman, J. D. and Lovering, J. F., 1967, Uranium distribution studies by fission track registration in Lexan plastic prints: Atomic Energy Austrlia, 10, No 4, 3-8.

Kogarko, L. N., 1974, Role of volatiles. In: The alkaline rocks (ed. Sorensen, H.), John Wiley and Sons, New York.

Kozlova, P. S. and Gurvich, M. Y., 1979, The behaviour of uranium in post-magmatic alteration of potassic alkali rocks: Geochem. Internat., 2, 109-117.

Kynaston, H. and Hill, J. B., 1908, The geology of the country near Oban and Dalmally: Mem. Geol. Surv. Scotland.

Labhart, T. P. and Rybach, L., 1971, Abundance and distribution of uranium and thorium in the syenite of Piz Giuv (Aar - Massif, Switzerland): Chem. Geol., 7, 237-251.

Lachenbruch, A. H., 1968, Preliminary geothermal model of the Sierra Navada: J. Geophys. Res., 73, 6977-6989.

Lachenbruch, A. H., 1970, Crustal temperature and heat production: implications of the linear heat flow relation: J. Geophys. Res., 75, 3291-3300.

Lachenbruch, A. H., 1971, Vertical gradients of heat production in the continental crust, 1, Theoretical detectability from near-surface measurements: J. Geophys. Res., 76, 3842-3851.

Larsen, E. S. and Gottfried, D., 1960, Uranium and thorium in selected suites of igneous rocks: American J. Sci., 258-A, 151-169.

Larsen, E. S., Phair, G., Gottfried, D. and Smith, W. L., 1955, Uranium in magmatic differentiation: U.S. Geol. Surv. Prof. Paper 300, 65-74.

Leake, B. E., 1973, Granite emplacement: the granites of Ireland and their origin. In: Crustal evolution in northwest Britain and adjacent regions (eds. Bowes, D. R. and Leake, B. E.), Geol. J. Spec. Issue No 10, 221-248.

Leonova, L. L. and Renne, O. S., 1964, Distribution of uranium, thorium and potassium in homogeneous granites: Geochem. Internat., 4, 775-781.

Levinson, A. A. and Coetzee, G. L., 1978, Implications of disequilibrium in exploration for uranium ores in the surficial environment using radiometric techniques - A review: Minerals Sci. Engng., 10, No 1, 19-27.

Locke, C. A., 1980, Geophysical investigations of Caledonian granites within a regional classification: Unpublished Ph.D. thesis, University of Liverpool.

Lopez-Escobar, L. and Oyarzun, J. M., 1974, Uranium in calc-alkaline granitoids of Central Chile: Pacific Geol., 8, 47-50.

Lovborg, L., 1972, Assessment of uranium by gamma-ray spectrometry. In: Uranium prospecting handbook (eds. Bowie, S. H. U., Davis, M. and Ostle, D.), Instn. Mining Metall., London, 157-173.

Lovborg, L., Wollenberg, H., Sorensen, P. and Hansen, J., 1971, Field determination of uranium and thorium by gamma-ray spectrometry, exemplified by measurements in the Ilimaussaq alkaline intrusion, South Greenland: Econ. Geol., 66, 368-384.

Mackie, W., 1925, The heavier accessory minerals in the granites of Scotland: Trans. Edin. Geol. Soc., 12, 22-40.

McCarthy, T. S. and Robb. L. J., 1978, On the relationship between cumulus mineralogy and trace and alkali element chemistry in an Archean granite from the Barbeton region, South Africa: Geochim. Cosmochim. Acta., 42, 21-26.

McKerrow, W. S., and Cocks, L. R. M., 1976, Progressive faunal migration across the Iapetus Ocean: Nature, 262, 304-306.

McKerrow, W. S., Leggett, J. K. and Eales, M. H., 1977, Imbricate thrust model of the Southern Uplands of Scotland: Nature, 267, 237-239.

Miller, J. A. and Brown, P.E., 1965, Potassium-argon age studies in Scotland: Geol. Mag., 102, 106-134.

Miller, T. P. and Bunker, C. M., 1976, A reconnaissance study of the uranium and thorium contents of plutonic rocks of the southeastern Seaward Peninsula, Alaska: U.S. Geol. Surv. J. Res., 4, 367-377.

Miller, C. F. and Stoddard, E. F., 1981, The role of manganese in the paragenesis of magmatic garnet: An example from the Old Woman-Piute Range, California: J. Geol., 89, 233-246.

Mitchel, A. H. G. and McKerrow, W. S., 1975, Analogous evolution of the Burma Orogen and the Scottish Caledonides: Geol. Soc. America Bull., 86, 305-315.

Moreau, M., 1976, L'uranium et les granitoides - essai d'interpretation. In: Geology, mining and extractive processes of uranium (ed. Jones, M. J.), Instn. Mining Metall., London, 83-102.

O'Connor, P. J., 1981, Radioelement geochemistry of Irish granites: Mineral. Mag., 44, 485-495.

Ormaasen, D. E. and Raade, G., 1978, Heat generation versus depth of crystallisation for Norwegian monzonite rocks: Earth Planet. Sci. Letts., 39, 145-150.

Oxburgh, E. R., Richardson, S. W., Bloomer, J. R., Martin, A. and Wright, S., 1977, Subsurface temperature studies from heat flow studies in the United Kingdom. In: Seminar on geothermal energy, Commision of the Europian Communities EUR 5920, 1, 155-173.

Pagel, M., 1979, Particularites geochemiques uranium, thorium dans les complexes du massif des Ballons (Vosges meridionales): C. R. Acad. Sci. Paris, series D, 289, part 2, 53-56.

Pagel, M., 1982, The mineralogy of uranium, thorium and rare-earth elements in two radioactive graites of the Vosges, France: Mineral. Mag., 46, 151-163.

Pal, S. and Terrell, D. J., 1978, Instrumental neutron activation analysis of twenty-nine international geochemical reference standards: Geostand. Newslett, 2, 187-197.

Pankhurst, R. J., 1979, Isotope and trace element evidence for the origin and evolution of Caledonian granites in the Scottish Highlands. In: Origin of granite batholiths; geochemical evidence (eds. Atherton, M. P. and Tarney, J.), 18-33.

Pankhurst, R. J. and Sutherland, D. S., 1982, Caledonian granites and diorites of Scotland and Ireland. In: Igneous rocks of the British Isles (ed. Sutherland, D. S.).

Parker, R. L. and Fleischer, M., 1968, Geochemistry of niobium and tantalum: U.S. Geol. Surv. Prof. Paper 612.

Phair, G. and Gottfried, D., 1964, The Colorado Front Range, Colorado, U.S.A. as a uranium and thorium province. In: The natural radiation environment (eds. Adams, J. A. S. and Lowder, W. M.), University of Chicago Press, Chicago, 7-38.

Phillips, W. J., Fuge, R. and Phillips, N., 1981, Convection and crystallisation in the Criffel-Dalbeattie pluton: J. Geol. Soc. London, 138, 351-366.

Phillips, W. E. A., Stillman, C. J. and Murphy, T., 1976, A Caledonian plate tectonic model: Quart. J. Geol. Soc. London, 132, 579-609.

Pidgeon, R. T. and Aftalion, M., 1978, Cogenetic and inherited zircon U-Pb systems in granites: Palaeozoic granites of Scotland and England: Geol. J. Spec. Issue 10, 183-220.

Pitcher, W. S., 1983, Granite type and tectonic environment. In: Mountain Building Processes (ed. Hsu, K.), Academic Press, 19-40.

Pitcher, W. S., and Berger, A. R., 1972, The geology of Donegal: a study of granite emplacement and unroofing: Wiley-Interscience, London.

Plant, J. A., Brown, G. C., Simpson, P. R. and Smith, R. T., 1980, Signatures of metalliferous granites in the Scottish Caledonides: Trans. Instn. Mining. Metall. (sect. B: Appl. Earth. Sci.), 89, 198-210.

Pliler, R. and Adams, J. A. S., 1962, The distribution of thorium and uranium in a Pennsylvanian weathering profile: Geochim. Cosmochim. Acta., 26, 1137-1146.

Pollack, H. N. and Chapman, D. S., 1977, On the regional variation of heat flow, geotherms and lithospheric thickness: Tectnophysics, 38, 279-296.

Potts, P. J., Thorpe, O. W. and Watson, J. S., 1981, Determination of the rare-earth element abundances in 29 international rock standards by instrumental neutron activation analysis: A critical appraisal of calibration errors: Chem. Geol., 34, 331-352.

Price, P. B. and Walker, R. M., 1963, A simple method of measuring low uranium concentrations in natural crystals: Appl. Phys. Letts., 2, 23-25.

Ragland, P. C., Billings, G. K. and Adams, J. A. S., 1967, Chemical fractionation and its relationship to the distribution of thorium and uranium in a zoned granite batholith: Geochim. Cosmochim. Acta., 31, 17-33.

Ranchin, G., 1968, Contribution a l'etude de la repartition de l'uranium dans les roches granitiques saines. Exemple du Massif de St. Sylvestre dans le Limousin: Sci. de la Terre, 13, 159-205

Read, H. H., 1961, Aspects of Caledonian magmatism in Britain: Liverpool and Manchester Geol. J., 2, 653-683.

Read, H. H., MacGregor, A. G. and Johnstone, G. S., 1966, The Grampian Highlands: British Regional Geol. 3rd edition.

Reed, S. J. B., 1975, Electron microprobe analysis, Cambridge University Press.

Richardson, K. A., 1963, Thorium, uranium and potassium in the Conway Granite, New Hampshire, U.S.A. In: The natural radiation environment (eds. Adams, J. A. S. and Lowder, W. M.), University of Chicago Press, Chicago, 51-62.

Richardson, S. W., 1975, Heat flow processes. In: Geodynamics today, Roy. Soc., London, 123-132.

Richardson, S. W. and Oxburgh, E. R., 1978, Heat flow, radiogenic heat production and crustal temperatures in England and Wales: Quart. J. Geol. Soc., 135, 323-337.

Richardson, S. W. and Oxburgh, E. R., 1979, The heat flow field in mainland U.K.: Nature, 282, 565-567.

Roberts, J. L., 1966, Ignimbrite eruptions in the volcanic history of the Glencoe cauldron subsidence: Liverpool and Manchester Geol. J., 5, 173-184.

Rogers, J. J. W. and Ragland, P. C., 1961, Variation of thorium and uranium in selected granitic rocks: Geochim. Cosmochim. Acta., 25, 99-109.

Rogers, J. J. W. and Adams, J. A. S., 1978, Uranium (92), thorium (90). In: Handbook of Geochemistry (Exec. ed. Wedepohl K. H.), Springer-Verlag, Berlin-Heidelberg.

Rogers, J. J. W., Ragland, P. C., Nishimori, R. K., Greenberg, J. K. and Hauck, S. A., 1978, Varieties of granitic uranium deposits and favourable exploration areas in the Eastern United States: Econ. Geol., 73, 1539-1555.

Rollin, K. E., 1982, Investigation of the geothermal potential of the U.K.: A review of data relating to hot dry rock and selection of targets for detailed study: Institute of Geological Sciences, London, Report.

Rosholt, J. N., Zartman, R. E. and Nkomo, I. T., 1973, Lead isotope systematics and uranium depletion in the Granite Mountains, Wyoming: Geol. Soc. America Bull., 84, 989-1002.

Routti, J. T. and Prussin, S. G., 1969, Photo-peak method for the computer analysis of gamma-ray spectra from semi-conductor detectors: Nucl. Instru. Methods, 72, 125-142.

Roy, R. F., Blackwell, D. D. and Birch, F., 1968, Heat generation of plutonic rocks and continental heat flow provinces: Earth Planet. Sci. Letts., 5, 1-12.

Rumble, D. III, 1976, Oxide minerals in metamorphic rocks. In: Oxide minerals (ed. Rumble, D. III.), Mineral. Soc. America Short Course Notes, 3, R1-R20.

Rybach, L., 1976, Radioactive heat production: a physical property determined by the chemistry of rocks. In: The physics and chemistry of minerals and rocks (ed. Strens, R. G. J.), John Wiley and Sons, New York.

Rybach, L. and Buntebarth, G., 1981, Heat-generating radioelements in granitic magmas: J. Volcan. Geotherm. Res., 10, 395-404.

Sclater, J. G. and Francheteau, J., 1970, The implications of terrestial heat flow observations on current tectonic and geochemical models of the crust and upper mantle of the Earth: Geophys. J. Roy. Astr. Soc., 20, 509-542.

Shand, S. J., 1927, The eruptive rocks, Wiley, New York.

Simmonds, G., 1967, Interpretation of heat flow anomalies, 1, Contrasts in heat production: Rev. Geophys., 5, 43-52.

Simpson, P. R., Plant, J. A. and Cope, M. J., 1977, Uranium abundance and distribution in some granites from northern Scotland and southwest England as indicators of uranium provinces. In: Geology, mining and extractive processes of uranium (ed. Jones, M. J.), Instn. Mining Metall., London, 126-139.

Simpson, P. R., Brown, G. C., Plant, J. A. and Ostle, D., 1979, Uranium mineralisation and granite magmatism in the British Isles: Phil. Trans. Roy. Soc. London, 291, 385-412.

Sorensen, H., 1970(1), Occurence of uranium in alkaline igneous rocks. In: Uranium Exploration Geology, Internat. Atomic Energy Agency, Vienna, 161-168.

Sorensen, H., 1970(2), Low-grade uranium deposits in agpaitic nepheline syenites, South Greenland. In: Uranium Exploration Geology, Internat. Atomic Energy Agency, Vienna, 151-159.

Staatz, M. H. and Miller, T. P., 1976, Uranium and thorium content of radioactive phases of the Zane Hills Pluton: U.S. Geol. Surv. Circ. 733, 39-41.

Steenfelt, A., 1982, Uranium and selected trace elements in granites from the Caledonides of East Greenland: Mineral. Mag., 46, 201-210.

Steinnes, E., 1971, Epithermal neutron activation analysis of geological material. In: Activation analysis in geochemistry and cosmochemistry (eds. Brunfelt, A. O. and Steinnes, E.), Universitets Forlayet, Oslo, 113-128.

Stuckless, J. S. and Ferreira, C. P., 1976, Labile uranium in granitic rocks. In: International symposium on exploration of uranium ore deposits, Proc., Vienna: Internat. Atomic Energy Agency Tech. Reports Series, 717-730.

Stuckless, J. S., Millard, H. T., Bunker, C. M., Nkomo, I. T., Rosholt, J. N., Bush, C. A., Huffman, C. and Keil, R. L., 1977, A comparison of some analytical techniques for determining uranium, thorium and potassium in granitic rocks: J. Res. U.S. Geol. Surv., 5, No 1, 83-91.

Stuckless, J. S., Bunker, C. M., Bush, C. A., Doering, W. P. and Scott, J. H., 1977, Geochemical and petrological studies of a uraniferous granite from the Granite Mountains, Wyoming: J. Res. U.S. Geol. Surv., 5, No 1, 61-81.

Stuckless, J. S. and Nkomo, I. T., 1980, Preliminary investigations of U-Th-Pb systematics in uranium-bearing minerals from two granitic rocks from the Granite Mountains, Wyoming: Econ. Geol., 75, 289-295.

Stuckless, J. S., Nkomo, I. T. and Doe, B. R., 1981, U-Th-Pb systematics in Hydrothermally altered granites from the Granite Mountains, Wyoming: Geochim. Cosmochim. Acta., 45, 635-645.

Swanberg, C. A., 1972, Vertical distribution of heat generation in the Idaho Batholith: J. Geophys. Res., 77, 2508-2513.

Swanberg, C. A. and Blackwell, D. D., 1973, Areal distribution and geophysical significance of heat generation in the Idaho Batholith and adjacent intrusions in Eastern Oregon and Western Montana: Geol. Soc. America Bull., 84, 1261-1282.

Talwani, M. and Ewing, M., 1960, Rapid computation of gravitational attraction of three-dimensional bodies of arbitrary shape: Geophys., 25, 203-225.

Tammemagi, H. Y. and Smith, N. L., 1975, A radiogeologic study of the granites of SW England: J. Geol. Soc. London, 131, 415-427.

Tanner, A. B., 1964, Radon migration in the ground: a review. In: The natural radiation environment (eds. Adams, J. A. S. and Lowder, W. M.), University of Chicago Press, Chicago, 161-190.

Taylor, H. P., Jr., 1971, Oxygen isotope evidence for large-scale interaction between meteoric ground waters and Tertiary granodiorite intrusions, Western Cascade Range, Oregon: J. Geophys. Res., 76,

7355-7874.

Thirlwall, M. F., 1982, Systematic variation in chemistry and Nd-Sr isotopes across a Caledonian calc-alkaline volcanic arc: Implications for source materials: Earth Planet. Sci. Letts., 58, 27-50.

Thorpe, R. S., 1981, Precambrian igneous rocks of England, Wales and Southeast Ireland. In: Igneous rocks of the British Isles (ed. Sutherland, D. S.), John Wiley, New York.

Tieh, T. T. and Ledger, E. B., 1981, Fission track study of uranium in two granites of Central Texas: Contrib. Mineral. Petrol., 76, 12-16.

Tieh, T. T., Ledger, E. B. and Rowe, M. W., 1980, Release of uranium from granitic rocks during in-situ weathering and initial erosion (Central Texas): Chem. Geol., 29, 227-248.

Tilling, R. I. and Gottfried, D., 1969, Distribution of thorium, uranium and potassium in igneous rocks of the Boulder Batholith region, Montana, and its bearing on radiogenic heat production and heat flow: U.S. Geol. Surv. Prof. Paper 614-E.

Tilling, R. I., Gottfried, D. and Dodge, F. C. W., 1970, Radiogenic heat production of contrasting magma series: Bearing on interpretation of heat flow: Geol. Soc. America Bull., 81, 1447-1462.

Tindle, A. G., 1982, Petrogenisis of the Loch Doon granitic intrusion, Southern Uplands of Scotland: Unpublished Ph.D. thesis, Open University.

Tindle, A. G. and Pearce, J. A., 1981, Petrogenetic modelling of in-situ fractional crystallisation in the zoned Loch Doon pluton, Scotland: Contrib. Mineral. Petrol., 78, 196-207.

Turekian, K. K., 1978, Strontium. In: Handbook of geochemistry (Exec. ed. Wedepohl, K. H.), Springer-Verlag, Berlin-Heidelberg.

Tweedie, J. R., 1979, Origin of uranium and other metal enrichments in the Helmsdale granite, eastern Sutherland, Scotland: Trans. Instn. Mining. Metall. (sect. B: Appl. Earth Sci.), 88, 145-153.

Upton, B. G. J., Aspen, P., Graham, A. and Chapman, N. A., 1979, The pre-Paleozoic basement of the Scottish Midland Valley: Nature, 260, 517-518.

Vlasov, K.A., 1966, Geochemistry and mineralogy of rare-elements and genetic types of their deposits, Vol II, Mineralogy of rare elements: Acad. Sci. U.S.S.R., Oldbourne Press, London.

Watson, J. V. and Plant, J., 1979, Regional geochemistry of uranium as a guide to deposit formation: Phil. Trans. Roy. Soc. London, A291, 321-328.

Wenner, D. B. and Spaulding, J. D., 1982, Uranium and thorium geochemistry in the Elberton Batholith of the southern Appalachians, U.S.A.: Mineral. Mag., 46, 227-231.

Wheildon, J., Francis, M. F. and Thomas-Betts, A., 1977, Investigations of the SW England thermal anomaly zone. In: Seminar on geothermal energy (Brussels), Directorate-General for Research, Science and Education, Commission of European Communities, 175-188.

Wheildon, J., Francis, M. F. and Thomas-Betts, A., 1980, Exploration and interpretation of the SW England geothermal anomaly. In: Proc. 2nd. International Seminar on the results of the E C Geothermal Energy Research (Stasbourg, France), (eds. Strub, A. S. and Ungemach, P.), Dordrecht, Holland, D. Reidel Pub. Co., 456-465.

Whitfield, J. M., Rogers, J. J. W. and Adams, J. A. S., 1959, The relationship between the petrology and the thorium and uranium contents of some granitic rocks: Geochim. Cosmochim Acta., 17, 248-271.

Wilson, M. R. and Akerblom, G. V., 1980, Uranium enriched granites in Sweden: Serv. Geol. Unders., Rapp. Och. Medd. 19.

Wilson, M. R. and Akerblom. G.V., 1982, Geological setting and geochemistry of uranium rich granites in the Proterozoic of Sweden: Mineral. Mag., 46, 233-245.

Wollenberg, H. A., 1971, Fission-track radiography of uranium and thorium in radioactive minerals: Riso. Rep., 228, 347-358.

Wollenberg, H. A. and Smith, A. R., 1964, Radioactivity and radiogenic heat in the Sierra Nevada plutons: J. Geophys. Res., 69, 3471-3478.

Wollenberg, H. A. and Smith, A. R., 1968, Radiogeological studies in the central part of the Sierra Nevada Batholith, California: J. Geophys. Res., 73, No 4, 1481-1495.

Wormald, M. R. and Clayton, C. G., 1976, Observations on the accuracy of gamma spectrometry in uranium prospecting. In: International Symposium on Exploration of Uranium Ore Deposits, I.A.E.A. (Vienna).

Yeliseyeva, O. P., 1977, Content and distribution of uranium, thorium, yttrium and the rare-earths in accessory minerals in granitoids: Geochem. Internat., 9, 1338-1351.

Yeliseyeva, O. P., Ryabchikov, I. D. and Bogatyreva, N. A., 1974, On the types of distribution of uranium in accessory zircon: Geochem. Internat., 9, 1389-1398.

Zielinski, R. A., 1978, Uranium abundances and distribution in associated glassy and crystalline rhyolites of the western United States: Geol. Soc. America Bull., 89, 409-414.

Zielinski, R. A., Peterman, Z. E., Stuckless, J. S., Rosholt, J. N. and Nkomo, I. T., 1981, The chemical and isotopic record of rock-water interaction in the Sherman Granite, Wyoming and Colorado: Contribs. Mineral. Petrol., 78, 209-219.

APPENDIX A ADDITIONAL ANALYTICAL METHODS

A1 Preparation of rock powders

Visible weathering was removed from all samples using a hammer and a hydraulic splitter. Samples were then split to approximately 3-4 cm cubes and coarse crushed in a hardened steel jaw crusher. Approximately 100 g of quartered crush was powdered to less than 200 mesh in a tungsten-carbide tema. Powders were dryed overnight at 120 °C.

A2 Energy dispersive X-ray fluorescence

An energy dispersive XRF technique was used to analyse for the following elements:

Rb, Sr, Y, Zr, Nb -- analyses on pellets

Si, Ti, Al, Fe, Mn, Mg, Ca, Na, P, K -- analyses on glass beads

Pellets were prepared by mixing 8 g of rock powder with Moviol binder and pressing into 3 cm discs. Beads were prepared by mixing the equivalent of 0.400 g of rock powder (after loss on ignition) with 2.40 g of lithium metaborate/tetraborate flux (Spectroflux 100B) and fusing at 1100 °C for 10-15 minutes.

Analytical equipment comprised a Link Systems Meca 10-44 energy dispersive spectrometer and integral 860 Analyser System. Details of the operating system and calibration can be found in Potts et al. (in press) The system was calibrated using a series of international standards with a range of compositions greater than that expected in normal silicate rocks. Samples analysed for trace elements on pressed powder pellets were also analysed for major elements in order to apply mass absorption correctipns.

Precision is better than 2% for all major elements except Al, Mg, and Na (2,3 and 10% relative respectively). Precision is better than 2% for all trace elements analysed.

Samples from the Etive Complex were analysed for trace elements, SiO_2, TiO_2 and P_2O_5 on pellets, by ED-XRF. Samples from the Cairngorm Granite were analysed for major elements on beads, by ED-XRF and for trace elements on pellets, by wavelength dispersive XRF at Nottingham University. Analyses of international standards on both systems are presented in Table A1.

	AGV-1				GSP-1		
	Abbey (1980)	Notts pellets n=3	O.U. pellets n=4	O.U. beads n=4	Abbey (1980)	Notts pellets n=3	O.U. pellets n=12
SiO_2	60.24		60.82	59.79	67.90		67.12
TiO_2	1.07		1.03	1.08	0.67		0.63
Al_2O_3	17.37			17.08	15.41		
Fe_2O_3	6.86			7.05	4.29		
MnO	0.10			0.10	0.04		
MgO	1.54			1.61	0.98		
CaO	4.99			4.94	2.05		
Na_2O	4.37			4.33	2.83		
K_2O	2.95			2.96	5.56		
P_2O_5	0.52		0.48	0.49	0.28		0.27
Ba	1200	1222			1300	1256	
Ce	71	74			360	347	
Rb	67	69	69		250	256	251
Sr	660	665	668		240	236	237
Y	19	24	21		29	26	29
Zr	230	233	234		500	498	505
Nb	16	15	15		23	25	25

Table A1. Major and trace element data for U.S.G.S. standards analysed during this study, compared with the recomended values of Abbey (1980). Major elements are quoted in wt. % oxides and trace elements in ppm.

A3 Instrumental neutron activation analysis

Abundances of REEs (La, Ce, Nd, Sm, Eu, Gd, Tb, Tm, Yb, Lu) are routinely determined at the Open University by INAA (see Potts et al., 1981)

Powdered rock samples are prepared for irradiation as described for ENAA (Section 4.2) using AC(OURS) as a primary standard and a suitable international standard as a secondary standard. Batches are irradiated in a thermal neutron flux of 5×10^{12} n cm^{-2} s^{-1} for 24-30 hours at the University of London Reactor Centre, Ascot. Energy spectra are counted for 800 s on the LEPS detector (for Sm) and then on the coaxial Ge(Li) detector (for La and Sc) followed by a further half day on the LEPS for all remaining elements. Peak areas are calculated using the peak fitting program, Sampo (Routti and Prussin 1969), and corrected for neutron flux variations, decay times of specific isotopes between standard and unknown, sample weight and count time.

Precision is better than 5% on all REEs (see Potts et al.,1981). Comparison of analyses for NIM-G with expected values is presented in Table A2.

	Potts et al. (1981)	This study 2 analyses
La	114	113.5
Ce	210	210.0
Nd	76.4	75.8
Sm	16.1	15.4
Eu	0.35	0.35
Tb	2.88	3.16
Tm	2.3	2.08
Yb	14.4	14.20
Lu	2.2	2.12

Table A2. INAA data for REEs in NIM-G compared with the expected values from Potts et al. (1981). Data are in ppm.

APPENDIX B DENSITY MEASUREMENTS OF ETIVE SAMPLES

Rocks were soaked in water for several weeks so that saturated densities could be measured. The weight of each sample was measured using a counter-balance, a) with the rock suspended in air, and b) with the rock suspended in water. Using Archimedes' principle, the density is given by:

$$\rho = \frac{W_A}{W_A - W_W}$$

where ρ = density, W_A = weight in air, W_W = weight in water

This procedure was repeated five times on sample N58 to asses the experimental error on density measurements:

Dry weight ($kg \times 10^{-3}$)	Saturated weight ($kg \times 10^{-3}$) In air	In water	Saturated density ($kg\ m^{-3}$)
115.1	116.20	70.27	2530
115.1	116.28	70.86	2560
115.1	116.56	69.75	2490
115.1	116.38	70.01	2510
115.1	116.36	70.73	2550

Mean density = 2530 + 30 kg m^{-3} (1.2% error).

Results;

Unit	Sample number	Dry weight ($kg \times 10^{-3}$)	Saturated weight ($kg \times 10^{-3}$) In air	In water	Saturated density ($kg\ m^{-3}$)
Quarry Intrusion	YR907	347.5	349.2	223.1	2770
	YR911	461.7	463.1	297.1	2790
S Cruachan	N55	546.2	347.8	217.0	2660
	N54	255.0	256.5	163.6	2760
	N238	482.6	484.1	310.0	2780
	SB3	103.7	104.8	64.5	2600
	SB9	278.9	279.9	176.2	2700
Meall Odhar	SB10	448.4	451.0	274.1	2550
Outer Starav	N240	232.6	233.7	143.8	2600
	N239	246.4	248.5	153.3	2610
	SB130	125.3	126.3	77.2	2570
Central Starav	N58	see above			2530
	N59	375.2	377.3	231.6	2590
	SB210	163.0	164.1	101.2	2610
	SB23	254.6	255.9	155.9	2560
	SB22	230.0	231.1	140.5	2550
	SB8	386.3	388.9	238.2	2580

Unit	Mean density ($kg\ m^{-3}$)
Quarry Intrusion	2780
S Cruachan units	2700
Meall Odhar Granite	2550
Outer Starav Granite	2593
Central Starav Granite	2570

APPENDIX C GEOCHEMICAL ANALYSES FOR THE ETIVE COMPLEX

Rare Earth Element analyses for Etive samples

Sample No	YR912	SB73	YR1200	N56	SB98	SB121	SB131	SB94	SB20	SB134
La	29.7	60.5	38.0	34.6	39.9	14.9	28.0	37.2	23.7	16.2
Ce	58.2	139.0	71.5	57.0	59.5	48.1	52.9	66.6	42.9	28.4
Nd	26.4	(65.0)	29.0	(19.3)	19.0	14.4	20.4	27.0	16.5	(8.6)
Sm	5.2	10.2	4.7	3.5	3.0	2.8	3.4	3.8	2.7	1.4
Eu	1.55	2.38	1.16	0.98	0.60	0.41	0.94	1.05	0.39	(0.09)
Tb	0.65	1.03	0.66	0.37	0.58	0.54	0.42	0.42	0.46	0.22
Tm	--	(0.36)	--	--	--	--	--	--	(0.2)	--
Yb	1.48	1.90	1.34	1.05	1.30	1.38	0.88	1.03	1.09	0.71
Lu	((0.3))	(0.27)	(0.18)	--	((0.14))	(0.17)	(0.13)	--	(0.16)	(0.14)
Ba	--	992	553	574	343	135	730	679	174	--
Total REEs	123.48	280.64	146.65	116.80	124.11	82.53	107.07	137.10	88.10	55.76

All values expressed in ppm.
Data in single parentheses have analytical error (1 sigma on peak fit) of 10-20%
Data in double parentheses have analytical error (1 sigma on peak fit) of 20-40%

Major and trace element analyses for Etive samples

Sample No	SiO_2	TiO_2	P_2O_5	Rb	Sr	Y	Zr	Nb
Quarry Intrusion								
E3	48.0	1.11	0.13	9	562	16	90	8
YR786	56.3	1.51	0.57	48	1487	25	133	9
YR780	63.8	0.73	0.21	73	930	17	155	11
YR766	63.5	0.76	0.24	65	965	18	165	10
YR1098	65.5	0.78	0.32	61	1061	18	174	10
Cruachan S lobe								
YR1368	59.0	1.04	0.40	57	1236	16	287	9
SB91	59.1	0.76	0.19	63	1109	8	510	8
SB9	59.9	1.00	0.45	62	893	21	143	11
YR1198	60.1	1.01	0.41	66	1055	17	210	11
N238	60.2	1.19	0.71	61	1167	17	115	11
SB73	61.4	0.99	0.30	88	999	24	432	14
E8	61.6	0.92	0.26	56	1110	15	496	11
SB115	61.9	1.03	0.28	65	1110	15	583	11
N54	62.8	1.11	0.39	73	1121	22	120	9
SB138	63.0	0.58	0.18	83	660	15	174	12
N236	64.5	1.08	0.34	68	1148	11	556	9
YR1209	65.8	0.68	0.20	70	946	10	488	9
YR1289	66.5	0.55	0.13	69	846	16	432	8
YR1190	68.9	0.56	0.21	104	625	14	141	12
N55	69.5	0.61	0.20	106	564	19	174	13
SB2	70.4	0.54	0.21	89	610	15	172	13
YR1373	72.1	1.51	0.05	105	354	9	88	8
N56	72.7	0.55	0.22	82	631	12	170	13
Cruachan N lobe								
SB99	67.0	0.51	0.17	121	569	17	181	12
E30	69.3	0.44	0.11	131	533	19	185	11
SB96	70.4	0.40	0.14	148	468	17	162	12
SB124	71.2	0.44	0.14	135	523	20	179	11
SB97	--	0.19	--	192	142	17	112	11
Meall Odhar								
SB108	70.8	0.26	0.05	77	114	11	141	9
SB76	75.6	0.15	0.06	85	37	6	107	7
SB121	76.7	0.14	0.03	99	33	15	111	12
SB59	--	0.15	--	123	96	16	137	10
SB10	78.2	0.18	0.03	131	64	11	141	13
Outer Starav								
SB130	64.8	0.45	0.17	120	561	18	149	13
SB131	69.3	0.42	0.18	107	656	12	150	11
SB140	--	0.33	--	118	388	15	119	11
SB1	71.6	0.50	0.22	96	643	15	171	12
SB80	--	0.44	--	100	681	14	127	12
N239	73.8	0.38	0.16	99	553	11	154	13
N241	74.4	0.26	0.08	124	312	10	119	14
N240	75.7	0.28	0.13	101	410	10	109	12
Central Starav								
N59	74.5	0.25	0.08	119	312	10	100	11
SB8	74.3	0.11	0.03	144	325	9	58	8
N58	76.1	0.13	0.03	163	102	11	76	13
SB133	76.1	0.14	0.08	169	118	10	81	13
SB21D	76.0	0.11	0.03	174	103	10	81	12
SB21C	--	0.13	--	173	106	14	92	16
SB20	76.6	0.15	0.07	176	131	13	97	15
SB23	76.8	0.12	0.04	175	99	11	77	16
SB134	75.8	0.07	--	333	7	12	67	26
SB21B	79.5	0.13	--	167	27	6	43	14

Trace elements expressed in ppm. Major elements are from analyses on pellets, expressed in wt. %.

APPENDIX D RADIOELEMENT DATA AND SAMPLE LOCATIONS FOR THE ETIVE COMPLEX

Reduced data for gamma-ray spectrometer stations

Station number	Sample number	Grid Ref.	Th (ppm)	U (ppm)	Th/U	K20 (%)	Rock Description
Quarry Intrusion							
E3	Core E3	010 330	0.9	0.4	2.3	0.4	Qtz. diorite
E6	SB32	126 295	6.1	2.0	3.1	3.1	Qtz. diorite
S Cruachan units							
E105		063 338	7.1	0.9	7.9	2.5	Monzodiorite
E104		073 334	7.0	1.1	6.4	2.9	"
*E103		078 338	3.8	0.7	5.4	2.3	Diorte
E103		078 338	4.1	0.5	8.2	2.3	Monzodiorite
E102		072 342	12.9	2.2	5.9	3.7	Granodiorite
E101		066 343	5.9	1.7	3.5	2.5	Monzodiorite
*E100		056 352	4.3	1.0	4.3	2.6	"
E100		056 352	8.7	0.7	12.4	4.6	"
E100		056 352	7.6	1.4	5.4	4.3	"
*E99		022 347	13.2	2.2	6.0	5.9	Granodiorite
E99		022 347	5.1	1.7	3.0	3.2	Monzodiorite
E99		022 347	14.3	4.3	3.3	4.2	Granodiorite
E98	SB178	047 339	6.2	1.5	4.1	3.1	Monzodiorite
E97		037 331	10.9	2.1	5.2	3.4	"
E94		006 350	9.1	1.9	4.8	3.4	"
*E92		026 348	8.2	1.6	5.1	3.2	"
E92		026 348	9.3	1.7	5.5	4.4	"
E91		027 348	7.9	2.2	3.6	2.5	"
E79		176 470	8.2	1.9	4.3	2.9	"
*E76		150 477	13.7	3.8	3.6	4.4	Granodiorite
E76		150 477	9.7	2.5	3.9	3.3	Monzodiorite
E67	SB55	086 485	15.5	2.8	5.5	4.9	Granodiorite
E66		072 478	8.2	2.3	3.6	2.8	Monzodiorite
E64		081 480	8.7	2.1	4.1	3.4	"
E63		081 473	10.0	2.6	3.9	3.4	"
E61	SB51	090 473	5.9	1.7	3.5	3.3	"
E60		091 474	9.3	2.3	4.0	3.4	"
*E59		091 482	10.0	2.3	4.3	3.2	"
E59	SB50	091 482	5.2	1.6	3.2	3.1	"
E58	SB49	102 483	10.5	2.5	4.2	3.6	"
E57		098 485	8.6	2.1	4.1	3.6	"
*E56	SB46	099 488	7.8	2.2	3.5	3.3	"
E56	SB47	099 488	7.6	2.2	3.4	2.7	"
E54		106 487	10.1	2.8	3.6	4.0	"
E53	SB44a	114 487	9.1	2.1	4.3	3.4	"
E42		135 478	9.1	2.4	3.8	4.2	"
E41		128 480	7.7	1.9	4.0	4.2	"
E40		122 488	6.5	1.5	4.3	3.8	"
E39	SB47	127 487	8.0	2.0	4.0	3.5	"
E38		143 484	6.7	2.1	3.2	2.9	"
E14		045 370	8.6	1.7	5.1	2.7	"
E13	SB38	044 359	9.5	2.1	4.5	5.3	Granodiorite
E12		021 336	9.9	2.2	4.5	3.3	Monzodiorite
*E10	SB34	040 351	8.8	2.3	3.8	2.2	"
E10	SB35	040 351	12.5	2.5	5.0	4.1	Granodiorite
E10		040 351	5.8	1.8	3.2	2.4	Monzodiorite
E10	Core E10	040 351	10.9	2.2	4.9	4.2	"
E9		036 343	7.2	1.8	4.0	2.9	"

Station number	Sample number	Grid Ref.	Th (ppm)	U (ppm)	Th/U	K20 (%)	Rock Description
E8	Core E8	030 339	5.3	1.9	2.8	2.4	Monzodiorite
E7		039 333	6.7	1.8	3.7	3.4	"
E5		029 348	12.2	2.3	5.3	4.3	Granodiorite
E4		024 343	5.9	1.6	3.7	2.3	Monzodiorite
N Cruachan Adamellite							
E125		240 502	13.5	5.5	2.4	4.1	
E124		222 499	26.8	6.0	4.5	4.5	
E123	SB183	214 502	27.3	8.6	3.2	4.7	
E122		204 505	19.8	6.0	3.3	4.2	
E113		204 513	18.1	5.4	3.3	3.6	
E112	SB181	200 514	19.6	6.5	3.0	4.4	
E89		203 514	19.1	5.6	3.4	4.7	
E87	SB65	208 524	19.0	5.3	3.6	4.8	
E86		204 523	23.1	5.1	4.5	5.2	
E85	SB64	200 523	25.2	6.4	3.9	6.0	
E84		194 500	11.0	2.7	4.1	3.9	
E83		189 493	16.0	4.3	3.7	4.6	
E82		188 487	10.0	2.6	3.8	3.3	
E81		187 483	12.7	3.4	3.7	4.9	
E50		184 510	15.8	4.0	3.9	4.6	
E32		184 511	14.8	4.0	3.7	4.8	
E31		198 513	19.0	4.8	3.6	5.1	
E30	Core E30	212 516	18.6	4.3	4.3	5.2	
E29		225 524	12.0	3.3	3.6	3.9	
Meall Odhar Granite							
E93	SB68	015 345	17.0	2.9	5.9	5.1	
E80	SB61	181 475	13.1	2.6	5.0	5.3	
E79	SB59	176 470	15.3	3.5	4.4	5.1	
Outer Starav Granite							
E121		095 395	10.8	2.2	4.9	4.1	
E120		099 381	9.9	1.7	5.8	3.6	
E119		106 386	9.8	2.4	4.1	3.8	
E118		115 385	10.9	2.4	4.5	3.9	
E77		166 470	13.1	3.4	3.8	4.6	
E76		150 477	15.0	5.0	3.0	4.6	
E75		146 476	11.3	3.0	3.8	4.3	
E74		088 449	8.8	2.8	3.1	4.4	
E73		086 442	14.6	3.4	4.3	4.0	
E72		079 429	12.9	2.5	5.1	4.6	
E71		085 426	13.5	2.8	4.8	5.0	
E62	SB52	090 469	8.8	2.2	4.0	3.3	
E52		106 467	10.3	3.2	3.2	4.2	
E51		114 457	12.0	3.2	3.8	4.3	
E35		141 475	8.5	2.6	3.3	5.1	
E25		058 387	9.9	1.9	5.2	4.2	
E24		064 407	9.0	2.8	3.2	4.3	
E23		063 414	10.5	2.9	3.6	4.4	
E22	SB39	059 420	8.2	2.6	3.1	3.8	
E21		055 411	9.6	2.4	4.0	4.1	
E20		058 407	6.8	1.9	3.6	3.7	
E19		062 400	9.7	2.1	4.6	4.6	
E18	Core E18	066 401	12.3	2.9	4.2	4.0	
E17		079 404	10.7	3.1	3.4	3.4	
E16	Core E16	056 395	10.7	2.1	5.1	4.3	
E15		052 373	9.1	1.8	5.1	3.7	
E14		045 370	8.4	1.7	4.9	3.9	

Station number	Sample number	Grid Ref.	Th (ppm)	U (ppm)	Th/U	K20 (%)	Rock Description
Central Starav Granite							
*E133		109 418	5.9	2.0	3.0	4.0	
E133		109 418	16.7	6.6	2.5	4.1	Microgranite
E132		112 420	18.2	6.8	2.7	4.1	
E131	SB186	114 422	30.2	16.8	1.8	5.1	Microgranite
E130		112 424	21.1	9.3	2.3	4.5	Microgranite
E129		109 428	17.1	6.7	2.5	5.2	
E128		115 429	14.4	4.9	2.9	4.5	
E117		121 392	12.1	4.3	2.8	4.3	
E116		115 397	13.7	4.6	3.0	5.3	
E115		104 396	14.7	4.4	3.3	5.5	
E114		095 409	7.1	1.9	3.7	3.8	
E111		137 439	17.4	6.6	2.6	4.4	
E110		133 431	13.1	3.1	4.2	4.4	
E109		126 427	18.5	2.5	7.4	4.6	
E108	SB179	127 436	10.5	1.6	6.6	3.9	
E107		133 450	19.4	5.5	3.5	4.4	
E106		136 460	18.6	4.9	3.8	4.6	
E70		091 422	18.9	5.1	3.7	5.9	
E69		102 436	13.7	4.5	3.0	4.9	
E68		108 448	20.6	5.2	4.0	5.7	
E49		127 454	22.0	4.6	4.8	4.9	
E48		119 445	16.5	4.1	4.8	4.7	
E47		115 437	16.3	5.0	3.3	4.5	
E46		113 435	14.8	4.3	3.4	4.3	
E45		136 460	13.1	3.0	4.4	4.9	
E37		109 452	14.2	3.4	4.2	4.1	
E36		120 459	9.4	2.2	4.3	4.3	
Aplites							
E76		150 477	19.2	6.0	3.2	6.6	
!E56	SB48a	099 488	13.3	3.4	3.9	3.9	
E46	SB49	113 435	19.5	5.4	3.6	4.4	
Dykes							
E84	SB63	194 500	9.3	2.1	4.4	3.8	
E113	SB182	204 513	9.4	2.5	3.8	2.9	
E112	SB180	200 514	10.4	3.9	2.7	3.5	
E103		078 338	10.7	3.2	3.3	3.6	
E88	SB66	212 521	10.5	2.6	4.0	3.5	
E88	SB67	212 521	13.1	2.9	4.5	4.1	
E83		189 493	13.4	4.0	3.4	5.2	
E81	SB62	187 483	14.5	3.9	3.7	4.9	
E30	SB46	212 516	10.5	2.6	4.0	3.5	
E29	SB44	225 524	6.7	1.8	3.7	3.0	
E28	SB42	233 532	5.1	1.8	2.8	2.7	
E11	SB36	043 358	11.4	2.8	4.1	4.3	
Country rocks							
E2		004 338	9.7	1.5	6.5	3.0	Phyllites
E28	SB41	233 532	4.9	1.5	3.3	2.4	Quartzites + pelites
E33		158 509	6.4	1.6	4.0	5.0	Quartzites + pelites
E34		147 493	6.5	1.8	3.6	3.1	Quartzite
E43	SB48	136 492	13.3	2.5	5.3	4.7	Mica-schist
E44		137 491	16.9	3.0	5.6	4.5	Mica-schist + Granite vein
E27	Core E27	244 543	7.0	2.1	3.4	3.8	Rannoch Moor Granite

Station number	Sample number	Grid Ref.	Th (ppm)	U (ppm)	Th/U	K20 (%)	Rock Description
E65	SB54	072 479	6.9	1.8	3.8	2.8	Phyllites
E90		-018 373	7.9	1.8	4.4	4.5	Phyllites
E126	SB184	246 511	8.4	3.4	2.5	2.5	Quartzose schist
E127		250 523	4.3	1.4	3.1	2.7	Quartzose schist

* More than one intrusive phase at this location
Readings low due to insufficiently large outcrop
! Readings low as width of aplite only 30-40 cm

Data for samples analysed by ENAA and XRF

Sample number	Grid Ref.	Th (ppm)	U (ppm)	Th/U	K20 (%)	Rock Description
Quarry Intrusion						
YR902	080 278	4.9	1.5	3.3	--	Qtz. diorite
YR1090	078 286	6.3	2.2	2.9	--	Diorite
YR906	080 278	4.2	1.3	3.2	--	Qtz. diorite
YR896	080 278	4.7	1.5	3.1	--	" "
YR912	080 278	4.2	1.4	3.0	--	" "
YR909	080 278	4.0	1.1	3.6	--	" "
YR898	080 278	2.9	1.1	2.6	--	" "
YR911	080 278	3.5	1.2	2.9	--	" "
YR907	080 278	3.6	1.2	3.0	--	" "
SB111	082 281	6.2	2.0	3.1	--	" "
S Cruachan units						
N238	045 370	8.5	1.7	4.7	2.0	Monzodiorite
N236	014 335	6.1	1.4	4.3	3.2	"
N235	014 335	--	4.5	--	4.1	Granodiorite
N57	140 475	--	3.6	--	--	"
N56	144 484	8.8	2.4	3.3	3.9	Monzodiorite
N55	150 497	10.6	3.0	3.5	4.9	Granodiorite
N54	150 497	5.6	1.2	4.7	2.5	Monzodiorite
N53	154 503	--	1.6	--	--	"
YR1200	083 298	12.4	3.8	3.3	--	Granodiorite
YR1276	084 308	10.2	1.7	6.0	--	"
YR1340	115 321	7.0	1.7	4.1	--	Monzodiorite
YR1339	115 321	8.0	1.7	4.7	--	"
YR1371	117 324	4.4	1.3	3.4	--	"
YR1294	079 318	7.7	1.7	4.5	--	"
YR1374	091 317	6.7	1.8	3.7	--	"
SB3	029 340	13.0	5.6	2.3	--	Granodiorite
SB4	011 331	6.1	2.7	2.2	--	Diorite
SB115	111 315	6.4	1.6	4.0	2.9	"
SB116	101 319	6.0	1.5	4.0	--	"
SB117	092 319	9.6	2.4	4.0	--	Monzodiorite
SB113	126 314	10.3	1.6	6.4	--	"
SB91	010 390	10.7	1.2	8.9	3.9	"
SB105	095 356	7.9	1.6	4.9	--	"
SB114	118 318	5.7	1.5	3.8	--	Diorite
SB102	094 290	9.5	2.6	3.7	--	Monzodiorite
SB92	009 421	12.5	1.3	9.6	--	"
SB87	032 384	8.4	2.4	3.5	--	"
SB104	095 296	10.0	2.2	4.5	--	Granodiorite
SB119	068 323	6.6	1.6	4.1	--	Diorite
SB112	129 311	8.1	2.2	3.7	--	Monzodiorite

Sample number	Grid Ref.	Th (ppm)	U (ppm)	Th/U	K20 (%)	Rock Description
SB118	081 321	7.1	1.6	4.4	—	"
SB88	019 387	9.6	2.9	3.3	—	"
SB107	076 304	6.7	1.7	3.9	—	"
SB119	068 323	5.3	1.5	3.5	—	Diorite
SB101	080 293	9.4	2.4	3.9	—	Monzodiorite
SB101a	080 293	5.6	2.0	2.8	—	"
SB106	086 356	11.6	1.5	7.7	—	"
SB78	037 370	13.3	4.1	3.2	—	Granodiorite
SB93	027 421	2.3	1.4	1.6	—	Monzodiorite
SB71	025 357	8.1	1.8	4.5	—	"
SB72	018 363	6.9	1.6	4.3	—	"
SB73	005 363	10.8	2.2	4.9	3.6	"
SB74	004 367	7.0	1.5	4.7	—	"
SB75	015 371	6.9	1.6	4.3	—	"
SB77	023 372	5.0	1.6	3.1	—	"
SB69	019 352	8.1	1.7	4.8	—	"
SB138	144 362	6.9	2.1	3.3	3.7	Foliated monzodiorite
N Cruachan Adamellite						
SB124	222 499	18.4	5.0	3.7	4.5	
SB99	230 485	15.7	3.4	4.6	4.3	
SB100	245 477	15.2	4.3	3.5	—	
SB96	203 501	21.0	4.6	4.6	4.8	
SB98	219 493	23.2	9.5	2.4	—	
SB97	209 498	31.7	10.6	3.0	—	
Meall Odhar Granite						
SB122	204 505	16.3	1.8	9.1	—	
SB10	033 382	16.7	2.5	6.7	5.7	
SB120	059 318	15.8	2.2	7.2	—	
SB121	052 311	18.1	3.3	5.5	5.9	
SB108	067 305	15.4	2.5	6.2	5.5	
SB109	061 294	17.4	1.6	10.9	—	
SB86	033 384	13.1	1.7	7.7	—	
SB90	023 399	16.1	2.4	6.7	—	
SB76	020 371	8.2	1.1	7.5	5.9	
SB12	037 386	6.5	1.0	6.5	—	
Outer Starav Granite						
N241	080 405	10.9	2.6	4.2	4.7	
N240	066 401	11.8	4.2	2.8	4.1	
N239	055 396	10.9	2.0	5.5	4.1	
N59	120 459	10.6	1.5	7.1	5.0	
SB125	187 458	9.3	2.7	3.4	—	
SB131	152 376	7.5	3.0	2.5	4.6	
SB126	187 450	10.4	2.4	4.3	—	
SB11	038 385	4.8	1.7	2.8	—	
SB1	055 378	11.4	3.0	3.8	4.2	
SB123	203 434	15.6	3.0	5.2	—	
SB137	121 358	7.8	2.4	3.3	—	
SB85	070 427	12.1	3.2	3.8	4.5	
SB82	049 436	11.0	2.4	4.6	—	
SB141	186 404	12.4	3.3	3.8	—	
SB130	190 414	10.3	2.6	4.0	4.5	
SB94	034 408	9.8	2.6	3.8	—	
SB80	048 418	9.5	2.5	3.8	—	
SB57	091 456	9.8	3.2	3.1	—	
SB79	051 404	10.8	1.5	7.2	—	
SB83	050 449	11.0	2.5	4.4	—	
SB84	067 445	9.7	2.2	4.4	—	

Sample number	Grid Ref.	Th (ppm)	U (ppm)	Th/U	K20 (%)	Rock Description
SB81	047 427	10.6	2.2	4.8	--	
SB82	049 436	8.1	2.2	3.7	--	
SB58	099 463	15.3	2.9	5.3	--	
Central Starav Granite						
SB22	139 450	--	6.7	--	--	
SB21a	137 446	--	6.5	--	--	
SB21b	137 446	22.5	8.0	2.8	--	
SB21c	137 446	21.3	6.2	3.4	5.2	
SB133	138 402	17.9	6.3	2.8	5.0	
SB135	159 418	16.3	6.1	2.7	5.0	
SB8	091 418	7.8	3.8	2.1	5.9	
SB128	180 437	12.1	3.5	3.5	--	
SB129	181 425	10.1	2.3	4.4	--	
SB127	174 447	20.9	4.5	4.6	5.2	
SB132	142 384	13.3	2.9	4.6	--	
N58	106 452	15.2	7.0	2.2	5.0	
SB50	137 442	17.2	7.1	2.4	5.3	
SB23	138 458	19.5	10.7	1.8	5.1	
SB134a	144 416	23.0	11.6	3.1	--	Microgranite
SB134b	144 416	25.2	8.0	6.8	--	Microgranite
Aplites						
SB53		29.6	4.2	7.0	--	
SB21d	137 446	25.7	7.1	3.6	4.9	
SB56		18.4	2.7	6.8	--	
Dykes						
N229	014 335	--	3.2	--	--	Qtz. porphyry
YR899	080 278	4.9	1.5	3.3	--	Microdiorite
SB7		7.6	2.3	3.3	--	Porphyritic
SB6	011 331	11.0	3.0	3.7	5.3	Qtz. porphry

Sample number prefixes are:
YR - Collected from tunnels of the Loch Awe Power Station; D Smith, IGS Edinburgh
N - Collected by G Brown, J Cassidy and J Hughes
SB - Collected during this study

APPENDIX E PROCEDURE FOR ESTIMATING URANIUM AND THORIUM CONTRIBUTIONS FROM SPHENE AND THORITE

a) Uranium and Th contributions from zircon and apatite are subtracted from whole rock values to give Th_{rem} and U_{rem}.

b) Then:

$$\frac{Th_{rem} - Th_{sp}}{U_{rem} - U_{sp}} = (Th/U)_{thor}$$

where Th_{sp} = Th contribution from sphene

U_{sp} = U contribution from sphene

$(Th/U)_{thor}$ = Th/U ratio of thorite from microprobe analyses

i.e. all remaining U and Th is assumed to reside in sphene and thorite.

c) Substituting $\frac{Th_{sp}}{U_{sp}} = (Th/U)_{sp}$ in the above equation gives;

$$U_{sp} = \frac{(Th/U)_{thor} \times U_{rem} - Th_{rem}}{(Th/U)_{thor} - (Th/U)_{sp}}$$

and $$Th_{sp} = U_{sp} \times (Th/U)_{sp}$$

d) Calculating a new remainder by subtracting contributions from sphene and assuming all remaining Th is located in thorite;

$$\text{ppm } Th_{rem} = \text{ppm } Th_{thor} = \frac{\text{ppm thorite} \times \% \text{ thorite}}{100}$$

e) If the rock density = D g cm^{-3} then in 1 cm^3 of rock we need;

$$\frac{D \text{ (ppm thorite)}}{10^6} \text{ grams of thorite}$$

f) The density of thorite is approximately 5.3 g cm^{-3} (Frondel, 1958) therefore, in 1 cm^3 of rock we need;

$$\frac{D \text{ (ppm thorite)}}{10^6 \times 5.3} \ cm^3 \text{ thorite}$$

g) Assuming approximate 3-dimensional symmetry of thorite crystals and that all are approximately the same size, then the volume of each crystal (from photomicrgraphs) is $\sim 6.8 \times 10^{-6}$ cm^3

h) The volume density of thorite required to satisfy the Th excess is then given by;

$$\frac{D \text{ (ppm thorite)}}{10^6 \times 5.3 \times 6.8 \times 10^{-6}} \text{ per cm}^3$$

$$= \frac{D \text{ (ppm thorite) } 100}{(\% \text{ Th})_{thor} \times 36.04} \text{ per cm}^3$$

APPENDIX F GEOCHEMICAL ANALYSES FOR THE CAIRNGORM GRANITE

Rare Earth Element analyses for Cairngorm samples

Sample No	SB161	SB170	SB177	SB162	N190	N187
La	61.0	49.5	44.5	34.0	34.6	53.7
Ce	103.5	93.8	87.6	70.7	71.0	115.1
Nd	42.0	34.3	35.0	30.1	33.3	50.7
Sm	6.3	5.4	7.7	7.4	9.0	13.4
Eu	1.09	(1.10)	0.27	0.20	0.18	0.03
Gd	(8.4)	--	(12.9)	(11.9)	(14.0)	17.4
Tb	0.75	0.60	1.25	1.03	1.82	2.84
Tm	(0.33)	--	0.79	0.87	1.25	2.59
Yb	2.04	1.89	5.10	5.53	8.41	15.95
Lu	(0.29)	(0.30)	(0.60)	(0.73)	1.13	(2.17)
TOTAL REEs	225.6	186.9	195.7	164.7	174.7	274.2

All values expressed in ppm.
Data in parentheses have analytical error (1 sigma on peak fit) of 10-20%.

Major and trace element analyses for Cairngorm samples

Sample Number	Unit	SiO	TiO	Al O	Fe O	MnO	MgO	CaO	Na O	P O	Rb	Sr	Y	Zr	Nb	Ba	Ce	Rb/Sr
SB160	N.E. Granite	71.01	0.37	14.72	2.22	0.04	0.37	1.28	3.80	0.12	200	179	28	202	21	684	102	1.12
SB161	"	70.34	0.35	15.58	2.21	0.04	0.62	1.25	3.72	0.15	211	220	26	181	18	777	112	0.96
SB170	"	70.62	0.31	15.45	1.86	0.04	0.30	1.31	3.93	0.08	208	221	26	141	17	756	100	0.94
N198	Porph. Granite	74.71	0.21	13.86	1.55	0.05	0.16	0.84	3.24	0.06	323	124	23	160	16	668	60	2.60
N191	Microgranite	74.51	0.16	14.04	1.19	0.03	0.09	0.35	3.21	0.05	348	84	32	127	25	358	117	4.14
N192	"	--	--	--	--	--	--	--	--	--	269	107	27	127	18	504	120	2.51
N193	"	74.63	0.18	13.64	1.21	0.03	0.07	0.53	3.70	0.06	248	108	26	122	18	485	105	2.30
N208	Main Granite	--	(0.21)	--	(1.69)	--	--	--	--	--	287	80	33	152	22	240	69	3.59
N209	"	--	(0.19)	--	(1.21)	--	--	--	--	--	286	66	19	147	17	194	79	4.33
N210	"	--	--	--	--	--	--	--	--	--	300	57	28	116	23	175	118	5.26
N186	"	--	(0.16)	--	(1.03)	--	--	--	--	--	345	71	27	86	33	202	48	4.86
N184	"	--	(0.16)	--	(1.08)	--	--	--	--	--	356	62	34	116	30	226	77	5.74
SB178	"	75.51	0.10	13.46	0.99	0.05	0.01	0.41	4.00	0.04	358	44	67	083	40	145	31	8.14
SB167	"	75.23	0.14	13.05	0.99	0.04	0.12	0.40	3.89	0.03	395	49	52	110	33	160	73	8.06
N164	"	--	(0.15)	--	(1.18)	--	--	--	--	--	424	45	37	106	39	149	64	9.42
SB177	"	76.57	0.14	12.74	1.12	0.04	0.15	0.34	3.16	0.06	440	46	45	105	41	176	58	9.56
N169	"	--	(0.12)	--	(1.00)	--	--	--	--	--	446	52	24	114	26	170	43	8.58
SB162	"	77.17	0.11	12.29	0.87	0.06	0.06	0.32	3.49	0.03	452	31	50	99	41	114	54	14.58
N165	"	--	(0.14)	--	(1.33)	--	--	--	--	--	454	54	44	131	33	212	74	8.41
N197	"	--	--	--	--	--	--	--	--	--	457	48	36	91	41	123	33	9.52
N188	"	76.73	0.10	13.44	0.73	0.06	0.10	0.43	3.86	0.05	458	42	49	69	44	126	32	10.90
N170	"	--	(0.15)	--	(1.31)	--	--	--	--	--	474	36	59	85	42	144	59	13.17
N187	"	72.80	0.21	14.68	1.66	0.07	0.30	0.47	3.82	0.05	476	49	113	113	56	158	77	9.71
N168	"	--	(0.15)	--	(1.32)	--	--	--	--	--	482	53	21	118	38	195	71	9.09
N190	"	76.93	0.09	12.73	0.81	0.03	0.09	0.44	3.73	--	484	34	67	87	60	129	56	14.23
N212	"	77.92	0.07	12.65	0.82	0.03	0.20	0.33	3.85	0.04	519	6	72	77	72	13	74	86.50
N189	"	--	--	--	--	--	--	--	--	--	549	19	66	70	53	57	49	28.89
N167	"	--	(0.08)	--	(0.85)	--	--	--	--	--	567	27	40	97	54	105	48	21.00
N166	"	--	(0.07)	--	(0.78)	--	--	--	--	--	590	25	33	89	45	121	51	23.60
N211	"	76.62	0.08	13.01	0.72	0.05	0.07	0.32	3.63	0.03	618	16	62	78	67	54	46	38.62
N83	"	--	(0.05)	--	(0.09)	--	--	--	--	--	604	16	49	37	76	9	22	37.75
N82	"	--	(0.03)	--	(1.01)	--	--	--	--	--	765	14	65	44	57	33	32	54.64

Major element oxides expressed in wt %. Trace elements expressed in ppm. Data in parentheses analysed by P. Webb.

APPENDIX G RADIOELEMENT DATA AND SAMPLE LOCATIONS FOR THE CAIRNGORM GRANITE

Reduced data for gamma-ray spectrometer stations

Station number	Sample number	Grid Ref.	Th (ppm)	U (ppm)	Th/U	K20 (%)	
N E Granite							
C61		149 065	25.6	4.7	5.4	4.4	
C63	SB160	115 066	21.8	2.8	8.0	4.8	
C64	SB161	098 063	21.8	3.7	5.9	5.0	
C65		088 068	20.3	4.6	4.4	4.8	
C66		072 063	29.2	3.7	7.9	4.3	
C67		064 066	30.8	3.3	9.8	4.2	
C73		072 051	44.0	6.3	7.0	4.0	
C93		088 054	20.7	2.3	9.0	4.8	
C101	SB170	099 061	24.6	7.1	3.5	5.5	
Porphyritic Granite							
C11		904 035	34.1	5.8	8.1	4.4	
C13		888 012	19.9	5.2	3.8	4.5	
C27		907 020	32.3	5.1	6.3	4.5	
C30		903 989	25.6	3.8	6.7	4.3	
C31		904 984	22.0	9.1	2.4	4.3	
Main Granite							
C2	SB178	914 071	23.1	14.2	1.7	4.7	
C3		911 064	20.9	6.9	3.0	4.4	
C4		919 057	23.4	5.7	4.1	4.4	
C5		911 054	17.1	4.9	3.5	4.5	
C6		900 048	19.0	4.3	4.4	4.4	
C7		899 056	22.3	5.0	4.5	4.5	
C8		901 066	17.7	5.5	3.2	3.9	
C10		891 053	25.0	10.6	2.4	5.5	
C12		882 044	17.1	11.8	1.4	4.8	
C14		866 019	20.5	5.3	3.9	4.2	
C15		870 027	18.2	5.2	3.5	4.6	
C16		876 035	18.9	5.6	3.4	4.3	
C17		859 971	18.1	10.5	1.7	4.9	
C17		859 971	19.6	20.5	1.0	5.1	Mineralised joint
C18		861 010	19.4	7.0	2.8	4.5	
C19	SB150	966 054	39.8	16.4	2.4	5.7	
C20		961 052	31.1	14.1	2.2	4.6	
C21		955 061	33.8	16.9	2.0	4.7	
C22		994 066	40.9	11.5	3.6	4.6	
C23		000 058	35.3	9.5	3.7	4.8	
C24		004 053	38.5	10.9	3.5	4.8	
C25		003 068	55.3	11.7	4.7	5.4	
C26		001 069	42.3	9.0	4.7	4.7	
C28		907 008	37.6	7.9	4.8	4.1	
C29		905 002	40.5	5.9	6.9	4.3	
C32		880 955	23.9	11.9	2.0	6.1	
C33		873 960	19.0	6.0	3.2	4.3	
C34		988 072	27.9	8.7	3.3	4.9	
C35		966 065	40.7	12.6	3.2	4.6	
C36		967 072	20.2	9.3	2.2	4.3	
C37		979 037	32.8	10.7	3.1	5.1	
C38		983 043	29.6	8.6	3.4	4.4	
C39		978 015	28.3	9.7	2.9	4.3	
C40	SB151	983 026	32.7	10.2	3.2	4.5	

Station number	Sample number	Grid Ref.	Th (ppm)	U (ppm)	Th/U	K20 (%)
C41		996 030	30.2	10.1	3.0	4.5
C42		999 035	31.6	9.9	3.2	4.0
C43		998 041	27.8	13.4	2.1	4.6
C44		993 046	33.8	9.2	3.7	4.4
C45		013 054	41.7	9.3	4.5	4.3
C46		016 061	40.7	9.2	4.4	3.7
C47		016 075	36.4	10.6	3.4	4.3
C48	SB152	015 081	31.8	10.4	3.1	4.6
C49		942 019	33.9	14.9	2.3	4.3
C49A		947 018	36.6	18.4	2.0	4.9
C50	SB153	868 008	20.6	8.1	2.5	5.1
C51	SB154	866 010	19.2	7.2	2.7	6.0
C52	SB155	863 010	28.2	12.4	2.3	5.4
C53	SB156	861 010	17.8	7.8	2.3	4.6
C56		162 054	53.3	9.1	5.9	4.6
C57		159 044	52.8	7.4	7.1	4.7
C58		152 033	51.1	10.1	5.1	4.6
C59		139 029	53.8	8.1	6.6	4.5
C60		127 035	36.9	4.1	9.0	4.3
C68		050 061	40.8	11.5	3.5	4.7
C69		050 058	37.0	13.1	2.8	4.5
C70		047 052	38.9	15.8	2.5	4.6
C71		048 051	44.0	11.8	3.7	4.8
C72	SB162	054 045	41.3	13.9	3.0	4.8
C74		919 981	25.9	8.2	3.2	5.0
C75		921 978	18.1	6.1	3.0	4.8
C76	SB163	926 981	21.2	6.1	3.5	4.7
C77		934 986	25.6	8.0	3.2	4.6
C78	SB164	946 993	34.8	12.1	2.9	4.8
C79		952 998	34.9	11.1	3.1	4.4
C80	SB165	956 000	32.9	6.9	4.8	4.4
C81		964 005	29.5	13.0	2.3	4.9
C82		963 013	31.4	11.2	2.8	5.0
C83		963 022	28.2	9.0	3.1	4.4
C84		960 029	33.9	13.1	2.6	4.8
C85		959 038	28.9	11.1	2.6	5.3
C86		017 041	38.9	10.2	3.8	5.0
C87		012 030	38.1	6.8	5.6	4.4
C88		003 023	38.5	10.9	3.5	4.6
C89		998 021	37.9	11.0	3.4	4.7
C90	SB166	992 020	27.1	12.9	2.1	4.6
C91	SB167	988 071	36.0	10.6	3.4	5.0
C94		082 034	48.1	8.7	5.5	4.4
C95		088 025	31.6	7.8	4.0	4.8
C96		092 002	30.8	9.3	3.3	4.6
C97		109 005	43.5	8.9	4.9	4.5
C98		105 015	41.2	9.2	4.5	4.4
C99	SB169	112 025	55.3	10.8	5.1	4.8
C100		105 038	34.5	5.6	6.2	4.4
C103		988 902	30.5	6.2	4.9	4.3
C104		976 904	27.7	7.7	3.6	4.5
C105		969 909	21.3	6.4	3.3	4.8
C106	SB171	948 926	13.9	9.5	1.5	4.7
C107	SB172	944 931	19.2	6.5	2.9	4.1
C108		957 937	17.2	7.8	2.2	4.3
C109		969 939	26.8	7.6	3.5	4.5
C110		038 941	24.5	5.4	4.5	4.7

Station number	Sample number	Grid Ref.	Th (ppm)	U (ppm)	Th/U	K20 (%)	
C111		037 947	20.5	5.1	4.0	4.2	
C112	SB173	025 957	35.3	9.7	3.6	4.8	
C113		019 964	38.4	9.1	4.2	4.6	
C114	SB174	018 954	40.0	11.4	3.5	4.6	
C115	SB175	019 944	20.2	4.5	4.5	4.3	
C116	SB176	027 938	25.0	17.3	1.4	5.3	
C118	SB177	973 053	38.2	7.1	5.6	4.4	
Aplites							
C61	SB158	149 065	32.8	10.3	3.2	6.6	
Country rocks - Moine schists							
C1		914 090	8.4	1.6	5.1	4.3	
C9		889 068	9.0	1.6	5.6	2.8	
C48		015 081	19.5	5.7	3.4	4.3	At contact
C54	SB157	860 010	13.5	4.3	3.1	3.9	At contact
C55		860 010	14.7	4.3	3.4	4.0	Near contact
C62	SB159	156 068	25.4	7.8	3.3	4.4	Near contact,qtz. + granite veins
C92	SB168	175 072	31.7	6.2	5.1	5.0	Near contact,qtz. + granite veins
C102		015 886	11.0	3.1	3.5	3.2	
C117		067 900	13.0	2.9	4.5	3.2	

Data for samples analysed by ENAA and XRF

Sample number	Grid Ref.	Th (ppm)	U (ppm)	Th/U	K20 (%)
Microgranite					
N191	974 005	21.2	5.3	4.0	5.4
N192	972 016	20	4	5.0	--
N193	966 024	21	4	5.3	--
Porphyritic Granite					
N198	910 997	21	8	2.6	5.4
Main Granite					
N82	858 009	12	8	1.5	5.1
N83	860 010	8	7	1.1	4.8
N164		34	9	3.8	4.9
N165	985 025	43	13	3.3	5.2
N166	007 039	34	9	3.8	5.1
N167	996 044	41	17	2.4	4.8
N168	997 057	59	14	4.2	5.5
N169	995 058	33	8	4.1	5.1
N170	994 065	31	10	3.1	5.3
N184		37	10	3.7	4.9
N186	028 938	28	10	2.8	4.9
N187	011 939	59.2	30.9	1.9	6.3
N188	986 949	24.1	14.5	1.7	5.0
N189	984 975	32.8	15.3	2.1	--
N190	973 991	35.2	17.7	2.0	4.9
N197	922 999	21	8	2.6	4.6
N208	042 077	49	5	9.8	5.3
N209	048 049	47	10	4.7	4.9
N210	041 031	47.6	11.5	4.1	--
N211	049 030	40.8	16.7	2.4	4.8
N212	060 032	47.1	18.5	2.5	4.8